Lateral mixing in shallow cumulus convection

de Rooij, W.C.

DOI
10.4233/uuid:7f93540c-b40a-4eb4-a206-1127aa400a25

Publication date
2023

Document Version
Final published version

Citation (APA)
de Rooij, W. C. (2023). *Lateral mixing in shallow cumulus convection*. [Dissertation (TU Delft), Delft University of Technology]. https://doi.org/10.4233/uuid:7f93540c-b40a-4eb4-a206-1127aa400a25

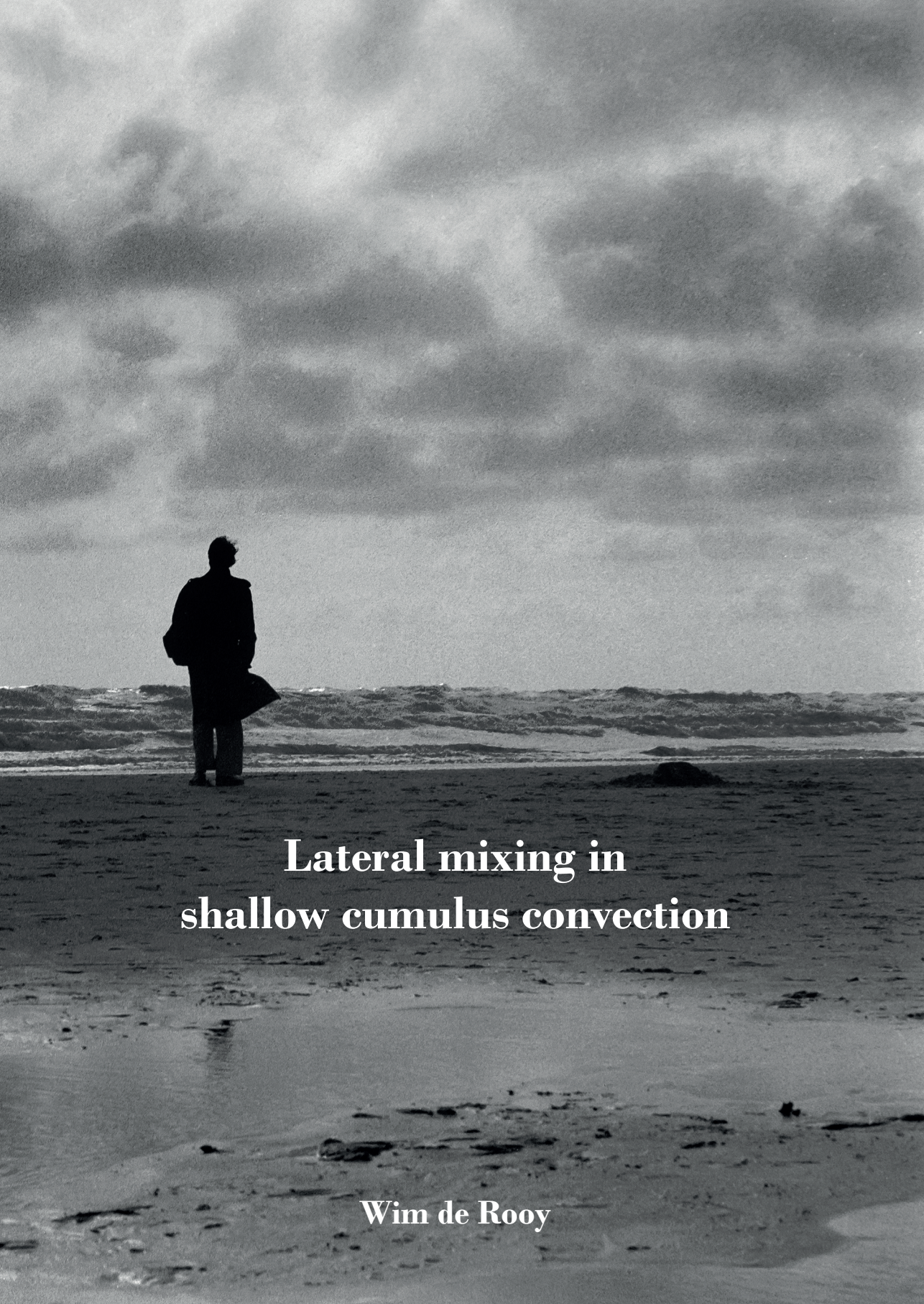

Lateral mixing in shallow cumulus convection

Wim de Rooy

LATERAL MIXING IN SHALLOW CUMULUS CONVECTION

LATERAL MIXING IN SHALLOW CUMULUS CONVECTION

Proefschrift

ter verkrijging van de graad van doctor
aan de Technische Universiteit Delft,
op gezag van de Rector Magnificus prof.dr.ir. T.H.J.J. van der Hagen,
voorzitter van het College voor Promoties,
in het openbaar te verdedigen op dinsdag 23 mei 2023 om 12:30 uur

door

Wilhelmus Cornelis DE ROOIJ

doctorandus in de Meteorologie en Fysische Oceanografie, Universiteit Utrecht
geboren te Breda, Nederland

Dit proefschrift is goedgekeurd door de

promotor: Prof. Dr. A.P. Siebesma

Samenstelling promotiecommissie:

Rector Magnificus,	voorzitter
Prof. Dr. A.P. Siebesma	Technische Universiteit Delft en KNMI
Onafhankelijke leden:	
Prof. Dr. Ir. H.W.J. Russchenberg	Technische Universiteit Delft
Prof. Dr. H.J.J. Jonker	Technische Universiteit Delft
Prof. Dr. J. Vila-Guerau de Arellano	Wageningen Universiteit
Prof. Dr. R.A.J. Neggers	Universität zu Köln,
Dr. S.J. Böing	University of Leeds
Dr. A.A. Nuijens	Technische Universiteit Delft

Drukwerk:	www.proefschriftprinten.nl
Ontwerp omslag:	Peter Rothengatter, www.hetfotoatelier.nl
Foto omslag:	Wim de Rooy (Pa aan de Noordzee)
ISBN:	978-94-6469-365-2

Voor Pa

If you wish to see the valleys
climb to the mountain top
if you desire to see the mountain top
rise into the cloud
but if you seek to understand the cloud
close your eyes and think.

Khalil Gibran

CONTENTS

SAMENVATTING

Cumuluswolken ontstaan doordat relatief warme en lichte lucht opstijgt, ook wel convectie genoemd, en op grotere hoogte dusdanig afkoelt dat er zich wolkendruppeltjes vormen. In dit proefschrift gaat het met name over de kleine ondiepe cumuluswolken waaruit het niet of nauwelijks regent en die we associëren met een vriendelijk en rustig weertype. Het is daarom misschien verrassend dat deze wolken toch een belangrijke rol spelen in het weer en klimaat op lokale en zelfs globale schaal. Dit komt niet alleen door het effect op de straling maar vooral door het vertikale transport van wind, temperatuur en vocht, door die cumuluswolken. Het is dus belangrijk dat we deze wolken goed beschrijven in weer- en klimaatmodellen.

In weer- en klimaatmodellen worden wind, temperatuur en vocht in de atmosfeer uitgerekend op een 3-dimensionaal rooster. Zelfs met moderne, krachtige computers liggen die roosterpunten te ver uit elkaar om kleine cumuluswolken expliciet te beschrijven. Daarom schatten we de impact van ondiepe cumuluswolken op hun omgeving met een vereenvoudigde beschrijving van de fysische processen, in een zogenaamde parameterisatie. Voor cumuluswolken gebruiken we daarvoor meestal een massaflux benadering waarin het totale vertikale transport door alle cumuluswolken binnen een model roostercel wordt beschreven door 1 convectieve opwaartse luchtstroom oftewel massaflux.

Een cumuluswolk is niet volledig afgeschermd maar zal lucht uitwisselen met zijn omgeving. Deze horizontale (laterale) uitwisseling wordt beschreven door 2 parameters genaamd de entrainment (letterlijk op de trein stappen) en de detrainment. Entrainment is de instroom van omgevingslucht de cumulus wolk in. De tegenhanger is de detrainment die de lucht beschrijft die de cumulus wolk verlaat en in de omgeving wordt opgenomen. Deze uitwisseling heeft belangrijke gevolgen voor het vertikale transport door de wolk. Zo veranderen door het invangen van omgevingslucht (entrainment) de eigenschappen van de opwaartse luchtstroom zoals vochtigheid, temperatuur, en daarmee het stijgvermogen. Hiermee verandert dus ook het vertikale transport van vocht en temperatuur en de hoogte tot waar de opwaartse luchtstroom kan komen. Entrainment en detrainment behoren dan ook tot de meest gevoelige parameters in een weer- en klimaatmodel en zijn het hoofdonderwerp van dit proefschrift. We bepalen hoe entrainment en detrainment in een massaflux concept variëren en hoe we die kennis vervolgens kunnen toepassen in een weer- of klimaatmodel.

Voor deze studie is veelvuldig gebruik gemaakt van "Large Eddy Simulation" (LES) modellen. Deze LES modellen rekenen op een dermate fijn rooster (10 ~ 100 m) dat ze cumuluswolken, inclusief de bijbehorende luchtstromingen, kunnen beschrijven zonder parameterisatie. Hiermee zijn ze dan ook buitengewoon geschikt om entrainment en detrainment te bestuderen. LES roostercellen zijn echter dermate klein dat we voor een praktische weersverwachting zeer veel cellen nodig zouden hebben voor een voldoende groot rekengebied. De huidige computerkracht is hier nog ontoereikend voor. Roostercellen in operationele weer- (1 ~ 20 km) en klimaatmodellen (20 ~ 200 km) zijn dan ook beduidend groter dan in LES modellen. Daarom bevindt in één weer- of klimaatmodel roostercel zich typisch een ensemble van enkele grote en vele kleinere cumuluswolken. LES resultaten worden dan ook gebruikt om geschikte entrainment en detrainment formuleringen te bepalen die horen bij zo'n ensemble van wolken.

Het analyseren van LES data voor verschillende situaties met cumuluswolken, leidde tot een verrassende ontdekking: Van geval tot geval, en van uur tot uur, blijkt er een veel grotere variatie te zitten in de detrainment dan in de entrainment (hoofdstuk 2). Het gevolg is dat de entrainment al redelijk goed te beschrijven is met een eenvoudige functie die alleen afhangt van de hoogte. Voor een goede schatting van de detrainment moeten we echter meer moeite doen.

De Large Eddy simulaties laten allereerst zien dat de detrainment sterk variëert met de wolkenlaagdiepte. Dit kunnen we verklaren vanuit geometrische overwegingen (hoofdstuk 2). De detrainment blijkt echter ook te variëren met 2 andere factoren. Ten eerste: Als de omgevingslucht heel droog is zullen er bij het invangen van deze lucht in een cumulus wolk veel wolkendruppels verdampen. Hierdoor zal het mengsel sterk afkoelen en misschien zelfs zwaarder worden dan de omgevingslucht en daardoor de opwaartse luchtstroom verlaten. Hiermee is droge lucht dus destructief voor de cumuluswolk en zal deze leiden tot hogere detrainment waardes. Ten tweede: Als cumuluswolken een groot drijfvermogen hebben (veel lichter zijn dan hun omgeving) is er veel omgevingslucht nodig om een mengsel te maken dat zwaarder is dan de omgevingslucht. Dit komt overeen met kleine waardes van detrainment. In hoofdstuk 2 wordt uitgelegd dat het gecombineerde effect van beide processen mooi kan worden beschreven met 1 parameter, de kritische mengfractie. Dit is de fractie omgevingslucht die nodig is om het mengsel van cumuluswolk- en omgevingslucht precies even zwaar te maken als de omgevingslucht. Het is aannemelijk dat er nog meer processen bijdragen aan de goede correlatie tussen detrainment en de kritische mengfractie. Wolken met een groot drijfvermogen zijn over het algemeen ook grote wolken, met een relatief klein oppervlakte om te mengen en een hoge opwaartse snelheid. Zodoende mengen deze wolken relatief minder met de omgeving, overeenkomend met weinig massaverlies. Ook vanuit dit oogpunt bezien komen hoge

kritische mengfracties overeen met kleine detrainment waardes.

LES laten dus zien dat de detrainment veel meer variëert van geval tot geval dan de entrainment. Hiermee heeft de detrainment dan ook een veel grotere invloed op fluktuaties in het massafluxprofiel. We weten echter nog niet waarom dat zo is. Om daar achter te komen is de uitwisseling tussen cumuluswolk en zijn omgeving beschreven in budgetvergelijkingen (hoofdstuk 3). We maken hierbij onderscheid tussen turbulente uitwisseling door kleine werveltjes en georganiseerde, grootschaligere uitwisseling. Het beeld dat uit de budgetvergelijkingen naar voren komt is als volgt: Individuele wolken in het ensemble hebben alleen een georganiseerde entrainment net onder de wolkenbasis. Bij het stijgen van een wolk is er wel uitwisseling met de omgevingslucht via kleine turbulente wervels maar daarbij gaat ongeveer net zoveel lucht de wolk in als uit en daarmee verandert de sterkte van de individuele opwaartse luchtstroom dus niet. Uiteindelijk komt de individuele wolk op een bepaalde hoogte echter tot stilstand en verliest op die hoogte al zijn massa aan de omgeving, de georganiseerde detrainment. De hoogtes waarop die georganiseerde detrainment van de individuele wolken plaatsvinden bepalen uiteindelijk de afname van de totale opwaartse luchtstroom (massaflux) die het gehele cloudensemble representeert. Hiermee is duidelijk dat het niet de entrainment maar de detrainment is die het massafluxprofiel in de wolkenlaag domineert.

Het is uiteindelijk de bedoeling om de hierboven beschreven kennis over entrainment en detrainment toe te passen in een weer- of klimaatmodel om de verwachtingen te verbeteren. Het model dat hiervoor gebruikt wordt is het HARMONIE-AROME model (HIRLAM ALADIN Research on Mesoscale Operational NWP in Euromed - Application of Research to Operations at MEsoscale) dat ontwikkeld is door verscheidene Europese landen waaronder Nederland. Dit model heeft een rooster waarbij de rekenpunten 2.5 km van elkaar liggen en is daarmee niet in staat om kleine cumuluswolken expliciet te beschrijven. Daarom heeft HARMONIE-AROME een convectieparameterisatie voor ondiepe cumuluswolken nodig. Hoewel entrainment en detrainment hierin cruciale parameters zijn, worden de uiteindelijke prestaties mede bepaalt door andere modelcomponenten. Bovendien zijn er sterke koppelingen met andere parameterisaties. Ontwikkeling en optimalisatie van deze schema's kan dan ook het beste integraal worden aangepakt. Een voorbeeld hiervan vinden we in hoofdstuk 4 waarin het convectieschema en sterk daaraan gekoppelde parameterisaties, alsmede substantiële aanpassingen daarin, worden beschreven. Zoals wordt aangetoond leiden deze aanpassingen tot sterke verbeteringen in de HARMONIE-AROME verwachtingen, met name voor lage wolken.

De rode draad door dit proefschrift is als volgt samen te vatten: In de introductie (hoofdstuk 1) leiden we het onderzoeksonderwerp in en geven we een his-

torisch overzicht van studies naar laterale menging in cumuluswolken. Empirische bevindingen op grond van LES resultaten voor laterale menging in ondiepe cumulus, en de uitwerking daarvan voor een weer- of klimaatmodel, worden beschreven in hoofdstuk 2. Een theoretische onderbouwing van deze empirische resultaten is te vinden in hoofdstuk 3. Hoe al deze kennis tenslotte in een weer- en klimaatmodel in de praktijk wordt gebracht en is ingebed in schema's die daar sterk aan gekoppeld zijn, is het onderwerp van hoofdstuk 4. Dit proefschrift illustreert dat modelonderzoek en ontwikkeling op het gebied van modelfysica een lange adem nodig heeft maar ook dat deze kunnen leiden tot belangrijke verbeteringen in de verwachtingen.

SUMMARY

Cumulus clouds originate by the rise of relatively warm and light air through convection. During the rise, the air cools and cloud droplets are formed by condensation. This thesis mainly concerns small shallow cumulus clouds that produce no, or almost no, precipitation and that we associate with calm, nice weather. Therefore, it might come as a surprise that these clouds still play an important role in weather and climate, not only on a local but even on a global scale. This is not only due to the impact on radiation, but even more by the vertical transport of heat, humidity and wind by these cumulus clouds. Hence, an adequate representation of these cumulus clouds in weather and climate models is key.

In weather and climate models, wind, temperature and humidity in the atmosphere are calculated on a 3 dimensional grid. Even with modern, powerful computers these grid points are too far apart to explicitly describe small cumulus clouds. Therefore, the impact of these clouds have to be estimated by a simplified representation of the physical processes in what is called a parameterisation. For cumulus clouds the most applied approach is a mass flux approximation in which the total vertical transport by all cumulus clouds in a model grid cell is represented by one convective updraft or mass flux.

Cumulus clouds do not develop in isolation but will exchange air with their environment. This horizontal (lateral) exchange is described by 2 parameters: the entrainment (literally getting on the train) and the detrainment. Entrainment is the inflow of environmental air into the cumulus cloud, whereas its counterpart the detrainment describes the outflow of updraft air into the environment. This exchange has important consequences for the vertical transport by the cloud. For example, by capturing environmental air the properties of the upward air flow like humidity and temperature, and thereby the buoyancy, will change. Consequently, the vertical transport of humidity and heat, as well as the termination height of the cloud is influenced by lateral mixing. Entrainment and detrainment belong to the most sensitive parameters in weather and climate models and are the main subject of this thesis. We determine how entrainment and detrainment vary within the mass flux concept and how we can apply this knowledge in weather and climate models.

Many analyses of this thesis are based on results of "Large Eddy Simulation" (LES) models. These LES models perform their calculations on such a fine grid ($10 \sim 100$ m) that cumulus clouds, including the corresponding air flows, can be

well numerically resolved without the use of detailed parameterisations. Therefore, they are extremely useful to study entrainment and detrainment. However, an LES grid mesh is so fine that many cells are needed to cover a sufficiently large domain for making useful weather forecasts. This generally puts a too high demand on present-day computer power. Hence, the grid size in operational weather (1 ~ 20 km) and climate models (20 ~ 200 km) is much larger than in LES models. Consequently, one weather or climate model grid cell usually contains an ensemble of several clouds with typically a few large and many small clouds. Therefore, LES results are used to determine suitable formulations of entrainment and detrainment that correspond to such an ensemble of clouds.

Analyses of LES data for several shallow cumulus cloud cases has led to an unexpected discovery: from case to case and hour to hour, the variation in detrainment turned out to be much larger than the variation in entrainment (chapter 2). As a result, entrainment can already be represented reasonably well with a simple function, only depending on height. However, more effort is needed for an adequate description of the detrainment.

First of all, LES results clearly reveal that the detrainment varies strongly with cloud layer depth. This can be explained from geometrical considerations (chapter 2). Furthermore, the detrainment also varies with two other conditions. Firstly, cloud droplets in cumulus clouds will more easily evaporate if they are subjected to entrainment of dry air from the environment. Consequently, the mixture will cool strongly and possibly become heavier than the environment and leave the updraft. Therefore, dry air is destructive for the cumulus cloud and will lead to high detrainment values. Secondly, if cumulus clouds are highly buoyant a lot of environmental air is needed to produce a mixture that is heavier than the environmental air. As a result the detrainment values will be small. In chapter 2 it is explained how the combined effect of both processes mentioned above can be captured in one parameter, the critical mixing fraction. This is the fraction of the environmental air necessary to make the mixture of cumulus and environmental air just as heavy as the environmental air. It is plausible that also other processes contribute to the high correlation between the critical mixing fraction and the detrainment. Highly buoyant clouds are generally large clouds with a relatively small surface and high upward velocities. As a result, large clouds remain rather unaffected by the environment. They mix less and will loose relatively less mass, corresponding with small detrainment values.

As mentioned before, LES reveal that detrainment varies much more from case to case than entrainment. As a result, the detrainment has a much larger influence on fluctuations in the mass flux profile. But how can we explain this behaviour? To investigate this, the exchange between cumulus clouds and their environment is described in terms of budget equations (chapter 3). Hereto, a dis-

tinction is made between between turbulent exchange due to small scale eddies and organized, more large scale exchange. The physical picture that emerges from the budget equations is the following: individual clouds in the ensemble only experience a massive entrainment just below cloud base. During their rise there is an exchange between the individual clouds and the environment via small scale turbulent eddies but the inflow is approximately balanced by the outflow. Consequently, the strength of the individual updrafts does not change with height. Lastly, at the height where an individual cloud will stop rising, it will detrain its mass to the environment, called massive detrainment. The heights at which this organized detrainment of the individual clouds occur, will ultimately determine the decrease of the total upward air flow (mass flux) that represents the cloud ensemble. This physical picture explains that it is not the entrainment but the detrainment, that determines the mass flux profile in the cloud layer to a large extent.

Ultimately, our aim is to apply the knowledge about entrainment and detrainment in a weather and climate model to improve its predictions. The model that is used is HARMONIE-AROME (HIRLAM ALADIN Research on Mesoscale Operational NWP in Euromed - Application of Research to Operations at MEsoscale), developed and operationally applied by several European countries, including The Netherlands. This model currently runs at a grid where calculations are made every 2.5 km. With such a resolution, this model is not capable to resolve small cumulus clouds and therefore needs a parameterisation for shallow convection. Although, entrainment and detrainment are crucial parameters in such a parameterisation, the ultimate model performance will also depend on other model components. Moreover, there are strong feedbacks between the convection and other parameterisations. Development and optimisation of these schemes should therefore be done in an integral way. Following such an approach, chapter 4 describes the convection scheme and strongly coupled parameterisations including substantial modifications. As shown, these modifications result in strong improvements of the model performance in HARMONIE-AROME, most notably in the predictions of low clouds.

The common thread through this thesis can be summarised as follows: Chapter 1 introduces the main subject of this thesis and provides a historical overview of studies concerning lateral mixing in cumulus convection. Empirical results for lateral mixing in shallow cumulus convection based on LES are described in chapter 2, together with an elaboration of this into a practical application for weather and climate models. A theoretical bases for the empirical findings in chapter 2 is presented in chapter 3. How this knowledge is finally applied in practice and is embedded in parameterisations strongly coupled to the convection scheme, is the subject of chapter 4. This thesis illustrates that the development

and implementation of physical parameterisations takes a long time but can lead to significant model improvements.

1

INTRODUCTION

1.1. CUMULUS CLOUDS

1.1.1. CLOUD TYPES

Clouds appeal to the imagination of many people and they are a beloved subject of painters like Turner and Ruysdael. In general we are referring here to cauliflower shaped, or cumulus, clouds (Fig. 1.1b and c) and not the, maybe less inspiring, layered stratus clouds (Fig. 1.1a). This thesis is about cumulus clouds, in particular the shallow version (Fig. 1.1b). You can typically see these clouds on a beautiful summer day, without, or almost without, rain. Maybe to your surprise, the friendly looking, serene shallow cumulus clouds play an important role in the weather and climate on earth.

Part of this chapter is published as: de Rooy, Wim C., et al. 2013: Entrainment and detrainment in cumulus convection: an overview, Quart. J. Roy. Met. Soc., Vol. 139, 1-19, doi:10.1002/qj.1959 © Royal Meteorological Society


(a)

(b)

(c)

Figure 1.1: Examples of cloud types: (a) stratus, (b) shallow cumulus, and (c) deep cumulus.

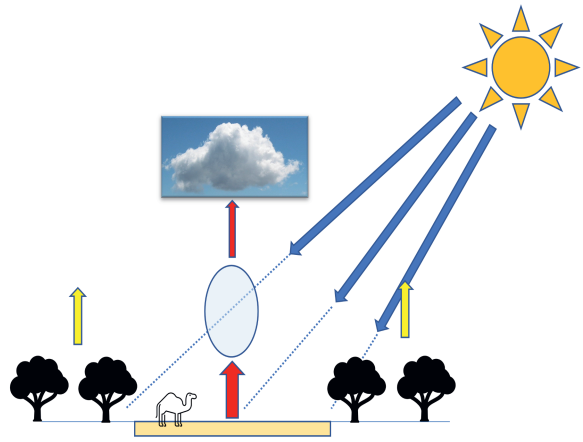

Figure 1.2: The origination of cumulus clouds by differential heating of the earth's surface.

1.1.2. THE FORMATION OF CUMULUS CLOUDS

Cumulus clouds can form in different ways and we here describe the most common way. When the sun heats the surface, the warmth will partly be absorbed by the surface, partly be released to the atmosphere as heat and vapour. Because the characteristics of the surface can change, the warming will not be the same everywhere. This is illustrated in Fig. 1.2, where the air above a dry sandy soil will be heated up much more than above a forest. Because warmer air is lighter, it will start to rise in a thermal bubble or plume (see section 1.2.2). This process is called convection. Due to the decreasing pressure with height, the temperature in the bubble will decrease due to the adiabatic expansion. If the temperature of the bubble becomes equal to its environment, it will loose its buoyancy and will finally stop rising. However, in case of cumulus convection there is another process we need to consider. At some stage during the rise, the thermal temperature will become too low to contain all humidity as a gas, and cloud droplets start to form. The corresponding condensational heating will increase the temperature, and herewith also the buoyancy, of the bubble.

To accurately determine the buoyancy, we need to take the density of gaseous and liquid humidity into account. For this we introduce the virtual temperature:

$$T_v \approx T(1 + 0.61 q_v - q_l) \tag{1.1}$$

where, T is the temperature, q_v is the water vapour specific humidity, and q_l is the liquid water specific humidity. To also compensate for the adiabatic temperature changes related to the rise and descend of air, we introduce the potential virtual temperature:

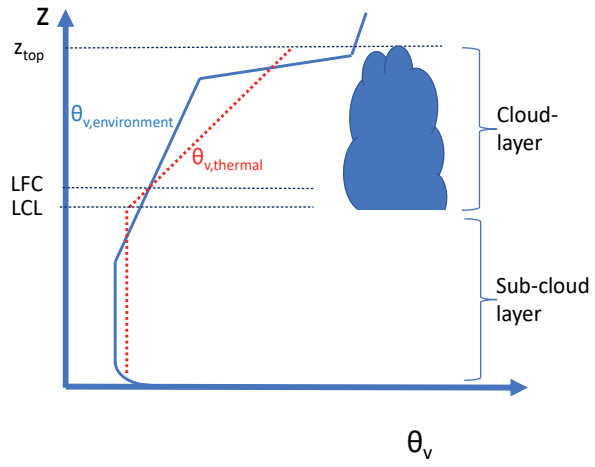

Figure 1.3: Schematic θ_v diagram of a rising thermal in a shallow cumulus cloud layer. The virtual temperature of the thermal and the environment are shown with respectively a red dashed and a blue solid line. Additionally, some important height levels are indicated (see text)

$$\theta_{\mathrm{v}} = \frac{T_{\mathrm{v}}}{\Pi} \tag{1.2}$$

where Π is the Exner-function:

$$\Pi = \left(\frac{p}{p_0}\right)^{\frac{R_{\mathrm{d}}}{c_{\mathrm{p}}}} \tag{1.3}$$

where p is the pressure, p_0 is a reference pressure (usually 1000 hPa), R_{d} is the specific gas constant for dry air and c_{p} is the specific heat capacity of dry air. θ_{v} is equivalent to the virtual temperature the air would have were it expanded or compressed adiabatically to the reference pressure p_0. As long as θ_{v} of the thermal is higher than θ_{v} of the environment, there is a positive upward bouyancy force.

Now that we have defined a convenient measure for the density and buoyancy, let us take a closer look to the thermodynamic structure of the atmosphere during the rise of a convective thermal (Fig. 1.3). As discussed before, starting near the surface, the thermal will have a slightly higher (virtual) temperature than the environment, i.e. $\theta_{\mathrm{v,thermal}} > \theta_{\mathrm{v,environment}}$. Consequently, it will rise in the well mixed sub-cloud layer with a constant potential temperature profile. Near the top of the sub-cloud layer, the potential environmental temperature increases with height. Here, the parcel will become heavier than the environment, i.e. $\theta_{\mathrm{v,thermal}} < \theta_{\mathrm{v,environment}}$ which results in a negative buoyancy. However, if the thermal has enough kinetic energy, it can reach the level from where condensa-

tion starts, called lifting condensation level (LCL, Fig. 1.3) and the thermal starts to appear as a cumulus cloud. As mentioned above, the condensation process heats the thermal, as reflected by the increase in $\theta_{v,\text{thermal}}$ with height from LCL onwards. If the increase of the thermal virtual temperature with height exceeds that of the increase of the environmental temperature with height, the thermal can become positive buoyant again at what is called, the level of free convection (LFC). With the condensation booster on board, the cloudy thermal will rise until it finally hits a layer with a strong increase in the environmental potential temperature with height, becomes negatively buoyant again, decelerates and finally stops at the cloud top level, z_{top} (Fig. 1.3).

1.1.3. THE IMPORTANCE OF CUMULUS CONVECTION

It is difficult to overemphasise the importance of cumulus convection in climate and weather. It is a key process in the hydrological and energy cycle through the vertical transport of heat, moisture and momentum, it determines precipitation and the clouds associated with the moist convection directly and largely affects the global energy balance through their interaction with the solar radiation. An example that the serene looking shallow clouds have a substantial impact on the weather and climate even on a global scale, is their role in the Hadley circulation (Fig. 1.4). In the trade wind regions north and south of the equator, shallow cumulus clouds are very common. They effectively transport the moisture from the surface to the atmosphere. Subsequently this moist air is advected by the trade winds towards the intertropical convergence zone (ITCZ) around the equator. In the ITCZ, deep convection transports the moisture to a height of about 15 km. At that level the air is blown north and southwards to the dry sub-tropics around $30\,^{o}$N and $30\,^{o}$S, where it descends. By strengthen the uptake of humidity in the atmosphere, trade wind shallow cumulus clouds substantially enhance the Hadley circulation.

But also on a more local scale the importance of an adequate description of cumulus convection is evident. One example is provided here. As a result of different processes, the stability of the atmosphere changes. For example, radiative long-wave cooling will push the atmosphere to conditional instability. This instability can be consumed by cumulus convection. On the other hand, large-scale subsidence leads to inversions that inhibit the initiation of cumulus convection and consequently a large conditional available potential energy (CAPE) in the atmosphere can gradually build up. In this way, the moment of triggering of cumulus convection determines the ultimate intensity of the convection.

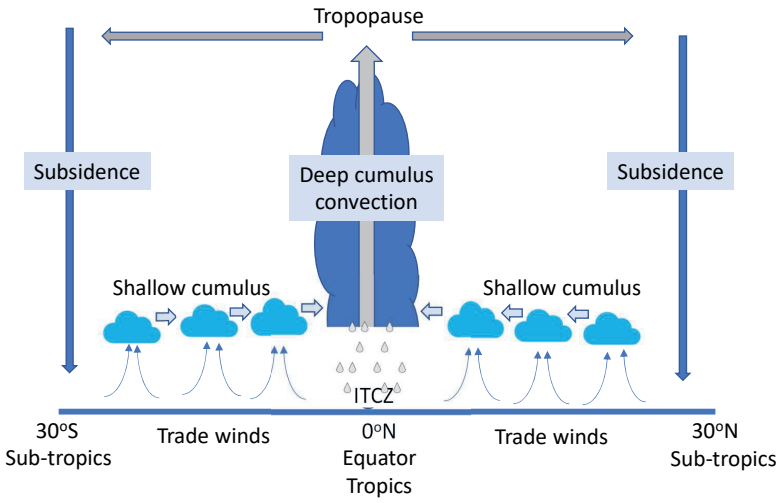

Figure 1.4: Schematic meridional cross-section of the north and south cell of the Hadley circulation. Shallow convection in the trade wind regions enhances the transport of moisture from the surface to the atmosphere. The trade winds transport this moisture towards the Intra Tropical Convergence Zone (ITCZ) where deep convection takes place and moisture is moved upwards to the tropopause at approx. 15 km height. From there the air blows south and north-wards until the sub-tropics where the air subsides.

1.1.4. THE DESCRIPTION OF CUMULUS CONVECTION IN MODELS

In weather and climate models the atmosphere is discretized in grid cells. Typically, the horizontal size of these cells range from a few kilometres in weather models to tens of kilometres in climate models. The vertical size of these cells varies between several metres near the surface to hundreds of metres at higher levels. In every cell the changes of wind, temperature and humidity are calculated. The calculations are done using the Navier-Stokes equations for conservation of momentum, the conservation laws for heat, moisture and mass, and the equation of state (see e.g. Stull, 1988). The distance between the grid points determines the resolution of the model and the size of the processes the model can explicitly describe, or resolve. Sub-grid processes that take place at sizes smaller than the grid size are not resolved but can have a large impact on the cell variables. Figure 1.5 shows the temporal versus the spatial scales of the complete range of meteorological processes; from the planetary waves spanning thousands of kilometres to the smallest sub-metre microscale turbulence. As indicated in Fig. 1.5, the horizontal size of shallow convection is in the order of 100 to 1000 m. Here, a distinction is made between models that do and do not resolve shallow convection. Large Eddy Simulation (LES) models run at such a high resolution that they are well capable of resolving all convection (Fig. 1.5).

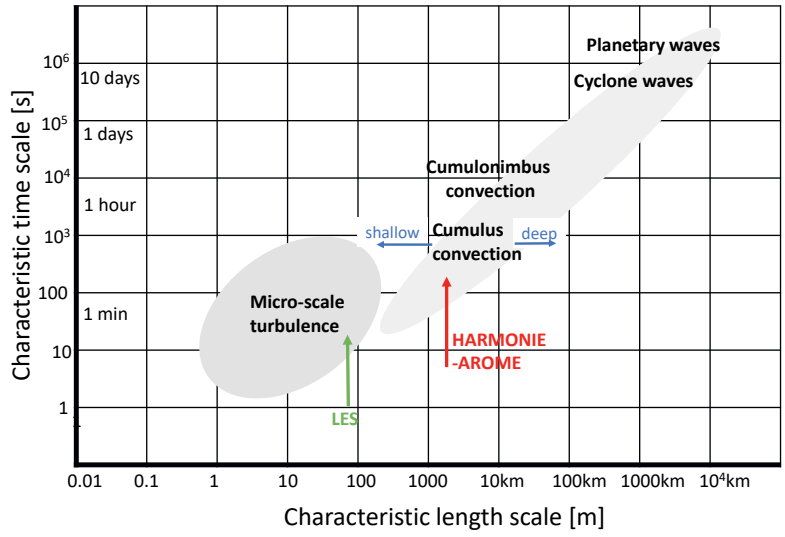

Figure 1.5: Schematic diagram showing temporal and spatial scales of meteorological phenomena as well as the resolution of the current HARMONIE-AROME model and a typical LES model. Scales larger than the resolution of the model can (roughly) be resolved.

On the other hand, climate and weather models do not resolve shallow convection. The climate and weather model used in this study is HARMONIE-AROME (HIRLAM ALADIN Research on Mesoscale Operational NWP in Euromed - Application of Research to Operations at Mesoscale). This model currently runs at a typical resolution of 2.5 km, too coarse to resolve shallow convection. Nevertheless, shallow convection does transport heat, moisture, and momentum in the vertical and will therefore have a substantial impact on the grid cell variables in HARMONIE-AROME. To account for the effect of sub-grid processes, like in this case shallow convection, they have to be described in a simplified way in terms of the grid cell, resolved variables in what is called a parameterisation. Note that with the current HARMONIE-AROME grid size and the scale of shallow cumulus clouds, a grid cell actually contains an ensemble of clouds with typically a few large and many more small clouds.

1.2. LATERAL MIXING IN CUMULUS CONVECTION

1.2.1. INTRODUCTION

Even state-of-the-art Numerical Weather Prediction (NWP) and climate models like HARMONIE-AROME have insufficient resolution to resolve most cumulus cloud related processes, and therefore these need to be incorporated in a statistical way through the use of parameterisations in terms of the resolved variables.

The most common way to parameterise the vertical transport of heat, moisture and momentum is through the use of so-called mass flux schemes. In short, in such schemes the updraft strength of a cumulus ensemble is characterised by a mass flux that quantifies the amount of mass that is transported in the vertical. Combining this mass flux with a cloud updraft model for temperature, moisture and momentum allows for the determination of the parameterised convective transport of these quantities. A key process that modifies the mass flux and the variables of the cloud updraft model is the mixing between clouds and their environment by the so-called entrainment and detrainment processes that describe respectively the inflow of environmental air into the cloud and the outflow of cloudy air into the environment. The precise nature of these mixing processes is still an active field of research and its parameterisation is still in its infancy. Sensitivity studies with climate models (Murphy et al., 2004, Klocke et al., 2011) in which the values of many parameterised processes are varied, have demonstrated that the mixing processes in cumulus convection are amongst the most sensitive ones for determining the strength of the cloud climate feedback.

Nowadays the mass flux concept is also used for dry convection in the increasingly popular Eddy Diffusivity Mass Flux (EDMF) schemes (Siebesma et al., 2007, Soares et al., 2004). Nevertheless, lateral mixing process in dry convection will not be considered here (except in chapter 4).

In accordance with its importance, numerous papers on entrainment and detrainment appeared over the last 70 years. We will start with a historical overview of studies concerning lateral mixing in cumulus convection (section 1.2.2). The subsequent sections describe some recent developments which can roughly be divided in studies aiming at a better fundamental understanding how the mixing processes take place (section 1.2.3) and studies that are more targeted towards a better representation of lateral mixing within a parameterisation context (section 1.2.4). We believe both type of studies are important and relevant. In view of the large extend of the field we do not claim to give a complete overview of all notable studies.

1.2.2. HISTORY

The importance of lateral mixing in cumulus convection has been recognised already for a long time, starting with the seminal paper of Stommel, 1947. However, it turned out to be a just as challenging as tough subject since even some of the fundamental questions related to it are still a matter of debate. This applies for instance to the question whether cumulus convection should be represented by a bubble or a plume, a topic already discussed by Squires and Turner, 1962. Or: Is the dilution of the cloudy updraft predominantly caused by lateral or cloud top entrainment? Furthermore, whereas early studies concentrated more on the

mixing of a single cloud, nowadays due to its application in parameterisations in NWP and climate models there is a need to describe the effect of lateral mixing for a whole cumulus ensemble.

THERMAL OR PLUME?

As mentioned above, Squires and Turner, 1962 discussed the differences between the plume or jet and the bubble as a thermal concept for describing convection. Looking at a large thunderstorm with its rather tall and slender current, they suggest an analogy with a steady state buoyant turbulent plume, having a continuous source of heat from below cloud base and no significant mixing at cloud top. On the other hand for small clouds, being about as deep as wide, a non-steady bubble model seems more appropriate in which the air in the wake near the top will be the dominant mixing process. In line with the current general view, Squires and Turner, 1962 presumed that a realistic model of cumulus convection should include features of both models. Nevertheless, contemporary convection schemes mainly possess the characteristics of a plume model.

DISTINGUISHING DIFFERENT LATERAL MIXING PROCESSES

Dilution of a cumulus cloud by entrainment of environmental air was described for the first time by Stommel, 1947. After Stommel numerous observational studies of cumulus clouds with aircrafts followed (e.g. Warner, 1955). In these studies entrainment strength was quantified through the ratio between the measured liquid water and its adiabatic value and provided observational evidence of the entrainment of drier air from outside the cloud.

More precise quantitative descriptions of entrainment originated from laboratory water tank experiments of thermal plumes (Morton et al., 1956; Turner, 1963) describing an increasing mass flux M with height.

$$M^{-1}\frac{\partial M}{\partial z} = \varepsilon \simeq \frac{0.2}{R} \tag{1.4}$$

where ε denotes the fractional entrainment, R is the radius of the rising plume and $M = \rho w_c a_c$ kg m^{-2}s^{-1} denotes the upward mass flux that consists of the product of the density ρ, the plume updraft velocity w_c and the associated plume fractional area a_c. We deliberately choose here for the suffix c as we will associate in the remainder of this chapter the updraft properties with cloudy updrafts. According to (1.4), larger thermals (clouds) have smaller fractional entrainment which is a consequence of the fact that larger areas have a relatively smaller perimeter. Many of the early, but also more recently developed cloud models use entrainment rates still based on this entraining plume model.

An important further refinement on the entrainment formulation (1.4) was first pointed out by Houghton and Cramer, 1951. They made a distinction be-

tween dynamical entrainment due to larger scale organised inflow (noted as ε_{dyn}) and turbulent entrainment caused by turbulent mixing at the cloud edge (noted as $\varepsilon_{\text{turb}}$).

$$M^{-1}\frac{\partial M}{\partial z} = \varepsilon_{\text{dyn}} + \varepsilon_{\text{turb}} \tag{1.5}$$

Whereas the first type of entrainment has the characteristics of advective transport across the interface, turbulent entrainment is of diffusive nature and is therefore often described with an eddy diffusivity approach (Kuo, 1962, Asai and Kasahara, 1967). Since the dynamical and turbulent fractional entrainment rates are by definition positive, they cause the mass flux to increase with height. This is in agreement with old water tank experiments without stratification where all laterally entrained fluid was considered to be part of the bubble. Here bubble was defined as a turbulent fluid in contrast with the non-turbulent environment of the bubble. For rising dry thermals a similar argumentation might hold. However cumulus clouds contain liquid water and evaporative cooling plays an important role in the mixing process. Due to the mentioned turbulent mixing at the cloud edge a mixture of in-cloud and environmental air is made. This mixture can become negatively buoyant by evaporative cooling and will in this case detrain from the cloud (possibly after some time), represented by δ_{turb}. In tank experiments with stratification as well as for clouds in the atmosphere, also the cloud or thermal itself can become negatively buoyant. As a result, it stops rising and is usually dissolved in the environment. This process is called massive or dynamical detrainment and is represented by δ_{dyn}. So if we finally include all distinguished mixing processes the change of the mass flux with height can be written as:

$$M^{-1}\frac{\partial M}{\partial z} = \varepsilon_{\text{dyn}} + \varepsilon_{\text{turb}} - \delta_{\text{dyn}} - \delta_{\text{turb}}. \tag{1.6}$$

STEADY–PLUME ASSUMPTION

As mentioned above, most contemporary convection schemes have adopted the entraining/detraining plume concept. In the traditional plume model, several assumptions are made. First of all the interior of individual plumes is considered to be homogeneous. So just entrained air is homogeneously mixed instantaneously. Observations (e.g. Ludlam and Scorer, 1953) as well as LES (Zhao and Austin, 2005a, Heus, Jonker, et al., 2009) show that especially large clouds (with longer life times) are a succession of bubbles rising from roughly the same place, each penetrating further than it predecessor. This will result in an inhomogeneous interior of individual plumes. Secondly, the entraining/detraining plume model assumes steady state. However, in reality clouds experience a life cycle with time scales mainly related to cloud size. For example a decaying cloud at

the end of its life will have completely different characteristics from a still developing cloud. The steady state assumption is a more valid one, if we, instead of single clouds, consider the overall impact of a (large) cloud ensemble containing all kinds of cloud sizes and clouds in different stages of their life cycle. Moreover, considering the contemporary grid sizes of climate and most NWP models, convection schemes should actually describe the overall effect of an ensemble of clouds rather than a single cloud. Historically, a steady state plume model has been considered a reasonable starting point for describing a cloud ensemble.

A first example how this can be done, and still the basis for several existing convection schemes (e.g. Wagner and Graf, 2010), is the seminal work of Arakawa and Schubert, 1974. They assume that the change of the large scale, in model context grid point, properties is slow in comparison with the response of individual clouds, called quasi equilibrium. Further Arakawa and Schubert, 1974 describe the overall transport by an ensemble of entraining plume-like cumili rising to different heights because they have a spectrum of initial sizes and hence different entrainment rates, defined by (1.4). However, most contemporary mass flux parameterisations employ a bulk approach in which all active cloud elements are represented in one steady state updraft representing the whole cloud ensemble.

BULK PLUME CONVECTION PARAMETERISATIONS

Numerous entrainment and detrainment parameterisations have been proposed for bulk mass flux schemes. Popular formulations proposed by Tiedtke, 1989, Bechtold et al., 2008, Nordeng, 1994 and Gregory and Rowntree, 1990 can be ordered in terms of the right-hand side (RHS) of (1.6). Tiedtke, 1989 and Nordeng, 1994 assume that $\varepsilon_{\text{turb}}$ and δ_{turb} are equal and given by (1.4), while in Bechtold et al., 2008, $\varepsilon_{\text{turb}}$ depends on the saturation specific humidity. Gregory and Rowntree, 1990 also propose (1.4) for $\varepsilon_{\text{turb}}$ but utilise a systematically smaller δ_{turb}. Dynamical entrainment ε_{dyn} is based on moisture convergence in Tiedtke, 1989, on momentum convergence in Nordeng, 1994, on relative humidity in Bechtold et al., 2008 and absent in Gregory and Rowntree, 1990. Organised detrainment is in general formulated as a massive lateral outflow of mass around the neutral buoyancy level although the precise details differ in the cited parameterisations. The above cited parameterisations typically use (1.4) assuming a fixed radius of $R \simeq 500\,\text{m}$ for shallow clouds and $R \simeq 2000\,\text{m}$ for deep convection.

Another class of entrainment/detrainment parameterisations, that does not explicitly distinguish between dynamical and turbulent mixing is based on the "buoyancy sorting" concept introduced by Raymond and Blyth, 1986. This buoyancy sorting concept is transformed into an operational parameterisation by Kain and Fritsch, 1990 (section 1.2.4). In their parameterisation an ensemble of mixtures of cloudy and environmental air is formed, where each ensemble member

has a different concentration of environmental air. If resulting mixtures are positively buoyant, they remain in the updraft and are part of the entrainment process while negatively buoyant mixtures are rejected from the updraft and are part of the detrainment process. A number of recently proposed shallow cumulus convection schemes are based on or make use of this buoyancy sorting concept (section 1.2.4).

LATERAL VERSUS VERTICAL MIXING

Entrainment of environmental air into clouds tends to dilute cloud properties and degrade the buoyancy characteristics of cloudy air, both of which affect the vertical transport by clouds. Knowing the characteristics of the air entering the cloud, which is strongly related to knowing the source height of the entrained air, is therefore naturally regarded as a crucial issue. In this respect it is most surprising that two radically opposing views, referred here as 'lateral entrainment' versus 'cloud-top entrainment', have been able to coexist for a long time in the cloud sciences community. The origin of these views go back as least as far as Stommel, 1947 (lateral entrainment) and Squires, 1958 (cloud-top entrainment). In the former view, cloudy air, carrying the properties of cloud base, gets continually diluted during its ascent by mixing air entrained into the cloud via the lateral cloud edges. It is this view that has served as the basis for parameterisations of moist convective transport in operational models. Conversely, in the cloud-top entrainment view, environmental air predominantly gets entrained at or near the top of the cloud, after which it descends in the cloud via penetrative downdraughts, finally diluting the rising cloudy air by turbulent mixing. A conceptual picture of how this could look is given in Figure 13.8 in Stull, 1988. Clearly the two views sketched above differ enormously with respect to the source height of entrained air, and therefore they differ also crucially with respect to the properties of air that dilute the cloud. It should be noted that in principle both views are not mutually exclusive since both mechanisms could be active at the same time, but the question really is which of the two mechanisms dominates. Also, a rather contrived argument would be needed to anticipate that both mechanism are equally effective.

Ample evidence for the importance of lateral entrainment can be found in the literature (e.g.Lin and Arakawa, 1997; Raga et al., 1990). Also, though perhaps more indirectly, the lateral entrainment view derives justification from the appreciable predictive quality of the moist convective parameterisations that are based on it (e.g. Kain and Fritsch, 1993; Siebesma and Cuijpers, 1995). On the other hand, compelling observational evidence for the cloud-top entrainment view came from the elegant analysis of Paluch, 1979, who plotted in-cloud values of conservative variables (total specific humidity and equivalent potential

temperature) in a diagram which now carries her name. Rather than displaying significant scatter, the in-cloud values observed during a cloud transect at a particular level were found to collapse onto a distinct line. Such a 'mixing line' is commonly taken as strong evidence for a two-point mixing scenario: if one mixes air from two (but not more) different sources, any mixture must show up on a line in such a diagram due to the nature of conservative variables. By extrapolating the line, Paluch identified the two source-levels as cloud-base and cloud-top (or a level significantly higher than the level of the cloud transect). It is important to note that, at face value, the analysis of Paluch seems to leave no room for significant lateral entrainment since mixing with more than two sources would yield significant scatter away from the mixing line. Later studies (e.g. Betts, 1982, 1985; Boatman and Auer, 1983; Jensen et al., 1985; Lamontagne and Telford, 1983) confirmed the findings of Paluch, thus providing further support the importance of cloud-top entrainment. The historical shift from a lateral entrainment oriented view towards a cloud-top entrainment oriented view can very clearly be noted in the overview paper by Reuter, 1986, for example.

Criticism and warning comments, not so much directed at the location of data points in the Paluch diagrams itself, but rather at the interpretation drawn from them, were given by Siebesma, 1998; Taylor and Baker, 1991. Siebesma pointed to the strong self-correlation that exists in the conserved variables chosen for the Paluch-diagrams, which makes it hard for the data *not to line-up* ; see for example Fig. 1 of Heus et al., 2008. Taylor and Baker, 1991 drew attention to the phenomenon of 'buoyancy sorting' which makes that essentially only a biased selection of data-points can show up in Paluch diagrams. Simply put, a bias is introduced because it is less likely to observe buoyant air parcels coming from above, as well as it is unlikely to observe negatively buoyant parcels coming from below. Consequently most observed data points are related to buoyant parcels coming from below and negatively buoyant parcels from above. As explained in detail in their paper, this effect puts serious limits to the possible values one can observe at a particular cloud level: essentially the data points are confined to a triangle that very much resembles a line. They conclude "The graphical analysis of non-precipitating cloud composition shows that the apparent mixing line structure of single level in-cloud points on a conserved tracer diagram can result from a continuous series of entrainment events occurring throughout the cloud depth if buoyancy sorting is dominant throughout the flow." A final answer to the controversy between cloud top and lateral mixing seem to be provided by Heus et al., 2008. In this paper detailed particle tracking studies in LES show unambiguously that cloud-top entrainment plays no significant role in the mixing process compared to lateral mixing

THE USE OF LES TO STUDY ENTRAINMENT AND DETRAINMENT

Obtaining accurate observations of entrainment and detrainment is notoriously difficult. Nevertheless, inventive studies like Raga et al., 1990 and Yanai et al., 1973 linked observations to entrainment rates. However, the translation from observed lateral mixing coefficients to an appropriate ε and δ for use in a bulk mass flux framework is far from trivial. Fortunately, LES models matured since the 1990s, initiating a strong revival of entrainment/detrainment studies. The resolution of these models is high enough to resolve the largest eddies (Fig. 1.5), which are responsible for the majority of the convective transport. Comparison with various different field observations like BOMEX Siebesma et al., 2003, ARM Brown et al., 2002, ATEX Stevens et al., 2001, has shown that modern LES is capable of accurately simulating cumulus cloud dynamics and resolving the intricacies of entrainment processes, even down to non-trivial geometrical properties of the cloud edge (Siebesma & Jonker, 2000).

Before lateral mixing can be studied in LES one first have to define cloud and environment (called sampling method). Often applied is the cloud core sampling where all LES grid points that contain liquid water ($q_l > 0$) and are positively buoyant ($\theta_v > \overline{\theta_v}$) are considered to be part of the cloudy updraft. Here q_l is the liquid water content, θ_v is the virtual potential temperature (being a measure of density) and $\overline{\theta_v}$ is the slab-averaged virtual potential temperature.

In the 1990s computer resources were too limited to perform large eddy simulations of deep convection. However, early LES results provided important insight in shallow convection including lateral mixing. For example, Siebesma and Cuijpers, 1995 showed in a careful analysis of LES results, that the turbulent transport can be accurately described with a bulk mass flux approach, especially when the cloud core sampling method is applied. So diagnosing ε and δ in this way from LES gives a strong guideline to the ε and δ that should be used in a NWP or climate model bulk mass flux scheme. Therefore, LES provide a powerful tool to study the qualitative and quantitative behavior of the lateral mixing coefficients. For example Siebesma and Cuijpers, 1995 found out that the typical entrainment/detrainment values for shallow convection usually applied by that time were an order of magnitude too small.

Large Eddy Simulation studies have also been utilised to investigate lateral mixing in a more fundamental way. For example Heus and Jonker, 2008 and H. J. J. Jonker et al., 2008 described the influence of a subsiding shell on lateral mixing. Further, Heus et al., 2008 convincingly showed that lateral mixing is responsible for diluting the cloudy updraft and not cloud top mixing as was thought for a long time (Squires, 1958, Paluch, 1979). LES studies like Zhao and Austin, 2005b investigated the mixing between clouds and their environment during the life cycle of single clouds. Finally, two recent LES studies de-

rived more direct, locally evaluated entrainment and detrainment coefficients (Romps, 2010, Dawe and Austin, 2011b, see section 1.2.3). Whereas Dawe and Austin, 2011b accomplishes this by carefully determining the net velocity through the cloud environment interface, Romps, 2010 uses an inventive definition of entrainment and detrainment. Compared to LES results diagnosed within the bulk mass flux framework, both latter studies diagnosed significantly larger lateral mixing coefficients. This discrepancy can be explained by the fact that the lateral transport in Romps, 2010 and Dawe and Austin, 2011b involves less distinct properties between cloud and environment.

Due to increased computer resources, LES models are now capable of simulating deep convection (e.g. Kuang and Bretherton, 2006, Khairoutdinov and Randall, 2006, Khairoutdinov et al., 2009, Böing et al., 2012). Such LES studies turned out to be very insightful. A complicating factor is the important role of the microphysics on cloud dynamics which still needs to be parameterised in LES of deep convection.

1.2.3. NEW INSIGHTS IN ENTRAINMENT AND DETRAINMENT PROCESSES

INTRODUCTION

So far, in our historical review we have been rather vague on the precise definition of the entrainment and the detrainment processes. The purpose of this section is to make a more precise notion of these mixing processes and to explore their behaviour in a more fundamental way. First we will provide basic definitions of the entrainment and detrainment processes. We will proceed to apply these first on a rising dry plume which is governed by a purely entrainment process. Subsequently, entrainment and detrainment will be reviewed in the context of the steady state cloud model of Asai and Kasahara, 1967 which will make the notion of organised versus turbulent entrainment and detrainment more precise. We will proceed by reviewing the various ways of determining the exchange rates from LES.

GENERAL DEFINITIONS

Basic definitions are introduced here following the line of Siebesma, 1998. A convenient starting point is the conservation law of a scalar variable ϕ

$$\frac{\partial \phi}{\partial t} + \nabla \cdot \mathbf{v}\phi = F, \tag{1.7}$$

where $\mathbf{v}$ denotes the three dimensional velocity vector and where all possible sources and sinks of ϕ are collected in F. For the sake of simplicity we assume a Boussinesq flow, implying that the density in (1.7) is constant and has been divided out of (1.7). We consider a domain with a horizontal area A and we are

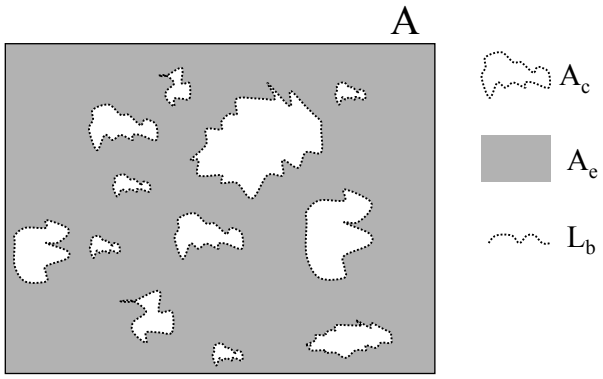

Figure 1.6: Schematic diagram showing an ensemble of clouds at a certain height. A, A_c, and A_e represent resp.; the total horizontal domain area ($A_\mathrm{c} + A_\mathrm{e}$), the cloudy area (white), and the environmental area (gray). The interface between the cloudy area and the environment is plotted as a dashed line and has a total length L_b. (adopted from de Rooy and Siebesma, 2010, chapter 3)

interested in the lateral mixing between a cloudy area A_c and a complementary environmental area A_e at a given height z such as sketched schematically in Fig. 1.6.

At this point we do not need to be more specific on the precise definition of cloudy area but it should be noted that it may consist of many different "blobs" (or clouds) that can change in shape and size as a function of time and height. By integrating (1.7) horizontally over the cloudy area $A_\mathrm{c}(z,t)$, applying Leibniz integral rule and the Gauss divergence theorem, a transparent conservation equation of the cloudy area for ϕ can be deduced (Siebesma, 1998)

$$\frac{\partial a_\mathrm{c}\phi_\mathrm{c}}{\partial t} + \frac{1}{A}\oint_{\text{interface}} \hat{\mathbf{n}}\cdot(\mathbf{u}-\mathbf{u}_\mathrm{i})\phi\, dl + \frac{\partial a_\mathrm{c}\overline{w\phi}^\mathrm{c}}{\partial z} = a_\mathrm{c}F_\mathrm{c} \tag{1.8}$$

where $a_\mathrm{c} = A_\mathrm{c}/A$ is the fractional cloud cover, $\hat{\mathbf{n}}$ is an outward pointing unit vector perpendicular to the interface, $\mathbf{u}$ is the full 3D velocity vector at the interface, and $\mathbf{u}_\mathrm{i}$ is the velocity of the interface. Overbars and variables subscripted with c denote averages over the cloudy part. In the special case $\phi = 1$, and $F_\mathrm{c} = 0$ we recover the continuity equation

$$\frac{\partial a_\mathrm{c}}{\partial t} + \frac{1}{A}\oint_{\text{interface}} \hat{\mathbf{n}}\cdot(\mathbf{u}-\mathbf{u}_\mathrm{i})\, dl + \frac{\partial a_\mathrm{c} w_\mathrm{c}}{\partial z} = 0 \tag{1.9}$$

Equation (1.9) has a simple geometrical interpretation. The net change of the cloud fraction is a result of the net lateral inflow of mass across the cloudy interface on the one hand and the vertical mass flux divergence on the other hand.

Let us emphasize that it is the mass velocity $\mathbf{u}$ *relative* to the interface velocity $\mathbf{u}_\mathrm{i}$ that enters in the interface term. This way it is guaranteed that there is no net inflow if a cloud is simply advected by the mean wind. Since entrainment is usually associated with the inflow of mass into the cloudy area whereas detrainment with the complementary outflow it seems natural to define these processes as

$$\begin{aligned} E &= -\frac{1}{A}\oint_{\hat{\mathbf{n}}\cdot(\mathbf{u}-\mathbf{u}_\mathrm{i})<0} \hat{\mathbf{n}}\cdot(\mathbf{u}-\mathbf{u}_\mathrm{i})\,dl, \\ D &= \frac{1}{A}\oint_{\hat{\mathbf{n}}\cdot(\mathbf{u}-\mathbf{u}_\mathrm{i})>0} \hat{\mathbf{n}}\cdot(\mathbf{u}-\mathbf{u}_\mathrm{i})\,dl, \end{aligned} \tag{1.10}$$

so that indeed, realizing that $E \equiv \varepsilon M$ and $D \equiv \delta M$, (1.9) reduces under steady state conditions to

$$M^{-1}\frac{\partial M}{\partial z} = \varepsilon - \delta \tag{1.11}$$

Although it is relative straightforward to determine $E-D$ as a residual from (1.9), it is by no means trivial to determine entrainment and detrainment rates separately, neither in laboratory experiments nor in numerical simulations. We will come back to this point in subsection 1.2.3.

DRY PLUMES

While entrainment and detrainment are easily defined mathematically, the physical processes involved are not always fully understood and in fact can depend on how we define the interface across which the mixing processes are defined. Buoyant dry plumes, which rise in a non-turbulent environment, is a relatively simple example. They entrain environmental air and show virtually no detrainment. Such plumes rise and grow almost indefinitely, until they are diluted to an extent that they are absorbed in the chaos of molecular motions. If we denote the length of the perimeter of the plume by L_b, define u_b as the net mean velocity at the boundary of the plume

$$\overline{u}^b \equiv u_\mathrm{b} \equiv \frac{1}{L_\mathrm{b}}\oint_{\text{interface}} \hat{\mathbf{n}}\cdot(\mathbf{u}-\mathbf{u}_\mathrm{i})\,dl \tag{1.12}$$

and assume steady state and a circular geometry, i.e. $A_\mathrm{c} = \pi R^2$ and $L_\mathrm{b} = 2\pi R$, it is straightforward to rewrite (1.9) as

$$M^{-1}\frac{\partial M}{\partial z} = \frac{L_\mathrm{b}}{A_\mathrm{c}}\frac{u_\mathrm{b}}{w_\mathrm{c}} \simeq \frac{1}{R}\frac{2u_\mathrm{b}}{w_\mathrm{c}}. \tag{1.13}$$

which provides a justification for the famous entrainment relationship for plumes (Morton et al., 1956) and a physical interpretation of the proportionality constant in (1.4).

STEADY STATE SINGLE CLOUD

Atmospheric clouds however differ from dry plumes. Entrainment of unsaturated environmental air leads to the evaporation of cloud liquid water. Some cloud parcels will loose their buoyancy and ultimately their liquid water and are then by definition detrained. This naturally asks for including the detrainment process. It is not possible to make more precise statements on the entrainment and detrainment processes unless we become more specific on the physics that plays a role in these processes. A popular model has been proposed by Asai and Kasahara, 1967, in which a steady state cloud is assumed to be cylinder shaped with a radius R. Further they presume a scale separation between turbulent exchange across the cloud interface and a larger scale in- or outflow resulting from the buoyancy driven mass flux convergence or divergence inside the cloud.

This is done by applying a Reynolds decomposition of the flux across cloud boundary for thermodynamic conserved variables ϕ

$$\overline{u\phi}^{\mathrm{b}} \equiv u_{\mathrm{b}}\phi_{\mathrm{b}} + \overline{u'\phi'}^{\mathrm{b}} \tag{1.14}$$

in which by convention u_{b} is positive if it is pointing outward of the cloud and the mean property of ϕ along the cloud boundaries, ϕ_{b} is defined as

$$\overline{\phi}^{\mathrm{b}} \equiv \phi_{\mathrm{b}} \equiv \frac{1}{L_{\mathrm{b}}} \oint_{\mathrm{interface}} \phi dl \tag{1.15}$$

This scale separation allows the introduction of turbulent entrainment and detrainment on the one hand and organised entrainment driven by convergence and organised detrainment driven by divergence on the other hand. More specifically if we, following Asai and Kasahara, 1967 approximate the turbulent flux by an eddy diffusivity approach and make an upwind approximation of the organised in- and outflow (i.e. $\phi_{\mathrm{b}} = \phi_{\mathrm{c}}$ if $u_{\mathrm{b}} > 0$ and $\phi_{\mathrm{b}} = \phi_{\mathrm{e}}$ if $u_{\mathrm{b}} < 0$) one can derive for the various terms on the right hand side of (1.6):

$$\varepsilon_{\mathrm{turb}} = \delta_{\mathrm{turb}} = \frac{2\eta}{R} \tag{1.16}$$

$$\varepsilon_{\mathrm{dyn}} = H(-u_{\mathrm{b}}) \frac{1}{w_{\mathrm{c}}} \frac{\partial w_{\mathrm{c}}}{\partial z} \tag{1.17}$$

$$\delta_{\mathrm{dyn}} = -H(u_{\mathrm{b}}) \frac{1}{w_{\mathrm{c}}} \frac{\partial w_{\mathrm{c}}}{\partial z} \tag{1.18}$$

where H denotes the Heaviside function, w_{c} is the average vertical velocity in the cloud, and η is a dimensionless constant analogous with the constant of proportionality between horizontal (here radial) and vertical velocity fluctuations in the mixing length theory, which is of the order $O(1)$. If these results are coupled to

updraft equations for temperature, moisture and vertical velocity and fed with the proper boundary conditions at cloud base, one typically finds net condensational heating in the lower part of the cloud that feeds the buoyancy leading to an acceleration of the updraft. This acceleration has a negative feedback since it will induce an inflow due to the organised entrainment that will eventually slow down the updraft leading to divergence and an organised detrainment in the upper part of the cloud. A few remarks should be made. First the fact that the turbulent mixing is assumed to be symmetric in terms of an equal entrainment and detrainment has been criticised by Randall and Huffman, 1982. In their model the interface is defined as the boundary of the mass of turbulent air associated with the cloud. They therefore model the turbulent mixing solemnly as a entrainment process and not as a turbulent mixing process as in Asai and Kasahara, 1967. Secondly the form of the organised entrainment and detrainment is a direct result of the strong assumption that the cloud has a constant radius R. With w_c predicted by an updraft equation, ε_{dyn} and δ_{dyn} are determined by eqs. (1.17) and (1.18). Therefore the constant R assumption can be seen as the organised entrainment and detrainment closure of the Asai and Kasahara model. If the interface is defined as the buoyant part of the cloud a thermodynamic constraint should determine how R varies with height. The buoyancy sorting principle put forward by Kain and Fritsch, 1990 is a step in that direction. In their model (see Section 1.2.4) equal masses of environmental and cloudy air are assumed to form various mixtures. It is then assumed that negative buoyant mixtures are detrained whereas positive buoyant mixtures are entrained. However in that case the closure problem is shifted to the choice of how much mass is available for supplying such mixtures and which probability distribution function to choose for the occurrence of the various mixtures. Another interesting idea is put forward by Neggers et al., 2009. In their approach a probability function of temperature and moisture within the cloud is reconstructed from different updrafts. Such a joint pdf allows the determination of the area of the cloud that is positive buoyant and hence the variation of its radius as a function of height.

DETERMINATION OF ENTRAINMENT AND DETRAINMENT FROM LARGE EDDY SIMULATIONS: BULK ESTIMATES

Large Eddy Simulations have been proven to be an extremely useful tool in determining entrainment and detrainment rates in cumulus clouds, initially for shallow cumulus (e.g. Siebesma and Cuijpers, 1995, Siebesma et al., 2003) but more recently also for deep convection (e.g. Kuang and Bretherton, 2006, Khairoutdinov et al., 2009). These studies have provided useful guidance for parameterisations of detrainment and entrainment in large scale models (e.g. de Rooy and Siebesma, 2010 (chapter 3), Siebesma and Holtslag, 1996, Gregory, 2001). The

traditional way to diagnose E and D is not through the direct use of (1.10) but rather through an effective bulk entrainment and detrainment rate defined as

$$\begin{aligned} E_\phi &\equiv -\frac{1}{A\phi_e}\oint_{\hat{\mathbf{n}}\cdot(\mathbf{u}-\mathbf{u}_i)<0} \hat{\mathbf{n}}\cdot(\mathbf{u}-\mathbf{u}_i)\phi dl, \\ D_\phi &\equiv \frac{1}{A\phi_c}\oint_{\hat{\mathbf{n}}\cdot(\mathbf{u}-\mathbf{u}_i)>0} \hat{\mathbf{n}}\cdot(\mathbf{u}-\mathbf{u}_i)\phi dl. \end{aligned} \tag{1.19}$$

where we have indexed the exchange rates E_ϕ and D_ϕ to indicate that there might be a ϕ dependence. Substituting these definitions in (1.8) then directly gives

$$\frac{\partial a_c\phi_c}{\partial t} = M(\varepsilon_\phi\phi_e - \delta_\phi\phi_c) - \frac{\partial a_c\overline{w\phi}^c}{\partial z} + a_cF_c \tag{1.20}$$

By combining (1.20) and (1.11), the bulk fractional entrainment and detrainment rates can be diagnosed from LES output. For this diagnosis the subplume term in $\overline{w\phi}^c$ is usually ignored, steady state is assumed and if we consider a conserved variable the source term F_c is zero, so that the entrainment can be diagnosed according to Betts, 1975

$$\frac{\partial\phi_c}{\partial z} = -\varepsilon(\phi_c - \phi_e) \tag{1.21}$$

Most importantly the exchange rates deduced in this way are used in a similar way in parameterisations. Indeed, virtually all parameterisations use (1.20) as a starting point and therefore need to be fed by the same effective bulk entrainment rates that are diagnosed in this way by LES. The price to be paid is that the bulk exchange rates ε_ϕ and δ_ϕ are now not necessarily a property of the turbulent flow anymore but can be dependent on the field ϕ (cf. Yano et al., 2004).

DETERMINATION OF ENTRAINMENT AND DETRAINMENT FROM LARGE EDDY SIMULATIONS: DIRECT ESTIMATES

The use of the "true" exchange rates as defined by (1.10) is far from trivial from a numerical point of view mainly because it is hard and until recently unclear how to diagnose the local velocity $\mathbf{u}_i$ of the interface. While in reality $\mathbf{u}$ and $\mathbf{u}_i$ are of the same order of magnitude, the cloudy surface in an LES model shifts one grid box in one time step, giving rise to very high unrealistic $\mathbf{u}_i$ values. However, two recent independent studies Romps, 2010 and Dawe and Austin, 2011b have been able to tackle this problem and derive E and D directly based on (1.10). Hereto Dawe and Austin, 2011b follow a straightforward method by applying a subgrid interpolation to determine the position of the cloud surface more accurately. Romps, 2010 follows a different approach. Instead of a bulk cloud sampling, Romps defines a local activity operator, $\mathscr{A}$, which is 1 if q_l and w_c exceed

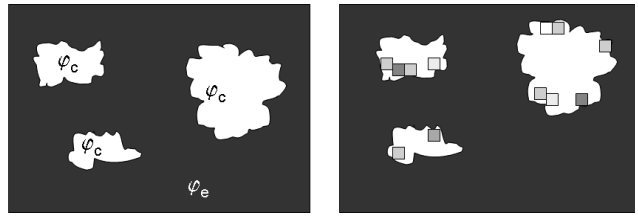

Figure 1.7: Schematic diagram showing the situation relevant for detrainment in a bulk mass flux scheme (left panel), and directly measured detrainment (Romps, 2010) (right panel). In the bulk concept detraining cloudy air always has the average properties of the cloudy area, ϕ_c. Within the direct measurement method the detraining gridboxes are represented by the squares and, as indicated by the gray scale, the detraining air has properties in-between the average cloudy and environmental air.

some threshold value. The local entrainment rate, E is then the local rate at which air flips from inactive to active and vice versa for the detrainment rate, D. Subsequently, Romps, 2010 diagnosis E and D as follows:

$$E = max[0, \frac{\partial}{\partial t}(\rho \mathscr{A}) + \nabla \cdot (\rho \mathbf{u} \mathscr{A})] \tag{1.22}$$

$$D = max[0, -\frac{\partial}{\partial t}(\rho \mathscr{A}) - \nabla \cdot (\rho \mathbf{u} \mathscr{A})] \tag{1.23}$$

where $\frac{\partial}{\partial t}(\rho \mathscr{A}) + \nabla \cdot (\rho \mathbf{u} \mathscr{A})$ is referred to as 'activity source', build up by the motion of the cloud surface (first term) and air advection into or out of the cloud (second term). Summing this 'activity source' over the complete period the grid cell is adjacent to the cloud surface can be seen as an implicit subgrid interpolation of the cloud surface and it also ensures that a pure advective cloud has $E = D = 0$.

As Romps, 2010 and Dawe and Austin, 2011b evaluate E and D locally, there are some important differences with the bulk approach. For example, bulk estimates of ε and δ are tracer dependent whereas direct measurements of the lateral mixing coefficients are only related to the local properties of the flow (Romps, 2010). However, the most striking result was that the bulk plume approach underestimates entrainment and detrainment by roughly a factor 2 (Romps, 2010). This is elucidated in Fig. 1.7a showing the conceptual picture following the bulk concept. The air that detrains from the cloud is supposed to have the same property as air averaged over all clouds ($\phi_{\text{detrainingair}} = \overline{\phi}^c \equiv \phi_c$). Fig. 1.7b illustrates the situation in Romps, 2010 local approach. Some gridboxes are diagnosed as

detraining according to the direct measurement technique, here presented by grey squares. In general the relatively less buoyant cloudy gridboxes will detrain. Possibly a grid box that just entrained but now detrains again. Consequently, the potential temperature of the detraining grid boxes will on average be lower than the potential temperature averaged over the complete cloudy area. Similarly, it will normally not be the most humid grid boxes that detrain. So detraining air will on average have properties in-between the average cloudy and average environmental air. The same arguments hold for entrainment. Because the difference between detraining and environmental air or entraining and cloudy air is larger in the bulk approach than in Romps framework, the corresponding ε and δ values should be smaller in the bulk approach to get the same correct lateral fluxes. Very recently, this discrepancy between bulk and directly measured ε and δ values is further investigated and quantitatively explained by Dawe and Austin, 2011a.

A potentially important result of Romps, 2010 and Dawe and Austin, 2011b is the change of the cloud properties due to detrainment because in their approach detraining air does not have the average cloud properties (see Fig. 1.7). This is in contrast with the entraining plume model of Betts, 1975 (Eq. 1.21) used in the bulk mass flux concept, where only ε determines the dilution. On the other hand, if ε is diagnosed in LES within the bulk framework it will describe the correct cloud dilution as long as it is applied in a bulk scheme. One might say that this diagnosed bulk ε implicitly takes into account the negative dilution due to detrainment.

Direct entrainment and detrainment calculations are very useful to understand the underlying processes. At the same time we should realize that ultimately the different approaches lead to the same, correct dilution of the cloud properties and turbulent transport as long as the mixing coefficients are diagnosed and applied in the same framework. Therefore, bulk diagnosed entrainment and detrainment values are appropriate for usage in a model bulk mass flux parameterisation.

1.2.4. ENTRAINMENT AND DETRAINMENT IN MASS FLUX PARAMETERISATIONS

For almost all NWP and climate models, convection is still a sub-grid process which thus has to be parameterised. One of the key questions is how the parameterisation should account for the influence of environmental conditions (like e.g. relative humidity). A wide variety of approaches exists. Here we discuss an entrainment and detrainment formulation that is widely applied in shallow convection schemes.

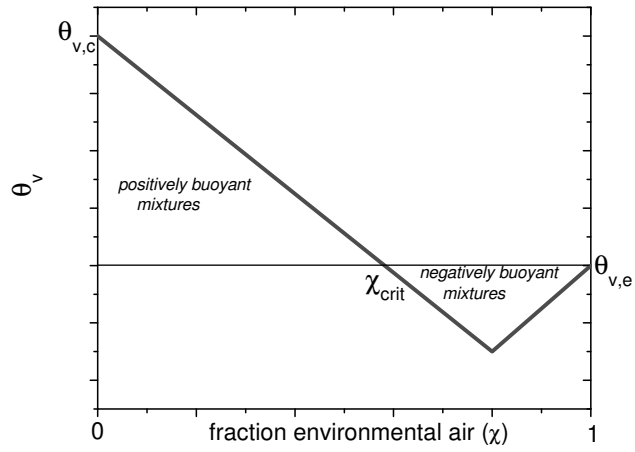

Figure 1.8: The virtual potential temperature of a mixture of cloudy air with environmental air as a function of the fraction, χ, of environmental air. The virtual potential temperature of the cloudy and environmental air is θ_{vc} and θ_{ve} respectively. χ_{crit} is the fraction environmental air necessary to make the cloudy air just neutrally buoyant.

KAIN FRITSCH TYPE BUOYANCY SORTING SCHEMES AND UPDATES

Convection schemes including the parameterisations of ε and δ show a large variety of complexity. On one hand of the spectrum are the simple bulk mass flux schemes with constant ε and δ values whose values are loosely based on (1.4). However it has been shown that such simple fixed values for the mixing coefficients are too limited since their values appear to be dependent on the environmental conditions (see e.g. Derbyshire et al., 2004, Kain and Fritsch, 1990). To take the environmental conditions into account Raymond and Blyth, 1986 and Kain and Fritsch, 1990 introduced the buoyancy sorting concept. These widely applied type of schemes together with some recent updates are described here. Although not specifically designed for shallow convection, the parameterisation of Kain and Fritsch, 1990 is widely applied as such. In their approach, different mixtures of in-cloud and environmental air are made. Negatively buoyant mixtures are assumed to detrain whereas positively buoyant mixtures entrain. Due to evaporative cooling, θ_{v} of the mixture, can drop below that of the environment, so leading to detrainment. This process is illustrated in Fig. 1.8 which shows the θ_{v} of a mixture of cloudy air with a fraction χ of environmental air. For example purely cloudy air has $\chi = 0$ and obviously $\theta_{\mathrm{v}}(\chi = 0) = \theta_{\mathrm{v,c}}$. The critical fraction χ_{crit} is defined as the fraction of environmental air needed to make the mixture just neutrally buoyant. In the original Kain-Fritsch (hereafter

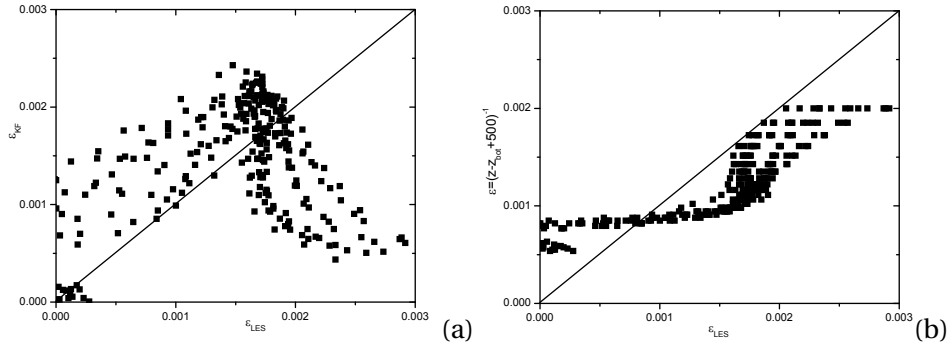

Figure 1.9: Fractional entrainment rates as diagnosed (using the core sampling) from LES, $\varepsilon_{\mathrm{LES}}$, and estimates according to (a) Eq. (1.24) with $\varepsilon_0 = 0.02$ (optimal value), $\varepsilon_{\mathrm{KF}}$ or (b) $\varepsilon = (z - z_{\mathrm{bot}} + 500)^{-1}$, where z is the height in (m) and z_{bot} is cloud base height. These results are for the BOMEX case (Siebesma et al., 2003).

KF) scheme, mixtures with $\chi < \chi_{\mathrm{crit}}$ are assumed to entrain while mixtures with $\chi > \chi_{\mathrm{crit}}$ are assumed to detrain.

To derive the fractional entrainment and detrainment coefficients within the KF concept, the amount of mass used for mixing (not discussed), as well as the probability density function (PDF) for the occurrence of the various mixtures has to be determined. As there is no a priori knowledge on which PDF should be chosen, it is natural to assume that all mixtures have an equal probability of occurence, which leads to (Bretherton et al., 2004)

$$\varepsilon_{\mathrm{KF}} = \varepsilon_0 \chi_{\mathrm{crit}}^2 \tag{1.24}$$

$$\delta_{\mathrm{KF}} = \varepsilon_0 (1 - \chi_{\mathrm{crit}})^2 \tag{1.25}$$

where ε_0 is the fractional mixing rate, i.e. the fractional mass available for mixing, which in the original KF concept is kept constant. We have used LES results from a shallow cumulus convection case based on observations made during BOMEX (Holland, 1972) in order to evaluate ε based on Eq. (1.24) and compared these with LES diagnosed values based on Eq. (1.21). Even if we choose a best estimate of ε_0, Fig. 1.9a shows a low correlation. Better results can already be obtained if ε is estimated with a simple decreasing function with height (see Fig. 1.9b).

When the original KF concept was used in practice, several deficiencies were reported, many of them related to the corresponding lateral mixing coefficients. These deficiencies, including some modifications to address them, are well summarised by Kain, 2004. In parallel, variations on KF schemes were developed like Bretherton et al., 2004. Kain, 2004 pointed out that, according to Eq. (1.24), dry conditions (corresponding to small χ_{crit}) will result in small ε values and consequently little dilution of the updraft. Hence, the original KF concept can lead to

the contra-intuitive result of deeper cloud layers in combination with drier (more hostile) environmental conditions. This behavior of the KF model was also confirmed by S. Jonker, 2005. Contrastly, LES results show considerably shallower cloud depths for drier environmental conditions (Derbyshire et al., 2004). To fix the above mentioned deficiency some of the newer versions of the KF scheme prescribe a lower limit to the entrainment of 50% of the environmental air involved in the mixing process and/or try to use state-dependent values for ε_0.

Another deficiency, this time related to Eq. (1.25) and discussed by Bretherton et al., 2004 is the excessive detrainment if all negatively buoyant mixtures are rejected from the updraft. Bretherton et al., 2004 dealt with this problem by introducing a length scale below which negatively buoyant parcels can remain the upward velocity and consequently do not detrain yet.

From the previous discussion it can be concluded that, although the KF concept contains interesting and important ideas, there are some fundamental problems. In practice these problems are solved by rather drastic modifications and tuning parameters which more or less undermine the physical attractiveness of the concept. Nevertheless, in this thesis we will show how the buoyancy sorting concept, and in particular parameter χ_{crit}, can be applied in an alternative formulation of the lateral exchange which circumvents the aforementioned problems.

1.3. AIM AND OUTLINE

Cumulus convection plays an important role in the earth's weather and climate system. Hence, an accurate representation of this process is crucial in every weather and climate model. Current models have insufficient resolution to resolve shallow convection and therefore incorporate the impact through the use of a parameterisation scheme, usually a bulk mass flux scheme. Key parameters in such a convection scheme are the entrainment and detrainment, that describe the lateral exchange between the updraft massflux and the environment. The main objective of this thesis is to gain insight in the behaviour of these mixing coefficients within the conceptual framework of a mass flux scheme and to apply this knowledge in practice in a model. Hereto, the following research questions are addressed:

1. *How do the entrainment and detrainment processes depend on environmental and geometrical conditions and how can this be used to improve convection parameterisations in weather and climate models?*

   In chapter 2, LES results for a wide variety of shallow cumulus cases are used to investigate the lateral mixing coefficients. Based on these results, formulations for entrainment and detrainment are proposed that include

the most important dependencies.

2. *What are the underlying principles that determine the behaviour of the lateral mixing processes?*

Based on budget equations of total water specific humidity and mass, analytical expressions are derived for entrainment and detrainment in chapter 3. From these expressions a physical picture emerges that explains the typical behaviour of the lateral mixing coefficients and provides a sound physical base for the formulations proposed in chapter 2. If these expressions are also combined with the budget equation for vertical velocity, new formulae for entrainment and detrainment rates are found that correlate well with traditionally LES diagnosed entrainment and detrainment values. These expressions can be used to evaluate existing formulations and as an inspiration for new parameterisations.

3. *How to improve model performance by means of improved physical parameterisations?*

Parameterisations have a strong impact on the model performance. Yet, it appears to be difficult to improve the model by improved parameterisations because the schemes are highly optimized and contain numerous compensating errors. Chapter 4 describes how three tightly coupled boundary layer schemes, including the shallow convection scheme, are included in a model in one comprehensive integral revision. The modifications are based on a wide variety of argumentations; from theoretical considerations, to LES results for idealized intercomparison cases, to more pragmatically tuning of uncertain parameters.

Finally, chapter 5 describes the main conclusions of this thesis, as well as an outlook on how the research area of parameterising convection will change with the continuous increase in model resolution.

2

A SIMPLE PARAMETERISATION FOR DETRAINMENT IN SHALLOW CUMULUS

ABSTRACT

For a wide range of shallow cumulus convection cases, Large-Eddy Simulation (LES) model results have been used to investigate the lateral mixing as expressed by the fractional entrainment and fractional detrainment rates. It appears that the fractional entrainment rates show much less variation from hour to hour and case to case than the fractional detrainment rates. Therefore, in the here-proposed parameterisation, the fractional entrainment rates are assumed to be described as a fixed function of height, roughly following the LES results. Based on the LES results a new more flexible parameterisation for the detrainment process is developed that contains two important dependencies. Firstly, based on cloud ensemble principles it can be understood that deeper cloud layers call for smaller detrainment rates. All current mass flux schemes ignore this cloud height dependence which evidently leads to large discrepancies with observed mass flux profiles. The new detrainment formulation deals with this dependence by considering the mass flux profile in a non-dimensionalized way. Secondly, the influence of environmental conditions in which both relative humidity of the environmental air and the buoyancy excess of the updraft affect the detrainment rates and therewith the mass flux profiles. This influence can be taken into account by borrowing a parameter from the buoyancy sorting concept and use it in a bulk sense. LES results show that with

Published as: de Rooy, Wim C. and A. Pier Siebesma, 2008: A simple parameterisation for detrainment in shallow cumulus. Mon. Wea. Rev. 136 , 560–576, doi:10.1175/2007MWR2201.1

this bulk parameter the effect of environmental conditions on the fractional detrainment rate can be accurately described. A simple practical but flexible parameterisation for the fractional detrainment rate is derived and evaluated in a Single Column Model (SCM) for three different shallow cumulus cases which shows the clear potential of this parameterisation. The here proposed parameterisation is an attractive and more robust alternative for existing more complex buoyancy sorting based mixing schemes, and can be easily incorporated in current mass flux schemes.

2.1. INTRODUCTION

Shallow cumulus convection plays an important role in the vertical transport of thermodynamic properties and influences large-scale circulations in both the Tropics as well as in midlatitudes. Therefore, an adequate parameterisation of this process is crucial both in numerical weather prediction (NWP) and climate models. With the exception of the socalled adjustment schemes (e.g. Betts and Miller, 1986, Janjic, 1994) virtually all shallow cumulus convection parameterisations use a mass flux concept. Within the mass flux framework the upward mass transport is usually described by a simple budget equation

$$\frac{\partial M}{\partial z} = (\varepsilon - \delta) M \tag{2.1}$$

where all notation is conventional, $M = \rho w_u a_u$ denotes the upward mass flux that consists of the product of the density ρ, the cloud updraft velocity w_u and the associated cloud updraft fraction a_u. Furthermore the fractional entrainment ε describes the inflow of environmental air into the cloudy updraft while the fractional detrainment δ describes the outflow of cloudy air into the environment.

Recently there has been a regained interest in the parameterisation of especially the fractional entrainment rate (Grant & Brown, 1999; Gregory et al., 2000; Neggers et al., 2002; Siebesma, 1998; Siebesma & Cuijpers, 1995). However, strangely enough, little attention has been paid to the parameterisation of the detrainment process although this counterpart of the cloud mixing process is equally important, or as we will see, probably even more important, for obtaining realistic mass flux profiles in cumulus convection.

The most simple, and still widely applied description of lateral mixing in a mass flux concept is the use of fixed fractional entrainment (ε) and detrainment (δ) rates. As we will demonstrate in this study there are at least two disadvantages to such an approach. Firstly, the dependency of detrainment rate on the cloud layer depth is ignored. Secondly, the use of fixed entrainment and detrainment rates leads to insensitivity to changes in the humidity of the environment of the convective updrafts, despite several studies that demonstrate the oppo-

site (Derbyshire et al., 2004; Kain & Fritsch, 1990). In order to address the latter deficiency Raymond and Blyth, 1986 and Kain and Fritsch, 1990 introduced a buoyancy sorting concept in convection schemes. More specific, in the concept proposed by Kain and Fritsch, 1990 different mixtures of in-cloud and environmental air are made. Subsequently, all negative buoyant mixtures are assumed to detrain instantly, whereas all positive buoyant mixtures are entrained. Hence, due to the stronger evaporative cooling, the mass flux will decrease more rapidly with height in a dryer environment. Although physically appealing, this concept uses difficult to determine functions and tunable parameters, like the probability density function (PDF) describing the probability of different mixtures. Besides, the Kain Fritsch scheme shows some unwanted characteristics. In this scheme all the negative buoyant mixtures are immediately detrained, which can lead to an excessive decrease of the mass flux with height. Bretherton et al., 2004 dealt with this problem by introducing a critical eddy mixing distance. Another problem of the Kain Fritsch scheme is the fact that in dryer environmental conditions ε will decrease resulting in less dilution of the core and consequently higher cloud tops (S. Jonker, 2005; Kain, 2004). This contrasts with Cloud Resolving Model (CRM) results (Derbyshire et al., 2004). Kain, 2004 handles this problem by imposing a minimum entrainment rate which is 50 percent of the maximum possible entrainment rate in the Kain Fritsch scheme.

Instead, in view of the complexity (Zhao & Austin, 2005a, 2005b) and our limited understanding of the lateral mixing process, we propose a simpler, but yet flexible parameterisation of this mechanism. This parameterisation shows the right sensitivity to cloud height and environmental conditions for a wide range of shallow cumulus convection cases.

We start with a description of the strategy, the models and the cases in section 2.2. Section 2.3 states the central problem to be investigated. In section 2.4 we analyze the lateral mixing process with LES which leads to the new detrainment parameterisation as introduced in section 2.5.1. Results with the new approach included in a Single Column Model (SCM) are presented in section 2.5.2. Finally, in section 2.6 the conclusions and discussions are given.

2.2. STRATEGY, MODELS AND CASES

2.2.1. STRATEGY AND MODELS

In order to develop a robust parameterisation for the detrainment process we adopt here the strategy that has been succesfully employed within GEWEX Cloud Systems Studies (GCSS) (Jakob, 2003; Randall et al., 2003). In short this strategy utilizes Large Eddy Simulation (LES) results along with observations of past field experiments to generate a detailed data base that can be used to develop and

evaluate parameterisations of cloud related processes in Single Column Model (SCM) versions of NWP and climate models. Past GCSS studies have shown that this strategy has worked extremely well for especially the cumulus topped boundary layer (Brown et al., 2002; Siebesma et al., 2003; Stevens et al., 2001). We therefore will use the results of the Dutch Atmospheric LES model DALES (Cuijpers & Duynkerke, 1993; Siebesma & Cuijpers, 1995) as pseudo observations for a number of shallow cumulus cases that have been analysed in detailed by the GCSS Working Group of Boundary layer Clouds (GWGBCL).

The SCM that we use for the present chapter is derived from a recent Hirlam NWP model version (Unden et al., 2002). Since the radiation, dynamical tendencies, and the surface fluxes or sea surface temperature (SST) are prescribed for all cases, only the turbulence, the convection, and the cloud scheme are relevant for this study. Further, the SCM uses a dry turbulent kinetic energy (TKE) scheme (Cuxart et al., 2000) with a mixing length scale according to Lenderink and Holtslag, 2004. For convection, the ECMWF Tiedtke, 1989 mass-flux scheme is incorporated. This convection scheme is updated with a new trigger function (Jakob & Siebesma, 2003) and a mass-flux closure following Neggers et al., 2004. As a starting point, we also adopt the detrainment and entrainment rates according to Siebesma and Cuijpers, 1995 and Siebesma et al., 2003 respectively (i.e. $\delta = 2.75 \times 10^{-3}\mathrm{m}^{-1}$ and $\varepsilon = c_\mathrm{e} z^{-1}\mathrm{m}^{-1}$ with $c_\mathrm{e} = 1.0$). Finally, a statistical cloud scheme code is used, based on the ideas of Cuijpers and Bechtold, 1995. The cloud scheme is coupled to the convection scheme following Lenderink and Siebesma, 2000, i.e. the convective activity partly determines the variance of the specific humidity. Vice versa, the convection scheme is coupled to the cloud scheme via the mass-flux closure of Neggers et al., 2004

$$M_b = 0.3 a_\mathrm{u}(z_\mathrm{b})\, w_* \tag{2.2}$$

where M_b and $a_\mathrm{u}(z_\mathrm{b})$ are resp. the mass-flux and the cloud updraft fraction at cloud base height z_b and w_* is the free convective vertical velocity scale of the subcloud layer. Note that this mass flux closure is closely related with a simpler closure proposed by Grant, 2001 in which the cloud base mass flux is directly proportional to w_*, i.e. $M_\mathrm{b} = 0.03 w_*$. The precipation in the SCM is turned off since we compare the SCM results exclusively with non-precipitive LES model results. This way a more precise and well focussed intercomparison between the LES results and the parametrized lateral mixing is facilitated. Furthermore, for all cases the timing of the convective activity and the mass flux at cloud base are in reasonably good agreement with the LES results. Therefore, discrepancies in the cloud layer between SCM and LES results can be mainly ascribed to differences in the lateral mixing mechanisms, i.e. the choices for ε and δ. The SCM configuration has 60 vertical levels with an effective resolution of around 100m

in the cloud layer and a timestep of 60 seconds is used.

Finally we would like to remark here that, although we demonstrate results for one specific SCM, the results are applicable for any bulk mass flux scheme in general.

2.2.2. CASES

In order to develop and evaluate a detrainment parameterisation we will make use of a suite of 3 shallow cumulus cases that have been succesfully subjected to GCSS intercomparison studies. In the remainder of this section we will give a short description of each of these three cases.

BOMEX

As a relatively simple shallow cumulus case we use results of the undisturbed period of phase 3 during the Barbados Oceanographic and Meteorological EXperiment (BOMEX, (Holland & Rasmusson, 1973)) For a detailed description of the forcings we refer to Siebesma and Cuijpers, 1995 (henceforth SC95). During this case shallow cumili , with cloud base and top at approximately 500 and 1500 m respectively, were observed under steady-state conditions. Therefore, temperature and total water specific humidity q_t profiles remain stationary.

ARM

The ARM case describes the development of shallow cumulus convection over land. This case is based on an idealization of observations made at the Southern Great Plains ARM site on 21^{st} June 1997 (Brown et al., 2002). From approximately 1000 LT (1500 UTC) cumulus clouds start to develop at the top of an initially clear convective boundary layer. From then on the cloud layer grows to a maximum depth of 1500 m at 1630 LT after which it starts to decrease. Finally, at 1930 LT at the end of the day, all clouds collapse and the cloud layer depth is shrinked back to zero.

RICO

The RICO (Rain In Cumulus over the Ocean) composite case is based on a three week period from December 16th to January 8th 2005 with typical trade wind cumili and a fair amount (0.3 mm/day) of precipitation. However, as mentioned before, in our SCM and in the LES precipitation is turned off. The measurement campaign took place in the vicinity of the Caribbean islands Antigua and Barbuda. The 24hr composite run is initialized with the mean state and driven by the mean large scale forcings of the 3 week period. More information about this case and the experimental set up of the composite run can be found on www.knmi.nl/samenw/rico

2.3. PROBLEM FORMULATION

Siebesma and Holtslag, 1996 already demonstrated that a well-chosen constant detrainment and entrainment rate can adequately reproduce the observed steady state profiles such as observed during BOMEX. Indeed, the standard parameterisation described in the previous section with fixed mixing rates, i.e. $\varepsilon = c_e z^{-1} \mathrm{m}^{-1}$ with $c_e = 1.0$ and $\delta = 2.75 \times 10^{-3}\,\mathrm{m}^{-1}$, produces almost perfect steady state θ and q_t profiles close to the observations (not shown). This result is not surprising since the choices of the entrainment and the detrainment rates are directly inspired on the diagnosed mixing rates as obtained from LES results based on BOMEX (Siebesma et al., 2003). The central and more interesting issue that we want to address in this chapter is to what extent a simple parameterisation with fixed entrainment and detrainment rates can be applied to more complicated cases such as the ARM diurnal cycle.

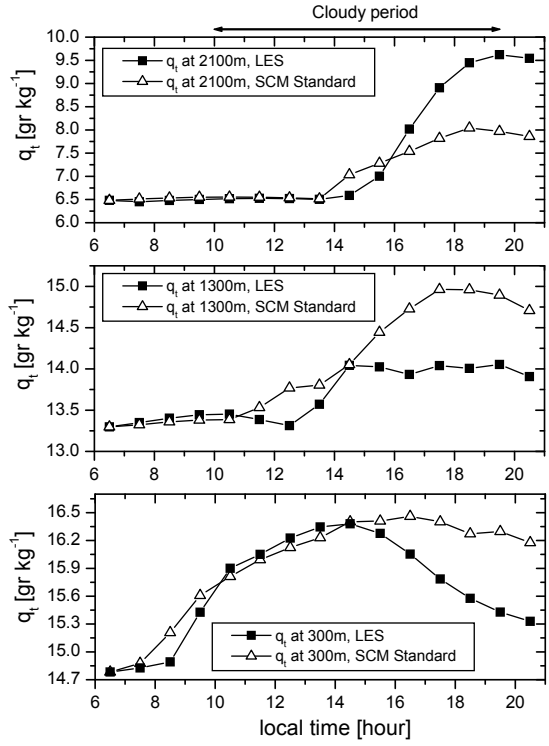

Figure 2.1: Time series of total water specific humidity during the ARM case at three levels (299, 1300, and 2100m) for LES and for the Standard SCM using the default fixed ε and δ.

In Figure 2.1 we show for the ARM case time series of total water specific humidity q_t in the subcloud layer at 300 m and at two heights in the cloud layer

(1300 m and 2100 m) for both the LES results and the SCM results with the standard parameterisation. The simple observation that can be made from these time series is that, in the latter half of the cloudy period (from 1000 to 1930 LT), the SCM overestimates the humidity in the subcloud layer and in the lower half of the cloud layer while the humidity in the upper half of the cloud layer is underestimated. This suggests that for this case the parameterized convective transport in the SCM is not active enough. This is also demonstrated in Fig. 2.2 in which the humidity profile is shown for the LES and the SCM results at 1930 LT (0030 UTC). Similar results (not shown) are obtained for the potential liquid water temperature θ_ℓ. The aforementioned discrepancies between SCM and the LES results for the ARM case are also present in the SCM results reported in Soares et al., 2004, who used $\varepsilon = 2 \times 10^{-3}$ and $\delta = 3 \times 10^{-3}\ \mathrm{m}^{-1}$. To explain and understand these differences between the LES data and SCM results we need to take a closer look to the lateral exchange rates such a diagnosed in the LES model. This will be the topic of the next section.

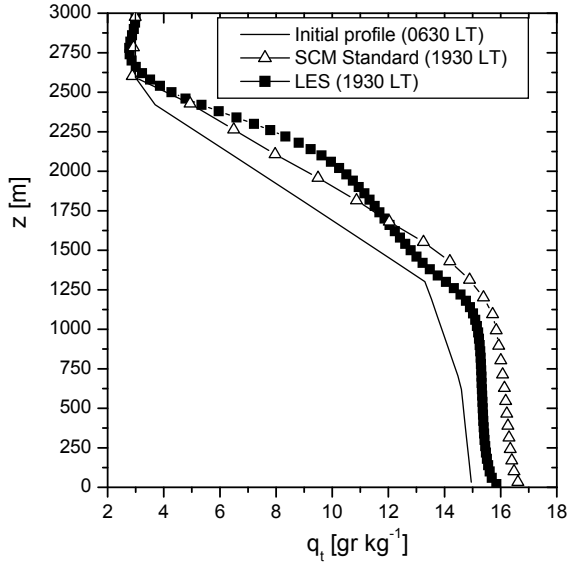

Figure 2.2: Total water specific humidity profiles for different simulation hours during the ARM case for the LES model and the Standard SCM using the default fixed ε and δ.

2.4. LATERAL MIXING AS DIAGNOSED BY LES

In order to diagnose bulk lateral entrainment and detrainment from LES results one can use a simple entraining plume model (Betts, 1975), which reads for moist

conserved variables

$$\frac{\partial \phi_u}{\partial z} = -\varepsilon(\phi_u - \overline{\phi}) \tag{2.3}$$

where ϕ refers to either the liquid water potential temperature θ_ℓ or the total water specific humidity q_t. The cloudy updraft variables ϕ_u (where u stands for updraft) and the mass flux can be easily diagnosed through conditional sampling of the LES output. Subsequently the fractional entrainment and detrainment rates can be determined through the use of (2.3) and (2.1). Throughout this chapter we only use the so-called cloud-core sampling in which the cloudy updraft is defined as all the LES grid points that contain liquid water ($q_\ell > 0$) and are positively buoyant ($\theta_v > \overline{\theta_v}$). Here θ_v is the virtual potential temperature and $\overline{\theta_v}$ is the slab averaged virtual potential temperature. The cloud-core sampling method is chosen because it describes the turbulent fluxes the best (SC95). It should be understood that for the remainder of this chapter "cloud-core" will be referred to as "updraft". For the analysis of the LES results in this section we will use the hourly averaged output of the ARM case, as this case contains a wide variety of cloud depths and environmental conditions.

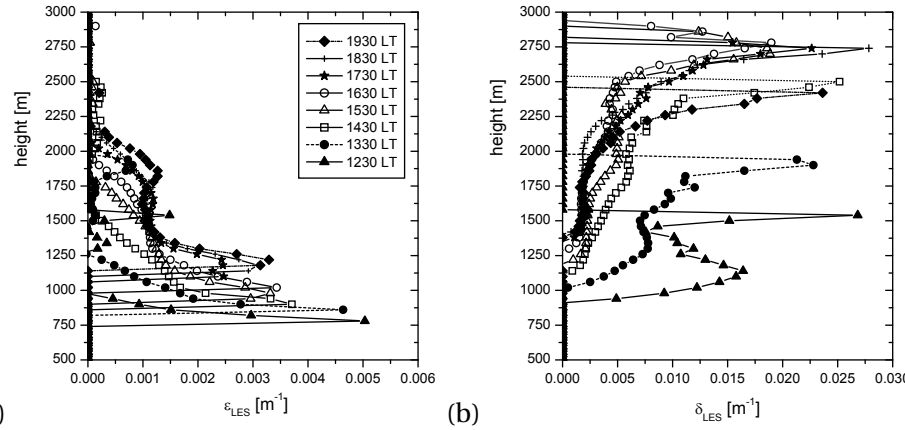

Figure 2.3: Hourly averaged fractional entrainment (a) and detrainment (b) rates diagnosed from LES results for the ARM case. Note the different x-axis scale for (a) and (b).

Figure 2.3 displays the LES diagnosed fractional entrainment and detrainment rates. It appears that the variation in δ during the simulation is much larger than for ε (note the different x-axis scale!). The limited variation in ε might be related to the presence of a protecting shell around the cloudy core (Zhao & Austin, 2005a, 2005b) with properties in-between core and environmental values. Due to this shell the influence of the environment on the cloudy core is damped leading to a relative insensitivity of ε for the environment.

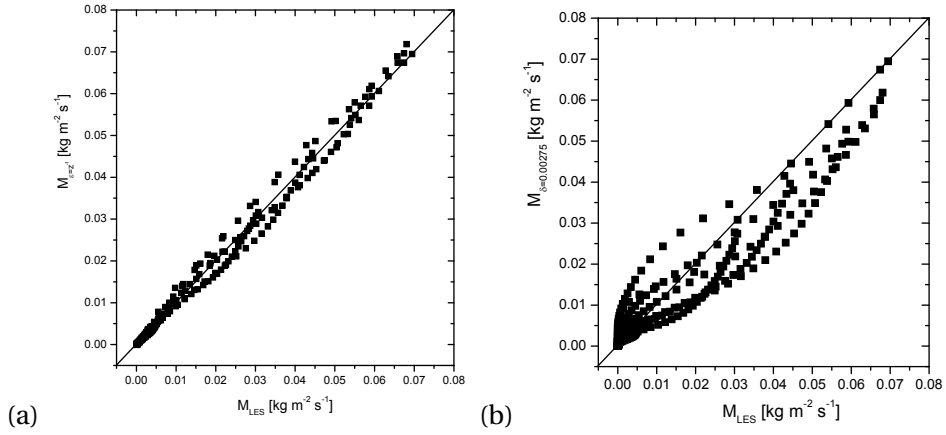

Figure 2.4: Comparison of the Mass flux for the ARM case as directly diagnosed from LES with (a) the mass flux obtained using a fixed parameterized fractional entrainment rate ($\varepsilon = z^{-1}$) along with the dynamical LES diagnosed δ or (b) with the mass flux obtained using a fixed parameterized fractional detrainment rate ($\delta = 2.75 \times 10^{-3}$) along with the dynamical LES diagnosed ε.

A more quantitative way to look at the (in)sensitivity of ε and δ is to compare the directly diagnosed mass fluxes from the LES with i) the mass flux obtained using a *fixed parameterized* fractional entrainment rate $\varepsilon = c_e z^{-1}$ along with the dynamical LES diagnosed fractional detrainment rate δ (Fig. 2.4a) and ii) the mass flux using a *fixed parameterized* fractional detrainment rate $\delta = 2.75 \times 10^{-3}$ along with the dynamical LES diagnosed fractional entrainment rate (Fig. 2.4b). This clearly shows that the fixed parameterized fractional entrainment profile along with hourly diagnosed fractional detrainment rates gives an excellent estimate of the mass fluxes. Conversely the combination of a dynamical LES diagnosed entrainment rate with the fixed fractional detrainment rate results in considerable scatter with under- and overestimations of the mass flux. So it seems more useful to concentrate on improving the mass flux profile by developing a more dynamical δ parameterisation. Therefore we will use a fixed function for ε and develop a dynamical detrainment formulation to produce the correct mass flux profiles. The above mentioned results are consistent with H. Jonker et al., 2006 who showed that, for a LES study based on the Small Cumulus Microphysics Study (SCMS) experiment (Neggers et al., 2003), the variation with cloud size of ε is an order of magnitude smaller than for δ.

Figure 2.5 presents the cloud layer height dependence of the LES fractional detrainment rate averaged over the cloud layer (noted as $< \delta_{\mathrm{LES}} >$). Most striking is, until 1530 LT, the decrease of δ with increasing cloud height. This can be explained as follows (see Fig. 2.6). Many studies considering shallow convection

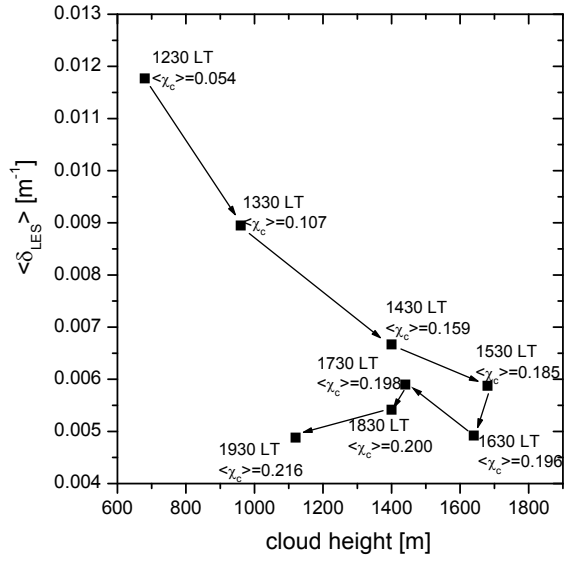

Figure 2.5: Mean detrainment rates (averaged over the cloud layer) diagnosed from LES results for the ARM case.

(e.g. SC95) showed that δ is larger than ε. Consequently, the mass flux profile decreases with height, reflecting an ensemble of clouds with the more shallow clouds losing their mass at relatively low heights, and larger clouds transporting mass in the upper part of the cloud layer (SC95). Constant entrainment and detrainment rates, e.g. the ones in our SCM, fix the mass loss per meter. In fact it is the difference between ε and δ (see eq. (1)) that determines how fast the mass flux decreases with height and the diagnosed values from SC95 are such that the mass flux profile decreases monotonically to zero for a cloud depth of 1000 m, i.e. the cloud depth observed during BOMEX. However, a bold application of these rates on a shallower cloud layer will result in a nonzero mass flux at cloud top while applying these rates on a deeper cloud layer will result in an almost zero mass flux already halfway through the cloud layer (see Fig. 2.6), all in disagreement with LES model results. The remedy to this unwanted behavior is also clear; the difference between the entrainment and the detrainment needs to be chosen such that the resulting mass flux is exhausted around cloud top , a suggestion already made in Siebesma, 1998. With a fixed ε, this calls for smaller detrainment rates for deeper cloud layers and larger detrainment rates for shallower clouds, all in qualitative agreement with the diagnosed detrainment rates displayed in Fig. 2.5

A second interesting feature that can be observed in Fig. 2.5 is that after simu-

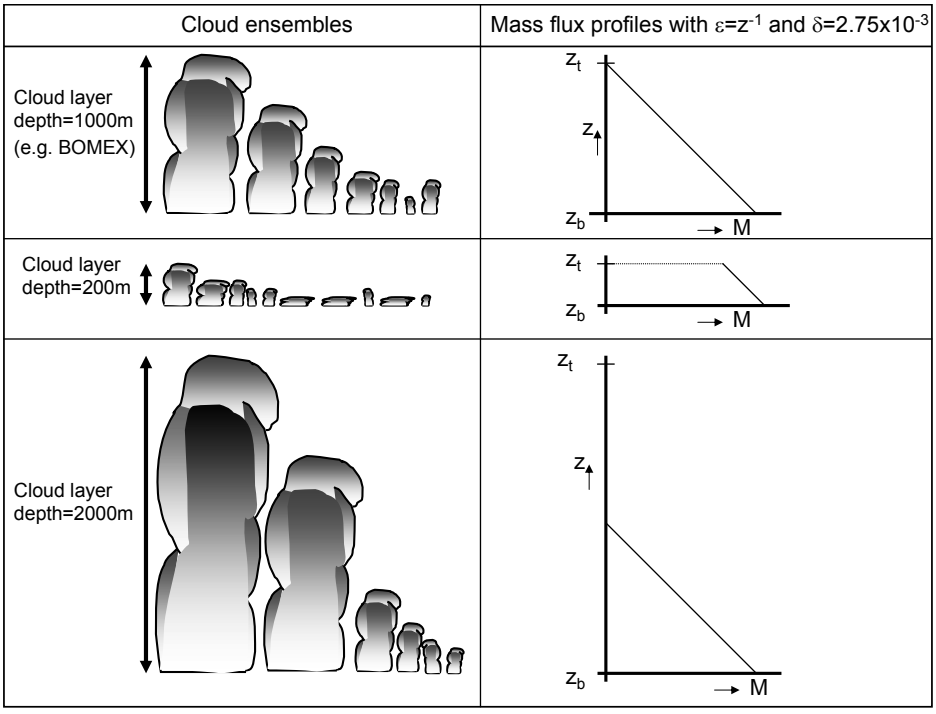

Figure 2.6: Cloud ensembles for different cloud layer depths and the corresponding mass flux profiles using fixed ε and δ based on a cloud layer depth of 1000 m.

lation hour 9 (1530 LT) the cloud height decreases without an increase in detrainment. A plausible explanation of this phenomenon is that for these hours the clouds rise in an environment that is already premoistened for several hours by detrainment from former clouds (see also Raymond and Blyth, 1986). Therefore the entrained air will be moistener and hence less evaporative cooling will occur resulting in lower detrainment rates than in a dryer environment. This effect has been demonstrated recently in great detail by Derbyshire et al., 2004 where they studied convective activity in a number of cases in which only the environmental relative humidity was varied. A good measure of this effect can be expressed by the critical fraction of environmental air, χ_c (Kain & Fritsch, 1990), a parameter coming from the buoyancy sorting concept. So, besides the detrainment rates Fig. 2.5 also shows the analytically determined (see Appendix A) mean critical fractions $< \chi_c >$ (averaged over the cloud layer).

Let us first elucidate the meaning of χ_c with Fig. 2.7. Plotted is the virtual potential temperature θ_v of a mixture of updraft air with a fraction, χ of environ-

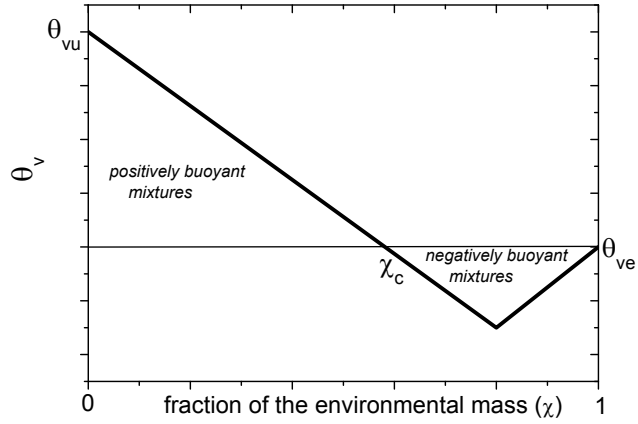

Figure 2.7: The virtual potential temperature of a mixture of updraft air with environmental air as a function of the fraction, χ, of environmental air. The virtual potential temperature of the updraft and environmental air is θ_{vu} and θ_{ve} respectively. χ_{c} is the fraction environmental air necessary to make the updraft air just neutrally buoyant.

mental air. For pure updraft air $\chi = 0$ and obviously $\theta_{\mathrm{v}}(\chi = 0) = \theta_{\mathrm{v,u}}$. Likewise for $\chi = 1$, the mixture consists of purely environmental air, $\theta_{\mathrm{v}}(\chi = 1) = \theta_{\mathrm{v,e}}$ (where subscript e stands for environment). Because of the evaporative cooling due to the mixing process the mixing line is not just a straight line from $\theta_{\mathrm{v,u}}$ to $\theta_{\mathrm{v,e}}$, but instead typically exhibits a minimum at the point where all the liquid water is evaporated. The critical fraction χ_{c} is defined as the fraction of environmental air that is needed to make the mixture neutral buoyant. The heart of the matter of the Kain-Fritch scheme is that it is assumed that all negative buoyant mixtures (i.e. mixtures with $\chi > \chi_{\mathrm{c}}$) will be detrained, while all positive buoyant mixtures (i.e. $\chi < \chi_{\mathrm{c}}$) are entrained into the cloudy updraft. Consequently, if the environmental air is drier and/or the buoyancy excess $(\theta_{\mathrm{v,u}} - \theta_{\mathrm{v,e}})$ is smaller, χ_c will be smaller and hence the fractional detrainment rate will be larger. Here we see that also an updraft property itself (namely $\theta_{\mathrm{v,u}}$) is involved in what we will still call the dependence on environmental conditions.

To recapitulate, the mean fractional detrainment rates shown in Fig. 2.5 are influenced by cloud height and environmental conditions. The two variables that can take this dependence into account are cloud depth $h = z_{\mathrm{t}} - z_{\mathrm{b}}$, where z_{t} indicates cloud top height, and the critical fraction χ_{c}. To investigate these dependencies on the mass flux profiles separately, Fig. 2.8a shows the non-dimensionalized mass flux $\hat{m} = M/M_{\mathrm{b}}$ as a function of the non-dimensionalized height $\hat{z} = (z - z_{\mathrm{b}})/h$, where z_{b} is defined as the height with maximum mass flux. By rescaling the height by the cloud depth we now filtered out the effect of cloud

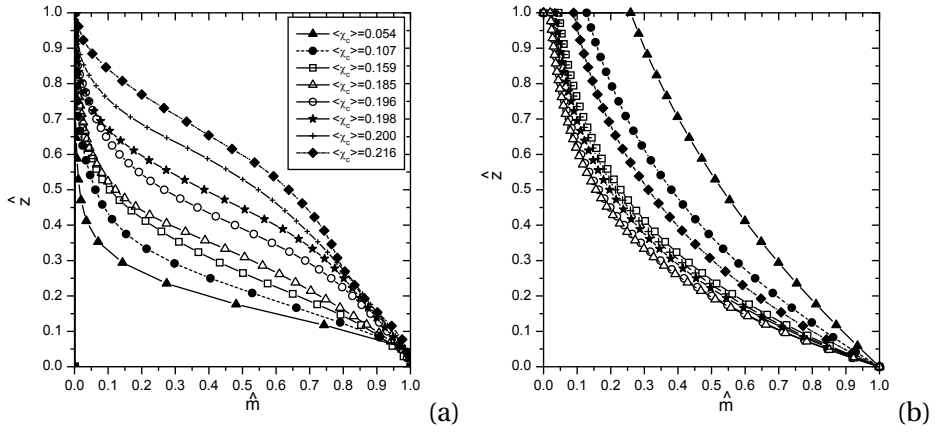

Figure 2.8: (a) LES non-dimensionalized mass flux profiles for the ARM case for different simulation hours (symbols as in Fig. 2.3). z_b is defined as the height with maximum mass flux. (b) As (a) but diagnosed with M_b, z_b and z_t from the LES model in combination with $\varepsilon = z^{-1}$ and $\delta = 2.75 \times 10^{-3}\,\mathrm{m}^{-1}$.

depth on the detrainment. If cloud depth would be the only parameter that determined δ, Fig. 2.8a would display a data collapse. Instead we still observe a variation in the shape of the mass flux profile that is likely due to the different environmental conditions as measured by $< \chi_c >$. Indeed, as expected we observe that larger values of $< \chi_c >$ lead to a relatively slower decrease of the mass flux profile and vice versa.

This observation is in clear conflict with the standard parameterisation, i.e. $\varepsilon = z^{-1}$ and $\delta = 2.75 \times 10^{-3}\,\mathrm{m}^{-1}$. This is illustrated in Fig. 2.8b in which the hourly averaged non-dimensionalized mass fluxes are calculated using the ARM LES results for M_b, z_b and z_t, but otherwise are constructed using the fractional entrainment and detrainment rates as given by the standard parameterisation. This parameterisation leads to erroneous mass flux profiles as can be clearly observed when comparing the parameterized mass flux profiles in Fig. 2.8b with the LES derived mass flux profiles such as displayed in Fig. 2.8a. In fact these discrepancies explain, consistent with Fig. 2.6, that for relatively shallow clouds the mass flux does not decrease rapidly enough whereas it decreases too rapidly for the deepest clouds. The latter also finally explains the too inactive convection with the SCM in the second half of the cloudy period of ARM, as discussed for Figs. 2.1 and 2.2.

2.5. A NEW DETRAINMENT PARAMETERISATION

2.5.1. SET UP OF THE NEW PARAMETERISATION

In the previous section it has been shown that the mass flux profile is dependent on cloud layer depth as well as on the enviromental conditions as measured by the χ_c parameter. Since the fractional entrainment does not vary nearly so much as the fractional detrainment rates from case to case, we keep the fractional entrainment formulation as in the standard parameterisation, i.e. $\varepsilon = c_e z^{-1}$ with $c_e = 1.0$, in reasonable agreement with LES results (also for other cases such as BOMEX and RICO). So in order to have a more flexible mass flux formulation, we have to construct a simple parameterisation for the fractional detrainment rate δ.

The simplest parameterisation for δ to guarantee a zero mass flux at the cloud top is (Siebesma, 1998)

$$\delta = \varepsilon(z) + \frac{1}{z_t - z} \tag{2.4}$$

which results in a linear decrease of the mass flux as can be checked easily by substituting (2.4) in (2.1). This parameterisation already takes into account the cloud layer height dependence but is still insensitive to the dependencies of the mass flux on the environment such as displayed in Fig. 2.8a. In order to include this effect we start with another approach. Let us assume for the time being that δ is constant with height (roughly following the LES results) and rewrite the mass continuity equation (2.1) as

$$\frac{1}{M} dM = (c_e \frac{1}{z} - \delta) dz \tag{2.5}$$

where we have substituted $\varepsilon = c_e z^{-1}$. This differential equation can be solved easily, using $M(z_b) = M_b$ as a lower boundary condition leading to

$$M = M_b \left(\frac{z}{z_b} \right)^{c_e} e^{-\delta(z - z_b)}. \tag{2.6}$$

Alternatively, we can non-dimensionalize this form through $\hat{z}$ and $\hat{m}$ (defined in section 2.4) so that

$$\hat{m} = \left(\hat{z} \left(\frac{h}{z_b} \right) + 1 \right)^{c_e} e^{-\delta h \hat{z}} \tag{2.7}$$

or, if we invert it, we find for fractional detrainment rate

$$\delta = \frac{c_e \ln\left(1 + \hat{z} \frac{h}{z_b}\right) - \ln \hat{m}}{h \hat{z}} \tag{2.8}$$

If we could come up with a parameterisation of $\hat{m}$ at one specific height we could plug this $\hat{m}$ into (2.8) to obtain the optimal value of a constant fractional

detrainment rate δ. Preferably we should take $\hat{m}$ at a height at which the differences between the various mass fluxes, such as displayed in Fig. 2.8a, are most pronounced. Figure 2.8a suggests taking $\hat{m}$ halfway the cloud layer, i.e. at $\hat{z} = 0.5$, so we will do so accordingly. From hereon the non-dimensionalized height and mass flux halfway the cloud layer are denoted as $\hat{z}_*$ and $\hat{m}_*$ respectively.

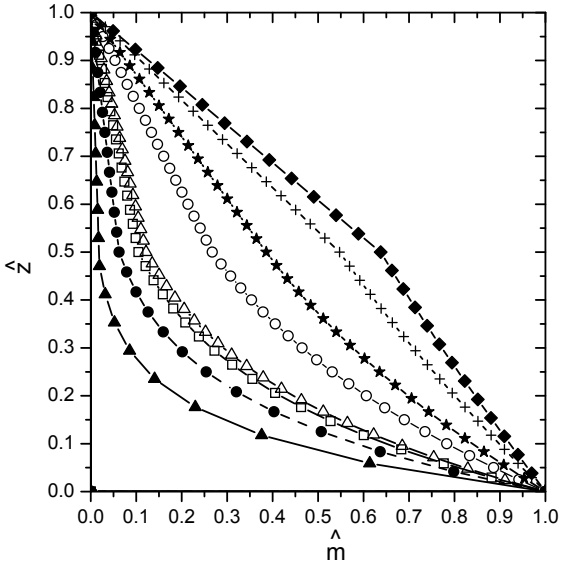

Figure 2.9: Non-dimensionalized mass flux profiles for different simulations hours (ARM case) as Fig. 2.8a but with $\varepsilon = z^{-1}$ m^{-1} and δ according to (2.8) with M_b, z_b, z_t and $\hat{m}_*$ (the non-dimensionalized mass flux halfway the cloud layer) as diagnosed from LES. Above $\hat{z}_*$ a linear decreasing mass flux profile is prescribed (see text).

To show the potential of this approach, Fig. 2.9 displays the parameterized non-dimensionalized mass flux profiles, using for $\hat{z} < 0.5$ a constant fractional detrainment rate obtained by (2.8) with the $\hat{m}_*$, M_b, z_b and z_t, all diagnosed by the LES model. Comparing Fig. 2.9 with Fig. 2.8a, shows that an optimal choice of a constant δ in the lower half of the cloud layer results in a realistic transition from a convex mass flux profile for small values of $\hat{m}_*$, to a concave profile for large $\hat{m}_*$. To ensure that the mass flux smoothly goes to zero between $\hat{z} = 0.5$ and $\hat{z} = 1$ we simply impose a linear decrease of the mass flux profile to zero at the cloud top by applying (2.4) in the upper half of the cloud layer. At first sight this last step might seem a crude approximation. However Fig. 2.8a reveals that for small $\hat{m}_*$ there is not much mass flux to spread out anymore and for large $\hat{m}_*$ the linear decrease seems to be a reasonable approach (in agreement with e.g. H. Jonker et al., 2006, Derbyshire et al., 2004, and Zhao and Austin, 2005a).

Although we believe that the first order improvements are well included with

the proposed set-up of the parameterisation, there is certainly room for improvement of the parameterisation in the upper half of the cloud layer. For example, it is plausible that the decrease of the non-dimensionalized mass flux in the upper half of the cloud layer depends on χ_c. Another disadvantage of the current set-up might be the incapability to produce a constant mass flux profile with height in the upper half of the cloud layer. However in practice we expect this to be a rare, if not non-existent, circumstance for shallow convection.

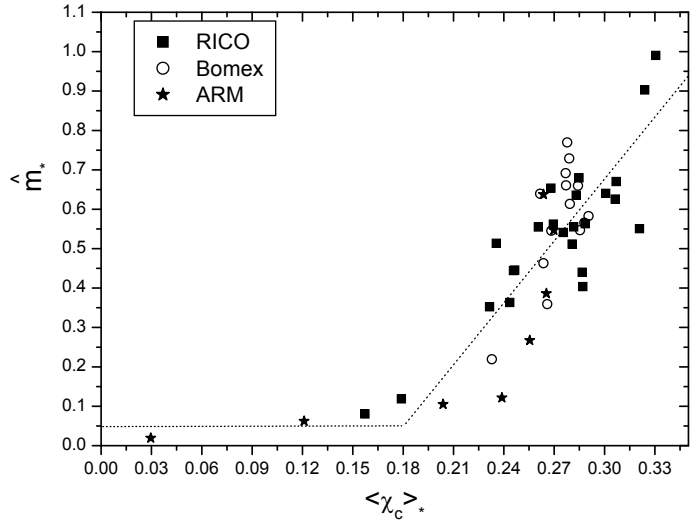

Figure 2.10: LES results showing the relation between $\hat{m}_*$ (the non-dimensionalized mass flux halfway the cloud layer) and $<\chi_c>_*$ (χ_c averaged over the lower half of the cloud layer) for RICO, BOMEX and ARM. The dotted line represents a linear approximation of this relation (eq. (2.9))

The main question that remains is how to determine $\hat{m}_*$ and therewith close our parameterisation. The most simple approach is to take a well chosen constant $\hat{m}_*$, e.g. 0.3 (see Fig. 2.8a). Now the non-dimensionalized mass flux profile is fixed and insensitive to dependencies of the mass flux on the environment. However this already results in a large improvement in comparison with the standard parameterisation with a fixed δ (see Fig. 2.8b), whereas the parameterisation is equally simple. This improvement is caused by the cloud layer height dependence included in eq. 2.8. Nevertheless the LES results of the former section clearly suggest to parameterize $\hat{m}_*$ as a function of χ_c. If we consider clouds as updrafts, it is plausible that the mass flux decrease with height is influenced by χ_c on the way. Since we want to parameterize the fraction of the mass flux that is left halfway the cloud layer, $\hat{m}_*$, we therefore average χ_c from cloud base up to $\hat{z}_*$ and we will denote this average for the remainder of this chapter as $<\chi_c>_*$. Instead of showing the non-dimensionalized mass flux profiles together with $<\chi_c>_*$ for

all cases, the results are compendiously presented in Figure 2.10 showing the dependence of $\hat{m}_*$ on $< \chi_c >_*$ according to the LES results for BOMEX, ARM and RICO. Figure 2.10 reveals a clear correlation between $< \chi_c >_*$ and $\hat{m}_*$ with, as could be expected, a rapid decrease of the mass flux profile (i.e. small $\hat{m}_*$) for low values of $< \chi_c >_*$ and vice versa. In practice, large values of $< \chi_c >_*$ can be associated with large clouds (large radius) with high updraft velocities that have large buoyancy excesses and/or clouds rising in a friendly, humid environment. For small $< \chi_c >_*$ values the opposite can be expected. This physical picture is consistent with results from literature, see e.g. H. Jonker et al., 2006 and Zhao and Austin, 2005a, that reveal a clear increase of $\hat{m}_*$ with increasing cloud sizes.

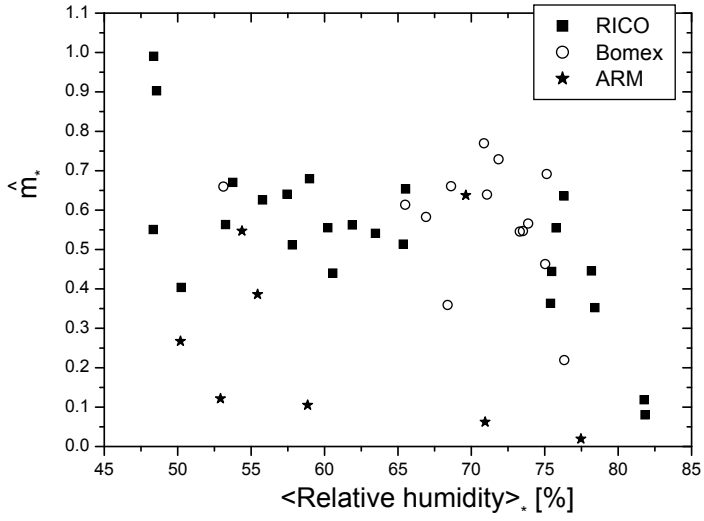

Figure 2.11: As 2.10 but now with the relative humidity averaged over the lower half of the cloud layer instead of $< \chi_c >_*$.

It is also interesting to examine the potential of the relative humidity of the environment as an alternative indicator to describe the mass flux decrease with height. Fig. 2.11 demonstrates the absence of any significant correlation between relative humidity and $\hat{m}_*$. This can be understood as follows. Normally relative humidity decreases with height and consequently low shallow clouds can go together with high values of averaged relative humidity. However, from our LES results we know that these type of clouds, as present shortly after the beginning of convection in the ARM case, can show a rapid decrease of the mass flux, probably due to their small buoyancy excess. So here we see that high values of mean relative humidity can go together with a rapid decrease of the mass flux. This again demonstrates the necessity to include the effect of not only en-

vironmental humidity but also buoyancy excess (as in $< \chi_c >_*$) to adequately parameterize variations in the non-dimensionalized mass flux profile.

The last step to be made is to find a parameterisation for $\hat{m}_*$ depending on $< \chi_c >_*$ in order to close our scheme. The question is to what extent the LES relation between $< \chi_c >_*$ and $\hat{m}_*$ presented in Fig. 2.10 is also applicable in a SCM. Although the χ_c profiles in our SCM, including the relative changes from hour to hour and case to case, resemble the LES profiles and changes, there are also differences. These differences are related to the explicit (cloud core) updraft definition in the LES model and the implicit updraft definition in a SCM. For instance, in the LES model the updrafts start at the level of free convection (lfc) determined by the level where the updrafts become just neutrally buoyant and thus have zero χ_c values. From this height the mass flux increases to a maximum at a level that is defined as the cloud base height in this chapter. In the SCM on the other hand, the mass flux starts, and is at its maximum, at the lifting condensation level (lcl). At this height the excess of the updraft properties, which influences the value of χ_c, is determined by the convection triggering parameterisation. Consequently, χ_c already has a positive value at cloud base (lcl in the SCM). This difference in updraft excess at cloud base between SCM and LES model also affects higher levels. In practice, this leads to somewhat higher $< \chi_c >_*$ values in the SCM compared to the LES model, mainly depending on the chosen convection triggering parameterisation. Two approaches can be followed to deal with the above mentioned discrepancy. Firstly, simply apply the LES relation between $< \chi_c >_*$ and $\hat{m}_*$ (Fig. 2.10) unaltered in the SCM. Secondly, and this approach will probably be favorite in an operational enviroment, adapt the relation between $< \chi_c >_*$ and $\hat{m}_*$ to the SCM, e.g. with a tuning based on one or more suitable 1D shallow convection cases. For soundness we here follow the first approach. Consequently, as the $< \chi_c >_*$ values are higher in the SCM, this will lead to a somewhat over-active convection scheme. Nevertheless, as we will see, the results are still good with large improvements in comparison with the standard parameterisation.

In order to make the cloud base definitions in the LES and the SCM more comparable we start the averaging of χ_c in the SCM one model level above the lcl. The LES relation between $< \chi_c >_*$ and $\hat{m}_*$ is approximated by a linear fit for $< \chi_c >_*$ values larger than 0.2 and a small minimum value of 0.05 resulting in the following expression for the SCM (see also Fig. 2.10):

$$\hat{m}_* = max(0.05, 5.24 < \chi_c >_* - 0.89) \tag{2.9}$$

This result combined with (2.8) finally complete our proposed detrainment parameterisation.

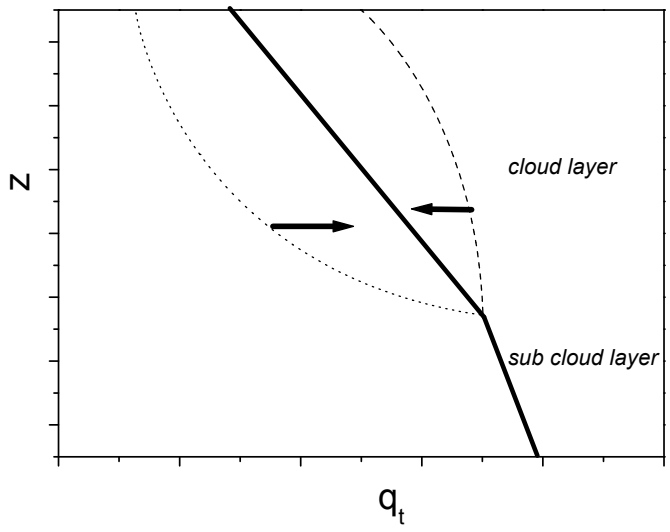

Figure 2.12: Schematic showing the stabilizing effect (negative feedback) of the new detrainment parameterisation on perturbations in the humidity. The solid line represents the initial humidity profile while the dotted and dashed lines show the perturbed drier and more moist profiles respectively. The arrows indicate the shifting of the perturbed profiles due to the changed, χ_c dependent detrainment rates. Similar arguments apply for temperature instead of humidity. See the text for a more detailed explanation.

An interesting and positive characteristic of the new detrainment parameterisation is the stabilizing effect through negative feedbacks. This is illustrated in Fig. 2.12. If an initial profile of temperature or humidity is changed, the parameterisation tries to compensate the disturbance. If e.g. a humidity profile becomes drier, χ_c will decrease leading to a larger fractional detrainment and consequently an increased moistening of the environment (see Fig. 2.12). Similar arguments apply for temperature. As a result the parameterisation works to an equilibrium state.

Finally, Fig. 2.13 shows how the new parameterisation is embedded in the convection scheme. Note that the convection scheme is purely sequential, without any multiple iterations.

2.5.2. SCM RESULTS WITH THE NEW DETRAINMENT PARAMETERISATION

Applying the new detrainment parameterisation (2.8) in combination with (2.9) for $\hat{z} < \hat{z}_*$ and (2.4) for $\hat{z} > \hat{z}_*$ in our SCM, we run the BOMEX, ARM and RICO cases.

As mentioned in section 2.3, the standard parameterisation as derived from LES for BOMEX, lead to almost perfect steady state humidity and temperature

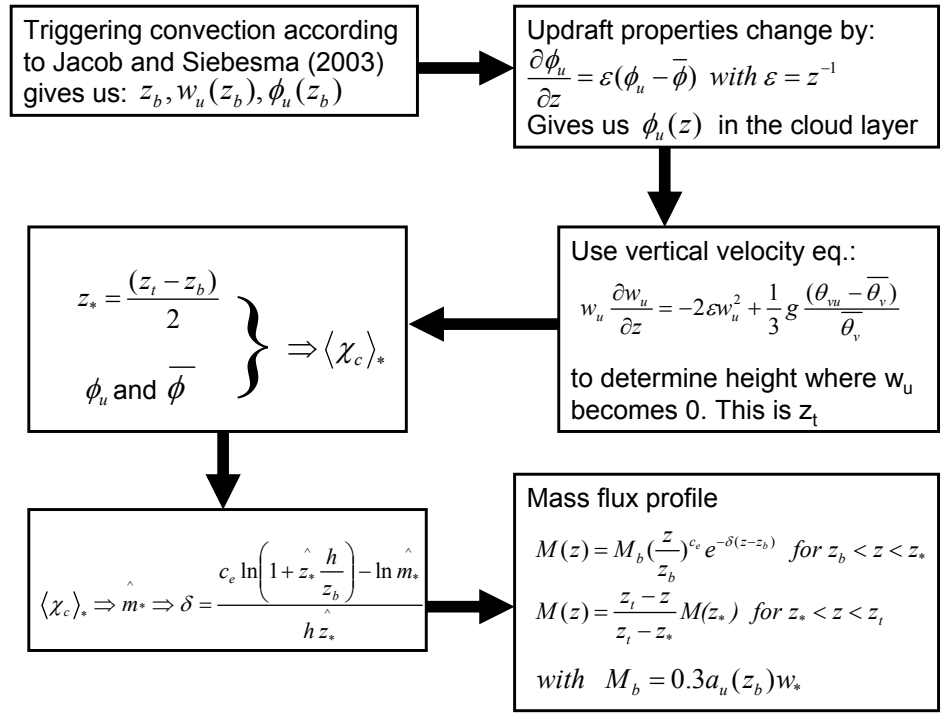

Figure 2.13: Flow chart showing how the new parameterisation is embedded in the convection scheme. $\phi = \{\theta_\ell, q_t\}$

profiles for BOMEX. With the new detrainment parameterisation the humidity and temperature profiles are highly comparable for this case (not shown).

As explained before, the ARM case poses stronger demands on the detrainment parameterisation because the cloud height as well as the environmental conditions vary substantially during this case. Figures 2.14 and 2.15 with the new detrainment formulation reveal the clear improvement of the time serie and total water specific humidity profile respectively in comparison with the corresponding Figures 2.1 and 2.2 with the standard parameterisation. Stronger convection during the second half of the cloudy period results in less humidity near cloud base and more humidity in the upper part of the cloud layer, in accordance with the LES. However, there is no clear improvement with the new parameterisation in the sub cloud layer. This problem is probably not related to the lateral mixing in the cloud layer.

One remark needs to be made in relation to Fig. 2.15. Since in the ARM case both the LES and the SCM are subjected to the same prescribed moisture surface fluxes, the vertical integrated moisture profile should be the same for both

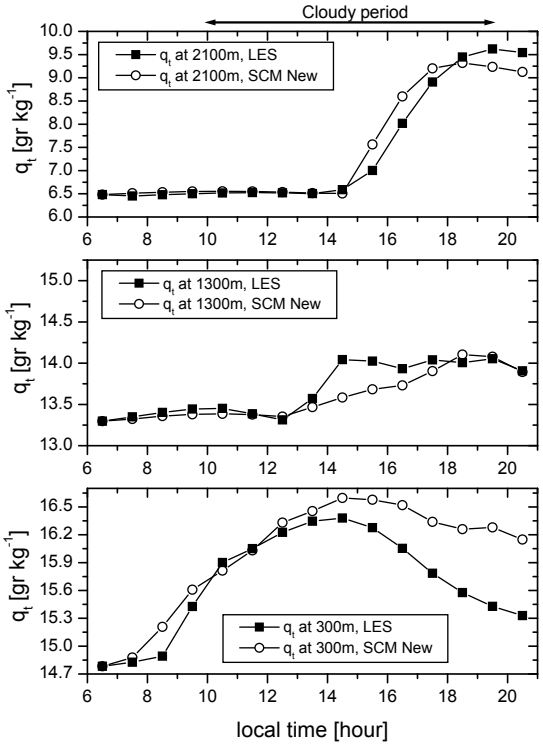

Figure 2.14: Time series of total water specific humidity during the ARM case at three levels (300, 1300, and 2100 m) for LES and for the SCM using the new detrainment parameterisation.

models. That this is not the case can be observed in Fig. 2.15 and is due to the fact that the LES models are usually formulated within the Boussinesq approximation which assumes a constant horizontally averaged density whereas in the SCM the decrease of density with height is taken into account. As is shown in Appendix B this causes small discrepancies between the moisture budgets of both models, that deteriorate with time. However it suffices here to notice that these discrepancies do not affect any of the conclusions drawn in this study.

Finally, Fig. 2.16 presents the results of the RICO case with LES, the standard and the new detrainment parameterisation, and an imposed linear decreasing mass flux profile (i.e. (2.4) throughout the cloud layer). We only show the profile after 24 hrs of simulation because other simulation hours just give "in-between results". The new parameterisation gives a very good match with the LES humidity profile although, as expected, the convective activity is somewhat overestimated because the, from LES results derived, relation (2.9) is not optimized for our SCM leading to a slight underestimation of the humidity at cloud base. There

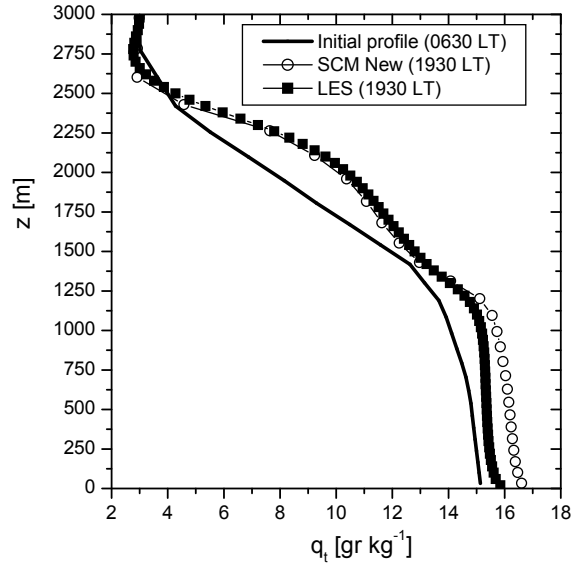

Figure 2.15: Total water specific humidity profiles for different simulation hours during the ARM case for the LES model and the SCM with the new detrainment parameterisation.

is also a large improvement on the results with the standard parameterisation which can be explained by the relatively deep and moist cloud layer in the RICO case, leading to a slow decrease of the mass flux profile (see Fig. 2.10) and significantly smaller fractional detrainment values as for the BOMEX case. Finally, the results with the imposed linear decreasing mass flux profile show that the included cloud height dependence results in increased convective activity and consequently better results in comparison with the standard parameterisation. However, the convective activity is still underestimated as this parameterisation does not reckon with the favourable conditions for updrafts during the RICO case (high $< \chi_c >_*$ values). This illustrates the additional value of the $< \chi_c >_*$ dependence in the new detrainment parameterisation.

2.6. CONCLUSIONS AND DISCUSSION

A correct simulation of the mass flux profile is very important because it determines the vertical transport of the thermodynamic variables. Apart from the mass flux closure at cloud base, the mass flux profile is determined by both the fractional entrainment and detrainment coefficients. LES results show that, for different cases and conditions, the fractional entrainment coefficient shows little variation. On the other hand LES results also reveal much more variation in the detrainment coefficient and its value seems to depend mainly on two factors.

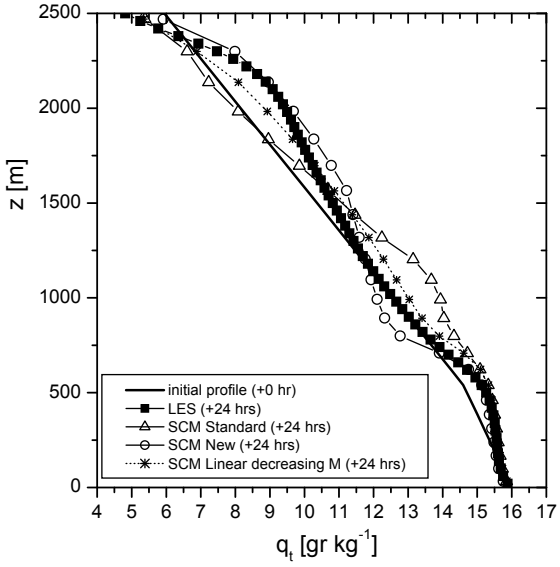

Figure 2.16: Total water specific humidity profiles after 24 hrs of simulation during the RICO case for the LES model and the SCM using fixed ε and δ, the new detrainment parameterisation, and an imposed linear decreasing mass flux profile (i.e. (2.4) throughout the cloud layer).

Firstly, and probably the most important, is the dependence on the cloud layer depth. Under normal conditions a shallow convection scheme in a NWP or climate model represents an ensemble of clouds, leading to a decreasing mass flux profile with height and zero mass flux at the top of the cloud layer (SC95). With an approximately fixed function for the entrainment coefficient it can be simply understood that this calls for smaller detrainment rates for deeper cloud layers, as also confirmed by LES. Nevertheless, current mass flux schemes ignore this cloud height dependence. We have shown that this can lead to large discrepancies with LES mass flux profiles. In our approach the mass flux profile is considered in a non-dimensionalized way, therewith dealing with the effect of the cloud layer height. Already in its simplest form, i.e. a fixed function for ε and the new δ formulation with only one constant parameter, our approach deals with the cloud layer depth dependence, leading to a substantial improvement in comparison with fixed ε and δ.

The second, important factor changing δ is the environmental condition. Many studies (e.g. Kain and Fritsch, 1990 and Derbyshire et al., 2004) showed the influence of the relative humidity of the environmental air surrounding the updrafts. If the surrounding air is more moist, less evaporative cooling will occur if this air is mixed with cloudy air and this leads to less detrainment. However, besides the humidity of the enviroment it is also the buoyancy excess of the updraft

air that determines if the mixture becomes negatively buoyant and consequently detrains. This combined effect is nicely captured by the so called critical fraction of the environmental air, χ_c (Kain & Fritsch, 1990). Indeed LES show that the non-dimensionalized mass flux profile, which is insensitive for cloud layer height, correlates well with the χ_c profile. With the dependence of δ on χ_c we implicitly also include the effect that clouds with a larger radius or a higher updraft velocity will detrain less because larger clouds and clouds with a higher updraft velocity will normally also have a larger buoyancy excess and consequently higher χ_c values.

Since Kain and Fritsch, 1990 introduced their convection scheme based on the buoyancy sorting concept, different modifications are proposed in the literature and has been applied in operational NWP models (see e.g. Bretherton et al., 2004 and Kain, 2004). Yet some important deficiencies with these type of schemes remain. In a Kain and Fritsch, 1990 like buoyancy sorting scheme mixtures are made of in-cloud and environmental air. Subsequently, all negatively buoyant mixtures detrain and positively buoyant mixtures entrain. The amount of entrained and detrained air is strongly influenced by the fraction of the mass flux that is used for mixing (the rate of environmental inflow, REI) and the probability density function (PDF) which describes the probability of different mixtures. Both influences are extreme simplifications of the mixing process in nature, which is, as we know from e.g. Zhao and Austin, 2005a, 2005b, quite complex. For example the entrained air does not have purely environmental but rather in-between properties. Apart from the above-mentioned considerations we should also realize that for common horizontal model resolutions a convection scheme describes an ensemble of clouds instead of one single updraft. All in all, it seems unlikely that parameters and functions like the PDF of the mixtures can be related to observations or LES results. Instead they rather can be seen as ways to tune the convection scheme. In our approach we take a step back in complexity (herewith strongly reducing the tunable parameters) and relate the non-dimensionalized mass flux profile directly to just one parameter, a bulk χ_c which, for several substantiated reasons, shows a clear correlation with the decrease of the non-dimensionalized mass flux profile. Note that by fixing the function of the entrainment coefficient we also circumvent the problem in current buoyancy sorting based lateral mixing schemes that a drier environment leads to less entrainment and consequently higher cloud tops, this in disagreement with LES.

A critical reader might wonder to what extent the cloud base mass flux parameterisation (2.2) influences the results in this chapter. To answer this we reproduced all SCM results but now applying the Grant cloud base mass flux closure (see Section 2.2.1). The result is that all conclusions in this chapter remain

in full force.

With the new detrainment parameterisation included in a SCM good results are obtained for all three investigated shallow convection cases. The complex ARM case, with increasing cloud height and changing environmental conditions, clearly reveals the shortcomings of fixed ε an δ and the substantial improvement with the new parameterisation. For the steady state BOMEX case, for which the fixed ε and δ are more or less optimized, the results with the new parameterisation are equally good. Finally, the RICO case with a relatively deep and moist cloud layer, demands small fractional detrainment rates. Hence the new parameterisation, which results in a very good match with LES, substantially improves the vertical mixing due to convection in comparison with the standard mixing model.

By coupling the non-dimensionalized mass flux profile directly to a bulk χ_c, the here proposed detrainment parameterisation can be seen as an alternative for existing more complex buoyancy sorting based convection schemes, without showing some of the disadvantages. Results from LES and a SCM show the clear potential of our approach for a wide range of shallow convection cases. Moreover, the here proposed parameterisation is computationally cheap and can be easily included in an existing mass flux scheme.

2.6.1. ACKNOWLEDGEMENTS

The authors would like to thank Geert Lenderink, Stephan de Roode, Kees Kok and Jan Fokke Meirink for stimulating and useful discussions. Geert Lenderink, Stephan de Roode, one anonymous referee and Jack Kain are acknowledged for critical reading of and useful suggestions for an earlier version of this chapter. Margreet van Zanten is thanked for providing the LES results for RICO.

APPENDIX A

An analytical expression for χ_c.

The calculation of the critical fraction χ_c can, of course, be done numerically. Here we present as an alternative the derivation of an analytical expression of χ_c in terms of solely environmental and updraft fields. Such an analytical result has the advantage that it makes the convection parameterisation computationally more efficient. Another advantage of an analytical expression is that it provides more insight in the way χ_c, and hence the detrainment reacts on the environmental and updraft conditions.

We start with the virtual potential temperature of a mixture, consisting of a fraction χ of environmental air and a fraction of $1-\chi$ of updraft air

$$\theta_v(\chi) = \theta(\chi)(1 + \lambda q_v(\chi) - q_\ell(\chi)) \tag{2.10}$$

where q_v is the water vapour specific humidity and $\lambda = R_v/R_d - 1 \approx 0.61$ with R_d and R_v being the specific gas constants for dry and moist air respectively. We further will use the total water specific humidity $q_t \equiv q_v + q_\ell$ and the liquid water potential temperature θ_ℓ, which reads in its linearized form

$$\theta_\ell \approx \theta - \frac{L q_\ell}{c_p \pi} \tag{2.11}$$

where L is the specific latent heat vaporization, c_p is the specific heat capacity of dry air at constant pressure, and $\pi \equiv T/\theta$ is the exner function.

The advantage of the moist conserved variables θ_ℓ and q_t is that they mix linear, i.e.

$$\begin{aligned} \theta_\ell(\chi) &= \theta_{\ell u} - \chi(\theta_{\ell u} - \theta_{\ell e}) \equiv \theta_{\ell u} - \chi \Delta\theta_\ell \\ q_t(\chi) &= q_{tu} - \chi(q_{tu} - q_{te}) \equiv q_{tu} - \chi \Delta q_t \end{aligned} \tag{2.12}$$

By eliminating q_v and θ in (2.10) in favour of the moist conserved variables and ignoring higher order moisture terms we readily find

$$\theta_v(\chi) = \theta_\ell(\chi)(1 + \lambda q_t(\chi) - (1+\lambda) q_\ell(\chi)) + \frac{L}{c_p \pi} q_\ell(\chi) \tag{2.13}$$

Since q_ℓ is not a moist conserved variable it does not obey a simple linear mixing line like (2.12). Therefore, the last preperation that we need to make is to find an expression for $q_\ell(\chi)$ in terms of updraft and environment variables. As long as the mixture contains liquid water we may write

$$q_\ell(\chi) = q_t(\chi) - q_s(p, T(\chi)) \tag{2.14}$$

where q_s is the saturation specific humidity which depends on the temperature of the mixture and the pressure p. Because we want an expression for χ_c it is enough to have an expression for $\theta_v(\chi)$ from $\chi = 0$ to $\chi = \chi_c$ which ensures that $q_\ell > 0$ and therewith the validity of (2.14). We proceed by making a Taylor expansion of $q_s(T(\chi))$ around the $T(\chi = 0) \equiv T_u$

$$q_s(T(\chi)) \approx q_s(T_u) + (T(\chi) - T_u) \frac{\partial q_s}{\partial T} |_{T_u} \tag{2.15}$$

By substituting (2.15) back in (2.14) and rewriting it in terms of moist conservative variables using (2.11) we obtain

$$q_\ell(\chi) = q_{\ell u} - \chi \frac{1}{1+\gamma} \left[\Delta q_t - \gamma \Delta\theta_\ell \right] \tag{2.16}$$

with $\gamma = L/c_p \partial q_s/\partial T\,|_{T_u}$.

We can now harvest by substituting (2.16) and (2.12) into (2.13), and rewriting it as a linear combination of updraft excesses $\Delta\theta_\ell$ and Δq_t. By ignoring higher order terms of χ and terms of the $O(10^{-2})$ in the prefactor of $\Delta\theta_\ell$ we find after some algebra

$$\theta_v(\chi) = \theta_{vu} - \chi\left[\beta\Delta\theta_\ell + (\beta-\alpha)\frac{L}{c_p\pi}\Delta q_t\right] \tag{2.17}$$

with

$$\begin{aligned}\beta &\equiv \frac{1}{1+\gamma}\left[1+(1+\lambda)\gamma\alpha\right]\\ \alpha &\equiv \frac{c_p}{L}\pi\theta_{\ell u}.\end{aligned}$$

Typical values for the cases considered in this chapter are: $\gamma \simeq 2.5$, $\alpha \simeq 0.12$ and $\beta \simeq 0.4$. Realising that χ_c is defined as the concentration of environmental air for which the buoyancy with respect to the environment is just zero, we finally find

$$\chi_c = \frac{\Delta\theta_v}{\left[\beta\Delta\theta_\ell + (\beta-\alpha)L/(c_p\pi)\Delta q_t\right]} \tag{2.18}$$

where obviously $\Delta\theta_v \equiv (\theta_{vu} - \theta_{ve})$ denotes the updraft buoyancy excess. We have here deliberately adopted the same notation as in (Randall, 1980) and (Bretherton et al., 2004) except that we use α and λ instead of ε and δ in order to avoid confusion with the notation in this chapter of the fractional entrainment and detrainment rates. Note that in contrast with (Bretherton et al., 2004) we find a slightly different form for the prefactor of the Δq_t term and, more importantly, a different sign of this term. Comparison of (2.18) with accurate numerical estimates of χ_c for typical values of the presented cases in this chapter show that (2.17) gives errors only of the order of 1 %.

To gain some more insight in the behaviour of χ_c we can simplify the result (2.18) even more by assuming that $T_u \simeq \overline{T}$. This allows us to write the excess terms as

$$\begin{aligned}\Delta\theta_\ell &\simeq -\frac{L}{c_p\pi}q_{\ell u}\\ \Delta q_t &\simeq q_{te} - q_{se} - q_{\ell u}.\end{aligned} \tag{2.19}$$

Using these approximations of the excesses and the definition of the relative humidity $RH \equiv q_{te}/q_{se}$ allows us to rewrite (2.18) as

$$\chi_c = (c_p\pi/L)\frac{\Delta\theta_v}{q_{se}(\beta-\alpha)(1-RH) - \alpha q_{\ell u}} \tag{2.20}$$

and shows how χ_c increases for larger buoyancy excess values and higher relative humidities.

APPENDIX B

Differences in tendencies between the LES model and the SCM

The DALES model used here is formulated, as most LES models, within the Boussinesq approximation. This implies that the horizontally averaged density does not change with height. The SCM used in this study, as all GCM's, RCM's and their SCM versions, does take the height dependance of the density into account. This difference has implications for the moisture tendencies and is hence a possible obstacle for precise comparisons between LES and SCM results. To quantify the difference consider a tendency equation of moisture of a SCM solemnly due to the turbulent flux divergence

$$\begin{aligned}\left(\frac{\partial \overline{q}}{\partial t}\right)_{\text{SCM}} &= -\frac{1}{\overline{\rho}}\frac{\partial \overline{\rho}\,\overline{w'q'}}{\partial z} \\ &= -\frac{\partial \overline{w'q'}}{\partial z} - \overline{w'q'}\frac{1}{\overline{\rho}}\frac{\partial \overline{\rho}}{\partial z} \\ &= \left(\frac{\partial \overline{q}}{\partial t}\right)_{\text{LES}} - \overline{w'q'}\frac{1}{\overline{\rho}}\frac{\partial \overline{\rho}}{\partial z}. \end{aligned} \tag{2.21}$$

The last term on the right hand side, the density term, quantifies the discrepancy in the moisture tendency if the dependency of the density on height is not taken into account. The term $\frac{1}{\overline{\rho}}\frac{\partial \overline{\rho}}{\partial z}$ is of the order $10^{-4}\,\text{m}^{-1}$ in the lower troposphere. If we furthermore assume for the sake of simplicity that the moisture flux is linear decreasing to zero between the surface and a height z_t so that

$$\left(\frac{\partial \overline{q}}{\partial t}\right)_{\text{LES}} \simeq \frac{\left(\overline{w'q'}\right)_{\text{srf}}}{z_\text{t}} \tag{2.22}$$

we can quantify the density term as

$$\overline{w'q'}\frac{1}{\overline{\rho}}\frac{\partial \overline{\rho}}{\partial z} \simeq 10^{-4}\,(z_\text{t} - z)\left(\frac{\partial \overline{q}}{\partial t}\right)_{\text{LES}} \tag{2.23}$$

which is as large as 10% at a height of only 1000 m with a cloudy boundary depth of $z_\text{t} \simeq 2000\,\text{m}$. If we realize that, e.g. a moisture surface flux of $6 \times 10^{-5}\,\text{ms}^{-1}$ moistens a boundary layer of 2000 m thick by 2.5 g/kg during a day, this implies that the density term is of the order of 0.25 g/kg over the entire depth, a number comparable with the discrepancy that can be observed in Fig. 2.15. So we can conclude that if we compare LES results, that are based on the Boussinesq approximation, with SCM output, differences may be expected for the moisture budget, which become significantly large after simulation periods beyond approximately 10 hours.

3

ANALYTICAL EXPRESSIONS FOR ENTRAINMENT AND DETRAINMENT IN CUMULUS CONVECTION

ABSTRACT

Analytical expressions for entrainment and detrainment are derived based on general total water specific humidity and mass budget equations. From these expressions, containing a small-scale turbulent and a larger scale organized term, a physical picture emerges for a shallow cumulus cloud ensemble in which the individual clouds have a massive entraiment at the bottom, lateral turbulent mixing with constant mass flux between bottom and top, and massive detrainment at the top. Combining these results with the general budget equation for vertical velocity, new formulas for entrainment and detrainment rates can be expressed in terms of buoyancy, vertical velocity and cloud fraction. For a variety of shallow convection cases, results from Large Eddy Simulations show a good correspondence of these new formulas with more traditional methods to diagnose entrainment and detrainment rates. Moreover, the formulas give insight into the behaviour and the physical nature of the mixing coefficients. They explain the observed large variability of the detrainment. The formulas can not be directly applied as a parameterisation. However, it is demonstrated how they can be used to evaluate existing parameterisation approaches and as a sound physical base for future parameterisation developments.

Published as: de Rooy, Wim C., A. Pier Siebesma, 2010: Analytical expressions for entrainment and detrainment in cumulus convection, Quart. J. Roy. Met. Soc., Vol. 136, 1216-1227, doi:10.1002/qj.640

3.1. INTRODUCTION

Lateral mixing between convective clouds and their environment represented by entrainment and detrainment are key processes in atmospheric moist convection and the uncertainty of its strength is still a main source in climate model uncertainty ((Murphy et al., 2004), (Rougier et al., 2009)). The strong positive impact of new entrainment and detrainment representation on the predictive skill of Numerical Weather Prediction (NWP) models (Bechtold et al., 2008) shows both the importance and the relative infancy of our knowledge of these processes.

The concept and relevance of entrainment of environmental quiescent air into convective cumulus updrafts was first pointed out by Stommel, 1947 and were followed by numerous observational studies of cumulus clouds with aircrafts (e.g. (Warner, 1955)). In these studies entrainment strength could be determined through the ratio between the measured liquid water in clouds and its adiabatic value. The first quantitative descriptions of entrainment originated from laboratory experiments of thermal plumes (Morton et al., 1956),(Turner, 1963) describing an increasing mass flux M with height

$$M^{-1}\frac{\partial M}{\partial z} = \varepsilon \simeq \frac{0.2}{R} \tag{3.1}$$

where R is the radius of the rising plume and ε is the fractional entrainment coefficient. Many of the early cloud models have adopted this entraining plume model. A distinction between entrainment due to turbulent mixing at the cloud edge and organized inflow of environmental air induced by the increase of the vertical velocity due to buoyancy was first pointed out by Houghton and Cramer, 1951 and its relevance has been recently re-emphasized by Holloway and Neelin, 2009

$$M^{-1}\frac{\partial M}{\partial z} = \varepsilon_{\text{dyn}} + \varepsilon_{\text{turb}} \tag{3.2}$$

Since the dynamical (organized) and turbulent fractional entrainment rates are by definition positive, they cause the mass flux to increase with height. This is in agreement with dry plumes where entrained air from the environment becomes part of the plume after the mixing process. However, cloudy updrafts can actually also exhibit a decreasing mass flux with height, for instance due to mixing of dry environmental air. The evaporative cooling can actually reduce the updraft area and/or the updraft velocity so that the mass flux can also decrease with height. This so called detrainment process, is in many respects the mirror image of entrainment and can also be subdivided in a dynamical and a turbulent part

$$M^{-1}\frac{\partial M}{\partial z} = \varepsilon_{\text{dyn}} + \varepsilon_{\text{turb}} - \delta_{\text{dyn}} - \delta_{\text{turb}}. \tag{3.3}$$

Mass flux parameterisations of cumulus convection in NWP and climate models have to take into account the effect of a whole ensemble of clouds rather than a single cloud element. With the exception of the seminal work of Arakawa and Schubert, 1974, most mass flux parameterisations employ a so called bulk approach in which all active cloud elements are represented in one steady state updraft representing the whole cloud ensemble.

Numerous entrainment and detrainment parameterisations have been proposed for such mass flux bulk schemes. Popular formulations proposed by Tiedtke, 1989, Bechtold et al., 2008, Nordeng, 1994 and Gregory and Rowntree, 1990 can be ordered in terms of the right hand side of (3.3). Tiedtke, 1989 and Nordeng, 1994 assume that $\varepsilon_{\text{turb}}$ and δ_{turb} are equal and given by (3.1), while in (Bechtold et al., 2008) $\varepsilon_{\text{turb}}$ depends on the saturation specific humidity. Gregory and Rowntree, 1990 also propose (3.1) for $\varepsilon_{\text{turb}}$ but utilize a systematic smaller δ_{turb}. Dynamical entrainment ε_{dyn} is based on moisture convergence in (Tiedtke, 1989), on momentum convergence in (Nordeng, 1994), on relative humidity in (Bechtold et al., 2008) and absent in (Gregory & Rowntree, 1990). Organized detrainment is in general formulated as a massive lateral outflow of mass around the neutral buoyancy level although the precise details differ in the cited parameterisations. In the above cited parameterisations typically a fixed value of $R \simeq 500$ m for shallow clouds and $R \simeq 2000$ m for deep convection is used.

Another class of entrainment/detrainment parameterisations, that does not distinguish between dynamical and turbulent mixing is based on the "buoyancy sorting" concept introduced by Raymond and Blyth, 1986. This buoyancy sorting concept is transformed into a operational parameterisation by Kain and Fritsch, 1990. In (Kain & Fritsch, 1990) an ensemble of mixtures of cloudy and environmental air is formed, where each ensemble member has a different concentration of environmental air. If resulting mixtures are positively buoyant, they remain in the updraft and are part of the entrainment process while negatively buoyant mixtures are rejected from the updraft and are part of the detrainment process. A number of recently proposed shallow cumulus convection schemes ((Neggers et al., 2009), (Bretherton et al., 2004), (de Rooy & Siebesma, 2008)) are based on this buoyancy sorting concept. Finally a large number of parameterisations for ε and (sometimes) δ have been published that are directly or indirectly inspired on Large Eddy Simulation (LES) results of shallow cumulus convection (e.g. (Siebesma, 1998), (Grant & Brown, 1999), (Neggers et al., 2002), (Gregory et al., 2000), (Lappen & Randall, 2001)).

The objectives of this chapter are twofold. Firstly, in order to create some ordening in all the proposed parameterisations, general expressions for the dynamical and turbulent entrainment and detrainment rates will be derived. Based on these expressions a physical picture emerges that resembles (Arakawa & Schu-

bert, 1974) and (Nordeng, 1994). Furthermore, through combining budget equations of mass, total water specific humidity and vertical velocity, we will derive analytical expressions for ε and δ that can be evaluated using LES. The latter expressions show that the entrainment formulations proposed by Gregory, 2001 and Nordeng, 1994 can be viewed as special cases. The analytical expressions for ε and δ can not be used directly as parameterisations as no closure assumptions have been imposed. Secondly, in Section 3.3 we use LES results for different shallow cumulus cases to critically evaluate these analytical expressions. With the help of the expressions different aspects of ε and δ can be explained, e.g. the large variability of the detrainment coefficient. Moreover, the expressions are used to evaluate existing parameterisation approaches and it is demonstrated how they can serve as a sound physical base for future parameterisation developments.

3.2. DERIVATION OF THE LATERAL MIXING EXPRESSIONS

3.2.1. BASICS

A convenient starting point is the conservation law for an arbitrary variable ϕ

$$\frac{\partial \phi}{\partial t} + \nabla \cdot \mathbf{v}\phi = F, \tag{3.4}$$

where $\mathbf{v}$ denotes the three dimensional velocity vector and where all possible sources and sinks of ϕ are collected in F. For the sake of simplicity we assume a Boussinesq flow, implying that the density in (3.4) is constant. We consider a domain with a horizontal area A and we are interested in the lateral mixing between a cloudy area A_c and a complementary environmental area A_e at a given height z such as sketched schematically in Fig. 3.1. At this point we do not need to be more specific on the precise definition of cloudy area but it should be noted that it may consist of many different "blobs" (or clouds) that can change in shape and size as a function of time and height.

By integrating (3.4) horizontally over the cloudy area $A_c(z,t)$ and applying Leibniz integral rule and Gauss divergence theorem, a transparent conservation equation of the cloudy area for ϕ can be deduced Siebesma, 1998

$$\frac{\partial a_c \phi_c}{\partial t} + \frac{1}{A}\oint_{\text{interface}} \hat{\mathbf{n}} \cdot (\mathbf{u} - \mathbf{u}_i)\phi dl + \frac{\partial a_c \overline{w\phi}^c}{\partial z} = a_c F_c \tag{3.5}$$

where $a_c = A_c/A$ is the fractional cloud cover, $\hat{\mathbf{n}}$ is an outward pointing unit vector perpendicular to the interface, $\mathbf{u}$ is the full 3D velocity vector at the interface, $\mathbf{u}_i$ is the velocity of the interface and w is the vertical component of the velocity field. Overbars and variables subscripted with c denote averages over the cloudy

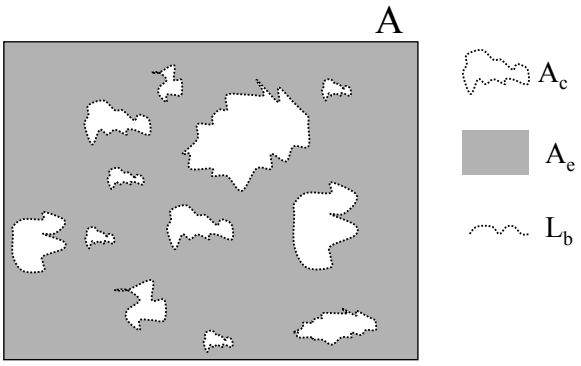

Figure 3.1: Schematic diagram showing an ensemble of clouds at a certain height. A, A_c, and A_e represent resp.; the total horizontal domain area ($A_c + A_e$), the cloudy area (white), and the environmental area (gray). The interface between the cloudy area and the environment is plotted as a dashed line and has a total length L_b.

part, i.e.

$$\overline{\phi}^{c} \equiv \phi_c \equiv \frac{1}{A_c} \iint_{\text{cloudy area}} \phi dx dy \tag{3.6}$$

In the special case $\phi = 1$, and $F_c = 0$ we recover the continuity equation

$$\frac{\partial a_c}{\partial t} + \frac{1}{A} \oint_{\text{interface}} \hat{\mathbf{n}} \cdot (\mathbf{u} - \mathbf{u}_i) dl + \frac{\partial a_c w_c}{\partial z} = 0 \tag{3.7}$$

As we are interested in the fluxes over the cloud boundary we also define averages over the interface as

$$\overline{u}^{b} \equiv u_b \equiv \frac{1}{L_b} \oint_{\text{interface}} \hat{\mathbf{n}} \cdot (\mathbf{u} - \mathbf{u}_i) dl \tag{3.8}$$

$$\overline{\phi}^{b} \equiv \phi_b \equiv \frac{1}{L_b} \oint_{\text{interface}} \phi dl \tag{3.9}$$

where u_b is the net mean velocity through the cloud boundaries, ϕ_b is the mean of property ϕ along the cloud boundaries, and L_b is the total length of the interface. For both the interface and the cloudy area we employ a decomposition of the fluxes into a mean and a fluctuating part

$$\overline{u\phi}^{b} \equiv u_b \phi_b + \overline{u'\phi'}^{b} \tag{3.10}$$

$$\overline{w\phi}^{c} \equiv w_c \phi_c + \overline{w'\phi'}^{c} \tag{3.11}$$

where the primes denote deviations with respect to the cloudy part or the interface dependent on the used average. The advantage of the decomposition of the flux on the interface is that it provides a natural distinction between the small scale diffusive, turbulent mixing ($\overline{u'\phi'}^{\mathrm{b}}$) and advective transport caused by organized motions across the interface ($u_{\mathrm{b}}\phi_{\mathrm{b}}$).

We assume that A is large enough to contain a large cumulus ensemble, so that eqs. (3.5) and (3.7) can be assumed to be time-independent (Siebesma & Cuijpers, 1995). The resulting stationary form of eqs. (3.5) and (3.7), together with eqs. (3.8), (3.9), (3.10), and (3.11) can be writen as

$$\frac{L_{\mathrm{b}}}{A_{\mathrm{c}}}(\overline{u'\phi'}^{\mathrm{b}} + u_{\mathrm{b}}\phi_{\mathrm{b}}) + \frac{1}{a_{\mathrm{c}}}\frac{\partial a_{\mathrm{c}} w_{\mathrm{c}}\phi_{\mathrm{c}}}{\partial z} + \frac{1}{a_{\mathrm{c}}}\frac{\partial a_{\mathrm{c}}\overline{w'\phi'}^{\mathrm{c}}}{\partial z} = F_{\mathrm{c}} \tag{3.12}$$

$$\frac{L_{\mathrm{b}}u_{\mathrm{b}}}{A_{\mathrm{c}}} + \frac{1}{a_{\mathrm{c}}}\frac{\partial a_{\mathrm{c}} w_{\mathrm{c}}}{\partial z} = 0 \tag{3.13}$$

In most previous theoretical studies on cumulus clouds and lateral mixing (see e.g. (Asai & Kasahara, 1967), (Randall & Huffman, 1982), (Cotton, 1975)) it has been assumed that the cloud fraction does not change with height. In that case there is a direct relationship between u_{b} and the divergence of the vertical velocity field. While constant cloud fraction might be a reasonable assumption for individual clouds, we will release this restriction in the present case where we are interested in the lateral mixing process between a whole shallow cumulus ensemble and its environment. In that case many LES studies showed that the cloud fraction varies strongly with height (see e.g. (Siebesma & Cuijpers, 1995), (Stevens et al., 2001), (Brown et al., 2002)).

The turbulent flux across the cloud interface can be well approximated by an eddy diffusivity approach (Asai and Kasahara, 1967 and Kuo, 1962)

$$\begin{aligned}
\overline{u'\phi'}^{\mathrm{b}} &\simeq K(\ell)\frac{(\phi_{\mathrm{c}} - \phi_{\mathrm{e}})}{\ell} \\
&\simeq \eta\ell \mid \Delta w(\ell) \mid \frac{(\phi_{\mathrm{c}} - \phi_{\mathrm{e}})}{\ell} \\
&\simeq \eta \mid w_{\mathrm{c}} \mid (\phi_{\mathrm{c}} - \phi_{\mathrm{e}})
\end{aligned} \tag{3.14}$$

In the first step the horizontal gradient of the field ϕ is evaluated at a scale ℓ which is of the order of the typical radius of a cloudy updraft. The eddy diffusivity K in the second step is expressed as the product of a length scale, a velocity difference over that length scale and a dimensionless constant η . Obviously we have taken the same length scale that is used to estimate the horizontal gradient. In the last step we used the fact that the vertical velocity in the environment is much smaller than in the cloud. From here on the modulo signs for w_{c} are omitted because we only consider updrafts.

For the advective transport term across the interface, $u_b\phi_b$, we use, following Asai and Kasahara, 1967, an upwind approximation

$$\phi_b = \phi_c \quad if\ u_b > 0 \quad \frac{\partial M}{\partial z} < 0 \ (divergence) \tag{3.15}$$

$$\phi_b = \phi_e \quad if\ u_b < 0 \quad \frac{\partial M}{\partial z} > 0 \ (convergence) \tag{3.16}$$

Note that the sign of u_b is directly determined by the vertical gradient of the mass flux $M \equiv a_c w_c$ (see Eq. (3.13)). Using (3.14), (3.15), and (3.16) in (3.12) and eliminating the interface velocity u_b by using the continuity equation (3.13) finally gives

$$H(-u_b)\left(\frac{1}{a_c}\frac{\partial a_c w_c}{\partial z}\right)(\phi_c - \phi_e) + \frac{L_b}{A_c}\eta w_c(\phi_c - \phi_e) + w_c\frac{\partial \phi_c}{\partial z} + \frac{1}{a_c}\frac{\partial a_c \overline{w'\phi'}^c}{\partial z} = F_c \tag{3.17}$$

where H denotes the Heaviside function. The first term in (3.17) represents the organized transport across the cloud interface. Note that this term only has a non-zero contribution in the case of convergence. In the case of divergence the organized term will show up in the equation for the environment which will not be considered in this chapter. The second term represents the turbulent lateral mixing, the third term the vertical advection and the fourth term represents the subplume contributions to the vertical transport.

3.2.2. BUDGET EQUATION FOR MOIST CONSERVED VARIABLES

So far we have not specified ϕ. For the ultimate expressions for entrainment and detrainment we will need budget equations for w_c (section 3.2.3) and a moist conserved variable. The cloudy area is often defined in such a way that the contribution of the subplume vertical fluxes of moist conserved variables is minimized (Siebesma & Cuijpers, 1995). In the validation section we will use a definition for the cloudy area as that part of the horizontal domain A that contains non-zero amounts of condensed water and that is also positively buoyant, known as the cloud core sampling method (see e.g. (Siebesma & Cuijpers, 1995)). This latter condition is added to make sure that passive cloud elements that do not contribute to the vertical transport are excluded. With such a definition the subplume covariance contribution for a moist conserved variable can usually be ignored (Siebesma & Cuijpers, 1995). Furthermore, for moist conserved variables such as the total water specific humidity q_t there are in the absence of precipitation no sources and sinks, i.e. $F_{c,q_t} = 0$. For (heavy) precipitating convection

$F_{c,qt}$ should be taken into account but here we will only investigate (almost) non-precipitating shallow convection cases. Ignoring the source/sink and the sub-plume term allows us to rewrite (3.17) with $\phi = q_t$ in a more familiar form

$$\frac{\partial q_{t,c}}{\partial z} = -[H(-u_b)(\frac{1}{M}\frac{\partial M}{\partial z}) + \eta\frac{L_b}{A_c}](q_{t,c} - q_{t,e}) \tag{3.18}$$

where we recognize the entraining plume form of Betts, 1975

$$\frac{\partial q_{t,c}}{\partial z} = -\varepsilon_{qt}(q_{t,c} - q_{t,e}) \tag{3.19}$$

in which the so called fractional entrainment rate ε appears. Note that so far we did not introduce ε in our derivation. This is in contrast with other studies (e.g. (Gregory, 2001)) where ε is introduced already in an earlier stage. Here we accept Eq. (3.19) as the definition of the fractional lateral entrainment ε because this equation describes how ε is used in parameterisation schemes as well as how ε is diagnosed from LES. Taking Eq. (3.19) as the definition of ε allows us to write the following expression for the entrainment based on the budget equation for q_t (3.18)

$$\varepsilon = \varepsilon_{turb} + \varepsilon_{dyn} = \frac{\eta L_b}{A_c} + H(-u_b)\frac{1}{M}\frac{\partial M}{\partial z} \tag{3.20}$$

where we made an explicit distinction between turbulent, ε_{turb}, and dynamical, ε_{dyn}, entrainment as introduced by Houghton and Cramer, 1951. It is natural to identify the first term on the RHS of (3.20) with ε_{turb} and the second term on the RHS of (3.20)) with ε_{dyn}. Likewise we can derive an expression for the fractional detrainment rate if we rewrite the steady state continuity equation (3.13) in a more familiar form

$$\frac{1}{M}\frac{\partial M}{\partial z} = (\varepsilon - \delta) \tag{3.21}$$

and use this simply as a definition of the fractional detrainment rate δ. In that case we find a similar expression for δ

$$\delta = \delta_{turb} + \delta_{dyn} = \frac{\eta L_b}{A_c} - H(u_b)\frac{1}{M}\frac{\partial M}{\partial z} \tag{3.22}$$

Again it is natural to identify the first term on the RHS of (3.22) with δ_{turb} and the second term on the RHS of (3.22)) with δ_{dyn}.

So for divergent conditions ($u_b > 0$ or $\frac{\partial M}{\partial z} < 0$) $\varepsilon_{dyn} = 0$ whereas for convergent conditions ($u_b < 0$ or $\frac{\partial M}{\partial z} > 0$) $\delta_{dyn} = 0$. In shallow convection cases the mass flux in the cloud layer will usually decrease (see e.g. (Siebesma & Cuijpers,

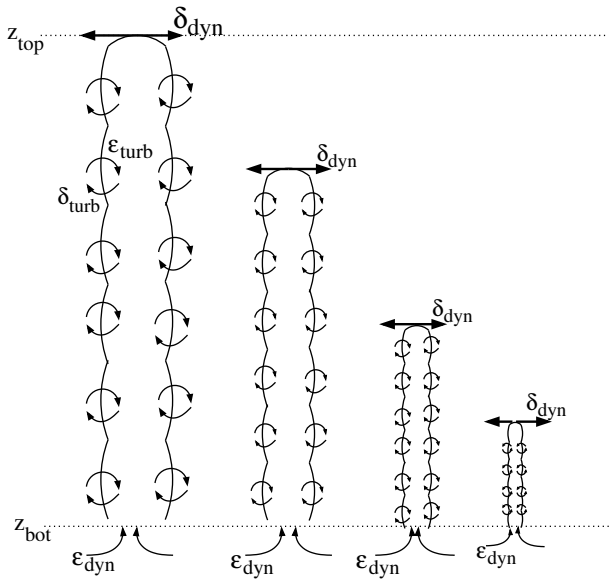

Figure 3.2: Schematic diagram of a cloud ensemble with massive entrainment, ε_{dyn}, at cloud base (z_{bot}) and massive detrainment, δ_{dyn}, at the top of individual clouds. From cloud base to the top of individual clouds turbulent lateral mixing takes place, presented by $\varepsilon_{\text{turb}}$ and δ_{turb}. For individual clouds the mass flux is constant with height. The deepest cloud reaches height z_{top}, the top of the cloud layer. This picture is valid for divergent conditions, i.e. $\frac{\partial M}{\partial z} < 0$, which is usually the case for shallow convection

1995), (de Rooy & Siebesma, 2008)). Consequently, (3.20) and (3.22) suggest a picture in line with Arakawa and Schubert, 1974 and Nordeng, 1994 of an ensemble of clouds where every individual cloud has a massive entrainment at the bottom, lateral turbulent mixing with constant mass flux in the cloud between bottom and top, and massive detrainment at the top (see Fig. 3.2). As a result of different cloud sizes in the ensemble, the massive detrainment of the various clouds shows up as a dynamical detrainment term. Different from (Arakawa & Schubert, 1974) is the appearance of a detrainment term in the turbulent lateral mixing, δ_{turb}. Figure 3.2 reveals that it is only the massive detrainment that regulates the shape of the cloud layer mass flux profile and consequently determines primarily where the updraft properties are deposited in the environment. This picture is consistent with (de Rooy & Siebesma, 2008) who use only the detrainment to describe variations in the shape of the shallow convection mass flux profile.

3.2.3. BUDGET EQUATION FOR VERTICAL VELOCITY

For the vertical velocity equation there are sinks and sources due to buoyancy and pressure perturbations

$$F_{\mathrm{c}}(w) = B - \overline{\frac{\partial p'}{\partial z}}^{\mathrm{c}} \tag{3.23}$$

with

$$B = g\frac{\theta_{\mathrm{v,c}} - \overline{\theta_{\mathrm{v}}}}{\overline{\theta_{\mathrm{v}}}} \tag{3.24}$$

where B is the buoyancy, p' in the second term on the RHS of (3.23) refers to pressure fluctuations with respect to the hydrostatic pressure, g is the acceleration due to gravity, and θ_{v} is the virtual potential temperature. As already mentioned by List and Lozowski, 1970 and Holton, 1973 the inclusion of the pressure pertubation term (second term on the RHS of (3.23)) can be important, certainly for heavy precipitating cumulus. Most recent studies, but in contrast to our approach, consider the effect of the pressure perturbation term within the context of a simplified vertical velocity equation, in which ε is already introduced. In some studies (e.g. (Siebesma et al., 2003)) the pressure perturbation term was then scaled with the entrainment term and sometimes with the buoyancy term as well (Bretherton et al., 2004). Uncommon was the approach of Gregory, 2001, who used the detrainment coefficient to scale the pressure perturbation term. However, in the original work of Simpson and Wiggert, 1969, and based on the work of Turner, 1963, the effect of pressure perturbations was taken into account with a virtual mass coefficient which reduced the buoyancy term.

Another approximation we have to make concerns the subplume (variance) term in the budget equation (3.17) for w_{c}. In contrast to the budget equation for q_{t}, the subplume term can not be ignored for vertical velocity. Recently, sophisticated parameterisations are developed within a mass flux framework (Lappen and Randall, 2001) to represent these subplume scale fluxes. In a more simple often applied approach the effect of this subplume turbulence term is scaled with the buoyancy and taken into account by a buoyancy reduction factor, α (see e.g. (Simpson & Wiggert, 1969), (Siebesma et al., 2003), (Gregory, 2001)). Formally the scaling of both the subplume term for vertical velocity and the pressure fluctuation term with the buoyancy can be written as

$$B - \overline{\frac{\partial p'}{\partial z}}^{\mathrm{c}} - \frac{1}{a_{\mathrm{c}}}\frac{\partial a_{\mathrm{c}}\overline{w'w'}^{\mathrm{c}}}{\partial z} \approx \alpha B \tag{3.25}$$

Preferably an adequate scaling of the pressure perturbation and subplume variance term should be determined from directly diagnosed vertical velocity

budget terms in LES for different shallow convection cases. Such LES experiments are outside the scope of this chapter but recent LES results (Voogd, 2009) adressing exactly this problem support the scaling of both the subplume and the pressure perturbation term with the buoyancy (like in (Simpson & Wiggert, 1969) and eq. (3.25)) using an optimal reduction factor α of approx. 0.6. Note that, based on laboratory experiments, Simpson and Wiggert, 1969 found a similar value for α, namely 2/3. Because the choice of a proper α is important we will return to this issue in the results section.

If we apply the above mentioned assumptions for the forcing terms and sub plume turbulence and taking the usual approximation in mass flux schemes $w_e << w_c$, (3.17) with $\phi = w$ results in the following vertical velocity equation:

$$H(-u_b)(\frac{1}{M}\frac{\partial M}{\partial z}) + \eta\frac{L_b}{A_c} = \frac{\alpha B}{w_c^2} - \frac{1}{w_c}\frac{\partial w_c}{\partial z} \tag{3.26}$$

3.2.4. ANALYTICAL EXPRESSIONS FOR ENTRAINMENT AND DETRAINMENT

A direct comparison of (3.26) with (3.18) allows new expressions of ε and δ in terms of the buoyancy and the vertical velocity and cloud fraction divergence

$$\varepsilon_w = \frac{\alpha B}{w_c^2} - \frac{1}{w_c}\frac{\partial w_c}{\partial z} \tag{3.27}$$

$$\delta_w = \frac{\alpha B}{w_c^2} - \frac{2}{w_c}\frac{\partial w_c}{\partial z} - \frac{1}{a_c}\frac{\partial a_c}{\partial z} \tag{3.28}$$

where subscript w is used to distinguish these expressions from ε diagnosed using (3.19), denoted as ε_{qt}, and δ diagnosed from (3.21) and (3.19), denoted as δ_{qt}. So by using (3.26) we have eliminated the net exchange coefficient, η, as well as the Heaviside function in front of the dynamical mixing terms. As a consequence of the latter elimination the analytical expressions (3.27) and (3.28) are now valid for both divergent and convergent conditions. Note that Eqs. (3.27) and (3.28) can not be used (directly) as a parameterisation because w_c and the buoyancy themselves depend on ε, nor is it straightforward to approximate $\frac{1}{a_c}\frac{\partial a_c}{\partial z}$. Validation of the expressions (3.27) and (3.28) as well as a discussion on the behavior of the separate terms will be presented in the validation section.

3.3. ANALYSIS AND VALIDATION WITH LES

3.3.1. VALIDATION SET-UP

To investigate the analytical expressions for ε and δ in more detail and to assess the validity, we use LES of the Dutch Atmospheric LES model (DALES; (Cuijpers & Duynkerke, 1993)) for three shallow convection cases. Two of the cases are

more or less steady state shallow convection cases over tropical oceans designed from the field campaigns BOMEX (Siebesma & Cuijpers, 1995) and RICO (Rauber et al., 2007). For RICO we use the 24-h composite run (more information about this case and the experimental setup of the composite run can be found online at www.knmi.nl/samenw/rico). The main differences between these two cases concern the cloud depth (~1000 m for BOMEX and ~1700 m for RICO) and the mass flux profiles (more variable in RICO). The third case is based on an idealization of observations made at the Southern Great Plains ARM (Atmospheric Radiation Measurement Program) site on 21 June 1997 (Brown et al., 2002). The ARM case describes the development of daytime shallow cumulus convection over land. After approximately 5 hrs of simulation, at 11:30 LT, clouds start to develop at the top of an initially clear convective boundary layer. From this moment on the cloud layer grows to a maximum depth of 1500 m at 16:30 LT, after which it starts to decrease. Finally, at the end of the day at 19:30 LT, all clouds collapse. For the ARM case we solely present results for the cloudy period. Because the ARM case is non-steady, it is pre-eminently suited as a thorough test of our expressions.

For all cases precipitation is turned off in the LES model (only for RICO observations show some light rain) and cloud base level is defined as the height where the mass flux is at its maximum (de Rooy & Siebesma, 2008). For BOMEX and RICO the first hour is excluded for spin-up reasons.

All presented LES results are hourly averaged and based on the cloud core sampling, i.e. all LES gridpoints that contain liquid water and are positively buoyant ($\theta_{v,c} > \overline{\theta_v}$) are considered to be part of the cloudy updraft. Note that recently a sampling method based on passive tracers has been developed (Couvreux et al., 2010) giving comparably good estimates of the total turbulent transport of moist conserved variables in the cloud layer. In principle such a sampling method could be used as an alternative for the core sampling to evaluate the analytical expressions.

Applying the cloud core sampling to determine the updraft properties, the entraining plume model (3.19) can be used to infer ε_{qt} from LES (Siebesma & Cuijpers, 1995). Subsequently, this ε_{qt} together with M as diagnosed with the LES cloud core sampling can be substituted in (3.21) to determine δ (referred to as δ_{qt}). So ε_{qt} and δ_{qt} are the lateral mixing coefficients as often diagnosed from LES (Siebesma et al., 2003) and they will be considered here as the reference. Concerning the validation, it is important to mention that δ_{qt} is a function of M which via $M = a_c w_c$ is related to $\frac{1}{a_c}\frac{\partial a_c}{\partial z}$ and this term is part of δ_w. Nonetheless, this dependence has no serious impact on the conclusions.

As mentioned by Siebesma et al., 2003 the plume model breaks down near the inversion because a simple bulk approach with a single positive entrainment

rate is not able to represent the behaviour of the core fields. It is therefore justifiable to exclude the top 15 % of the cloudy layer (where the cloud layer is defined as the layer where $a_c > 0$). Also negative ε_{qt} and/or δ_{qt} values indicate that the bulk approach breaks down and these situations are therefore excluded from our evaluation. However, when an expression or parameterisation of ε or δ results in a negative value, it is cut off to zero, as would be done in practice. Note that this cut off (instead of maintaining the negative value) has no significant impact on the results.

3.3.2. RESULTS

Before we show the results of the analytical expressions against LES, the sensitivity of (3.27) and (3.28) for α is investigated. This is done by varying α and showing in Fig. 3.3, for all three investigated cases together, the overall performance of (3.27) and (3.28) in terms of the RMSE defined as

$$RMSE = \sqrt{\frac{1}{N}\sum_{i=1,N}(X_{w,i} - X_{qt,i})^2} \tag{3.29}$$

where $X \in \{\varepsilon, \delta\}$ and i is an index over all presented ($N = 1009$) results. Fig. 3.3 reveals that the optimal α for ε_w and δ_w, viz 0.62, coincides and this value is also quite close to the values found by the aforementioned LES experiments (0.6, (Voogd, 2009)) as well as Simpson and Wiggert, 1969, (2/3). Hereafter all presented results are based on $\alpha = 0.62$.

We start with the non-steady state ARM case, showing in Figs. 3.4a and 3.4b scatterplots with ε_w and δ_w against resp. ε_{qt} and δ_{qt}. Apart from the positive bias for ε_w, the correspondence between the analytical expressions and the mixing coefficients as diagnosed from LES is generally good, especially considering the complicated, non-steady state nature of this case. On the other hand, Fig. 3.4a still reveals relatively large overestimations during the beginning (until 14:30 LT) and at the last hour (19:30 LT) of the cloudy period. Note that at 19:30 LT clouds start to collapse and the maximum cloud cover (at cloud base) for this hour is only 0.006 which can be interpreted as an indication that the results for this hour suffer from noise generated by a too small ensemble. In the discussion of the next figures we will return to the above mentioned overestimations of the entrainment.

The generally good correspondence of the expressions with the reference lateral mixing coefficients, including the correct height dependence, is confirmed by Fig. 3.5. For clarity reasons only some selected hours are plotted. Figure 3.5a reveals that the relatively large overestimations in the entrainment at 13:30 LT (see also Fig. 3.4a) occur near cloud base. This is also the case for 12:30 and 14:30

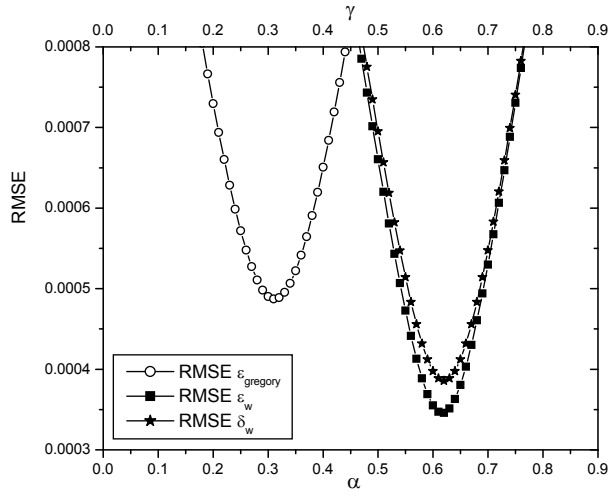

Figure 3.3: The Root Mean Square Error (RMSE) of $\varepsilon_{\text{Gregory}}$ (3.31) as a function of γ and ε_{w} (3.27) and δ_{w} (3.28) as a function of α for the ARM, BOMEX and RICO case together. The RMSE for optimal α (0.62) and γ (0.31) are mentioned in Table 3.1. Note that Gregory, 2001 found $\gamma = 12^{-1}$.

LT (not plotted). However, the aforementioned overestimations of the entrainment at 19:30 LT show a much different height dependence with a maximum error at 1800 m, about halfway the cloud layer (Fig. 3.5c). Noteworthy in the detrainment profile plots (Figs. 3.5b and d) is the large variation in time (note the different x-axis scale for ε and δ). As explained by de Rooy and Siebesma, 2008, the large δ values as observed during the first cloudy hours of the ARM case (Figs. 3.5b and 3.4b) are for an important part caused by the relative shallowness of the cloud layers. In a bulk sence (averaged over the cloud layer depth) shallower layers inevitably lead to larger $\frac{1}{M}\frac{\partial M}{\partial z}$ and $\frac{1}{a_{\text{c}}}\frac{\partial a_{\text{c}}}{\partial z}$ terms ($\frac{1}{M}\frac{\partial M}{\partial z} \sim \frac{1}{M}\frac{\triangle M}{\triangle z} \sim \frac{1}{\triangle z}$). Under the usual divergent conditions, these terms only affect the detrainment (see 3.22, and 3.28) explaining the large δ values observed during the first cloudy hours of ARM. Besides the depth of the cloud layer, the shape of the mass flux profile, and therewith δ, is also influenced by environmental conditions (see e.g. Derbyshire et al., 2004) as well as properties of the updraft itself (de Rooy & Siebesma, 2008). The above mentioned arguments support the approach of de Rooy and Siebesma, 2008 to describe the mass flux profile with a fixed function for ε but a flexible parameterisation for δ to account for the variations from hour to hour and case to case in the shape (e.g. a strong or no decrease of the mass flux in the lowest half of the cloud layer). An interesting variation on this approach is given by (Neggers et al., 2009) describing changes in the cloud fraction profile based on thermodynamical arguments.

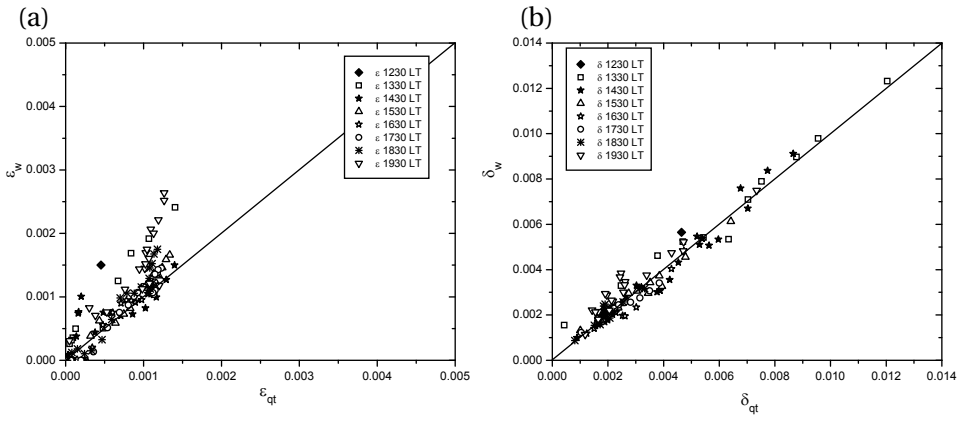

Figure 3.4: Comparison of (a) ε_{w} with $\varepsilon_{\mathrm{qt}}$ and (b) δ_{w} with δ_{qt} for different hours during the ARM case.

Now, again for the ARM case only, let us take a closer look at the different terms building up the expressions for ε and δ and their impact on the vertical profiles of ε_{w} and δ_{w} (Figs. 3.6a-d, again for the selected hours as in Fig. 3.5). We first return to the relatively large overestimations of the entrainment during the first cloudy hours and 19:30 LT mentioned before. Comparing Figs. 3.5a and c with Figs. 3.6a and c reveals that the large overestimations in ε are related to conditions with positive (or small negative) $-\frac{1}{w_{\mathrm{c}}}\frac{\partial w_{\mathrm{c}}}{\partial z}$ values. Also for 12:30 and 14:30 LT (not plotted) the largest overestimations in the entrainment occur when $-\frac{1}{w_{\mathrm{c}}}\frac{\partial w_{\mathrm{c}}}{\partial z} > 0$ (i.e. w_{c} decreases with height). The $-\frac{1}{w_{\mathrm{c}}}\frac{\partial w_{\mathrm{c}}}{\partial z}$ profile for 19:30 LT (Fig. 3.6c) is quite different from all other hours with a positive value halfway the cloud layer at 1800 m (also the height with the maximum error in ε_{w} and δ_{w} for this hour) and a decrease at the 400 m above. This atypical profile supports the aforementioned suspicion that the ensemble for this hour is too small.

The overall picture of Figs. 3.6a and c is that both terms in ε_{w} (3.27), i.e. $\frac{\alpha B}{w_{\mathrm{c}}^2}$ and $\frac{1}{w_{\mathrm{c}}}\frac{\partial w_{\mathrm{c}}}{\partial z}$, are of the same order of magnitude, with the buoyancy term being somewhat larger. However, for δ_{w} (Figs. 3.6b and d) the situation is different. Because the sum of the buoyancy and the vertical velocity terms in the expression for δ_{w} (3.28), i.e. $\alpha B w_{\mathrm{c}}^{-2} - 2w_{\mathrm{c}}^{-1}\frac{\partial w_{\mathrm{c}}}{\partial z}$ result mostly in small negative values for a large part of the cloud layer, the strongly fluctuating $\frac{1}{a_{\mathrm{c}}}\frac{\partial a_{\mathrm{c}}}{\partial z}$ term clearly dominates the height and time variation in δ. As a result δ_{w} can be reasonably well approximated by $-\frac{1}{a_{\mathrm{c}}}\frac{\partial a_{\mathrm{c}}}{\partial z}$ with generally underestimations near cloud base and overestimations near cloud top. Also a direct comparison between δ_{qt} and $-\frac{1}{a_{\mathrm{c}}}\frac{\partial a_{\mathrm{c}}}{\partial z}$ for all three cases together gives reasonable results (see Fig. 3.7a).

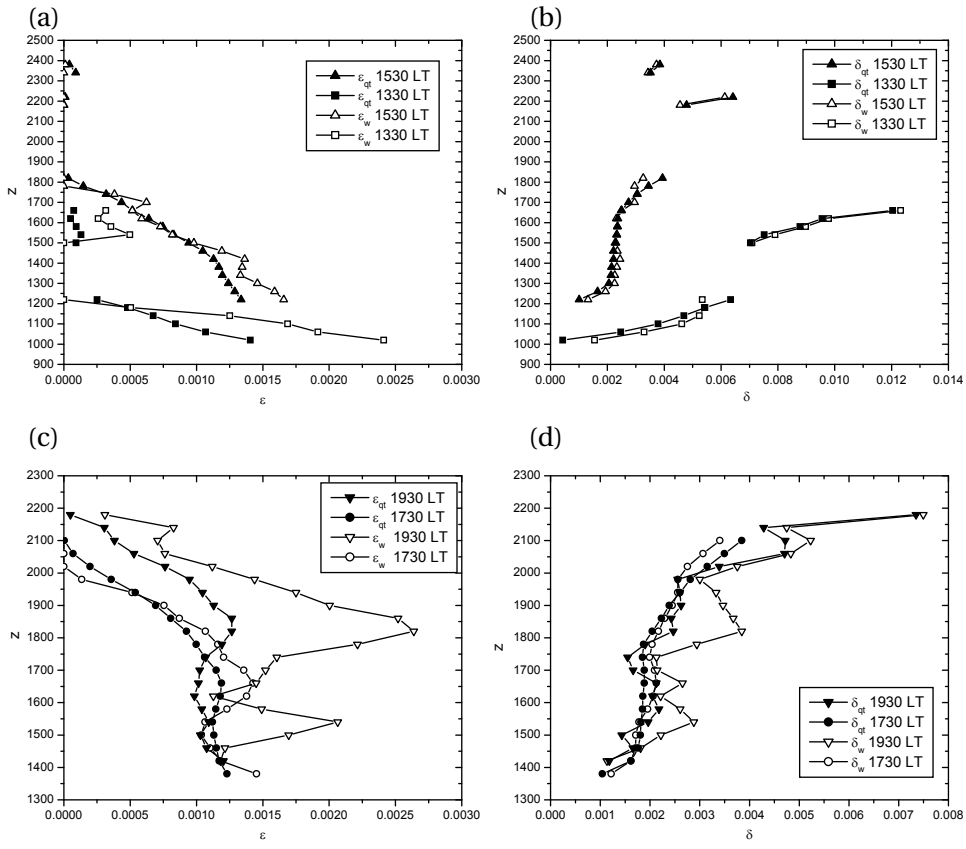

Figure 3.5: Profiles of $\varepsilon_{\mathrm{qt}}$ (closed symbols) and ε_{w} (open symbols) during the ARM case for hours 13 : 30 and 15 : 30 LT (a) and 17 : 30 and 19 : 30 LT (c). Panels (b) and (d) are as panels (a) and (c) but now for δ. Note the different x-axis scale for the entrainment and detrainment plots. Profiles can be discontinuous due to negative $\varepsilon_{\mathrm{qt}}$ and/or δ_{qt} values (see text).

$$\varepsilon_{\mathrm{Nordeng}} = \frac{1}{w_{\mathrm{c}}} \frac{\partial w_{\mathrm{c}}}{\partial z} \tag{3.30}$$

However, from Fig. 3.7b it becomes clear that although the aforementioned approximation works well for δ, it does not hold for ε where the equal order of magnitude of the different terms in the analytical expression makes this expression more sensitive. From an overestimation of high values of $\varepsilon_{\mathrm{qt}}$ in Fig. 3.7b, corresponding to values near cloud base, (3.30) underestimates ε values in the middle of the cloud layer and again overestimates the small ε values near the top of the cloud layer. For all three cases together, the RMSE for (3.30) is presented in Table 3.1.

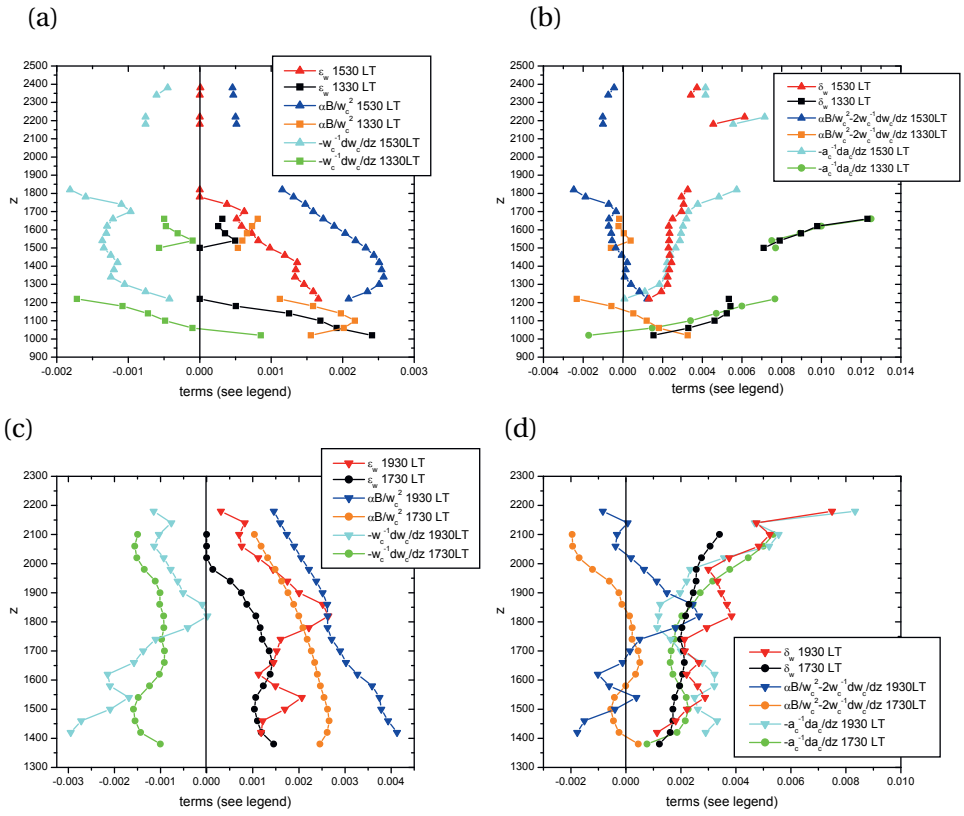

Figure 3.6: For different hours during the ARM case, profiles of (a,c) ε_w and (b,d) δ_w including the terms which build up the corresponding expressions, that is ($\alpha B w_c^{-2}$ and $-w_c^{-1}\frac{\partial w_c}{\partial z}$) for ε_w, and ($\alpha B w_c^{-2} - 2w_c^{-1}\frac{\partial w_c}{\partial z}$) and ($-a_c^{-1}\frac{\partial a_c}{\partial z}$) for δ_w (with $\alpha = 0.62$).

Yet another approximation can be made by simply ignoring the $\frac{1}{w_c}\frac{\partial w_c}{\partial z}$ term (Fig. 3.6a and c) in (3.27), leading to the following expression, as proposed by Gregory, 2001

$$\varepsilon_{\text{Gregory}} = \frac{\gamma B}{w_c^2} \tag{3.31}$$

where γ represents a tuning constant. Gregory, 2001 used $\gamma = 1/12$ and found a 50 % underestimation of his expression against LES for BOMEX. The sensitivity of (3.31) for γ is shown in Fig. 3.3 which suggests a much higher optimal value, namely $\gamma = 0.31$. To demonstate the potential of (3.31) we show results with latter optimal value. Figure 3.7c for all three cases reveals reasonable results for (3.31) but less good than with the full analytical expression (3.27) (compare Fig. 3.7c with Figs. 3.4a and 3.8a or see Table 3.1 or Fig. 3.3). Especially for BOMEX and

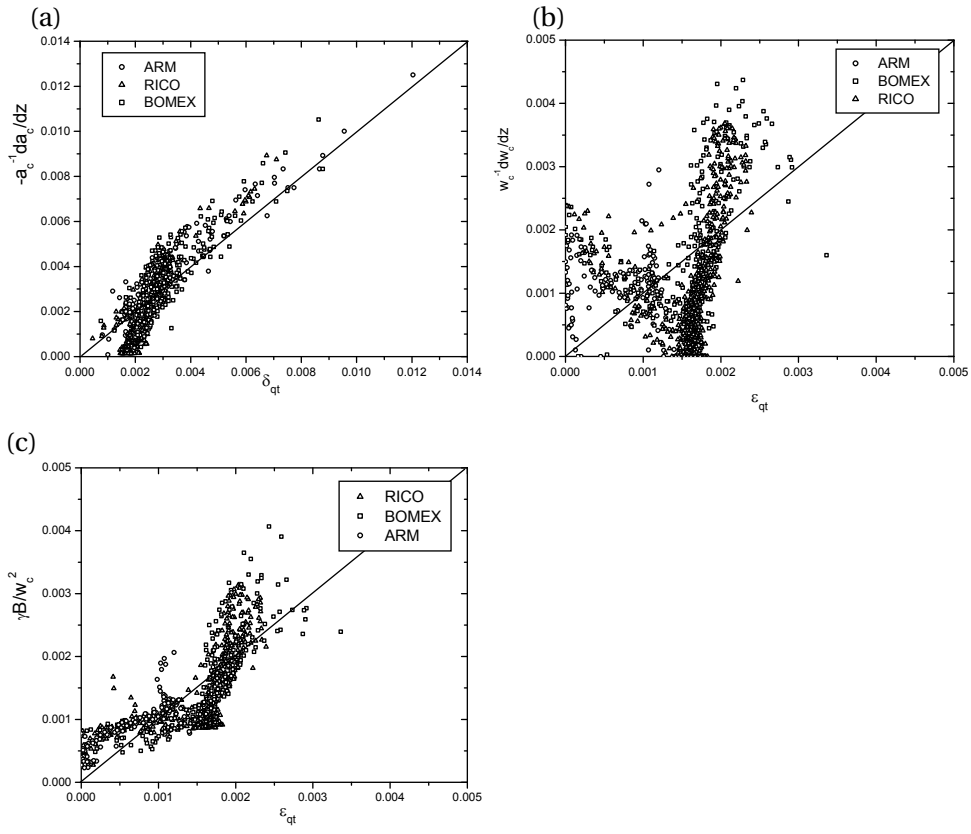

Figure 3.7: For the ARM, BOMEX, and RICO case, comparison of (a) δ_{qt} with $-a_{\mathrm{c}}^{-1}\frac{\partial a_{\mathrm{c}}}{\partial z}$, (b) $\varepsilon_{\mathrm{qt}}$ with $\varepsilon_{\mathrm{Nordeng}} = w_{\mathrm{c}}^{-1}\frac{\partial w_{\mathrm{c}}}{\partial z}$, and (c) $\varepsilon_{\mathrm{qt}}$ with $\varepsilon_{\mathrm{Gregory}} = \gamma B w_{\mathrm{c}}^{-2}$ with $\gamma = 0.31$.

RICO the $\frac{1}{w_{\mathrm{c}}}\frac{\partial w_{\mathrm{c}}}{\partial z}$ term (not shown) has relatively large values near cloud base and cloud top. Consequently, $\varepsilon_{\mathrm{Gregory}}$ in Fig. 3.7c reveals inevitably a bend in the scatterplot with overestimations near cloud base and top and underestimations halfway the cloud layer. Another indication that the influence of $\frac{1}{w_{\mathrm{c}}}\frac{\partial w_{\mathrm{c}}}{\partial z}$ can not be ignored in an expression for ε comes from examining the profiles in Fig. 3.5c in detail. Looking e.g. just above 1500 m, for 17:30 LT, ε atypically increases slightly with height. This increase is caused by the increase of $-\frac{1}{w_{\mathrm{c}}}\frac{\partial w_{\mathrm{c}}}{\partial z}$ at the corresponding height (see Fig. 3.6c). Although such increases in ε_{w} are generally at the approx. correct heights, they seem to be somewhat stronger than in $\varepsilon_{\mathrm{qt}}$, especially for hour 19:30LT. Apart from Gregory also Mironov, 2009 and Rio et al., 2010 mentioned the term $\frac{B}{w_{\mathrm{c}}^2}$ in an expression for the lateral mixing coefficients.

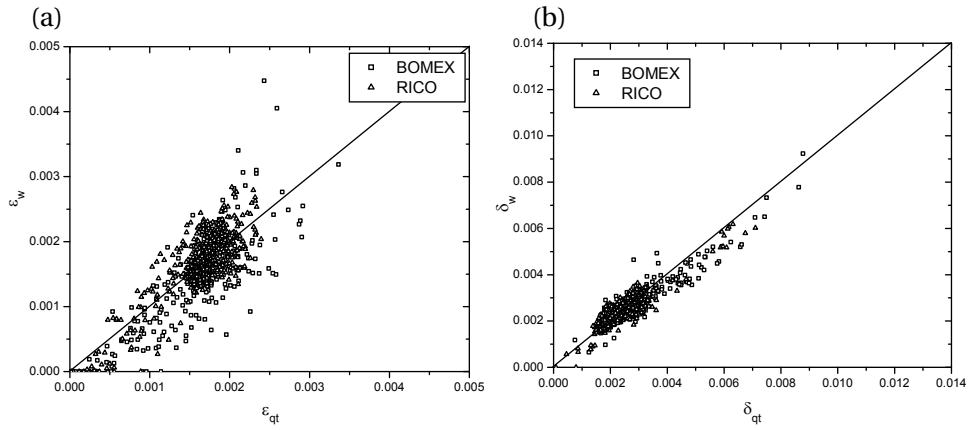

Figure 3.8: Comparison of (a) ε_{qt} with ε_w and (b) δ_{qt} with δ_w for all hours except the first during the BOMEX and RICO case.

As a validity check we also present results for the steady state cases BOMEX and RICO (Fig. 3.8). Again the correspondence between the usual LES diagnosed mixing coefficients and ε_w and δ_w is good. While the analytical expressions overestimated the entrainment for ARM they seem to underestimate the detrainment for BOMEX and RICO somewhat. The RMSE for the analytical expressions (3.27) and (3.28) for all cases together are presented in Table 3.1.

In comparison with δ the variations from hour to hour and case to case in ε are small (Fig. 3.5) and describing ε with some fixed (non-dimensionalized) function from cloud base to cloud layer top seems more feasible than a fixed function for δ (see also de Rooy and Siebesma, 2008). But despite the relative small variation in ε profiles, the results clearly show overall smaller entrainment rates for the ARM case than for the BOMEX and RICO case (compare Fig. 3.4a with Fig. 3.8). This is caused by the smaller $\frac{\alpha B}{w_c^2}$ term, and more specifically the larger vertical velocity in the ARM case. For example, at cloud base $w_c \approx 1.5\,\mathrm{ms}^{-1}$ for ARM whereas $w_c \approx 0.7\,\mathrm{ms}^{-1}$ for BOMEX and RICO. The higher velocities during the ARM case can be related to the more vigorous convection in the subcloud layer with strong surface heating above land. If we are able to make an adequate estimate of the vertical velocity of the updraft at cloud base in a NWP or climate model, this velocity can be used to refine the often applied parameterisation where ε is a fixed function of height (see e.g. Siebesma et al., 2003), i.e. parameterise the starting value of ε at cloud base with a function of the vertical velocity of the updraft and assume e.g. a z^{-1} lapse rate for the rest of the cloud layer. This is an example how insight given by the analytical expressions can be used for parameterisation developments. Note that the ARM case has a much

	RMSE
ε_{w}	$3.45 \cdot 10^{-4}$
$\varepsilon_{\mathrm{Gregory}}$	$4.87 \cdot 10^{-4}$
$\varepsilon_{\mathrm{Nordeng}}$	$1.01 \cdot 10^{-3}$
δ_{w}	$3.85 \cdot 10^{-4}$

Table 3.1: Root Mean Square Error (RMSE) of different expressions for ε and δ against resp. $\varepsilon_{\mathrm{qt}}$ and δ_{qt} for the ARM, BOMEX and RICO case together (N=1009). Results for ε_{w} and δ_{w} are based on $\alpha = 0.62$ and for $\varepsilon_{\mathrm{Gregory}}$ on $\gamma = 0.31$ (optimal value)

deeper subcloud layer than the other two cases enabling not only larger accelerations of the updraft thermals but also the development of larger thermals that will normally have smaller ε values. A seperation between these positively correlated updraft properties, high updraft vertical velocity and large sizes of the thermals, can not be made here.

3.4. CONCLUSIONS AND DISCUSSION

In contrast with other studies on fractional entrainment and detrainment (e.g. Siebesma et al., 2003, Gregory, 2001) where the development of parameterisations was the main goal, we here primarily wanted to gain more insight into the behavior and physical nature of ε and δ. For that, we derived analytical expressions for ε and δ starting from generally valid equations for arbitrary shaped in-cloud fields and subsequently applied assumptions known from literature. In contrast with most other theoretical studies on convection we did not assume a constant cloudy area fraction with height which is crucial because we consider an ensemble of updrafts for which it is known that the cloudy area fraction can vary strongly with height. One of the key assumptions in the derivation concerns the description of the fluxes across the cloudy boundaries, where we follow Asai and Kasahara, 1967 including the distinction between larger scale dynamical transport and small scale turbulent mixing.

From the derivation of the analytical expressions, the following physical picture (see Fig. 3.2) emerges for an ensemble of shallow cumulus clouds under the usual divergent situation ($\frac{\partial M}{\partial z} < 0$): Massive entrainment occurs just beneath cloud base (here defined as the level with maximum mass flux). From cloud base to cloud top individual clouds have a constant mass flux with only turbulent lateral mixing until the massive detrainment at the cloud top. This picture is in line with Arakawa and Schubert, 1974 and Nordeng, 1994 but now includes a turbulent detrainment term. As a result of different cloud sizes in the ensemble, the massive detrainment of the various clouds shows up as a dynamical detrainment

term and the overall mass flux decreases with height. Consequense of the above mentioned concept is that in the cloud layer ε is only determined by turbulent lateral mixing whereas δ is also influenced by dynamical transport ($\frac{1}{M}\frac{\partial M}{\partial z}$). As a result there is a strong correspondence between variations in δ and $\frac{1}{M}\frac{\partial M}{\partial z}$ (or $\frac{1}{a_c}\frac{\partial a_c}{\partial z}$), which supports the approach of de Rooy and Siebesma, 2008 to describe the mass flux profile with a fixed function for ε but a flexible parameterisation of δ to account for the often described substantial variations in the shape. For example, from de Rooy and Siebesma, 2008 we know that δ varies strongly with cloud layer depth. This can now be easily explained because in a bulk sense (averaged over the cloud layer) and under (the usual) divergent conditions, $\frac{1}{M}\frac{\partial M}{\partial z}$ and $\frac{1}{a_c}\frac{\partial a_c}{\partial z}$, and therewith δ, must increase with decreasing cloud layer depth.

Based on a continuity equation and budget equations for the updraft vertical velocity and total water specific humidity, analytical expressions for ε and δ are derived. The first term in the expressions, $\frac{\alpha B}{w_c^2}$ is similar to the expression for ε as proposed by Gregory, 2001. Further, it is shown that under certain assumptions both terms in the expression for ε together can be written as the expression suggested by Nordeng, 1994. Overall, results with $\varepsilon_{\text{Gregory}}$ and especially $\varepsilon_{\text{Nordeng}}$ are less accurate than the analytical expression ε_w. Moreover, with the help of the full expression biases in $\varepsilon_{\text{Gregory}}$ and $\varepsilon_{\text{Nordeng}}$ can be explained.

Although the variations from case to case and hour to hour in ε are smaller than in δ, the entrainment values diagnosed for the ARM case are significantly smaller than for the BOMEX and RICO case. The analytical expression for ε reveals that this difference can be related to the much smaller $\frac{B}{w_c^2}$ term, or more specifically much larger w_c values, in the ARM case. It is discussed how this insight given by the analytical expression for ε can be useful for the development of a new parameterisation.

Although we used assumptions already known from literature in the derivation of the expressions, this does not mean that all applied assumptions were straightforward and undisputed. A problematic point remains the determination of a proper value for the buoyancy reduction factor α which covers the sub plume turbulence term of the vertical velocity variance as well as the pressure perturbation term. In principle α should be objectively derived from a careful analysis of the vertical velocity budget terms in LES. But even then it is not yet established if α can be considered as approximately constant under all conditions. For example Holton, 1973 already pointed out that the importance of the pressure perturbation term will increase going from shallow to deep heavy precipitating convection. Nevertheless, recent results from LES experiments diagnosing the vertical velocity budget terms ((Voogd, 2009), (de Roode et al., 2012)),

early results based on water tank experiments ((Turner, 1963), (Simpson & Wiggert, 1969)), as well as the here presented results, all suggest a suitable value for α of around 0.62 for shallow convective conditions.

The presented analytical expressions are useful to identify important processes determining the behavior of ε and δ. It is shown that the expressions can be used as a starting point for the development of parameterisation approaches as well as to judge existing parmeterizations.

3.5. ACKNOWLEDGEMENTS

Three anonymous reviewers are thanked for their useful comments. Pier Siebesma acknowledges fruitful discussions in an early stage of this research with David Neelin and Harm Jonker. This study has benefited from meetings funded by COST ES0905.

4

MODEL DEVELOPMENT IN PRACTICE: A COMPREHENSIVE UPDATE TO THE BOUNDARY LAYER SCHEMES IN HARMONIE-AROME CYCLE 40

ABSTRACT

The parameterised description of subgrid-scale processes in the clear and cloudy boundary layer has a strong impact on the performance skill in any numerical weather prediction (NWP) or climate model and is still a prime source of uncertainty. Yet, improvement of this parameterised description is hard because operational models are highly optimised and contain numerous compensating errors. Therefore, improvement of a single parameterised aspect of the boundary layer often results in an overall deterioration of the model as a whole. In this chapter, we will describe a comprehensive integral revision of three parameterisation schemes in the High Resolution Local Area Modelling – Aire Limitée Adaptation dynamique Développement InterNational (HIRLAM-ALADIN) Research on Mesoscale Operational NWP In Europe – Applications of Research to Operations at Mesoscale (HARMONIE-AROME) model that together parameterise the boundary layer processes: the cloud scheme, the turbulence scheme, and the shallow cumulus

Published as: de Rooy, Wim C., Siebesma, A.P., Baas, P., Lenderink, G., de Roode, S.R., de Vries, H., van Meijgaard E., Meirink, J.F., Tijm, A.B.C., van 't Veen, B., 2022: Model development in practice: a comprehensive update to the boundary layer schemes in HARMONIE-AROME cycle 40, Geosci. Model Dev.

convection scheme. One of the major motivations for this revision is the poor representation of low clouds in the current model cycle. The newly revised parametric descriptions provide an improved prediction not only of low clouds but also of precipitation. Both improvements can be related to a stronger accumulation of moisture under the atmospheric inversion. The three improved parameterisation schemes are included in a recent update of the HARMONIE-AROME configuration, but its description and the insights in the underlying physical processes are of more general interest as the schemes are based on commonly applied frameworks. Moreover, this work offers an interesting look behind the scenes of how parameterisation development requires an integral approach and a delicate balance between physical realism and pragmatism.

4.1. INTRODUCTION

Due to ever-growing computer resources, numerical resolution of weather and climate models is steadily refined. Presently, limited area models operate routinely at resolutions of around 1 km and the first global intercomparison project for global storm-resolving models at resolutions of 5 km demonstrates that deep convective overturning processes are at least partly resolved by the new generation of weather and climate models (Stevens et al., 2019).

Prime atmospheric processes that remain to be parameterised at these scales are turbulent transport in the boundary layer, shallow cumulus convection, radiation, and cloud micro- and macrophysical processes of unresolved clouds. Traditionally, parameterisation of these processes has been developed as independent building blocks. The turbulence scheme describes the transport of heat, moisture, and momentum by the small-scale turbulent eddies in the boundary layer, whereas the convection scheme represents the transport by the larger-scale organised convective plumes. The cloud scheme aims to estimate the cloud fraction and the amount of condensed water.

Nowadays, it is recognised that the latter three parameterisation schemes need to be tightly coupled, as illustrated in Fig. 4.1. The cloud scheme requires information on the subgrid-scale variability of moisture and temperature as produced by the turbulence and convection scheme. Vice versa, the mixing by turbulence in the cloud boundary layer depends strongly on the cloud fraction. Clearly, optimisation of only one scheme will likely deteriorate the performance of another coupled scheme. This is why we describe in this chapter the revision and optimisation of a tightly coupled triplet of parameterisation schemes for boundary layer turbulence, shallow cumulus convection, and clouds.

As stated by Jakob, 2010, "Whereas early parameterisations development was aimed at finding suitable simple statistical relationships, modern parameterisations constitute complex conceptual models of the physical processes they are aiming to represent". Indeed, more physically based parameterisations should

be preferred as long as they improve the representation of essential processes, i.e. processes that significantly influence the resolved-scale variables. On the other hand, extra complexity in parameterisations should only be added if this does not imply introducing extra tunable parameters that cannot be constrained. Finding an acceptable level of physical realism and complexity without introducing too many tunable parameters that could give rise to overfitting, or even lead to an unstable system, is an important theme in this study.

The here-investigated parameterisations are part of the convection-permitting High Resolution Local Area Modelling – Aire Limitée Adaptation dynamique Développement InterNational (HIRLAM-ALADIN) Research on Mesoscale Operational NWP In Europe – Applications of Research to Operations at Mesoscale (HARMONIE-AROME) numerical weather prediction (Bengtsson et al., 2017) and climate model (Belusić et al., 2020). Bengtsson et al., 2017, from hereon B17, present the HARMONIE-AROME configuration of cycle 40 (cy40) including a brief description of the reference model physics, noted as cy40REF. In contrast to B17, this chapter provides a comprehensive description of the cloud, turbulence, and convection scheme. Moreover, we present numerous adjustments and improvements to the reference setup, included in a version referred to as cy40NEW. All these adjustments are accepted as the default options in the next release of HARMONIE-AROME, cycle 43.

The primary goal of these adjustments is to improve on what is considered one of the most important model deficiencies of HARMONIE-AROME cy40: a substantial underestimation of low cloud amount and overestimation of cloud base height.

The presented changes in the parameterisation schemes are primarily based on process studies and theoretical considerations. For example, long-term single-column model (SCM) runs are used to evaluate the turbulence scheme in terms of theoretical flux–gradient relationships, following the procedure of Baas et al., 2017. Based on these results, important modifications are made to the turbulence scheme. Additionally, several model intercomparison studies covering shallow cumulus, stratocumulus, and dry stable boundary layer conditions are used, most of which were based on observations collected during field campaigns. For these intercomparison cases, results of the Dutch Large Eddy Simulation (DALES, Heus et al., 2010) are compared in detail with SCM runs of HARMONIE-AROME. Finally, for the optimisation of the remaining uncertain parameters, we follow a more pragmatic approach by utilising 3-D model runs.

This chapter can be considered a description of a substantial model update concerning several parameterisation schemes. Although the parameterisations are embedded in the HARMONIE-AROME model, we believe that our findings are more generally applicable in numerical weather prediction (NWP) and cli-

mate models. Even though the schemes in other models may differ in details, the parameterisations in HARMONIE-AROME are based on widely applied frameworks: a statistical cloud scheme, a (bulk) mass flux convection scheme, and a turbulence kinetic energy (TKE)-based turbulence scheme. Hence, the here-described modifications and the impact of certain parameters, or combinations of them, are useful for any atmospheric model that requires a parameterised representation of the clear and cloudy boundary layer.

We start with a description of the convection, turbulence, and cloud scheme in Sect. 4.2. Section 4.2.2 provides the first complete and detailed description of the shallow convection scheme. Documentation of the turbulence scheme can be found in Lenderink and Holtslag, 2004 and Bengtsson et al., 2017. Therefore, only the parameters involved in the adjustments to the turbulence scheme are introduced in Sect. 4.2.3. Because of the comprehensive update to the statistical cloud scheme, a full description is provided in Sect. 4.2.4. Some of the adjustments introduced in Sect. 4.2 might seem arbitrary at first sight. However, Sect. 4.3 describes the experiments to motivate these adjustments. Several modifications are based on a comparison of SCM runs with large eddy simulation (LES) for the idealised case ARM (Sect. 4.3.1). SCM runs are also used to optimise the turbulence scheme against theoretical flux gradient relationships in Sect. 4.3.2. Section 4.3 further demonstrates the substantial improvements with the new configuration. For this, idealised cases of stratocumulus (Sect. 4.3.3), shallow convection (Sect. 4.3.1), and moderately stable conditions (Sect. 4.3.2) are used, as well as full 3-D model runs in Sect. 4.3.4. Finally, in Sect. 4.4, the discussions and conclusions are presented.

4.2. PARAMETERISATION SCHEMES

4.2.1. GENERAL FRAMEWORK

Before giving a more detailed description of the involved parameterisations in the next sections, we start by introducing the general parameterisation framework of the clear and cloud-topped boundary layer. The grid-box-averaged prognostic equations for the liquid water potential temperature θ_ℓ and the total water specific humidity q_t can be written as

$$\overline{D}_\mathrm{t}\overline{\theta}_\ell = -\frac{1}{\rho}\frac{\partial \rho \overline{w'\theta'_\ell}}{\partial z} + Q_\mathrm{rad} \tag{4.1a}$$

$$\overline{D}_\mathrm{t}\overline{q}_\mathrm{t} = -\frac{1}{\rho}\frac{\partial \rho \overline{w'q'_\mathrm{t}}}{\partial z} - G, \tag{4.1b}$$

where ρ is the average density, w the vertical velocity, G the autoconversion rate from condensed cloud water to rain water, and Q_rad the radiative heating ten-

dency. The primes denote deviation from the grid mean values. The operator D_t represent a total time derivative, while the overbars denote the grid box mean for an arbitrary variable ϕ. Note that the condensation and evaporation tendencies are not present because we use a formulation in terms of moist conserved variables. The terms on the right-hand side of Eq. (1) are all subgrid scale and require a parameterised description.

The turbulent fluxes are parameterised using the eddy-diffusivity mass flux (EDMF) framework (Siebesma & Teixeira, 2000). This framework has been designed in order to facilitate a unified description of the turbulent transport in the dry convective boundary layer (Siebesma et al., 2007) and the cloud-topped boundary (Rio & Hourdin, 2008; Soares et al., 2004). More recent refinements and developments can be found in Neggers et al., 2009 and Sušelj et al., 2013. The EDMF approach is inspired by the notion that cumulus convection is usually rooted in the subcloud layer from which rising thermals transport moist buoyant air into the cumulus clouds aloft. It is therefore natural to decompose the turbulence into organised convective updrafts and a remaining part consisting of smaller-scale turbulent eddies:

$$\overline{w'\phi'} = \overline{w'\phi'}^{\text{turb}} + \overline{w'\phi'}^{\text{conv}}. \tag{4.2}$$

As long as the updraft fraction a_u is much smaller than unity, the convective transport can be conveniently parameterised in a mass flux (MF) framework as

$$\overline{w'\phi'}^{\text{conv}} \approx \frac{M_u}{\rho}\left(\phi_u - \overline{\phi}\right), \; M_u = \rho a_u w_u, \tag{4.3}$$

where a bulk convective mass flux M_u has been introduced and where w_u denotes the vertical velocity in the updraft. Mass flux mixing (Eq. 4.3) involves the conserved variables for temperature and humidity as well as momentum. Although convective momentum mixing is less efficient than scalar mixing (Li & Bou-Zeid, 2011), they are parameterised here similarly. Convective momentum transport is an active and important area of research (see, e.g. Helfer et al., 2021; Saggiorato et al., 2020; Schlemmer et al., 2017) but is not investigated this chapter.

The remaining small-scale local turbulence is approximated by vertical diffusion by means of an eddy diffusivity (ED) approach:

$$\overline{w'\phi'}^{\text{turb}} \approx -K\frac{\partial\overline{\phi}}{\partial z}, \tag{4.4}$$

which completes the EDMF framework in its simplest form. Note that the parameterisation task is now reduced to finding appropriate expressions for the mass

flux M_u the updraft fields ϕ_u and the eddy diffusivity K. One prime advantage of the EDMF approach is that the mass flux description of the updrafts can be active for both the clear and cloud-topped boundary layer so that the transition between these regimes can occur in a more continuous manner without the need for explicit switches or trigger functions.

There is a strong interplay between turbulence and convection (see Fig. 4.1). For example, the transport of heat by the convective thermals produced by the mass flux scheme will establish a neutral to slightly stable stratification in the upper part of the convective boundary layer, thereby suppressing the diffusive transport by the TKE scheme in this area (Lenderink et al., 2004). Besides, there is also a direct (coded) link between these schemes as the mass flux is used as a source term in a TKE budget equation that is used to parameterise the eddy diffusivity K (see Fig. 4.1). This interaction mimics the turbulence energy cascade in which turbulent kinetic energy cascades from the larger eddies down to the smaller eddies and will be further discussed in Sects. 4.2.3 and 4.3.1.

The last parameterisation involved in the modifications is the cloud scheme. The task of the cloud scheme is to estimate the subgrid-scale cloud fraction and the condensed water. A common approach to calculate cloud cover and condensed water is to assume a subgrid-scale distribution of humidity and temperature and to determine the cloud cover as the fraction of the distribution above saturation. A key element in such a statistical cloud scheme is the estimate of the subgrid-scale variance of the relative humidity. Important contributions to this variance are the convective (Eq. 4.3) and turbulent (Eq. 4.4) transport, establishing a strong link between the cloud scheme and the turbulence and convection parameterisations (Fig. 4.1).

The specific parameterisation implementations in HARMONIE-AROME are described in more detail in the upcoming subsections. The parameterisations of the convective mass flux M_u and the updraft fields ϕ_u are discussed in Sect. 4.2.2. The eddy diffusivity parameterisation is discussed in Sect. 4.2.3 and finally the cloud scheme in Sect. 4.2.4.

4.2.2. SHALLOW CONVECTION SCHEME

The mass flux description is based on a dual mass flux approach (see, e.g. Neggers et al., 2009; from hereon N09) in which instead of one bulk updraft as in Eq. (4.3), we distinguish two updrafts: (1) a dry updraft describing all the thermals that do not convert into saturated updrafts in the cloud layer and (2) a moist updraft representing all updrafts that do reach the lifting condensation level (lcl) and continue their ascent in the cloud layer.

$$\rho \overline{w'\phi'}^{\text{conv}} \approx M_{\text{dry}} \left(\phi_{\text{u,dry}} - \overline{\phi} \right) + M_{\text{moist}} (\phi_{\text{u,moist}} - \overline{\phi}) \tag{4.5}$$

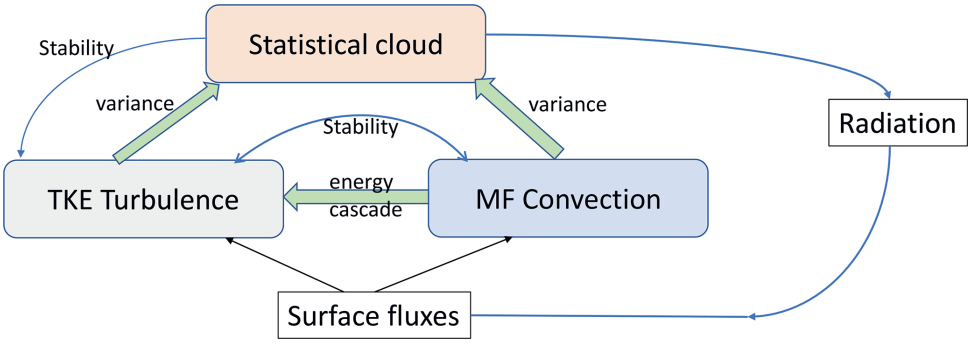

Figure 4.1: Schematic diagram illustrating the direct (thick arrows) and indirect (thin arrows) dependencies of parameterisation schemes with a focus on the schemes involved in the modifications.

As illustrated schematically in Fig. 4.2, we distinguish between two different convective boundary layer regimes: dry convective boundary layers with only a dry updraft and cloud-topped boundary layers with a dry and a moist updraft. Note that in contrast to B17 and N09, a stratocumulus-topped boundary layer in cy40NEW still uses a dry updraft (further discussed in Sect. 4.3.3).

The updraft profiles $\phi_{\mathrm{u,i}}$ of updraft i ($i \in \{\mathrm{dry}, \mathrm{moist}\}$) are determined by a conventional entraining plume model:

$$\frac{\partial \phi_{\mathrm{u,i}}}{\partial z} = -\varepsilon_{\mathrm{k}}(\phi_{\mathrm{u,i}} - \overline{\phi}) + \mu_{\phi}, \tag{4.6}$$

where ε_{k} denotes the fractional entrainment rate of the updraft and μ_{ϕ} represents cloud microphysical effects such as precipitation generation in the updraft (parameterised according to N09). The subscript k refers to different entrainment formulations for the dry updraft, the moist updraft in the subcloud layer, and the moist updraft in the cloud layer, i.e. $k \in \{\mathrm{dry}, \mathrm{sub}, \mathrm{cloudy}\}$. The various entrainment formulations are presented in Sect. (4.2.2).

The updrafts are initialised at the lowest model level with a temperature and humidity that exceed the mean values at that level. The excess values are determined by assuming that the temperature and humidity are Gaussian distributed with a variance estimated from the turbulent surface fluxes following the standard surface layer scaling of Wyngaard et al., 1971. The initialisation temperature and humidity values are then given by their $1 - a_{\mathrm{u}}$ percentiles, where a_{u} denotes the fractional updraft area. Hence, larger variances and smaller area fractions give stronger excess values. The updraft vertical velocity at the lowest model level is simply initialised at $0.1\,\mathrm{ms}^{-1}$ because the results are rather insensitive to the exact value. We refer to N09 for a more detailed description of the updraft initialisation. The updraft area fractions a_{u} are simply prescribed as fixed fractions

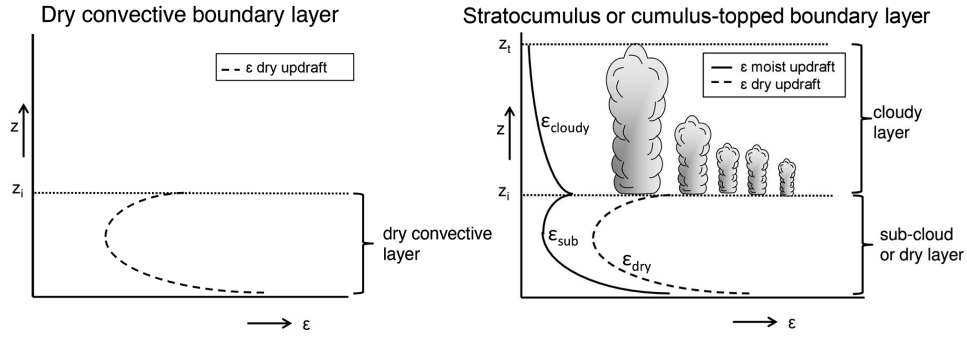

Figure 4.2: Schematic diagrams of the convective boundary layer regimes and the corresponding entrainment formulations (Eq. 4.8) of the dry (dashed line) and moist (solid line) updrafts. The inversion height and cloud top height are, respectively, denoted as z_i and z_t. Note that z_i can be different for the moist and dry updrafts and is therefore referred to as $z_{i,dry}$ and z_{lcl}, respectively. The shape of the entrainment profiles reflects the inverse dependency on the vertical velocity of the updraft (Sect. 4.2.2). This is a modified version of Fig. 4 in B17.

Table 4.1: Updraft area fractions per PBL regime in cy40NEW. Constants a_{dry} and a_{moist} are used to determine the initialisation of temperature and humidity excess at the lowest model level of the corresponding updraft (like in N09). Together with the dry updraft vertical velocity, a_{dry} also determines the dry updraft mass flux (see Eq. 4.3). The moist updraft mass flux, however, is calculated independently of a_{moist} (see Sect. 4.2.2).

PBL regime	Updraft fractions
Stable	$a_{dry} = a_{moist} = 0$
Dry convective	$a_{dry} = 0.1 \quad a_{moist} = 0$
Shallow convection or stratocumulus	$a_{moist} = 0.03 \quad a_{dry} = 0.1 - a_{moist}$

as in (B17) instead of the more flexible updraft fractions in N09. These fixed updraft fractions depend on the diagnosed boundary layer regime (Table 4.1). Like in N09, the total updraft fraction under convective conditions is always 0.1. How the planetary boundary layer (PBL) regime is diagnosed is described in the next section.

In addition to the updraft model for heat and moisture, a similar updraft equation is used for the vertical velocity w_u that can be used to estimate how deep the updrafts can penetrate (i.e. the height where w_u vanishes).

$$\frac{1}{2}\frac{\partial w_{u,i}^2}{\partial z} = a_k B_{u,i} - b_k \varepsilon_k w_{u,i}^2 \text{ with } B_{u,i} = \frac{g}{\overline{\theta}_v}(\theta_{v,u,i} - \overline{\theta}_v), \tag{4.7}$$

where $w_{u,i}$, $B_{u,i}$, and $\theta_{v,u,i}$ are, respectively, updraft vertical velocity, buoyancy, and virtual potential temperature of updraft i. g is the acceleration of gravity. In

Table 4.2: Applied a and b coefficients in the vertical velocity equation (Eq. 4.7).

	Dry or subcloud	Cloudy
a	$\frac{10}{7}$	$\frac{2}{3}$
b	$\frac{5}{7}$	1

Eq. (4.7), b_k and a_k are constants for dry (k = dry, sub, i.e. dry convective boundary layer (CBL) or subcloud layer) and cloudy (k = cloudy) parts of the boundary layer. Note that Eq. (4.7) is a highly parameterised vertical velocity equation as effects of pressure are absorbed in the constants b_k and a_k (see, e.g. de Roode et al., 2012). In the literature, a large variety of values for a and b can be found. Based on LES, de Roode et al., 2012 showed that the accuracy of the vertical velocity equation in the cloud layer depends on a correct combination of a and b. They found good correspondence with LES results for the combination of constants in Bechtold et al., 2001, de Rooy and Siebesma, 2010, and Rio et al., 2010, and we adopt these for the cloud layer (see Table 4.2). For dry updraft and subcloud layer part of the moist updraft, we adopt the formulation of Siebesma et al., 2007.

Fractional entrainment is not only applied in determining the updraft dilution in Eq. (4.6), but it also plays a role in the change of the mass flux with height, according to the following simple budget equation:

$$\frac{\partial M_u}{\partial z} = (\varepsilon - \delta) M_u, \tag{4.8}$$

where δ, the fractional detrainment, describes the outflow of updraft air into the environment. An accurate description of the lateral mixing between the updraft and the environment is key to every mass flux scheme (see, e.g. de Rooy et al., 2013). Hence, ε and δ are described in detail in the next sections.

FRACTIONAL ENTRAINMENT

Previously, the entrainment coefficients of the HARMONIE-AROME convection scheme have been discussed only briefly (B17). Here, they are described in detail. Further motivation for the parameter settings and adjustments is provided in Sect. 4.3.

We need to specify the fractional entrainment factors, ε, for both updraft types. Moreover, for the moist updraft, a distinction is made between the dry subcloud layer and the moist cloudy layer (Fig. 4.2). As demonstrated by de Rooy and Siebesma, 2008 and de Rooy and Siebesma, 2010, the fractional entrainment

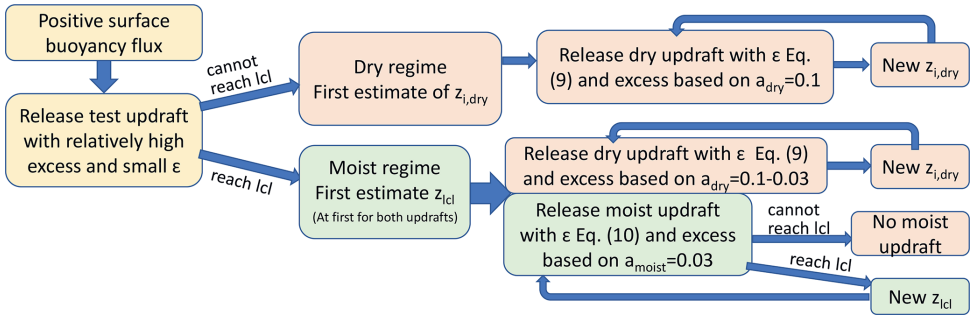

Figure 4.3: Schematic diagram of the subsequent steps in the shallow convection scheme to determine the ultimate inversion heights and corresponding entrainment formulations and the diagnosed regimes. After the test parcel (yellow), two iteration steps are done per entrainment formulation (red refers to dry and green to moist). Although the test parcel might have diagnosed a cloudy regime, it is possible that the ultimate moist updraft could not reach the lcl. In this case, no moist updraft is active (left panel of Fig. 4.2).

in the cloudy layer is mainly a function of the vertical extent of the cloud layer and reflects the general notion that a deeper cloud layers hosts larger clouds with lower fractional entrainment rates.

The entrainment formulations for the non-cloudy layers are based on existing LES-based formulations with the inversion height, z_i, as a parameter (Siebesma et al., 2007). However, the inversion height is not known a priori. To provide a first estimate of the inversion height, we therefore release a test parcel with an entrainment formulation inversely proportional to the vertical updraft velocity (Neggers et al., 2002, and N09 Eq. 19). The test parcel is only used for diagnostic purposes and does not affect the ultimate convective transport. Also note that here inversion height is actually the height where the dry updraft vertical velocity becomes 0 (so including the overshoot into the inversion) or the lifting condensation level in the case of the moist updraft. A flow diagram showing the steps in the convection scheme leading to the ultimate inversion heights and corresponding entrainment formulations, as well as the diagnosed regime(s), is presented in Fig. 4.3.

Apart from estimating z_i, the test parcel is also used to provide a first estimate of the boundary layer type to save computational time. If the updraft does not reach the lifting condensation level, the boundary layer type is dry convective with only a dry updraft (left panel of Fig. 4.2, and upper part of Fig. 4.1). If, on the other hand, the test parcel becomes saturated during its rise and condensation takes place, the boundary layer is estimated to be cloudy (right panel of Fig. 4.2, and lower part of Fig. 4.1). In this case, a dry and a moist updraft are considered. The relatively high excess and small ε of the test parcel ensure that cloudy

regimes are not missed.

After diagnosing the PBL regime and the inversion height with the test updraft, the updraft rise is again calculated but this time with the area fractions from Table 4.1, leading to different initial excess values, and with the refined entrainment rates as defined below (see Fig. 4.3). Hereby, the inversion height will alter, but already after two iterations (fixed) with the refined entrainment formulations, the results show no significant change anymore. Note that the final PBL regime could be dry, whereas the test parcel passed the lcl due to iteration with lower initial excess and refined ε formulation (Fig. 4.3).

In the event of an ultimately cloudy PBL, the cloud layer depth is diagnosed, and if it exceeds a threshold (currently set to 4000 m), the model is supposed to resolve moist convection, and only dry convection remains parameterised. Note that this threshold value should decrease with increased spatial resolution.

ENTRAINMENT OF THE DRY UPDRAFT

For any convective PBL regime, we need an entrainment formulation for the dry updraft. Based on LES results for a dry CBL, Siebesma et al., 2007 propose a formulation of ε as a fixed function of height, and we roughly adopt their formulation for the dry updraft:

$$\varepsilon_{\text{dry}} = c_{\text{dry}} \left(\frac{1}{z + a_1} + \frac{1}{z_{\text{i,dry}} - z + a_2} \right) \text{ for } z \leq z_{\text{i,dry}}, \tag{4.9}$$

where $c_{\text{dry}} = 0.4$ (Siebesma et al., 2007) and $z_{\text{i,dry}}$ is the dry updraft inversion height where the dry updraft stops rising. The shape of ε_{dry} using Eq. (4.9) (see Fig. 4.2a) reflects the expected increase in vertical velocity up to the middle of the dry convective boundary layer, resulting in decreasing ε values. From there, the updraft normally slows down, resulting in an increase of ε until the updraft finally stops at inversion height and ε becomes infinitely large. In practice, this ill definition of ε_{dry} is prevented by coefficient a_2 (similar to Soares et al., 2004). Again, similar to Soares et al., 2004, a_1 is introduced in cy40NEW to prevent very high entrainment values near the surface (see Sect. 4.3.1) and to reduce the dependence on the height of the lowest model level. Note that, due to the z^{-1} dependence of the entrainment formulation (Eqs. 4.9 and 4.10), the initialisation of the temperature and humidity excess becomes rather independent of the height of the lowest model level. This is explained in detail in Appendix A of Siebesma et al., 2007.

ENTRAINMENT OF THE MOIST UPDRAFT IN THE SUBCLOUD LAYER

Also for the entrainment of the moist updraft in the subcloud layer (Eq. 4.10), we build on the formulation of Siebesma et al., 2007 (Eq. 4.9) and Soares et al.,

2004, where the latter use a similar entrainment formulation as Eq. (4.10) but in a single updraft framework.

$$\varepsilon_{\text{sub}} = c_{\text{moist,sub}} \left(\frac{1}{z + a_1} + \frac{1}{z_{\text{lcl}} - z + \frac{z_{\text{lcl}}}{\frac{\varepsilon_{\text{lcl}}}{c_{\text{moist,sub}}} z_{\text{lcl}} - 1}} \right) \quad \text{for } z < z_{\text{lcl}}. \tag{4.10}$$

The formulation for the dry updraft (Eq. 4.9) needs to be adapted for the sub-cloud moist updraft for two reasons. Firstly, in contrast to the dry updraft, the moist updraft does not stop at inversion height (or cloud base), and therefore ε does not approach infinity. Instead, the entrainment at cloud base, noted as $\varepsilon_{z_{\text{lcl}}}$, is set to $0.002\,\text{m}^{-1}$, a reasonable value according to LES results (de Rooy et al., 2013; Siebesma et al., 2003). The apparently complicated last term in the dominator of Eq. (4.10) just ensures that the entrainment approaches its cloud base value apart from the term a_1. However, a_1 is negligible compared to typical z_{lcl} values. Secondly, the moist updraft represents stronger thermals than the dry updraft. LES results in Siebesma et al., 2007 reveal that the entrainment of stronger dry thermals (selected by changing the sampling criteria) corresponds to smaller c_{dry} values. Extending this to even stronger thermals that manage to become cumulus clouds, we set $c_{\text{moist,sub}} = 0.2$.

As argued in Appendix 4.5.3, $\varepsilon_{z_{\text{lcl}}} = 0.002\,\text{m}^{-1}$ replaces $\varepsilon_{z_{\text{lcl}}} = \frac{1.65}{z_{\text{lcl}}}$ in cy40REF where the dependence on z_{lcl} was included to reflect that deeper boundary layers will contain larger updrafts with relatively small entrainment values.

Similar to Eq. (4.9), Eq. (4.10) reflects an inverse correlation between the expected updraft vertical velocity and the shape of the entrainment profile (see Fig. 4.2). Like in Eq. (4.9), a_1 is introduced in Eq. (4.10) of cy40NEW (see Appendix 4.5.3 and Sect. 4.3.1).

ENTRAINMENT OF THE MOIST UPDRAFT IN THE CLOUDY LAYER

The final entrainment profile to be defined is $\varepsilon_{\text{cloudy}}$. In contrast to Soares et al., 2004, the formulations of ε_{sub} and $\varepsilon_{\text{cloudy}}$ are connected at cloud base. From cloud base, $\varepsilon_{\text{cloudy}}$ will normally decrease with height related to increasing vertical velocity. Moreover, our bulk scheme should represent an ensemble of clouds and at higher levels only the largest, and fastest-rising, thermals, with relatively small entrainment values, will survive. Although the exact shape of LES-diagnosed entrainment profiles in the cloud layer will depend on the precise sampling method, a decrease proportional to z^{-1} provides an acceptable fit and is used as a parameterisation.

$$\varepsilon_{\text{cloudy}} = \frac{1}{z - z_{\text{lcl}} + \frac{1}{\varepsilon_{z_{\text{lcl}}}}} \quad \text{for } z_{\text{lcl}} \leq z, \tag{4.11}$$

with, as mentioned before, $\varepsilon_{z_{\rm lcl}}$ =0.002 m^{-1} in cy40NEW. A comparison of Eq. (4.11) against LES-diagnosed entrainment rates is presented in Fig. 6 of de Rooy et al., 2013 and reveals a reasonably good correspondence, especially in comparison with estimates following a Kain–Fritsch type of formulation (Kain & Fritsch, 1990) as shown in Fig. 5 of de Rooy et al., 2013. Herewith, all entrainment rates in the dual mass flux scheme are defined.

THE MASS FLUX PROFILE

The counterpart of entrainment is detrainment, δ, describing outflow of updraft air into the environment; see Eq. (4.8). Together with entrainment, the detrainment determines the change of mass flux with height. The mass flux profile is important as it, e.g. determines where the properties of the updraft are deposited in the environment. Besides, mass flux is used as input for the turbulence and cloud scheme (Sect. 4.2.3 and 4.2.4).

Equation (4.8) is not applied for the dry updraft where area fraction is assumed to be constant, so applying the vertical velocity Eq. (4.7) suffices to solve M. Consequently, dry updraft mass flux simply varies with its updraft vertical velocity (like in N09).

For the moist updraft, we use the commonly applied mass flux closure at cloud base (Grant, 2001):

$$M_{z_{\rm lcl}} = c_{\rm b}\, w_*, \tag{4.12}$$

where $M_{z_{\rm lcl}}$ is the mass flux at cloud base and w_* is the usual convective velocity scaling derived from the surface buoyancy flux and using the cloud base as the boundary later depth (Grant, 2001). Further, $c_{\rm b}$ is a constant, set to 0.03 in cy40REF (according to Grant, 2001) and to 0.035 in cy40NEW (following Brown et al., 2002). In the subcloud layer, the moist updraft mass flux is imposed to increase linearly to the value at cloud base.

In the cloud layer, variations in the mass flux profile from case to case and hour to hour can be almost exclusively related to variations in the fractional detrainment as first pointed out by de Rooy and Siebesma, 2008 (from hereon RS08). This is supported by numerous LES studies (e.g. Böing et al., 2012; Derbyshire et al., 2011; de Rooy et al., 2013; H. Jonker et al., 2006). Apart from empirical evidence, the much larger variation in δ and its strong link to the mass flux is explained by theoretical considerations in de Rooy and Siebesma, 2010. Variations in δ partly arise from variations in cloud layer depth. This aspect is taken care of by evaluating and prescribing mass flux with a non-dimensionalised height, $\hat{z} = \frac{(z-z_{\rm lcl})}{h}$ and mass flux, $\hat{m} = \frac{M_{\rm u}}{M_{z_{\rm lcl}}}$, where h is the cloud layer depth, $z_{\rm t} - z_{\rm lcl}$, as diagnosed by the moist updraft. Here, $z_{\rm t}$ is the top of the cloud layer defined where $w_{\rm u,moist}$ becomes 0 ms^{-1} and $z_{\rm lcl}$ corresponds to the cloud base height. Variations in the shape of the non-dimensionalised mass

flux profile related to environmental conditions, like vertical stability and relative humidity, can be well described by a χ_{crit} dependence (RS08).

$$\hat{m}_* = c_1 \langle \chi_{\text{crit}} \rangle_* - c_2, \tag{4.13}$$

where $\hat{m}_*$ is the non-dimensionalised mass flux in the middle of the cloud layer (RS08) and χ_{crit} is the fraction of environmental air necessary to make updraft air just neutrally buoyant (Kain & Fritsch, 1990). The symbol $\langle\rangle_*$ denotes the average from cloud base to the middle of the cloud layer. So $\langle \chi_{\text{crit}} \rangle_*$ represents environmental conditions the updraft experiences along its rise up to the middle of the cloud layer. Note that apart from environmental conditions, also the buoyancy of the updraft itself determines χ_{crit} (RS08). As discussed in RS08, Eq. (4.13) describes a physically plausible relationship: "Large values of $\langle \chi_{\text{crit}} \rangle_*$ can be associated with large clouds (of large radii) with high updraft velocities that have large buoyancy excesses and/or clouds rising in a friendly, humid environment". For small $\langle \chi_{\text{crit}} \rangle_*$ values, the opposite can be expected. As discussed in RS08, updraft excess in LES (depending on sampling method) and in the model parameterisation will differ. Therefore, χ_{crit} values in LES and model will differ and consequently the optimal constants in Eq. (4.13). We apply $c_1 = 5.24$ (conform LES, RS08) and $c_2 = 0.39$. In addition, we limit $\hat{m}_*$ between 0.05 (strongly decreasing mass flux) and 1 (no net decrease in mass flux). The upper boundary can be reached in stratocumulus layers where χ_{crit} values can be high due to a high humidity environment.

With $\hat{m}_*$ known, and under the assumption that δ is constant with height (see, e.g. RS08) and that the entrainment varies as z^{-1}, the mass flux profile can be determined (for details, see RS08). The shape of the mass flux profile can vary from convex to concave up to the middle of the cloud layer; from there, mass flux decreases linearly to 0 at cloud layer top. Strong support for Eq. (4.13) can be found in Böing et al., 2012. Based on 90 LES runs covering a wide variety of relative humidity and stability of the environment, Böing et al., 2012 revealed a strong correlation of LES mass flux profiles with Eq. (4.13). Additionally, observations of trade wind cumuli mass flux reveal that the vast majority of the observations can be captured well with a simplified mass flux profile as described here (Lamer et al., 2015).

4.2.3. TURBULENCE SCHEME

In cycle 36 and older versions, HARMONIE-AROME made use of the CBR (Cuxart–Bougeault–Redelsperger) turbulence scheme (Cuxart et al., 2000) (Seity et al., 2011). As discussed by de Rooy, 2014 and B17, some model deficiencies can be related to the CBR scheme, most notably lack of cloud top entrainment. Therefore, the turbulence scheme HARATU (HArmonie with RAcmo TUrbulence) was

implemented. HARATU is based on a scheme originally developed for the Regional Atmospheric Climate Model (RACMO) (van Meijgaard et al., 2012) and is described in detail in Lenderink and Holtslag, 2004 (from hereon LH04). In comparison with LH04, some modifications were implemented in HARMONIE-AROME (see B17), mainly to ameliorate wind speed forecasts during stormy conditions. With HARATU, HARMONIE-AROME substantially improved on several aspects, especially wind speed (B17, de Rooy et al., 2010; de Rooy et al., 2017). On the other hand, together with updates of other parameterisations, HARATU contributed to the underestimation of low cloud cover and overestimation of cloud base height. Both output parameters are crucial for, e.g. aviation purposes, and eliminating these two specific shortcomings became a top priority in the HIRLAM consortium.

A full description of the turbulence scheme can be found in LH04 and B17 but for convenience here we introduce the components and parameters involved in the adjustments. In our turbulence scheme, the eddy diffusivity (see Eq. 4.4) is formulated as $K = l\sqrt{\mathrm{TKE}}$. The length-scale formulation in HARATU essentially consists of two length scales: one for (strongly) stable conditions, l_s, and one for weakly stable and unstable conditions, l_int. The latter, so-called integral length scale provides a "quadratic profile" for unstable conditions in the convective boundary layer and is also matched to surface similarity in near-neutral conditions. For more stable conditions, the common formulation,

$$l_\mathrm{s} = c_\mathrm{m,h}\frac{\sqrt{\mathrm{TKE}}}{N}, \tag{4.14}$$

is used, where $c_\mathrm{m,h}$ is a constant for momentum or heat, TKE is the turbulent kinetic energy, and N is the Brunt–Vaisala frequency.

To get the final length scale $l_\mathrm{m,h}$ for all stability regimes as applied in Eq. (4.4), we need to interpolate between the different length scales. The need for this arises because the different length scales do not match very well in the intermediate stability regimes; for example, the stable length scale approaches infinity for neutral stability. For this interpolation, the following ad hoc form is used:

$$\frac{1}{l_\mathrm{m,h}^\mathrm{p}} = \frac{1}{\left\{\sqrt{(l_\mathrm{int}^2 + l_\mathrm{min}^2)}\right\}^\mathrm{p}} + \frac{1}{l_\mathrm{s}^\mathrm{p}}, \tag{4.15}$$

where l_min is a minimum length scale:

$$\frac{1}{l_\mathrm{min}} = \frac{1}{l_\infty} + \frac{1}{0.5 c_\mathrm{n}\kappa z}, \tag{4.16}$$

with c_n is a constant and κ is the von Karman constant. Note that, close to the surface, the length scale is limited to half the neutral length scale, $c_\mathrm{n}\kappa z$. Equations (4.15) and (4.16) are needed to interpolate smoothly between the stable

length scale and the integral length scale near the surface and to provide a limit length scale for the free troposphere. We note that the square root term in Eq. (4.15) is in practice similar to taking the maximum of l_{int} and l_{min}, which is for instance needed to provide a background length scale for the free troposphere above the boundary layer where the integral length scale will be small or zero.

For most parameters in the length scale formulation, there is some theory that provides a reasonable range of values (LH04), but l_∞ is a tuning parameter and likewise the interpolation method is ad hoc based. In LH04, an inverse linear ($p = 1$) but also an inverse quadratic ($p = 2$) interpolation is discussed. In cy40REF, an inverse linear interpolation is used which suppresses mixing over a broad range of stability conditions. While the chosen form provides reasonably smooth transitions between the different stability regimes, results are sensitive to the interpolation and chosen constants, e.g. for l_∞, and this will be investigated in Sect. 4.3.2. Although the appropriate value for l_∞ is uncertain, this parameter significantly influences the entrainment flux and hence the preservation of the inversion at the top of the boundary layer (Sect. 4.3.4). The role of l_{min} resembles that of the free tropospheric length scale mentioned by Bechtold et al., 2008 and Köhler et al., 2011, who demonstrate the impact on inversion strength and consequently erosion of stratocumulus.

The last aspect of the turbulence scheme we discuss concerns the subcloud cloud interaction. The mass flux contribution to the total vertical transport results in a stable stratification in the upper part of the subcloud layer. Consequently, mixing by the TKE scheme will be strongly diminished in this area. These feedbacks between the mass flux and the turbulence scheme generally lead to an unrealistically strong inversion at cloud base. In many mass flux schemes, this runaway process is prevented by numerical diffusion which is dependent on the vertical resolution, and results of these schemes therefore tend to break down at very high resolution (Lenderink et al., 2004). For this reason, an ad hoc additional diffusion with constant $50 \cdot M_{\text{moist}}$ was added in cy40REF. In cy40NEW, we replaced this term with a more physically based energy cascade term.

Let us briefly discuss the underlying ideas of the energy cascade term. Its formulation is inspired by the prognostic equation of the mass flux vertical velocity variance (de Roode et al., 2000, Eq. 2.12 for w):

$$\begin{aligned} \frac{\partial a_{\text{u}}(1-a_{\text{u}})(w_{\text{u}}-w_{\text{env}})^2}{\partial t} &= -2M_{\text{u}}(w_{\text{u}}-w_{\text{env}})\frac{\partial \overline{w}}{\partial z} \\ -\frac{\partial (1-2a_{\text{u}})M_{\text{u}}(w_{\text{u}}-w_{\text{env}})^2}{\partial z} &- (\varepsilon+\delta)M_{\text{u}}(w_{\text{u}}-w_{\text{env}})^2 \\ +2a_{\text{u}}(1-a_{\text{u}})(w_{\text{u}}-w_{\text{env}})&(S_{\text{w}_{\text{u}}}-S_{\text{w}_{\text{env}}}) \end{aligned} \tag{4.17}$$

Here, S represents source terms and w_{env} is the vertical velocity of the up-

draft environment. Since for convective clouds $\|w_{\rm env}\| \ll w_{\rm u}$, $w_{\rm env}$ is, as usually, neglected. The left-hand side (LHS) of Eq. (4.17) represents the change of the organised (or updraft) vertical kinetic energy. The third term on the right-hand side (RHS), representing the impact of lateral mixing, is always a negative or sink term and can be related to the energy cascade from organised to smaller-scale eddies. We apply this term as a source in the TKE budget equation. However, considering the increased complexity of having two updraft types and to prevent too-high TKE values in the subcloud layer, we implemented the energy cascade term in an ad hoc simplified form:

$$W_{\rm casc} = W_{\rm casc,dry} + W_{\rm casc,moist} = c\varepsilon_{\rm dry} w_{\rm u,dry}^2 M_{\rm dry} + F w_{\rm u,moist}^2 M_{\rm moist}, \tag{4.18}$$

with function F:

$$F = E_\ell \left(\frac{z}{z_{\rm i}}\right)\left(\frac{1}{1+(\frac{z_{\rm i}-z}{Z_{\rm wl}})^2}\right) + E_{\rm t}\left(\frac{1}{1+(\frac{z_{\rm top}-z}{Z_{\rm wt}})^2}\right). \tag{4.19}$$

Here, $c = 0.5$, $Z_{\rm wl}$ =200 m, $Z_{\rm wt}$ =400 m. Further, E_ℓ =0.002 m^{-1} is a typical ε value near cloud base (consistent with Eqs. 4.10 and 4.11), and $E_{\rm t}$ =0.002 m^{-1} corresponds to a similar peak at the level of neutral buoyancy but this time associated with detrainment in the upper part of the cloud layer. Figure 4.4 shows a typical profile of Eq. (4.19). By ignoring the detrainment term in the dry updraft contribution (Eq. 4.18) and applying function F (Eq. 4.19) for the moist updraft, too-large TKE values in the lower part of the boundary layer are prevented, whereas the contribution to TKE near cloud base and in the upper part of the cloud layer is supported.

Next to the usual dissipation, transport, buoyancies and shear terms, $W_{\rm casc}$ is added as a source term in the TKE budget equation. LES results in Sect. 4.3.1 substantiate the need for the energy cascade term and demonstrate the improved turbulent transport in cy40NEW due to the inclusion of the energy cascade term.

4.2.4. STATISTICAL CLOUD SCHEME

Accurate predictions of clouds, liquid water, and ice are important because they have a large impact on radiation and therewith on several components of the model. This applies in particular to low boundary layer clouds such as stratocumulus and cumulus. In HARMONIE-AROME, high (ice) clouds are parameterised separately in a relative humidity scheme (B17) and are outside the scope of this chapter. The here-presented derivations, ideas, and modifications concerning parameterisation of low clouds in HARMONIE-AROME are valuable for statistical cloud schemes in general.

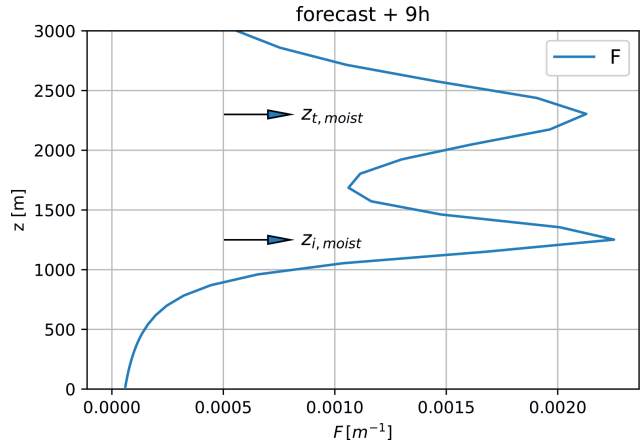

Figure 4.4: Profile of F (Eq. 4.19) at the ninth simulation hour of the ARM case (Sect. 4.3.1) with cy40NEW.

The concept of parameterising clouds with a statistical cloud scheme was already pioneered by Sommeria and Deardorff, 1977 and Mellor, 1977 and makes use of the fact that cloud cover and liquid water content can be easily derived once subgrid variability of moisture and temperature is known. This concept has been further developed by Bougeault, 1981 by assuming specific analytical forms of the joint probability density functions (PDFs) of total water specific humidity q_t and liquid water potential temperature θ_ℓ, which are the relevant thermodynamic moist conserved variables. From several successive papers (Bechtold et al., 1995; Bechtold & Siebesma, 1998; Cuijpers & Bechtold, 1995), it became clear that it is sufficient to have reliable estimates of only the grid box variances of q_t and θ_ℓ without making explicit assumptions on the shape of the underlying PDF. In statistical cloud schemes, relevant information on q_t and θ_ℓ is captured in one variable called s, distance to the saturation curve, $s \equiv q_t - q_s$ with q_s being the saturation specific humidity. If we non-dimensionalise s by its standard deviation σ_s, $t \equiv s/\sigma_s$, and presume a Gaussian PDF for t, the cloud fraction and liquid or ice water content can be written as a function depending only on the mean value of t:

$$\overline{t} = (\overline{q}_t - \overline{q}_s)/\sigma_s. \tag{4.20}$$

Because $\overline{q}_t - \overline{q}_s$ is readily available in a model, the cloud parameterisation problem is simply reduced to estimating σ_s.

The base of statistical cloud schemes is an expression of variance in s in terms of variances and covariance of q_t and θ_ℓ. Although the exact notation might be different, this expression should be the same for all schemes because the derivation is based on fundamental thermodynamics. Nevertheless, erroneous solu-

tions can be found in the literature as well as in cy40REF. Therefore, we provide a step-by-step derivation of the variance in s in Appendix 4.5.1, which finally results in the following expression:

$$\sigma_s^2 = \overline{s'^2} = \alpha^2 \overline{q_t'^2} - 2\alpha^2\beta\overline{q_t'\theta_\ell'} + \alpha^2\beta^2\overline{\theta_\ell'^2}, \tag{4.21}$$

with

$$\alpha = \frac{1}{1 + \frac{L}{c_p} q_{sl,T}}, \beta = \pi q_{sl,T} \tag{4.22}$$

$$\overline{q}_{sl,T} = \frac{\partial q_s(\overline{T}_\ell)}{\partial T}, \tag{4.23}$$

using the definition of the liquid water temperature:

$$T_\ell \equiv T - \frac{L}{c_p} q_\ell, \tag{4.24}$$

and where L is the latent heat of vaporisation and c_p the heat capacity of dry air at constant pressure, and π is the Exner function, defined as $\pi = (\frac{p}{p_0})^{\frac{R_d}{c_p}} = \frac{T}{\theta}$, in which R_d is the gas constant of dry air and p_0 a reference surface pressure.

In the literature, several approaches exist to estimate σ_s (e.g. Bechtold et al., 1995; Golaz et al., 2002). Here, we provide a full description of our estimate in which we include the contribution to the variance by turbulence and convection as well as an additional term to cover other sources of variance.

If we neglect advection, precipitation, and radiation terms, the budget equations for (co)variances are (see, e.g. Stull, 1988)

$$\frac{\partial \overline{a'b'}}{\partial t} = -\frac{\partial \overline{w'a'b'}}{\partial z} - \left[\overline{w'a'}\frac{\partial \overline{b}}{\partial z} + \overline{w'b'}\frac{\partial \overline{a}}{\partial z} \right] - \epsilon_{ab}, \tag{4.25}$$

where $a, b \in \{\theta_\ell, q_t\}$. The first term on the RHS of Eq. (4.25) is the transport term, the second and third terms represent the impact of the turbulent fluxes, and the last term covers dissipation. According to Bechtold et al., 1992, the transport term can be neglected during conditions with substantial cloud cover. The dissipation term, ϵ_{ab}, is modelled by a Newtonian relaxation back to isotropy:

$$\epsilon_{ab} = \epsilon_{ab,turb} + \epsilon_{ab,conv} = c_{ab}\left(\frac{\overline{a'b'}^{turb}}{\tau_{turb}}\right) + c_{ab}\left(\frac{\overline{a'b'}^{conv}}{\tau_{conv}}\right), \tag{4.26}$$

where c_{ab} is a constant and τ is a timescale for dissipation of turbulence (turb) or convection (conv). It is not clear if c_{ab} should be different for turbulence and

convection. Moreover, a large variation in its value can be found in the literature (see, e.g. Bechtold et al., 1992; Redelsperger and Sommeria, 1981). For turbulence, τ can be approximated by

$$\tau_{\text{turb}} = \frac{l_\epsilon}{\sqrt{\text{TKE}}}, \tag{4.27}$$

where $l_\epsilon = l_\text{m} c_0^2$ is the dissipation length scale with $c_0 = 3.75$ (see LH04, and consistent with the turbulence scheme). In cy40REF, however, $l_\epsilon = l_\text{m}$ (discussed in Sect. 4.5.2). The timescale for convection can be related to the cloud depth divided by a typical cumulus updraft velocity (Lenderink & Siebesma, 2000). However, for simplicity, we adopt the approach of Soares et al., 2004 taking $\tau_{\text{conv}} =$ 600 s.

Similar to dissipation, the turbulent fluxes in Eq. (4.25) consist of diffusive transport covered by the turbulence scheme:

$$\overline{w'a'} = -K\frac{\partial \overline{a}}{\partial z} = -l_{\text{m,h}}\sqrt{\text{TKE}}\frac{\partial \overline{a}}{\partial z}, \tag{4.28}$$

where all stability factors are included in length scale $l_{\text{m,h}}$ (LH04), and convective transport by the mass flux scheme:

$$\overline{w'a'} = M_\text{u}(a_u - \overline{a}). \tag{4.29}$$

As mentioned above, we neglect the transport term in Eq. (4.25) and assume a steady state, i.e. the LHS of Eq. (4.25), is 0. This means that production and dissipation of (co)variances are in balance. Note that the steady-state assumption is, at least for convection, debatable because the timescale for dissipation of convection is an order of magnitude larger than the typical time step of our model. On the other hand, cloud fractions for shallow, unresolved convection are usually small. Because we consider contributions of both turbulence and convection to the variance, we assume a balance between production and dissipation for both processes separately. Substituting Eqs. (4.26), (4.28), (4.29), τ_{turb}, and τ_{conv} in Eq. (4.25), including the assumptions mentioned above, leads to the following expressions:

$$\overline{a'b'}^{\text{turb}} = 2\frac{l_{\text{m,h}} l_\epsilon}{c_{\text{ab}}}\frac{\partial \overline{a}}{\partial z}\frac{\partial \overline{b}}{\partial z} \tag{4.30}$$

$$\overline{a'b'}^{\text{conv}} = \frac{-\tau_{\text{conv}}}{c_{\text{ab}}}\left(M_\text{u}(a_\text{u} - \overline{a})\frac{\partial \overline{b}}{\partial z} + M_\text{u}(b_\text{u} - \overline{b})\frac{\partial \overline{a}}{\partial z}\right). \tag{4.31}$$

So, for example, total variance in θ_ℓ due to turbulence and convection reads

$$\overline{\theta_\ell'^2} = 2\frac{l_\text{h} l_\epsilon}{c_{\text{ab}}}\left(\frac{\partial \overline{\theta_\ell}}{\partial z}\right)^2 - \frac{2\tau_{\text{conv}}}{c_{\text{ab}}}\left(M_\text{u}(\theta_{\text{l,up}} - \overline{\theta_\ell})\frac{\partial \overline{\theta_\ell}}{\partial z}\right). \tag{4.32}$$

Note that both turbulence and convection have a positive contribution to variance.

In the absence of convection and no noticeable amount of turbulent activity, variance will still be non-zero. In nature, other sources of variance exist like surface heterogeneity, horizontal large-scale advection, mesoscale circulations, and gravity waves. Instead of imposing a minimum value to variance to cover these sources, we apply an extra variance term with the characteristics of a relative humidity scheme. This additional term was already introduced in de Rooy et al., 2010, demonstrating its beneficial impact, and has been included in the HARMONIE-AROME reference code since cycle 36. Here, a more elaborate description of the additional variance term is given.

Let us assume a statistical cloud scheme with a uniform distribution of a fixed width 2Δ. Tompkins, 2005 shows that such a statistical cloud scheme can be considered a RH scheme with

$$\Delta = (1 - \mathrm{RH}_{\mathrm{crit}})\, q_{\mathrm{s}}, \tag{4.33}$$

with $\mathrm{RH}_{\mathrm{crit}}$ representing the relative humidity where cloud fraction starts to be non-zero. The corresponding cloud fraction reads

$$a_{\mathrm{c}} = 1 - \sqrt{\frac{1 - \mathrm{RH}}{1 - \mathrm{RH}_{\mathrm{crit}}}}. \tag{4.34}$$

The variance of such a uniform distribution is

$$\sigma_{q_{\mathrm{t}}}^2 = \frac{1}{3}\Delta^2. \tag{4.35}$$

Tompkins, 2005 and Quaas, 2012 demonstrated that a RH scheme as well a statistical cloud scheme with a fixed width distribution could be written purely in terms of specific humidity fluctuations; i.e. Eq. (4.21) reduces to

$$\sigma_{\mathrm{s}}^2 = \overline{s'^2} = \alpha^2 \overline{q_{\mathrm{t}}'^2} = \alpha^2 \sigma_{\mathrm{qt}}^2. \tag{4.36}$$

The combination of Eqs. (4.33), (4.35), and (4.36) leads to the following expression for $\mathrm{RH}_{\mathrm{crit}}$:

$$\mathrm{RH}_{\mathrm{crit}} = 1 - \frac{\sqrt{3}}{\alpha}\left(\frac{\sigma_{\mathrm{s}}}{q_{\mathrm{s}}}\right). \tag{4.37}$$

In HARMONIE-AROME, we introduced the additional standard deviation term:

$$\sigma_{\mathrm{s,extra}} = c\alpha q_{\mathrm{s}}. \tag{4.38}$$

With $c = 0.02$, this leads to a constant $RH_{crit} = 96\,\%$ (Eq. 4.37). Note that due to pre-factor α in Eq. (4.38), RH_{crit} becomes independent of α. For typical atmospheric conditions, $\alpha \simeq 0.4$ in the boundary layer, while higher up in the atmosphere α will asymptote towards unity. Therefore, without pre-factor α in Eq. (4.38), RH_{crit} would vary from $\simeq 91\,\%$ in the boundary layer to $\simeq 96\,\%$ in the upper atmosphere. However, sources of variance, not related to turbulence or convection, are particularly found higher up in the atmosphere (see, e.g. Quaas, 2012) and are, e.g. related to advection of long-lived cirrus clouds into the model grid box. Therefore, RH_{crit} should at least not increase with height. More investigation is needed to optimise the (height-dependent) formulation of the additional variance term. The total variance in s is the sum of the contributions from turbulence, convection, and Eq. (4.38).

From the description above and Appendix 4.5.2, it becomes clear that a statistical cloud scheme contains many uncertain terms and constants. We do not claim that our choices are all optimal. However, in comparison with the original scheme, the new setup is at least built upon a correct derivation of the thermodynamical framework. This is, e.g. important for the formulation of thermodynamic coefficients (Eq. 4.22). Therefore, we believe the new setup is more suitable as a starting point for further improvements. Some suggestions to do so are discussed in Sect. 4.3.1.

4.3. ARGUMENTATION AND EVALUATION OF MODEL UPDATES

This chapter describes a large variety of modifications to the current reference cloud, turbulence, and convection parameterisations. Argumentation of these adjustments is diverse. For example, part of the changes to the cloud and turbulence scheme have a theoretical basis, namely thermodynamics and surface layer similarity, respectively. Other modifications are substantiated by an in-depth comparison of 1-D model results with LES for several idealised intercomparison cases. Lastly, optimisation of some more uncertain model parameters is based upon evaluation of full 3-D model runs. Considering the large number of modifications and mutual influences, it is impossible to discuss the separate and incremental impact of them all. Instead, we focus on the performance of two HARMONIE-AROME configurations: firstly, the reference HARMONIE-AROME setup as described in B17, cy40REF, and, secondly, the new configuration, cy40NEW, as proposed in this chapter. Nevertheless, all adjustments are substantiated and the isolated impact of several of them is demonstrated. An overview of all modifications is presented in Table D1 in Appendix 4.5.5.

Many of the proposed adaptations are the result of a comparison of 1-D model with LES results as obtained with the DALES model (Heus et al., 2010). For an accurate comparison between LES and HARMONIE-AROME at the current model

resolution, LES results are diagnosed as the mean over HARMONIE-sized subdomains. In the ARM shallow cumulus case, for example, the turbulent transport in LES is the mean turbulent transport diagnosed in 100 subdomains of $2.5 \times 2.5\text{km}^2$, the current operational resolution of HARMONIE-AROME. However, differences between the mean over HARMONIE-sized subdomains and the mean across the full LES domain are generally small. We start in Sect. 4.3.1 with an elaborated comparison of 1-D model with LES results for the ARM case. This investigation involves many components of the parameterisations and several modifications are based on the ARM case. By making use of Monin–Obukhov theory (following Baas et al., 2017), important changes to the turbulence scheme are substantiated in Sect. 4.3.2. This section also shows the performance under moderately stable conditions in the GABLS1 case (Beare & M.K. Macvean, 2006). Section 4.3.3 mainly demonstrates the impact of the modifications on three stratocumulus cases. Finally, long-term and case-based verification with the 3-D model is presented in Sect. 4.3.4. This section demonstrates the large improvement with the updates in cy40NEW on low clouds but also elucidates the beneficial impact on precipitation.

4.3.1. ARM CASE

The ARM case (Brown et al., 2002), based on observations, describes a diurnal cycle of shallow convection above land: initiation of moist convection, gradual deepening of the cloudy layer, and finally collapse of the cumulus cloud layer. Such a dynamical case poses higher demands to convection parameterisation than, e.g. the steady-state Barbados Oceanographic and Meteorological Experiment (BOMEX) case over the sea (Holland & Rasmusson, 1973) and is therefore more suitable for optimisation purposes. To make optimal use of the dynamical character of the ARM case and to avoid a possible focus on the best results, we present results of all hours during the moist convective period (simulations from +4 to +12 h). The SCM runs for ARM use 79 vertical levels with the lowest model level at approximately 10 m.

ARM: MASS FLUX AND TOTAL TURBULENT TRANSPORT

With the current operational resolution of HARMONIE-AROME, turbulent transport in the ARM case is fully unresolved and is presented as the sum of parameterised convective and diffusive turbulent transport. In LES, however, shallow convection and the bulk part of the diffusive transport is resolved. By sampling LES data in the cloud layer, we can estimate that part of the total turbulent transport that should be described by a convection scheme. Although the convective transport by LES should be interpreted as a rather crude estimate, it is also the best available way to study the performance of our mass flux convection scheme

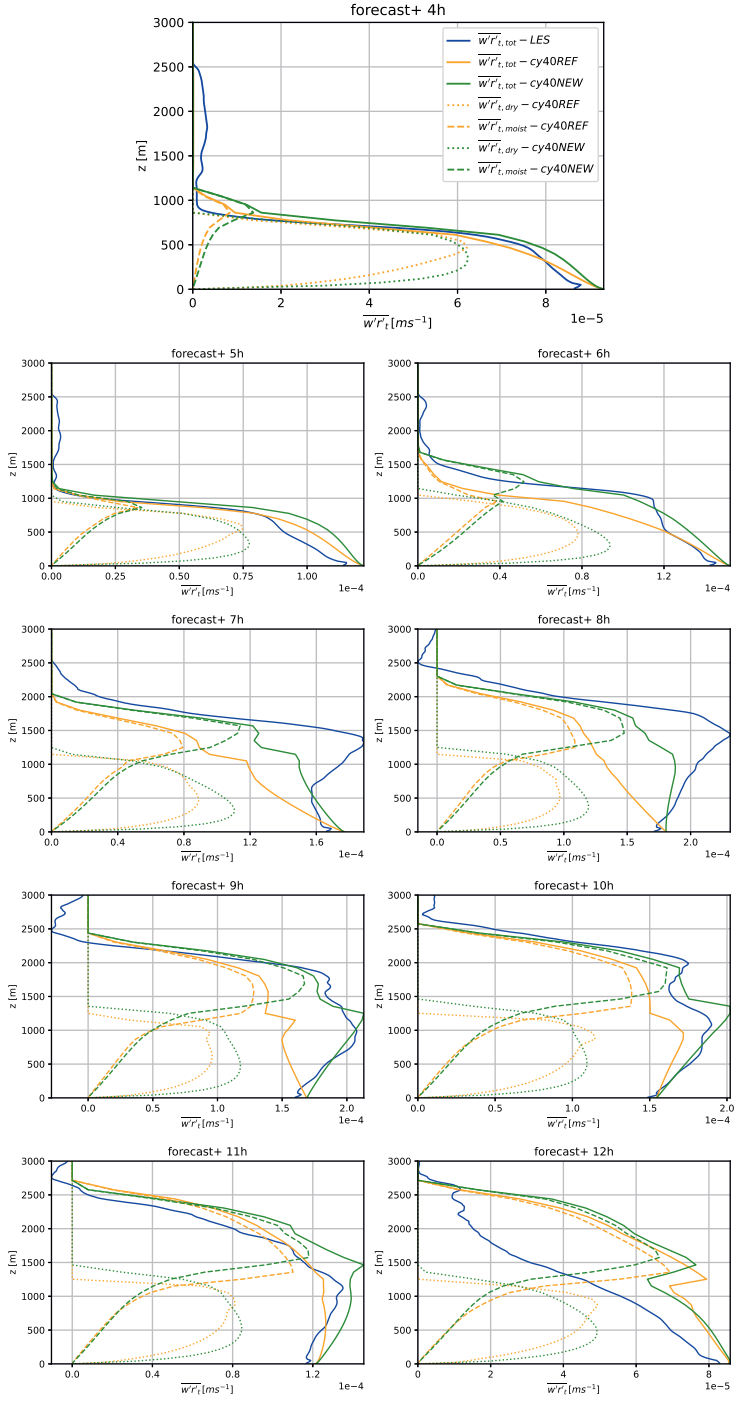

Figure 4.5: Total turbulent transport and transport by the dry and moist updraft (ms^{-1}) of the mixing ratio total humidity r_t during all convective hours of the ARM case, corresponding to simulation hours at +4 to +12 h. Plotted is total turbulent transport of cy40REF (orange solid line), cy40NEW (green solid line), and the total turbulent transport by the LES (blue). The dry updraft transport is shown as a dotted line (cy40REF in orange; cy40NEW in green). Similarly, the dashed lines show the transport by the moist updraft. Note that the x-axis scale is not constant. For readability of the legend, simulation hour +4 h is printed bigger.

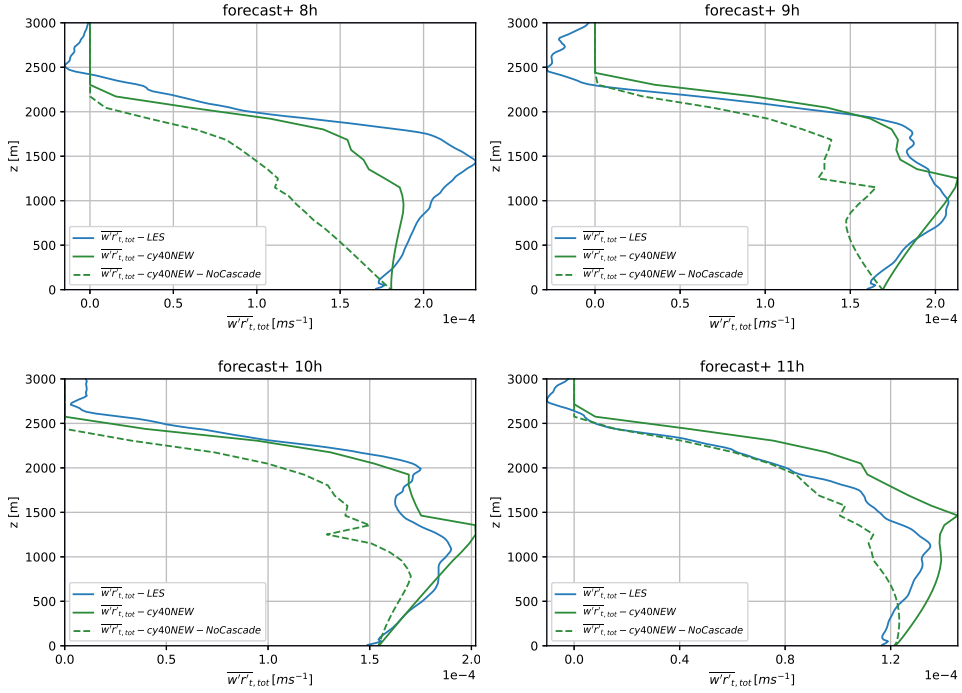

Figure 4.6: The kinematic total turbulent transport (ms^{-1}) during the last 4 h of the ARM convective period. Plotted is the transport according to LES (blue), cy40NEW (green), and cy40NEW but without energy cascade (green dashed). Note that the x-axis scale is not constant.

in the cloud layer. A detailed description of such an evaluation is provided in Appendix 4.5.3 and indicates that the convective transport in HARMONIE-AROME is underestimated in the first half of the convective period in the ARM case, but modifications to the convection scheme in cy40NEW result in a clear reduction of this underestimation (Appendix 4.5.3). Figure 4.6 further reveals that the energy cascade smoothens wiggles in turbulent transport around the inversion at cloud base. However, the ultimate goal of a convection and turbulence scheme is to provide an accurate estimate of the total turbulent transport. After all, the vertical divergence of the total turbulent transport determines the tendencies of the prognostic model variables. Whereas LES convective transport should be interpreted as an estimate, depending on the sampling method, LES total turbulent transport during the ARM case will be close to observed values. Besides, in contrast to convective transport, LES provides the total turbulent transport for the complete atmosphere, including the subcloud layer. Figure 4.5 shows the total turbulent transport of humidity by the model versions and LES, including the LES subgrid-scale parameterised contribution. Plots of heat transport provide

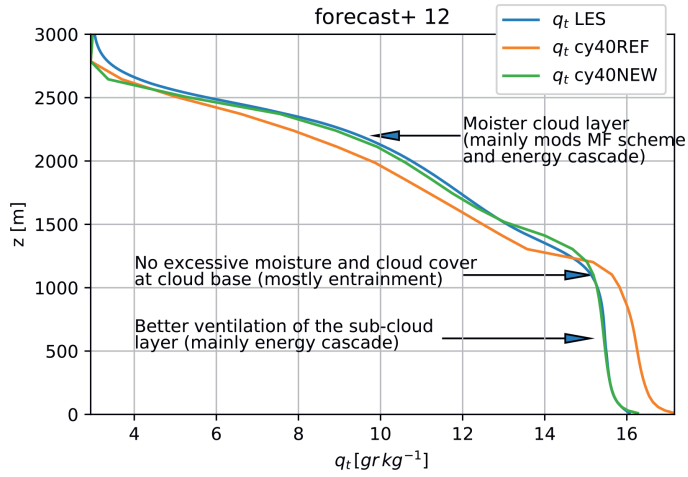

Figure 4.7: ARM case specific humidity profile after 12 h of simulation. These profiles can be seen as the accumulated impact of the total turbulent humidity transport during the ARM case.

a similar behaviour (not presented). In general, both model versions underestimate total turbulent transport but the new configuration results in a considerable improvement. Drying of the subcloud layer, i.e. increasing total turbulent transport with height, in the second half of the convective period is almost absent in the original configuration and better captured with cy40NEW. This improvement is mainly related to inclusion of the energy cascade (Eqs. 4.18 and 4.19) as demonstrated in Fig. 4.6.

Figure 4.7 shows the humidity profiles at the end of the convective period, therewith reflecting the accumulated impact of turbulent transport during the ARM case. There is a close agreement between the humidity profiles of Cy40NEW and LES, whereas the cy40REF run clearly leads to a too-moist subcloud and too-dry cloud layer. As discussed before, especially the more efficient subcloud-to-cloud transport in cy40NEW is responsible for the large improvement in the humidity profile.

A closer examination of Figs. 4.23 and 4.5 reveals something remarkable: if we compare LES organised cloudy updraft transport (Fig. 4.23) with LES total turbulent transport (Fig. 4.5) in the upper part of the cloud layer, it becomes clear that organised transport alone would overestimate total transport in this region. If we look, e.g. at the +10 h forecast, LES shows almost no total turbulent transport above 2500 m despite considerable convective transport. To investigate this, we decompose the total turbulent transport in LES. Following Siebesma and Cuijpers, 1995, total turbulent transport can be written as a sum of large-scale organised and small-scale subplume and environmental transport. In Appendix 4.5.4,

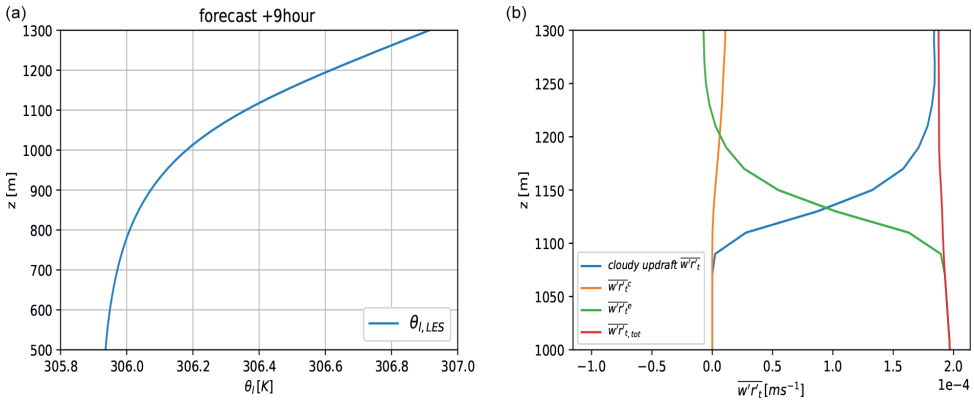

Figure 4.8: LES results around the cloud base inversion height for the ARM case at the ninth simulation hour. Panel **(a)** shows the θ_ℓ profile, whereas **(b)** presents a decomposition of the kinematic turbulent moisture fluxes (ms^{-1}). Plotted are LES cloudy updraft flux (blue), small-scale subplume transport (orange), small-scale environmental transport (green), and total transport (red). Note the different y-axis scale.

we elaborate on the nature of the turbulent transport in the upper part of the cloud layer by examining decomposed terms of the turbulent transport. This examination reveals that the rather good approximation of the total turbulent transport in the upper part of the cloud layer by the parameterisation seems to be the result of a compensation error in the ARM case; too-shallow mass flux transport is balanced by neglecting downward environmental turbulence (see Appendix 4.5.4).

Additionally, the decomposition is used to look specifically into the turbulent transport around the cloud base inversion height in relation to the energy cascade term (Eq. 4.18); see Fig. 4.8. As shown in Fig. 4.8a, the LES θ_ℓ profile around 1000 m height and after nine simulation hours is roughly the stable lapse rate (without phase changes) of the cloud layer. Considering this atmospheric stability, a standard turbulence scheme would provide little mixing at this level and higher. However, Fig. 4.8b reveals that the total turbulent transport is actually dominated by (small-scale) diffusive environmental turbulence up to considerably above the inversion height (in agreement with Fig. 7a and b in Siebesma and Cuijpers, 1995 for the BOMEX shallow convection case). A plausible explanation for the presence of diffusive transport despite the stable conditions is (dry) updrafts terminating around the inversion height, in this way feeding the energy cascade from larger to smaller scales. Figure 4.5 for the ninth hour confirms that the dry updraft turbulent transport decreases strongly between 1000 and 1300 m height. This roughly corresponds to the layer with substantial diffusive environmental turbulent transport in LES despite the strong inversion (Fig. 4.8). If we

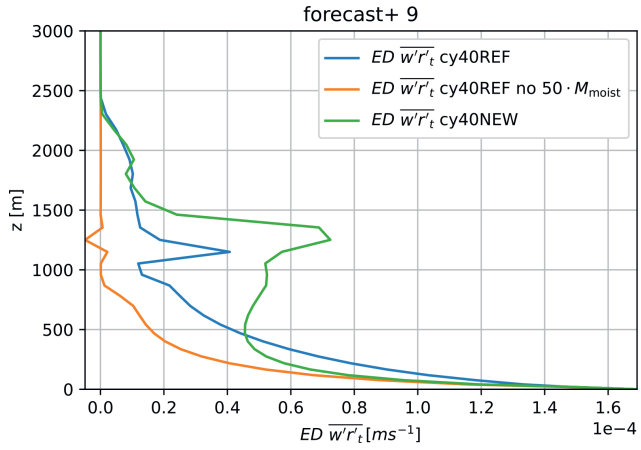

Figure 4.9: The eddy diffusivity (ED) turbulent moisture transport for ARM at the ninth simulation hour with three different model versions: cy40REF (blue), cy40REF but without $50 \cdot M_{\text{moist}}$ term (see Sect. 4.2.3) (orange), and cy40NEW (green).

compare the eddy diffusivity (ED) turbulent transport in the model versions, we see a clear increase from cy40REF without the $50 \cdot M_{\text{moist}}$ term (see Sect. 4.2.3), to cy40REF, to cy40NEW, which includes the energy cascade term (Fig. 4.9). In addition, organised entrainment at cloud base height (de Rooy & Siebesma, 2010) induced by acceleration of the moist updraft might further enhance small-scale environmental turbulence in this area. To describe the important contributions to the transport from subcloud-to-cloud layer as discussed above, the energy cascade term (Eq. 4.18) is added (Sect. 4.2.3).

Based on this shallow cumulus case, it is evident that the physical basis of our parameterisation is a strong simplification of reality. Moreover, the rather good approximation of the total turbulent transport during the ARM case is partly caused by a compensating error (Appendix 4.5.4). However, a realistic representation would require a substantial increase in complexity, introducing new uncertain, tuneable parameters. Moreover, the current set of parameterisations performs well on a wide variety of cases.

CLOUD COVER

A contour plot of cloud fraction during the ARM case (Fig. 4.10) reveals that cy40 NEW results in lower maximum cloud fraction (near cloud base) in better correspondence with LES. This is also reflected in reduced total cloud cover (Fig. 4.11). Figure 4.11 further reveals that observed maximum total cloud cover is higher than in LES and peaks earlier. Brown et al., 2002 argues that the difference in timing between model results and observations is caused by differences between the initial profiles as prescribed in the case setup and the observations.

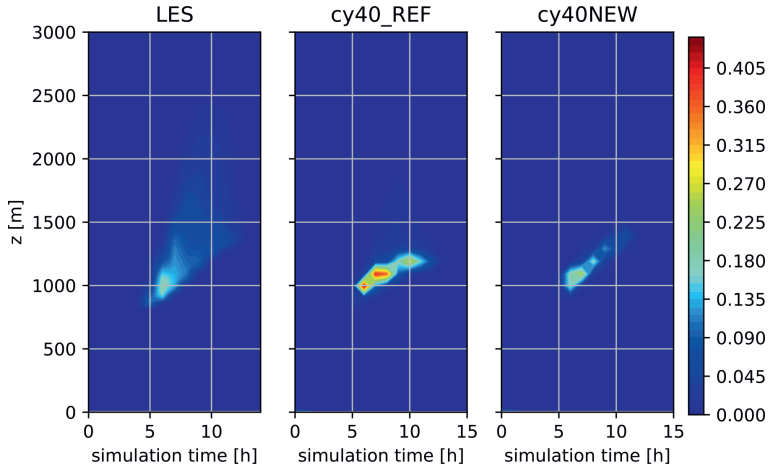

Figure 4.10: Contour plot of cloud fraction for the ARM case.

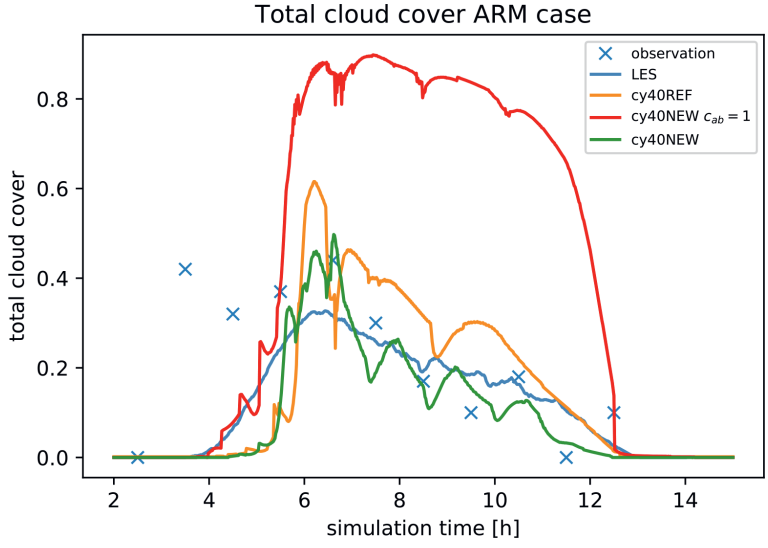

Figure 4.11: Total cloud cover for the ARM case. Plotted are observations (blue crosses), LES (blue), cy40REF (orange), cy40NEW with $c_{\mathrm{ab}} = 1$ (red; see Eqs. 4.26, 4.30, 4.31), and cy40NEW (green).

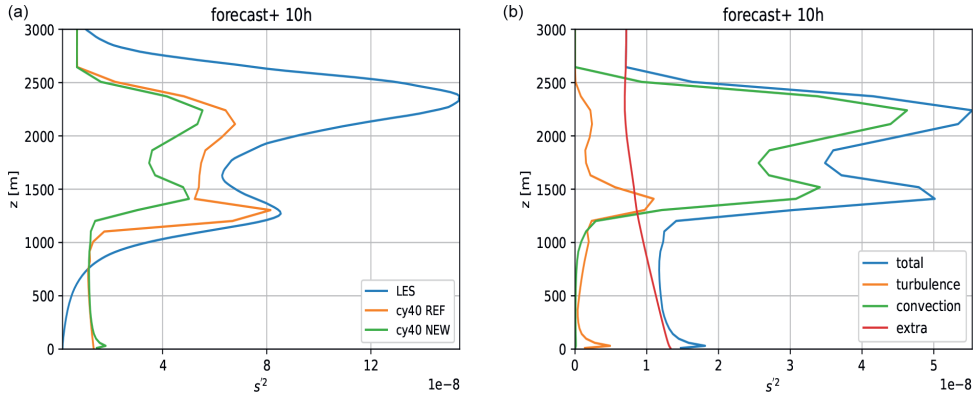

Figure 4.12: ARM case, 10th simulation hour. Panel **(a)** shows the profile of the variance in s in LES (blue), cy40REF (orange), and cy40NEW (green). Panel **(b)** shows the contribution of the turbulence (orange), convection (green), and the extra term (red) in Eq. (4.38) to the variance in s for cy40NEW.

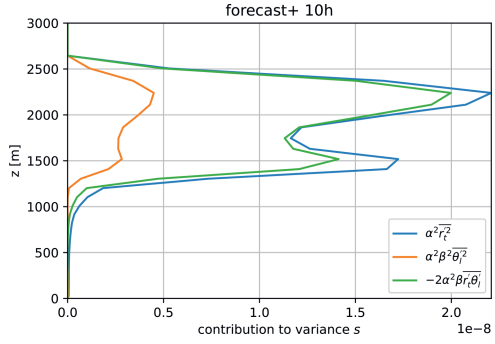

Figure 4.13: ARM case, 10th simulation hour. The convective contribution to the variance in s of cy40NEW from the variance in θ_ℓ (orange), total mixing ratio r_t (blue), and the covariance (green); see Eq. (4.21).

Observed differences in cloud fraction and cover between cy40REF and cy40NEW (Figs. 4.10 and 4.11, respectively) are the accumulated result of several modifications:

- As illustrated in Figs. 4.6 and 4.7, the reference configuration underestimates ventilation of the boundary layer leading to too-high humidity values near cloud base and therefore too-high maximum cloud fraction values. Especially the energy cascade (Eq. 4.18) is responsible for the enhanced ventilation (Sect. 4.3.1).

- Humidity near cloud base is also influenced by the dry updraft. In the reference formulation, Eq. (4.9) with $a_2 = 40$, entrainment, and therewith dilution of the updraft, remains rather small approaching the inversion. When this dry updraft finally terminates, relatively high amounts of moisture are detrained in the environment in cy40REF. With $a_2 = 1\,\mathrm{m}$, as in cy40NEW, this effect is mitigated.

- Another contribution to the different results stems from the removal of bugs in the reference cloud scheme. Most notable are erroneous thermodynamic coefficient β in Tudor and Mallardel, 2004 and double application of a factor of 2 on the contribution to the variance by convection (Appendix 4.5.2). Especially the latter bug in cy40REF leads to a substantial increase in variance and accordingly to higher cloud fraction at cloud base.

- The largest impact is related to the choice of parameter c_{ab} (Sect. 4.2.4 Eq. 4.26 and Appendix 4.5.2). If $c_{\mathrm{ab}} = 1$ from cy40REF would be applied in the new configuration, the variance, and with it the cloud cover, would be substantially overestimated as demonstrated in Fig. 4.11. Only in cy40NEW is c_{ab} in line with literature (Redelsperger & Sommeria, 1981), i.e. 0.139.

Apart from the (too)-high cloud fractions at cloud base, also the underestimation of low values of cloud fraction in the upper part of the cloud layer by both model versions stands out in Fig. 4.10. Because the humidity (see Fig. 4.7) and temperature (not shown) profiles of cy40NEW closely match LES, the underestimation of cloud fraction in the upper part of the cloud layer must be related to an underestimation of variance in s. Figure 4.12a (for a typical hour) indeed reveals that both model versions underestimate the variance in s in the cloud layer, although cy40REF values are closer to LES. While the new configuration generally improves the shape of the variance profile, the local maximum near cloud top should be more pronounced. Note that inclusion of the convective covariance term, $\overline{r_{\mathrm{t}}'\theta_{\ell}'}$, helps to increase the local maximum near cloud top (Fig. 4.13).

Figure 4.12b clearly demonstrates that the contribution of convection to the variance in s is essential to adequately describe the shape of the variance profile in the cloud layer, especially the maximum near cloud top. Furthermore, it was decided not to include the contribution of the dry updraft to variance. First of all, together with the extra variance term (Sect. 4.2.4, Eq. 4.38, Fig. 4.12b), variance in the lower half of the subcloud layer would be too high. Moreover, with fluctuations in the termination level of the dry updraft, cloud cover near cloud base height changes, which can lead to noisy cloud cover patterns (not shown).

Although the cloud scheme of cy40NEW already performs satisfactorily for a wide variety of weather conditions, there are clearly several options for further optimisation. Examples of possible improvement are the introduction of a height dependence of the extra variance term, partial replacement of the extra variance term by a dry updraft contribution in the subcloud layer, increasing τ_{conv} (Eq. 4.31) because the current value (Soares et al., 2004) seems to be on the low side (compare to, e.g. Siebesma et al., 2003), or modifying the energy cascade function (Eq. 4.19) to increase the local maximum around cloud top. An alternative way to address the underestimation of low cloud fraction values in the upper part of the cloud layer is the use of a skewed PDF (see, e.g. Bougeault, 1981), but this is not investigated here. Nevertheless, with a more sound physical basis and the removal of bugs, the new cloud scheme setup is already better suited as a base for such new developments.

4.3.2. OPTIMISING THE TURBULENCE SCHEME

Two important modifications in the turbulence scheme are based on an evaluation procedure as described by Baas et al., 2008 and Baas et al., 2017. They demonstrated that a comparison of the dimensionless gradients of heat, ϕ_{h}, and momentum, ϕ_{m}, versus the stability parameter, $\frac{z}{\Lambda}$ (Eq. 4.39), enables a more physically based choice of turbulence parameter settings for stable conditions.

$$\frac{z}{\Lambda} = \frac{-\kappa z \frac{g}{\theta_{\text{v}}} \overline{w'\theta'_{\text{v}}}}{u_*^3}, \tag{4.39}$$

where Λ is the local Obukhov length and u_* is the friction velocity. According to similarity theory there should be a universal relation between the dimensionless gradients and the stability parameter, although the uncertainty in these relations increases for stronger stratification, i.e. larger $\frac{z}{\Lambda}$ values. To investigate the mixing characteristics of our turbulence scheme in terms of the similarity relations, a SCM of HARMONIE-AROME is run for 1 year at the location of super-observation site Cabauw (Bosveld et al., 2020). The SCM is forced by output from daily three-dimensional forecasts of RACMO (van Meijgaard et al., 2008). The host model provides the advection and the initialisation of the surface. Every

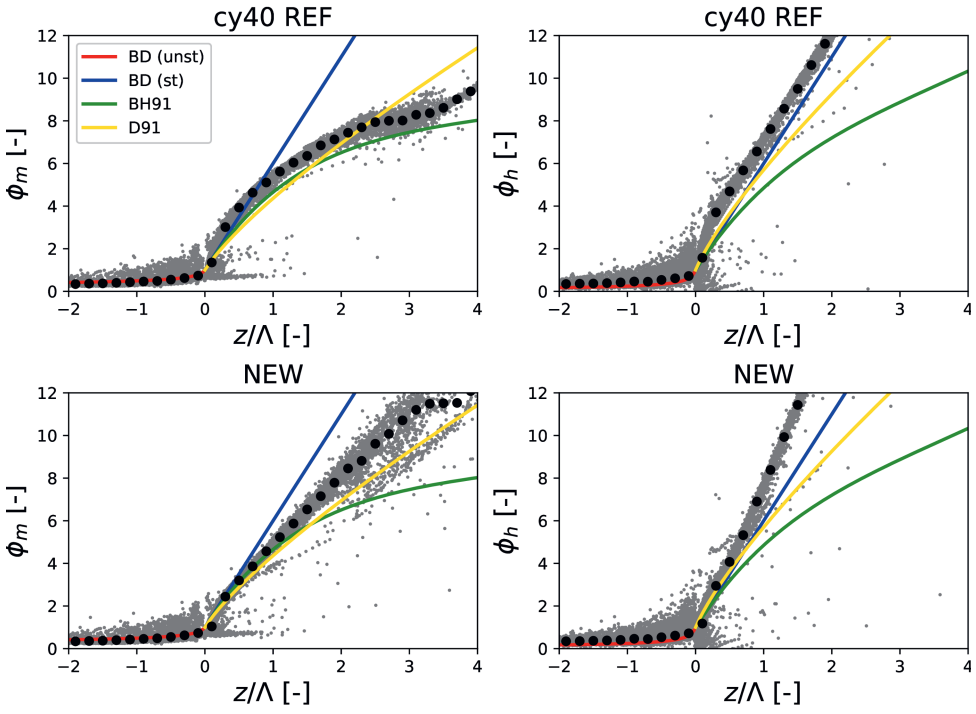

Figure 4.14: Dimensionless gradients of wind **(a, c)** and temperature **(b, d)** as a function of the local stability parameter $\frac{z}{\Lambda}$ as diagnosed from 1 year of SCM output (grey dots). Panels **(a, b)** and **(c, d)** show the results for cy40REF and cy40NEW, respectively. Black dots represent the mean of the modelled dimensionless gradients. Blue lines indicate $1+5\frac{z}{\Lambda}$ (Dyer, 1974); green lines (Beljaars & Holtslag, 1991) and yellow lines the relations proposed by Duynkerke, 1991. Explanations of the different formulations can be found in the text. For completeness, Dyer, 1974 formulations for unstable conditions are plotted (red line).

day at 12 : 00 UTC, the SCM produces a 72 h forecast with an interactive surface scheme. The SCM uses the same vertical resolution as the operational 3-D model, i.e. 65 layers with the lowest model level at approximately 12 m. Figure 4.14 shows the 1-year SCM output diagnosed in terms of flux–gradient relations for momentum and heat. We present results with default cy40REF settings; i.e. $p = 1$ (Eq. 4.15) and $c_\mathrm{h} = 0.15$ (Eq. 4.14) next to $p = 2$ and $c_\mathrm{h} = 0.11$ conform cy40NEW (see Sect. 4.2.3). Evaluation is restricted to stable boundary layer regimes, i.e. positive values of $\frac{z}{\Lambda}$. Apart from model results, also theoretical relations according to Dyer, 1974 in blue and Beljaars and Holtslag, 1991 (green) and Duynkerke, 1991 (yellow) are plotted. Many observational studies on flux–gradient relations report that for increasing stability the exchange of momentum is far more efficient than the exchange of heat, i.e. $\phi_\mathrm{h} > \phi_\mathrm{m}$ (see, e.g. Beljaars

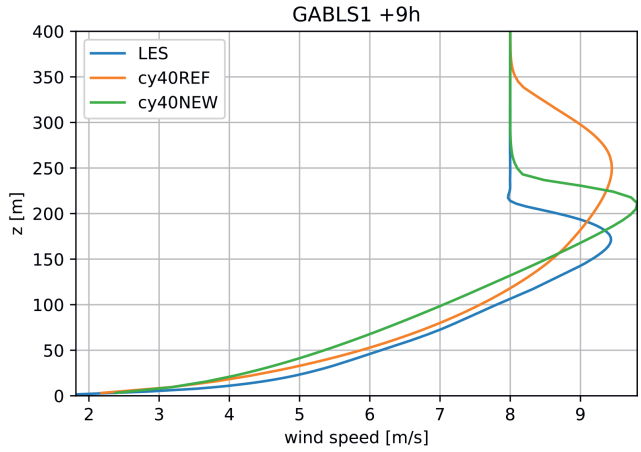

Figure 4.15: GABLS1 wind profile at the ninth simulation hour of LES model DALES (blue), cy40REF (orange), and cy40NEW (green). SCM runs use 64 levels with the lowest and highest model levels at 3 and 403 m, respectively. Note that results for GABLS1 with several LES models in Beare and M.K. Macvean, 2006 reveal a spread in the height of the wind maximum, ranging from 175 to 200 m. The latter height and the corresponding LES profile in Beare and M.K. Macvean, 2006 correspond well with cy40NEW.

and Holtslag, 1991). The relationship of Dyer, 1974 does not reflect this and we focus on the relations of Beljaars and Holtslag, 1991 and Duynkerke, 1991 that were both derived from Cabauw observations. The divergence between the latter two flux–gradient relations for increasing stability illustrates the uncertainty under very stable conditions (Baas et al., 2008). Therefore, most attention is paid to neutral to moderately stable regimes, roughly corresponding with $0 < \frac{z}{\Lambda} < 1$. Figure 4.14 shows that in this stability range, the reference setup underestimates mixing (overestimates the gradient) which can be related to linear interpolation between the length scales; i.e. $p = 1$. However, only changing interpolation to quadratic would lead to excessive mixing and unrealistic flux–gradient relations (not shown). This can be compensated by reducing the proportionality factor of the stable length scale, c_h to 0.11. The combined result of these changes is shown in Fig. 4.14, where the lower panels reveal a better correspondence with the flux–gradient relations in near-neutral to moderately stable conditions. For more stable conditions, agreement with theoretical relations seems to deteriorate with the new setup. However, as explained above, the flux–gradient relations become highly uncertain under these strongly stratified conditions. To explore the performance of the turbulence scheme in moderately stable conditions, cy40REF and cy40NEW are compared to LES for the GABLS1 case (Beare & M.K. Macvean, 2006), based on arctic observations. Although the change from $p = 1$ to $p = 2$ in the turbulence scheme (Sect. 4.2.3, Eq. 4.15) leads to increased mixing in near-

neutral to weakly stable conditions, most other modifications, that reduce mixing (see Sect. 4.2.3), dominate for more stable conditions (see also Fig. 4.14). Results for GABLS1 (Fig. 4.15), showing the wind speed profile after 9 h of simulation, indeed reveal more stable profiles and lower boundary layer heights with cy40NEW, in better correspondence with LES.

Due to increased mixing in near-neutral conditions with $p = 2$, the updates in HARATU to increase momentum mixing in strong wind conditions (see B17) are removed. Removing these updates together with the reduced c_h coefficient, overall decreases mixing at higher altitudes and therewith atmospheric inversions are better preserved. A similar impact stems from the last modification to the turbulence scheme we describe, decreasing the limiter on the minimum length scale, l_∞, from 100 to 40 (Sect. 4.2.3, Eq. 4.16). The exact value of l_∞ is highly uncertain, but also this parameter, active at higher altitudes, influences atmospheric inversion strengths. As demonstrated in the next sections, many of the improvements with cy40NEW arise from a more realistic representation of atmospheric inversions. In the next two sections, we demonstrate the impact of the modifications on low clouds and low cloud base heights.

4.3.3. STRATOCUMULUS-TO-CUMULUS TRANSITION CASES

Figures 4.16, 4.17, and 4.18 show the results of three stratocumulus cases (see de Roode et al., 2016; Neggers et al., 2017). Whereas ASTEX is based on observations, the slow and fast cases are composite, idealised cases. LES results are obtained with DALES (de Roode et al., 2016). SCM runs are performed with 80 vertical layers (slightly higher resolution than operational), with the lowest layer at approximately 10 m. SCM results for ASTEX are rather comparable, although the new setup shows a slightly thicker and less rising cloud layer, less in agreement with LES. Note that the lower vertical resolution in SCMs compared to LES will usually lead to a more gradually rising cloud layer (Neggers et al., 2017). The slow and fast cases (differentiated by the speed of the low-level cloud transition), however, illustrate the trouble of cy40REF to maintain a stratocumulus layer, consistent with the strong underestimation of low clouds we see in operational practice. The improved results with the new setup are related to the accumulated effect of several modifications. As a result of a more efficient moisture transport towards the inversion in combination with a decreased transport through the inversion (better preservation of the inversion strength), more moisture is accumulated beneath the inversion, visible as a continuous and rising stratocumulus layer in the cy40NEW runs (Figs. 4.17 and 4.18).

There is one specific difference between the model versions we need to mention concerning the slow case. In the results for this case, only a moist updraft (see right panel of Fig. 4 in B17) was invoked in cy40REF because the bulk dif-

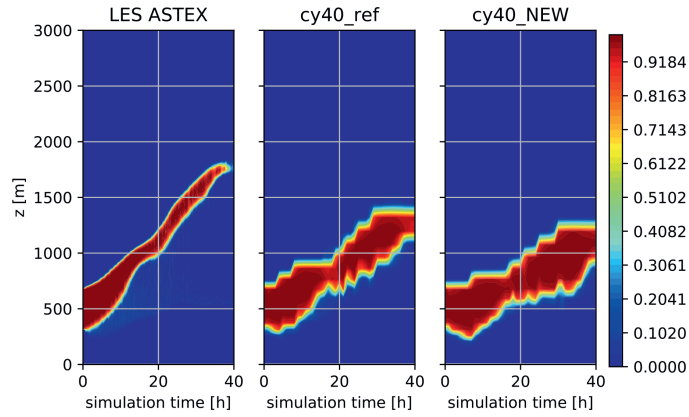

Figure 4.16: Cloud cover ASTEX case of LES (left panel), cy40REF (middle panel), and cy40NEW (right panel).

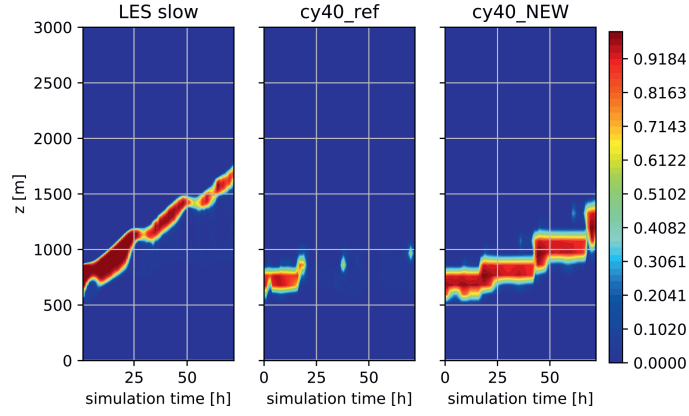

Figure 4.17: As Fig. 4.16 but for the slow case.

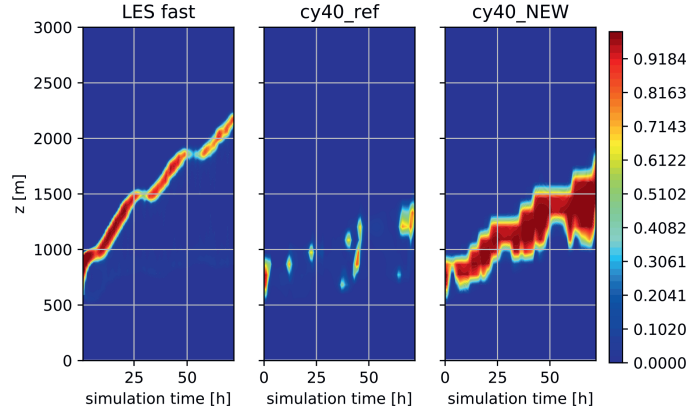

Figure 4.18: As Fig. 4.16 but for the fast case.

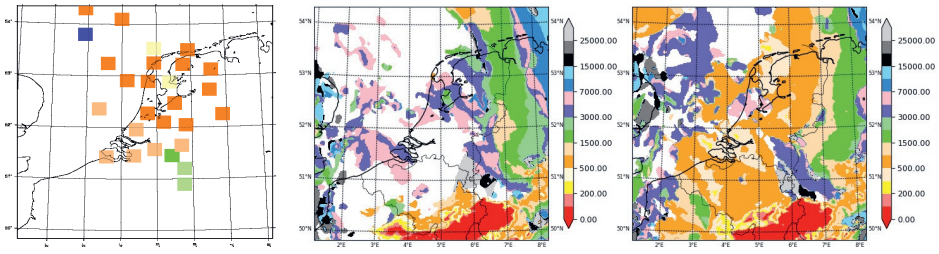

Figure 4.19: Cloud base height in feet (1 ft is 0.3048 m) on 19 December 2018 at 09:00 UTC as measured at discrete observation site locations in the Netherlands and part of the North Sea (left panel), forecasted by cy40REF (middle panel) and cy40NEW (right panel). Note that white in the left panel means that there is no observation available, whereas white spots in the middle and right panels mean no cloud base height was detected because all model levels have a cloud fraction $< \frac{5}{8}$.

ference in potential temperature between the surface and 700 hPa exceeds the threshold of 20 °C. The convective mixing with only a moist updraft in cy40REF is unable to transport enough moisture to the inversion. Even when the temperature inversion between surface and 700 hPa exceeds 20 °C, it still seems legitimate to presume the existence of an ensemble of relatively weak, dry updrafts and stronger, moist updrafts. Moreover, rigid and rather arbitrary thresholds in parameterisations, like the above-mentioned bulk temperature difference, should be avoided (Kähnert et al., 2021). Based on the considerations above, the removal of the stratocumulus regime with only a wet updraft is part of the cy40NEW configuration and therefore applies to all results of cy40NEW in this chapter.

4.3.4. HARMONIE-AROME 3-D MODEL RUNS

As mentioned in Sect. 4.1, the most urgent problem in cy40REF concerns the large underestimation of low clouds and overestimation of cloud base heights (i.e. the lowest model level where cloud fraction exceeds $\frac{5}{8}$). This model deficiency is most noticeable in wintertime conditions. As a typical example, we show 3-D model results for 19 December 2018 in Fig. 4.19. The cy40REF run reveals a severe overestimation of cloud base height. Moreover, for large areas with observed low stratus, cloud base height is not even detected due to too-small cloud fractions (shown as white, background colour). A key aspect of the large improvement with cy40NEW (Fig. 4.19, right panel) is again the better preservation of inversion strengths. Several modifications contribute to the improvement but the most substantial is the influence of reduced l_∞ (see Eq. 4.16) and c_h (Eq. 4.14) as well as removal of the HARATU updates, increasing the downward mixing described in B17 (see also Sect. 4.3.2). The large improvement on cloud base height is confirmed in longer-term verification, illustrated by the frequency

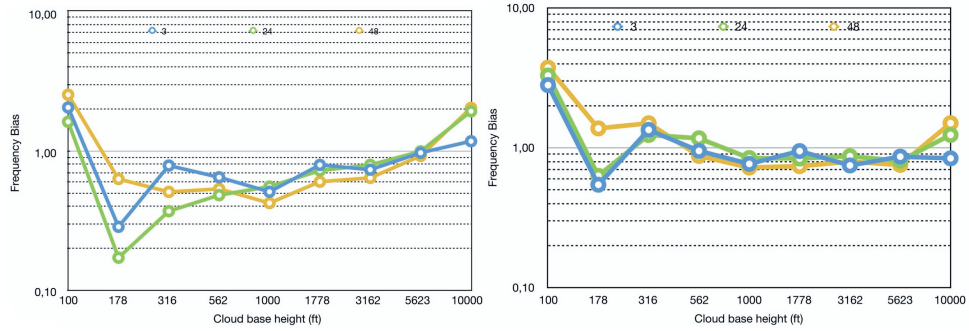

Figure 4.20: Frequency bias of the cloud base height in feet (1 ft is 0.3048 m) for December 2018 with cy40REF **(a)** and cy40NEW **(b)**. Blue, green, and orange lines refer to +3, +24, and +48 h forecasts, respectively.

bias for December 2018 (Fig. 4.20). Here, frequency bias means the ratio between the forecasted and observed number of cloud base heights in a certain bin. Note the extreme underestimation of cloud bases around 178 ft (approximately 54 m); less than 20 % of the observed number of cases are actually predicted in +24 h cy40REF forecasts. Over the complete range of low cloud base heights, cy40NEW outperforms cy40REF, except for the lowest cloud base, associated with fog cases. However, in fog, other processes (concerning microphysics and radiation) outside the scope of this study turn out to have a large influence. Verification for other months confirms the substantial improvement in low cloud base height climatology.

Apart from the impact on low clouds, the accumulation of moisture beneath atmospheric inversions also influences the triggering of resolved deep convection and the associated (heavy) precipitation. This is illustrated in Fig. 4.21, which presents a case on 10 September 2011 where deep convection was observed but its triggering was missed by cy40REF. The vertical atmospheric cross sections in Fig. 4.21 (third and fourth rows) reveal that relative humidity just under the inversion of the boundary layer accumulates more strongly in cy40NEW. This supports the model to start resolved upward motions as reflected in the increased boundary layer height near the local maximum in RH at the boundary layer top (fourth row, third column). As a result, only in cy40NEW, deep, resolved convection and precipitation starts (noisy pattern in the upper right corner of the fourth row and column). Figure 4.22, showing the averaged skewed temperature profile in the area where the deep convective shower develops (indicated by the rectangle in Fig. 4.21), confirms the stronger atmospheric inversion with cy40NEW.

Semi-operational, daily runs of cy40REF and cy40NEW for more than a year in parallel revealed several cases where cy40NEW did forecast resolved precip-

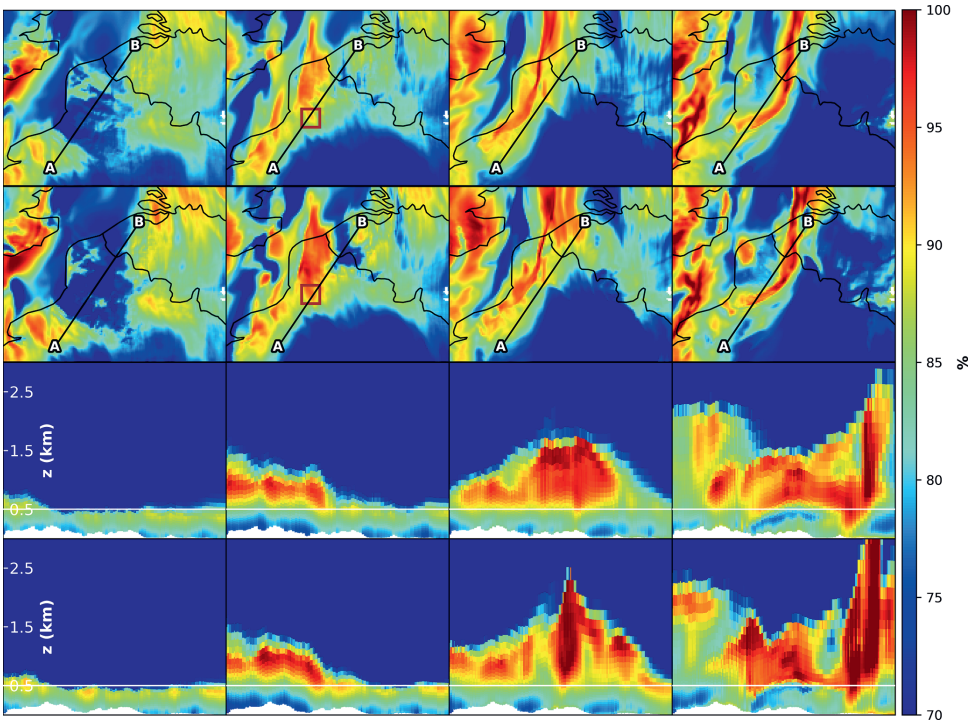

Figure 4.21: Relative humidity (RH) plots (red means high RH, blue low RH) for 10 September 2011. The four columns refer to hours 12 : 00, 14 : 00, 16 : 00, and 18 : 00 UTC. The first row (cy40REF) and second row (cy40NEW) show a map of RH at approximately 500 m height that covers parts of Belgium and northwest France, as well as a black line. Along this line, a vertical atmospheric cross section for the lowest 3 km is shown in the third (cy40REF) and fourth (cy40NEW) rows. In the cross sections, the boundary layer can be recognised by relatively high RH values. The white line at 500 m in the cross sections shows the height for which the RH is plotted in the two upper rows. The rectangle in the second column of the two upper rows indicates the area used to produce the skewed T profile in Fig. 4.22.

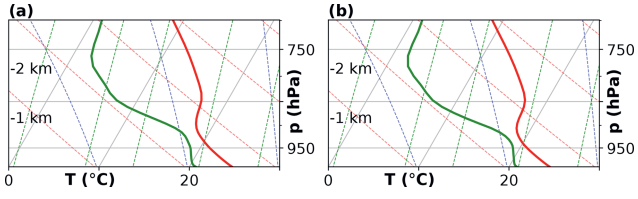

Figure 4.22: Profiles of the skewed temperature (solid red line) and dew point temperature (solid green line) against the pressure (hPa). The profiles for cy40REF **(a)** and cy40NEW **(b)** are determined as the average over the domain indicated by the rectangle in Fig. 4.21, where a strong shower did develop in cy40NEW but not in cy40REF. Dashed red, blue, and green lines show, respectively, the dry adiabat, the pseudo adiabat, and constant mixing ratio. Skewed thin grey lines represent constant temperature. In comparison with cy40REF, cy40NEW reveals a stronger inversion around the top of the boundary layer (approximately 1000 m height).

itation that was also observed but was missed in cy40REF. Moreover, 1 year of fraction skill score verification of precipitation forecasts against calibrated radar data demonstrated a significant improvement with cy40NEW (not shown). Verification of the near-surface variables reveals that the new configuration results in a slight deterioration in the negative 2 m temperature bias but no significant impact on 2 m humidity. Wind speeds at 10 m are slightly higher but with the same diurnal amplitude, resulting in no significant change in model performance. Note that in general, near-surface variables are strongly influenced by surface processes and potential representation mismatches between observation site and model grid box (see, e.g. de Rooy and Kok, 2004).

4.4. CONCLUSIONS AND DISCUSSION

As discussed in, e.g. Jakob, 2010 or de Rooy et al., 2013, model development, in particular by means of improved parameterisation schemes, is a slow and sometimes frustrating process. A scientifically improved parameterisation could remove a previous compensating model error and consequently cause an overall deterioration. In addition, together with increased physical realism, interactions between parameterisations become stronger. The considerations above advocate a more integral approach to develop strongly connected parameterisation schemes together. Following such an approach, this chapter describes a comprehensive model update to the boundary layer schemes. Because the involved parameterisations are all built on widely applied frameworks, the here-described modifications and the impact of certain parameters on different model aspects are not just specific to the HARMONIE-AROME model but also applicable to many NWP and climate models. Moreover, this chapter can be an inspiration for further improvements, and several suggestions for this are already provided, for example, amelioration of the variance in s estimates by increasing the convection timescale, τ_{conv} (Eq. 4.31), or including a height dependency in the extra variance term, Eq. (4.38).

Apart from being a slow and tough process, model development is often a compromise between a scientific and a pragmatic approach. In this chapter, we have tried to provide an "honest" description of the development process, thus including the more pragmatic optimisations and mentioning not only the successes but also the remaining shortcomings and (over)simplifications in the parameterisations.

The model update contains substantial modifications to the cloud, turbulence, and convection schemes based on a wide variety of argumentations. On one side of the spectrum are the more theoretically based modifications to the turbulence scheme – Monin–Obukhov similarity theory, following Baas et al., 2008 and Baas et al., 2017 – and the statistical cloud scheme (fundamental ther-

modynamics). On the other end of the spectrum, this chapter illustrates that parameterisations contain uncertain parameters, with largely varying values suggested in the literature, that at the same time have a substantial impact. To optimise these parameters, we inevitably have to rely on examination of cases and longer term 3-D runs. Finally, LES and SCM runs conducted for a variety of intercomparison cases have been analysed extensively and the outcomes are subsequently used as a basis for several modifications in all boundary layer schemes. As an example, we mention the incorporation of the lateral mixing term from the prognostic mass flux vertical velocity variance equation as a source term in the TKE equation. This term is related to the energy cascade from large to smaller scales and particularly enhances the subcloud-to-cloud layer transport improving the correspondence with LES results for shallow convection. An overview of all modifications is provided in Table D1.

The adjustments to the HARMONIE-AROME model described in this chapter have a substantial impact on several aspects of the model performance. The most outstanding result is the improvement on low cloud and low cloud base height forecasts. Being one of the most urgent deficiencies of HARMONIE-AROME cycle 40, increasing the quality on this aspect was also the main goal of this study. The low cloud climatology changes from a severe underestimation in the reference version to a well-balanced model. Obviously, low clouds have a large impact on radiation and therewith on several model parameters. Moreover, they are crucial for aviation safety purposes. Taking a closer look at the consequences of the model updates reveals that the better preservation of atmospheric inversion strengths plays a key role. Not only the formation of low clouds but also the triggering of deep-resolved convection and the associated (heavy) precipitation are influenced by atmospheric inversion strength. With stronger inversions, more humidity is accumulated beneath the boundary layer top, which supports the development of mesoscale resolved upward motions, ultimately leading to deep convection and rain showers.

Verification based on more than 1 year of parallel model runs with cy40REF and cy40NEW firmly substantiates the significant improvement on low cloud and precipitation forecasts. The modifications in cy40NEW did not result in a significant improvement or deterioration of near-surface temperature, humidity, and wind speed. All modifications have recently been incorporated in the default configuration of HARMONIE-AROME cycle 43. Herewith, they will also become available in the HARMONIE-AROME climate version (Belusić et al., 2020) undoubtedly with impact on, e.g. precipitation extremes in future weather experiments.

An important spin-off of this project is the increased understanding of how parameter settings impact particular model output and how they influence each

other via underlying physical processes. With this insight, we decided to use the proportionality constant of the stable length scale, $c_{\mathrm{m,h}}$ (Eq. 4.14) and the minimum asymptotic length scale, l_∞ (Eq. 4.16) within a SPP (stochastically perturbed parameterisation) EPS framework (Frogner et al., 2019). Verification reveals that these parameters have the most beneficial impact on spread/skill of all parameters investigated (Inger-Lise Frogner, personal communication, 2021).

4.5. APPENDIX

4.5.1. DERIVATION OF THE VARIANCE IN S

Here, we provide a step-by-step derivation of the variance in s.

Suppose we know the PDF that describes subgrid variability of θ_ℓ and q_t in a grid box of an atmospheric model. Then the resulting cloud cover, a_c, and liquid water content (similarly for ice water content) can be written as

$$\begin{aligned} a_\mathrm{c} &= \int_{-\infty}^{\infty} H(q_\mathrm{t} - q_\mathrm{s}) P(\theta_\ell, q_\mathrm{t}) \mathrm{d}q_\mathrm{t} \mathrm{d}\theta_\ell \\ q_\ell &= \int_{-\infty}^{\infty} (q_\mathrm{t} - q_\mathrm{s}) H(q_\mathrm{t} - q_\mathrm{s}) P(\theta_\ell, q_\mathrm{t}) \, \mathrm{d}q_\mathrm{t} \mathrm{d}\theta_\ell, \end{aligned} \tag{4.40}$$

where q_s is the saturation specific humidity and H denotes the Heaviside function ($H(x) = 0$ for $x < 0$ and $H(x) = 1$ for $x > 0$) which probes that part of the integrand that is oversaturated. Because we only have to consider $q_\mathrm{t} - q_\mathrm{s} > 0$, the distance to the saturation curve s can be defined as

$$s \equiv \overline{s} + s' = q_\mathrm{t} - q_\mathrm{s}(p, T) = q_\ell \text{ for } s > 0, \tag{4.41}$$

where $\overline{s}$ is the (grid box) average of s, primes denote excursions from the mean, and q_s is a function of pressure, p, and temperature T. Using a Taylor expansion around $\overline{T_\ell}$, the saturation specific humidity at T can be written as

$$q_\mathrm{s}(T) \simeq \overline{q}_\mathrm{sl} + \overline{q}_\mathrm{sl,T}(T - \overline{T}_\ell), \tag{4.42}$$

with the usual abbreviations:

$$\overline{q}_\mathrm{sl} = q_\mathrm{s}(\overline{T}_\ell), \ \overline{q}_\mathrm{sl,T} = \frac{\partial q_\mathrm{s}(\overline{T}_\ell)}{\partial T}, \tag{4.43}$$

using the definition of the liquid water temperature:

$$T_\ell \equiv T - \frac{L}{c_\mathrm{p}} q_\ell, \tag{4.44}$$

where L is the latent heat of vaporisation and c_p the heat capacity of dry air at constant pressure. Equation (4.42) can be rewritten as

$$q_s(T) \simeq \overline{q}_{sl} + \overline{q}_{sl,T}(T_\ell + \frac{L}{c_p} q_\ell - \overline{T}_\ell) = \overline{q}_{sl} + \overline{q}_{sl,T} \times \left(\pi\theta'_\ell + \frac{L}{c_p} H(s)s\right), \tag{4.45}$$

where we have applied Eq. (4.41) and the Exner function, $\pi = (\frac{p}{p_0})^{\frac{R_d}{c_p}} = \frac{T}{\theta}$, with R_d the gas constant of dry air and p_0 a reference surface pressure. Equation (4.45) substituted in Eq. (4.41) leads to

$$s = \overline{q}_t + q'_t - \overline{q}_{sl} - q_{sl,T}\pi\theta'_\ell - q_{sl,T}\frac{L}{c_p} H(s)s. \tag{4.46}$$

As mentioned before, we only consider $s > 0$, so $H(s) = 1$. Writing s explicitly in Eq. (4.46) leads to

$$s = \alpha[q'_t - \beta\theta'_\ell + (\overline{q}_t - \overline{q}_{sl})], \tag{4.47}$$

with α and β defined in Eq. (4.22). To determine s', we follow a similar derivation as shown above but now for $\overline{s}$.

$$\overline{s} = \overline{q}_t - \overline{q}_s(\overline{T}) \tag{4.48}$$

$$\overline{q}_s(\overline{T}) \simeq \overline{q}_{sl} + \overline{q}_{sl,T}(\overline{T} - \overline{T}_\ell), \tag{4.49}$$

with $(\overline{T} - \overline{T}_\ell) = \frac{L}{c_p}\overline{q}_\ell = \frac{L}{c_p}\overline{s}$ substituted in Eq. (4.48), $\overline{s}$ reads

$$\overline{s} = \alpha(\overline{q}_t - \overline{q}_{sl}). \tag{4.50}$$

Using Eqs. (4.47) and (4.50), we can write s' as

$$s' = s - \overline{s} = \alpha q'_t - \alpha\beta\theta'_\ell, \tag{4.51}$$

and the variance of s as

$$\sigma_s^2 = \overline{s'^2} = \alpha^2\overline{q'^2_t} - 2\alpha^2\beta\overline{q'_t\theta'_\ell} + \alpha^2\beta^2\overline{\theta'^2_\ell}. \tag{4.52}$$

4.5.2. SUMMARY OF THE DIFFERENCES BETWEEN THE CY40REF AND CY40NEW CLOUD SCHEMES

Here we present an overview of the differences between the cy40REF and cy40NEW cloud schemes. Firstly, an important difference concerns the formulation of the thermodynamic coefficients α and β in the expression for the variance in s (Eq. 4.21). The definitions and derivation in cy40NEW can be found in

the previous Appendix. In cy40REF, coefficient α is formulated as Eq. (4.22) except for a factor of 0.5 (see Tudor and Mallardel, 2004). Coefficient β in cy40REF is combined with α in one variable in a complex expression, described in Tudor and Mallardel, 2004 but without a derivation or reference. The values and typical atmospheric shape of the profile of β in the original code are wrong, as they deviate substantially from Eq. (4.22) (not shown). Furthermore, in cy40REF, it is assumed that l_ϵ equals l_m (Eq. 4.30), whereas in the new configuration we take l_ϵ consistent with its formulation in the turbulence scheme (see Eq. 4.27). Pre-factor c_ab in Eq. (4.26) was 1 in cy40REF but changed to 0.139, this time conforming to the literature (Redelsperger & Sommeria, 1981). In contrast to the reference code, the new setup of the cloud scheme includes the covariance term of the contribution from convection, i.e. Eq. (4.31) with $a = \theta_\ell$ and $b = q_\mathrm{t}$. Finally, pre-factor 2 of the variance contribution from convection (see, e.g. Eq. 4.32) was erroneously applied twice in cy40REF and removed in cy40NEW.

4.5.3. MODIFICATIONS IN THE CONVECTION SCHEME

To estimate the contribution from organised (updraft) transport, in a model represented by the convection scheme, to the total turbulent transport, LES data in the cloud layer are conditionally sampled. Different sampling methods exist (see Siebesma and Cuijpers, 1995) like cloudy updraft sampling, i.e. selecting LES grid boxes with $w_\mathrm{u} > 0$ and $q_\ell > 0$, and core sampling with the additional requirement of positive buoyancy. Cloudy updraft sampling is probably the most suitable to be compared with convective transport of a mass flux scheme because it includes the negatively buoyant, decelerating part of the updraft, just as in the parameterisation.

Figure 4.23 shows convective humidity transport according to LES (cloudy updraft sampling) and HARMONIE-AROME 1-D with the cy40REF and cy40NEW configurations. Plots of heat transport are not shown as they reveal a similar behaviour. The plotted HARMONIE-AROME values are the sum of dry and moist updraft transport, whereas the sampling method applied on the 3-D fields of LES will only produce estimates of convective transport in the cloud layer. To increase statistical significance, the model mass flux transport is obtained as hourly mean around validation time. From LES, only instantaneous hourly 3-D fields are available. However, as LES convective transport is the mean of 100 HARMONIE-sized domains, it can be considered an average over many realisations.

Figure 4.23 shows that during the main part of the convective period, both model versions underestimate convective transport in comparison with LES. Only during the last convective hours, fluxes are comparable, whereas at +12 h convection finally starts to collapse. The latter hour is highly dynamical and a

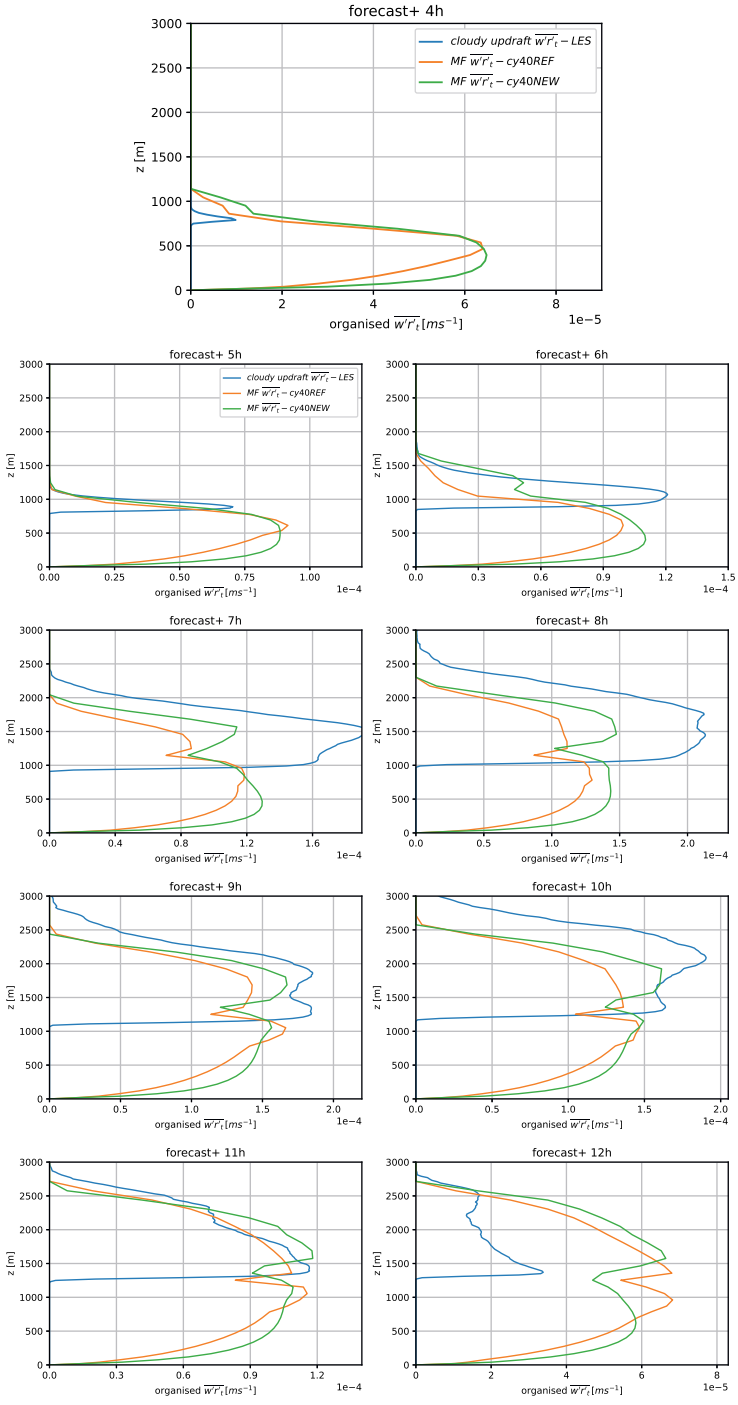

Figure 4.23: Kinematic convective transport (ms^{-1}) during all convective hours of the ARM case, corresponding to simulation hours +4 to +12 h. Plotted is the mass flux (MF) transport by the convection scheme (orange indicates cy40REF and green is cy40NEW) and the estimated (cloudy updraft sampling) convective transport by the LES (blue). Note that the x-axis scale is not constant and equal to the scale of the corresponding plots in Fig. 4.5. For readability of the legend, simulation hour +4 h is printed bigger.

slightly different (e.g. shorter) averaging time already has a large impact on the diagnosed flux profiles. Hence, +12 h results should be interpreted with care. Figure 4.23 further demonstrates that the new configuration increases convective transport, generally resulting in a better resemblance with LES. Several modifications in the convection scheme have contributed to this increase in mass flux transport. All modifications to the convection scheme, including their impact, are described below.

Firstly, we changed c_b in the mass flux closure (Eq. 4.12) from 0.03 (Grant, 2001) to 0.035 (Brown et al., 2002); see Sect. 4.2.2. Another contribution stems from the formulation of ε at $z = z_{lcl}$ (Eq. 4.10, Sect. 4.2.2). In the original expression, entrainment at cloud base (or inversion height) is inversely proportional to the inversion height. With a typically increasing inversion height during the convective period, this formulation will result in relatively high entrainment rates and therewith less effective mass flux transport in the early stages of convection. However, during this period, the convective transport is underestimated (see Fig. 4.23). Therefore, we pragmatically fixed moist updraft entrainment values at cloud base at 0.002, roughly in agreement with LES in de Rooy et al., 2013, Fig. 6, and Siebesma et al., 2003. However, more investigation is needed to establish a robust and adequate description of the entrainment at cloud base. Another aspect of the entrainment formulations in cy40REF are the quite large values near the surface due to the first term on the RHS in Eqs. (4.9) and (4.10). Apart from unwanted dependence on vertical resolution of the model, this will also result in a weak dependence of updraft excess values on surface fluxes. By adding a_1 =40 m to the entrainment formulations, similar to Soares et al., 2004, dependence on surface fluxes gets stronger, causing increased convective transport during hours with large surface fluxes (Brown et al., 2002, Fig. 3). Finally, a_2 in Eq. (4.9) is reduced from 40 to 1 m to increase entrainment values when the dry updraft approaches its termination height. Herewith, deposition of humidity in a too-thin layer just below the inversion is prevented, which contributes to the too-high humidity and cloud cover around cloud base in cy40REF (see Sect. 4.3.1).

Finally, Fig. 4.23 reveals a strong decrease in mass flux transport around inversion which is related to the termination height of the dry updraft (see Fig. 4.5) and the associated strong decrease of convective transport. However, as we demonstrate in Sect. 4.3.1, this decrease in convective transport is largely balanced by the diffusive transport leading to a rather smooth total turbulent transport profile (Fig. 4.5). This process is enhanced by the incorporation of the energy cascade term in the turbulence scheme (Sect. 4.2.3).

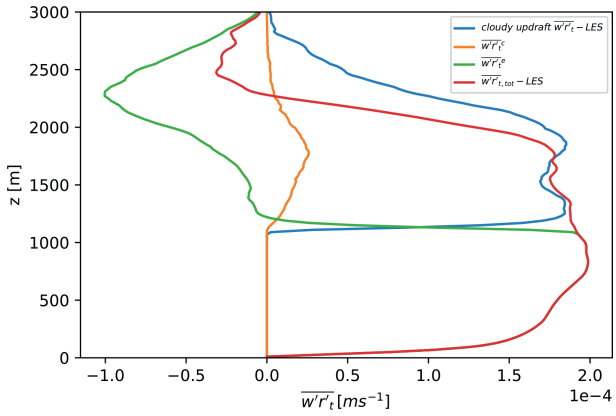

Figure 4.24: Decomposition of the turbulent fluxes for the ARM case, ninth simulation hour. Plotted are LES cloudy updraft flux (blue), small-scale subplume transport (orange), small-scale environmental transport (green), and total transport (red).

4.5.4. DECOMPOSITION OF THE TURBULENT TRANSPORT

Following Siebesma and Cuijpers, 1995, total turbulent transport can be written as a sum of large-scale organised and small-scale subplume and environmental transport. Figure 4.24 presents typical profiles during the ARM case of such a decomposition of total turbulent transport. The role of environmental turbulence in Fig. 4.24 is remarkable. In the lower half of the cloud layer, the negative contribution of environmental turbulence is roughly balanced by positive subplume turbulence. However, in the upper part of the cloud layer, a large negative contribution of environmental turbulence dominates and counteracts organised updraft transport. Consequently, the underestimation and too-shallow organised convective transport by the parameterisation (Fig. 4.23) are not translated in an underestimation of total turbulent transport (Fig. 4.5). Note that in Siebesma and Cuijpers, 1995, Fig. 7 for the BOMEX steady-state shallow convection case, environmental turbulence is always positive. Their figure is produced by applying cloud core sampling. However, repeating the decomposition experiments with different sampling methods leads to the same qualitative picture.

To investigate the relatively large contribution from environmental turbulence, the turbulent transport is decomposed further in three parts: cloudy updraft, cloudy downdraft, and environment (Siebesma & Cuijpers, 1995). As a result, we now distinguish 6 different turbulent fluxes contributing to the total turbulent transport of moisture (Fig. 4.25). Figure 4.25 reveals that less than half of the negative turbulent transport is caused by organised downdrafts, whereas the majority is caused by environmental turbulence outside cloudy up- and downdrafts. To visualise the downward transport, a horizontal cross section is taken at

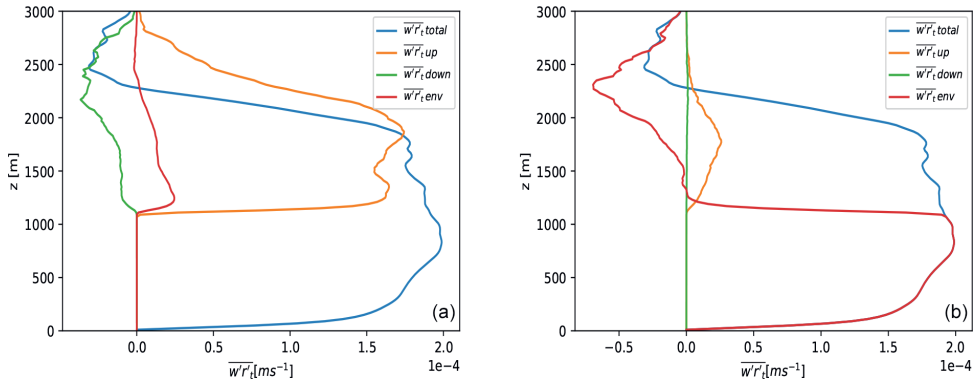

Figure 4.25: ARM case, ninth simulation hour. Panel **(a)** shows organised fluxes, distinguishing updrafts (orange), downdrafts (green), and environment (red) as well as the total turbulent transport (blue). Panel **(b)** shows the small-scale turbulent fluxes using similar colour coding to that in panel **(a)**.

the height of maximum downward turbulent moisture transport (Fig. 4.26). The largest downward transport (dark blue colour) is observed in two subdomains indicated by black squares and seems to be connected to strong upward transport. However, the two subdomains reveal a different behaviour (Figs. 4.26 middle and right panels). Whereas the right subdomain resembles the classical view with downward transport in the cloud (downdrafts), the left subdomain shows downward transport primarily outside the cloud (indicated by the red $q_\ell = 0$ line), possibly the remains of a large active updraft. Here, a substantial part of downward transport is associated with downdrafts containing relatively high humidity values but no liquid water. Possibly, these downdrafts are related to the subsiding shells as discussed by Heus, Pols, et al., 2009. Finally, Fig. 4.26a illustrates that LES runs for the ARM case at a smaller domain could easily miss rarely occurring large convective events that give rise to substantial downward transport. As a result, investigations on smaller domain LES could lead to different conclusions about the relative importance of the decomposed fluxes to the total turbulent transport.

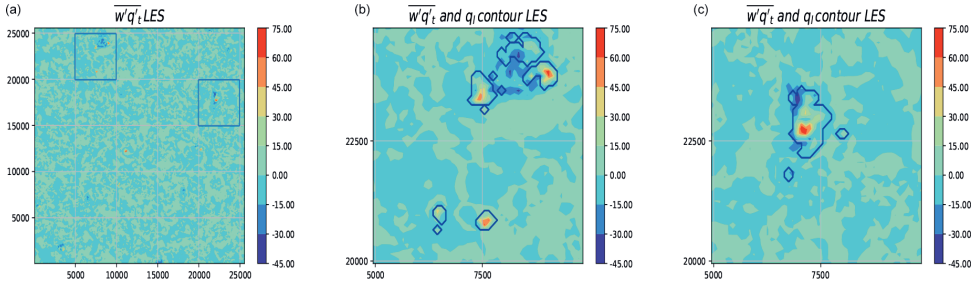

Figure 4.26: ARM case, ninth simulation hour, cross section of the kinematic turbulent moisture transport at 2310 m height (with q_t in gkg^{-1}). Blue and yellow/red colours refer to downward and upward transport, respectively. The x and y axes number the LES grid points (with the LES resolution of 100 m; the grey grid lines illustrate the size of a HARMONIE-AROME grid box). Panel **(a)** presents the full LES domain, whereas panels **(b)** and **(c)** show, respectively, the left and right subdomains as shown by the blue squares in panel **(a)**. The blue line defines the cloudy border, i.e. $q_\ell = 0$.

4.5.5. OVERVIEW OF THE MODIFICATIONS

description	cy40REF	cy40NEW	main impact/argumentation
Convection scheme			
separate regime for strato-cumulus? Section 4.2.2, Table 4.1	yes: $a_{dry} = 0m$	no: as in shallow cumulus i.e. $a_{dry} = 0.07m$	improvement in strato-cumulus cases and removal of arbitrary threshold
entrainment Eqs. (4.9), (4.10), (4.11)	a_1 not present	$a_1 = 40m$	reduction of dependence on vertical resolution and increase dependence on surface fluxes
	$a_2 = 40m$	$a_2 = 1m$	prevention humidity deposition in a too thin layer below inversion
	$\varepsilon_{lcl} = \frac{1.65}{z_{lcl}} m^{-1}$	$\varepsilon_{z_{lcl}} = 0.002 m^{-1}$ (de Rooy et al., 2013; Siebesma et al., 2003)	increase mass flux transport in the early stages of convection (conform LES)
mass flux closure Eq. (4.12)	$c_b = 0.03$ (Grant, 2001)	$c_b = 0.035$ (Brown et al., 2002)	increase mas flux (conform LES)
Turbulence scheme			
proportionality constant of stable length scale for heat, Eq. (4.14)	$c_h = 0.15$	$c_h = 0.11$	mixing for neutral to moderately stable conditions tuned against MO-theory
power of the inverse interpolation between length scales, Eq. (4.15)	$p = 1$	$p = 2$	as above
aymptotic free atmospheric length scale, Eq. (4.16)	$l_\infty = 100m$	$l_\infty = 40m$	strengthening atmospheric inversions and better preservation stratus clouds
turbulent diffusion link to convection, Eq. (4.18)	$50 \cdot M_u$	energy cascade W_{casc}	improvement turbulent transport (sub-cloud to cloud transport) conform LES
enhanced downward mixing in storm situations	included see Bengtsson et al. (2017)	removed	removal due to retuned c_h and p
Cloud scheme			
thermodynamic coefficients α and β, Eqs. (4.21), (4.22)	Tudor and Mallardel (2004) (bug)	see appendix 4.5.1	removal bug
dissipation length scale, Eq. (4.27)	$l_\epsilon = l_m$	$l_\epsilon = c_0^2 l_m$ (LH04)	consistency between turbulence and cloud scheme
dissipation term constant, Eq. (4.26)	$c_{ab} = 1$	$c_{ab} = 0.139$	consistency with literature (Redelsperger & Sommeria, 1981)
covariance term in the contribution of convection to s'^2, Eq. (4.31)	not included	included	improvement of the shape of the variance profile
convective contribution to the variance, see Eqs. (4.31), (4.32)	erroneous extra factor 2	-	removal bug

Table 4.3

4.5.6. CODE AVAILABILITY

The ALADIN and HIRLAM consortia cooperate on the development of a shared system of model codes. The HARMONIE-AROME model configuration forms part of this shared ALADIN-HIRLAM system. According to the ALADIN-HIRLAM collaboration agreement, all members of the ALADIN and HIRLAM consortia are allowed to license the shared ALADIN-HIRLAM codes to non-anonymous requests within their home country for non-commercial research. Access to the full HARMONIE-AROME codes can be obtained by contacting one of the member institutes of the HIRLAM consortium (http://www.hirlam.org/index.php/hirlam-programme-53, last access: 10 February 2022) and is subject to signing a standardised ALADIN-HIRLAM licence agreement (http://www.hirlam.org/index.php/hirlam-programme-53/access-to-the-models, last access: 10 February 2022).

The code of all routines involved in the modifications described in this chapter, together with the corresponding original routines, is available in the Supplement. The Supplement retains the directory structure as in the full HARMONIE-AROME model. Directory src/arpifs/phys_dym contains four modified routines: apl_arome.F90, vdfexcuhl.F90, vdfhghtnhl.F90, and vdfparcelhl.F90 that involve changes to, respectively, the cloud scheme, the turbulence scheme, the convection and turbulence scheme, and finally the convection scheme. Corresponding original routines are always indicated by the extension _ori. Directory mpa/micro/internals includes condensation.F90 with modifications to the cloud scheme. Finally, directory mpa/turb/internals contains five routines with modifications to the cloud scheme: compute_function_thermo_mf.F90, compute_mf_cloud_stat.F90, ini_cturb.F90, turb.F90, and turb_ver_thermo_corr.F90. In the same directory, two routines include modifications related to the turbulence scheme: turb_ver_dyn_flux.F90 and turb_ver_thermo_flux.F90. With reference to de Rooy et al., 2022, all routines in the Supplement file (https://doi.org/10.5281/zenodo.6037528) can be freely used, e.g. in other software.

4.5.7. DATA AVAILABILITY

DALES full 3-D fields (divided into eight subdomains), as well as derived LES data for the ARM case, can be downloaded from Zenodo: (https://doi.org/10.5281/zenodo.6037528). The LES data for GABLS1 (in ASCII, and only the ninth hour) and LES data for the stratocumulus cases (ASTEX, slow and fast) in NetCDF can be downloaded from Zenodo: (https://doi.org/10.5281/zenodo.6043384) All SCM results for all intercomparison cases can be found on Zenodo: (https://doi.org/10.5281/zenodo.6045761). The 1-year SCM dataset used for the optimisation of the turbulence scheme (Fig. 14) is available from Zenodo: (https://doi.org/

10.5281/zenodo.6053930). Figures 19 and 20 are based on 3-D model runs and observations which are provided on Zenodo: (https://doi.org/10.5281/zenodo.6074926).

4.5.8. AUTHOR CONTRIBUTION

WCdR contributed to all aspects of this chapter, including writing the original draft and revisions. PS, PB, GL, and SRdR contributed to the conceptualisation. PS and PB contributed to the formal analysis. PB, ST, and BvV contributed to the visualisation. PS contributed to the writing in the form of review editing. PS, PB, GL, SRdR, HdV, EvM, and JFM commented on the chapter.

4

4.6. ACKNOWLEDGEMENTS

This work has been done within the KNMI multi-annual strategic research (MSO) project CRIME (Cloud Representation IMprovement and Evaluation in HARMONIE-AROME) and the Norwegian Research Council (project no. 280573), "Advanced models and weather prediction in the Arctic: enhanced capacity from observations and polar process representations (ALERTNESS)". The support of Emiel van de Plas with Python is appreciated.

Financialsupport The study was supported by the Norwegian Research Council (project no. 280573).

Reviewstatement This chapter (as a paper) was edited by Sylwester Arabas and reviewed by two anonymous referees.

Competing interests The contact author has declared that neither they nor their co-authors have any competing interests.

Disclaimer Publisher's note: Copernicus Publications remains neutral with regard to jurisdictional claims in published maps and institutional affiliations.

5

CONCLUSIONS AND OUTLOOK

This thesis focuses on the behaviour of entrainment and detrainment as well as their representation within a mass flux concept. The study can be structured along the following three research questions:

1. *How do the entrainment and detrainment processes depend on environmental and geometrical conditions and how can this be used to improve convection parameterisations in weather and climate models?*

2. *What are the underlying principles that determine the behaviour of the lateral mixing processes?*

3. *How to improve model performance by means of improved physical parameterisations?*

The main conclusions of this thesis will be discussed along these questions in the next section. Hereafter, a brief outlook is presented.

5.1. CONCLUSIONS

1. *How do the entrainment and detrainment processes depend on environmental and geometrical conditions and how can this be used to improve convection parameterisations in weather and climate models?*

In chapter 2, LES results for a wide range of shallow cumulus cases are used to investigate the lateral mixing coefficients in the cloud layer. Surprisingly, the detrainment shows a much larger variation from case to case and from hour to hour, than the entrainment. LES suggests that entrainment can be reasonably well parameterised in terms of height only. For bulk parameterisations one can

use entrainment rates that decrease with height. This reflects the fact that near cloud base, the bulk entrainment is dominated by the many small clouds, while higher in the cloud layer, the entrainment is smaller since it is dominated by the larger clouds. For detrainment a somewhat more elaborated formulation is needed. LES reveals that two dependencies are important. Firstly, based on cloud ensemble principles it can be understood that deeper cloud layers call for smaller detrainment rates. This dependency is simply ignored by previous mass flux schemes. The new parameterisation deals with this dependency by considering the mass flux profile in a non-dimensionalized way. Secondly, the influence of environmental conditions in which both the relative humidity of the environmental air as the buoyancy excess of the updraft itself affects the detrainment rate. Both dependencies can be taken into account by the critical mixing fraction, a parameter borrowed from the buoyancy sorting concept, and use it in a bulk sense. The ultimate parameterisation can be easily understood from physical considerations. Small critical mixing fraction values correspond to marginally buoyant, often relatively small, clouds rising in a dry, hostile environment. It is likely, and confirmed by LES, that under such conditions the mass flux will decrease rapidly (large detrainment). The opposite is true for large buoyant clouds rising in a friendly, humid environment, corresponding to large critical mixing fraction values (small detrainment). Via the critical mixing fraction dependence, the detrainment and the mass flux profile are varying not only with the RH of the environment, but also with the properties (buoyancy) of the updraft itself.

One of the important distinctions between the new parameterisation and other mass flux schemes is that the entrainment and the shape of the mass flux profile are treated separately. This is based on the much larger variation of detrainment in comparison with the entrainment and therewith its much larger impact on variations in the mass flux profile. So in principle the mass flux profile itself is parameterised and therewith the concept of detrainment becomes obsolete. One of the consequences of such a framework, is that the entrainment formulation can be dedicated to an adequate description of the change of the cloud properties with height and therewith the cloudy updraft termination height, without being used for the mass flux profile. In this way, several problems with conventional convection schemes can be circumvented.

The parameterisation of the lateral mixing and the mass flux profile in the cloud layer as described above, is supported by observational (Lamer et al., 2015) and LES studies (H. Jonker et al., 2006, Derbyshire et al., 2011). However, the most convincing support from LES can be found in Böing et al., 2012 who used 90 LES runs to explore the sensitivity of entrainment, detrainment and the mass-flux profile to a broad spectrum of relative humidities and stability of the environment. This study not only confirms the much larger variation of detrainment

and its strong link with the mass-flux profile, but also reveals a strong correlation between the non-dimensionalized mass flux as diagnosed in his LES runs, and the mass flux profile according to the parameterisation as described in chapter 2.

2. *What are the underlying principles that determine the behaviour of the lateral mixing processes?*

Based on budget equations for total water specific humidity and mass , analytical expressions are derived for entrainment and detrainment. From these expressions, containing a small-scale turbulent and a larger scale organized term, a physical picture emerges for a shallow cumulus cloud ensemble. Individual clouds have a massive entrainment at cloud base, lateral turbulent mixing with constant mass flux between bottom and top, and massive detrainment at the top. As a result of different cloud top heights in the ensemble, the massive detrainment at the various cloud tops shows up as a dynamical detrainment term throughout the cloud layer. This physical picture and the corresponding formulations explain the strong correspondence between the detrainment and the mass flux profile and support the parameterisation approach in chapter 2.

If these results are combined with the budget equation for vertical velocity, new formulas for entrainment and detrainment rates can be expressed in terms of buoyancy, vertical velocity and cloud fraction. The formulation for detrainment explicitly reveals the strong connection with the mass flux and cloud fraction profile and also explains the dependence on cloud layer depth. LES reveals a good correspondence of these new formulas with more traditional methods to diagnose entrainment and detrainment rates. Although these expressions can not be applied directly as parameterisation, it is demonstrated how they can be used to evaluate existing parameterisations approaches and as a sound physical base for future parameterisations.

3. *How to improve model performance by means of improved physical parameterisations?*

Parameterisations have a strong impact on the model performance. Yet, it appears to be difficult to improve the model by improved parameterisations because the schemes are highly optimized and contain numerous compensating errors. Improvement of a single parameterised aspect of the boundary layer often results in an overall deterioration of the model as a whole. For example, due to reduced mixing in stable conditions in the optimized turbulence scheme (chapter 4), excessive moisture could build up under boundary layer inversions. However, other modifications (see chapter 4) like the increased sub-cloud to cloud layer transport by including the energy cascade term, as well as modi-

fications in the entrainment coefficients in the convection scheme, are able to redistribute this moisture. It is clear that an integral approach is needed. Following such an approach, chapter 4 describes how three tightly coupled boundary layer schemes, namely the shallow convection scheme, the cloud scheme and the turbulence scheme, are included in the HARMONIE-AROME model in one comprehensive integral revision. The modifications are based on a wide variety of argumentations; from theoretical considerations, to LES results for idealized intercomparison cases, to more pragmatically tuning of uncertain parameters, based on verification results. As an example of the more theoretically based revisions we mention the modifications to the turbulence scheme, based on Monin-Obukhov similarity theory (following Baas et al. (2008) and Baas et al. (2017)). As an example of an LES based modification we mention the incorporation of the lateral mixing term from the prognostic mass flux vertical velocity variance equation as a source term in the TKE equation. This term is related to the energy cascade from large to smaller scales and particularly enhances the sub-cloud to cloud layer transport, clearly improving the correspondence with LES results for shallow convection.

The adjustments to the HARMONIE-AROME model described in chapter 4 have a substantial impact on several aspects of the model performance. The most outstanding result is the improvement on low cloud and low cloud base height forecasts. Being one of the most urgent deficiencies of HARMONIE-AROME cycle 40, increasing the quality on this aspect was also the main goal of this study. The low cloud climatology changes from a severe underestimation in the reference version to a well balanced model. The new revised parametric descriptions provide not only an improved prediction of low clouds but also of precipitation. Both improvements can be related to a stronger accumulation of moisture under the atmospheric inversion. All modifications have been incorporated in the default configuration of the next official HARMONIE-AROME cycle (cycle 43). Herewith, they will also become part of the HARMONIE-AROME climate version (Belusić et al., 2020).

An important spin-off of the study in chapter 4 is the increased understanding in how parameter settings impact particular model output and how they influence each other via underlying physical processes. With this insight we decided to use the proportionality constant of the stable length scale, and the minimum asymptotic length scale, within a SPP (stochastically perturbed parameterisations) EPS framework (Frogner et al., 2019). Verification reveals that these parameters have the most benificial impact on spread/skill of all parameters investigated.

5.2. OUTLOOK

Over the last 20 years we have witnessed a renaissance of entrainment and detrainment studies, mainly due to the fact that LES have become an extremely useful tool for diagnosing these mixing processes. This thesis is another example of the importance of LES in this area of research.

Although parameterisations for entrainment and detrainment as described in this thesis, have proved successful, LES results in chapter 4 also reveal that a bulk mass flux scheme is only a crude approximation of reality, e.g. by ignoring the influence of subsiding shells (Heus & Jonker, 2008). On the other hand, incorporating more processes would require more complex parameterisations, containing several unknown tunable parameters, a disadvantage not to be underestimated.

Another complicating factor not considered in this thesis is the impact of meso-scale organisation. Recent studies reveal that cumulus convection often self-aggregates into meso-scale circulations, mostly induced by rain. An example of this are cold pool structures. Organised cumulus convection does not match the physical picture of an ensemble of independent cumulus clouds as mentioned in chapter 3. Therefore, our conclusions concerning the behaviour of entrainment and detrainment as well as the proposed parameterisations are restricted to unorganized cumulus convection.

However, together with the continuously increasing resolution of NWP and climate models, several more fundamental shortcomings of the mass flux concept arise. One of the problematic assumptions in a mass flux concept is the convective quasi-equilibrium. Relatively slow large scale forcings, like long wave radiative cooling, push the atmosphere to a conditionally unstable state. Cumulus convection counteracts this effect by stabilising the atmosphere. Because the stabilisation by the convective process is much faster than the large-scale destabilisation, a quasi-equilibrium can be assumed. Moreover, it is assumed that there is a one-to-one correspondence between the large scale forcing and the convective response. In a model context, the slow large scale forcings are associated with the grid point variables and the fast cumulus response is the parameterised sub-grid convective transport. This one-to-one response holds when a sufficiently large ensemble of cumulus updrafts is present in a grid cell. Such an ensemble will contain updrafts in many stages of their life cycle, from just arising to already dissolving. Due to a large number of cumulus updrafts in the ensemble, the convective response can be described by the large scale forcing, i.e. the grid cell variables. However, with increased resolution a grid cell contains only one or a few cumulus clouds and the convective response is just one of the many possible realisations. In this case the quasi-equilibrium approach is no longer valid. To represent the variable convective response at high resolutions, intrinsi-

cally stochastic convection schemes are developed (see e.g. Dorrestijn, 2016).

Together with the existence of only a few clouds in the grid cell instead of a large ensemble, more assumptions become unjustified (Arakawa et al., 2011). For example our diagnosis of LES and the consequences for cumulus parameterisation in chapter 2 and 3 are based on the existence of a large enough cumulus cloud ensemble. With e.g. only one cloudy updraft in the grid cell, the analysis in chapter 3 suggests a constant entrainment in the cloud layer that is equal to the detrainment, and therefore a constant mass flux with height, except for the massive detrainment at the cloud top. It is clear that this picture is incompatible with the parameterisation in chapter 2 which assumes a linearly decreasing mass flux in the upper part of the cloud layer. Yet another mass flux assumption that breaks down is the updraft area fraction being much smaller than the grid size. As a consequence of this assumption the grid cell average and the average over the environment of the updraft is the same which clearly does not hold for large updraft area fractions.

Yet another important complicating factor at high resolutions is that the model will start to partly resolve shallow convection. As a result, keeping the parameterised convection at full strength would hinder the model to resolve convection itself and herewith reduce the added value of high resolution runs. A very pragmatic way to adapt the parameterised convective activity to increasing resolution, is to decrease the threshold of the diagnosed cloud layer height in the mass flux scheme at which the model shuts down parameterised convection. A more sophisticated way to include scale-awareness in the convection scheme is based on a special diagnosis of LES runs for several convection cases (see Honnert et al., 2011). They show how the ratio between sub-grid parameterised and resolved turbulent transport changes as a function of the non-dimensionalised mesh size, i.e. the ratio between model grid size and the sum of the sub-cloud and cloud layer boundary height. Lancz et al., 2018 describe a first attempt to utilise this non-dimensionalised mesh size in a convection scheme for the grey zone. A similar approach could be applied to our convection scheme. Moreover, in our convection scheme a separate adaptation of dry and moist convection is possible because they are treated separately (chapter 4). The relatively smaller dry convection scales can be related to the termination height of the dry updraft and similarly for the relatively larger scales of moist convection. Note that although being scale-aware, the aforementioned concept does not capture the stochastic nature of convection in the grey zone.

Ultimately, when the model resolution is high enough to resolve even the smallest cumulus clouds, the parameterisation of convection will become obsolete. Because LES results for shallow convection are rather independent of grid sizes below $100m$, this resolution will suffice to run NWP and climate models

without a convection parameterisation. However, smaller scale processes like diffusive turbulent mixing will have entered the model grey zone, providing new challenges for model developers.

REFERENCES

Arakawa, A., Jung, J., & Wu, C. (2011). Toward unification of the multiscale modeling of the atmosphere. *Atmos. Chem. Phys., 11*, 3731–742. https://doi.org/10.5194/acp-11-3731-2011

Arakawa, A., & Schubert, W. H. (1974). Interaction of a cumulus cloud ensemble with the large-scale environment, part i. *J. Atmos. Sci., 31*, 674–701.

Asai, T., & Kasahara, A. (1967). A theoretical study of the compensating downward motions associated with cumulus clouds. *J. Atmos. Sci., 24*, 487–496.

Baas, P., de Roode, S. R., & Lenderink, G. (2008). The scaling behaviour of a turbulent kinetic energy closure model for stably stratified conditions. *Boundary-Layer Meteorol., 127*, 17–36. https://doi.org/10.1007/s10546-007-9253-y

Baas, P., van de Wiel, B. J. H., van der Linden, S. J. A., & Bosveld, F. C. (2017). From near-neutral to strongly stratified: Adequately modelling the clear-sky nocturnal boundary layer at cabauw. *Boundary-Layer Meteorol., 166*, 217–238. https://doi.org/10.1007/s10546-017-0304-8

Beare, R., & M.K. Macvean, e. a., A.A.M. Holtslag. (2006). An intercomparison of large-eddy simulations of the stable boundary layer. *Boundary-Layer Meteorol., 118*, 247–272. https://doi.org/10.1007/S10546-004-2820-6

Bechtold, P., Bazile, E., Guichard, F., Mascart, P., & Richard, E. (2001). A mass flux convection scheme for regional and global models. *Q. J. R. Meteorolog. Soc., 127*, 869–886. https://doi.org/10.1002/qj.49712757309

Bechtold, P., Cuijpers, J. W. M., Mascart, P., & Trouilhet, P. (1995). Modeling of trade wind cumuli with a low-order turbulence model: Toward a unified description of cu and sc clouds in meteorological models. *J. Atmos. Sci., 52*, 455–463. https://doi.org/10.1175/1520-0469(1995)052<0455:MOTWCW>2.0.CO;2

Bechtold, P., Fravalo, C., & Pinty, J. (1992). A model of marine boundary-layer cloudiness for mesoscale applications. *J. Atmos. Sci., 49*, 1723–1744. https://doi.org/10.1175/1520-0469(1992)049<1723:AMOMBL>2.0.CO;2

Bechtold, P., Kohler, M., Jung, T., Doblas-Reyes, F., Leutbecher, M., Rodwell, M., Vitart, F., & Balsamo, G. (2008). Advances in simulating atmospheric variability with the ecmwf model: From synoptic to decadal time-scales. *Q. J. R. Meteorolog. Soc., 134*, 1337–1351. https://doi.org/10.1002/qj.289

Bechtold, P., & Siebesma, A. P. (1998). Organization and representation of boundary clouds. *J. Atmos. Sci.*, *55*, 888–895. https://doi.org/10.1175/1520-0469(1998)055<0888:OAROBL>2.0.CO;2

Beljaars, A., & Holtslag, A. (1991). Flux parameterization over land surfaces for atmospheric models. *J. Appl. Meteorol. Clim.*, 327–341. https://doi.org/10.1175/1520-0450(1991)030<0327:FPOLSF>2.0.CO;2

Belusić, D., de Vries, H., Dobler, A., Landgren, O., Lind, P., Lindstedt, D., Pedersen, R., Sánchez-Perrino, J., Toivonen, E., van Ulft, B., Wang, F., Andrae, U., Batrak, Y., Kjellström, E., Lenderink, G., Nikulin, G., Pietikäinen, J., Rodríguez-Camino, E., Samuelsson, P., … Wu, M. (2020). Hclim38: A flexible regional climate model applicable for different climate zones from coarse to convection-permitting scales. *Geosci. Model Dev.*, *13*, 1311–1333. https://doi.org/10.5194/gmd-13-1311-2020

Bengtsson, L., Andrae, U., Aspelien, T., Batrak, Y., Calvo, J., de Rooy, W. C., Gleeson, E., Hansen-Sass, B., Homleid, M., Hortal, M., Ivarsson, K.-I., Lenderink, G., Niemelä, S., Nielsen, K. P., Onvlee, J., Rontua, L., Samuelsson, P., Munoz, D. S., Subias, A., … Koltzow, M. O. (2017). The harmonie–arome model configuration in the aladin–hirlam nwp system. *Mon. Weather Rev.*, *145*, 1919–1935. https://doi.org/10.1175/MWR-D-16-0417.1

Betts, A. K. (1975). Parametric interpretation of trade-wind cumulus budget studies. *J. Atmos. Sci.*, *32*, 1934–1945.

Betts, A. K. (1982). Saturation point analysis of moist convective overturning. *Journal of the Atmospheric Sciences*, *39*(7), 1484–1505. https://doi.org/10.1175/1520-0469(1982)039<1484:SPAOMC>2.0.CO;2

Betts, A. K. (1985). Mixing line analysis of clouds and cloudy boundary-layers. *Journal of the Atmospheric Sciences*, *42*(24), 2751–2763.

Betts, A. K., & Miller, M. (1986). A new convective adjustment scheme. part ii: Single column tests using gate wave, bomex and artic air-mass data sets. *Q. J. R. Meteorolog. Soc.*, *112*, 677–691.

Boatman, J. F., & Auer, A. H. (1983). The role of cloud top entrainment in cumulus clouds. *Journal of the Atmospheric Sciences*, *40*(6), 1517–1534. https://doi.org/0.1175/1520-0469(1983)040<1517:TROCTE>2.0.CO;2

Böing, S. J., Siebesma, A., Korpershoek, J., & Jonker, H. (2012). Detrainment in deep convection. *Geophys. Res. Lett.*, *39*. https://doi.org/10.1029/2012GL053735

Bosveld, F. C., Baas, P., Beljaars, A., Holtslag, A., de Arellano, J. V.-G., & van de Wiel, B. J. H. (2020). Fifty years of atmospheric boundary-layer research at cabauw serving weather, air quality and climate. *Boundary-Layer Meteorol.*, *177*, 583–612. https://doi.org/10.1007/s10546-020-00541-w

Bougeault, P. (1981). Modeling the trade-wind cumulus boundary layer. part i: Testing the ensemble cloud relations against numerical data. *J. Atmos. Sci.*, *38*, 2414–2428. https://doi.org/10.1175/1520-0469(1981)038<2414:MTTWCB>2.0.CO;2

Bretherton, C. S., McCaa, J. R., & Grenier, H. (2004). A new parameterization for shallow cumulus convectionn and its application to marine subtropical cloud-topped boundary layers. part i: Description and 1d results. *Mon. Weather Rev.*, *132*, 864–882.

Brown, A. R., Cederwall, R. T., Chlond, A., Duynkerke, P. G., Golaz, J.-C., J., Khairoutdinov, M., Lewellen, D. C., Lock, A. P., Macvean, M. K., Moeng, C.-H., Neggers, R. A. J., Siebesma, A. P., & Stevens, B. (2002). Large-eddy simulation of the diurnal cycle of shallow cumulus convection over land. *Q. J. R. Meteorolog. Soc.*, *128*, 1075–1094. https://doi.org/10.1256/003590002320373210

Cotton, W. (1975). On parameterization of turbulent transport in cumulus clouds. *J. Atmos. Sci.*, *32*, 548–564.

Couvreux, F., Hourdin, F., & Rio, C. (2010). Resolved versus parameterized boundary-layer plumes. part i: A parameterization-oriented conditional sampling in large-eddy simulations. *Boundary-Layer Meteorol.*, *134*, 441–458.

Cuijpers, J., & Bechtold, P. (1995). A simple parameterization of cloud water related variables for use in boundary layer models. *J. Atmos. Sci.*, *52*, 2486–2490. https://doi.org/10.1175/1520-0469(1995)052<2486:ASPOCW>2.0.CO;2

Cuijpers, J., & Duynkerke, P. (1993). Large-eddy simulation of trade-wind cumulus clouds. *J. Atmos. Sci.*, *50*, 3894–3908.

Cuxart, J., Bougeault, P., & Redelsperger, J.-L. (2000). A turbulence scheme allowing for mesoscale and large-eddy simulations. *Q. J. R. Meteorolog. Soc.*, *126*, 1–30. https://doi.org/10.1002/qj.49712656202

Dawe, J. T., & Austin, P. (2011a). The influence of the cloud shell on tracer budget measurements of les cloud entrainment. *J. Atmos. Sci.*, *68*, 2209–2920.

Dawe, J. T., & Austin, P. (2011b). Interpolation of les cloud surfaces for use in direct calculations of entrainment and detrainment. *Mon. Weather Rev.*, *139*, 444–456.

Derbyshire, S., Beau, I., Bechtold, P., Grandpeix, J.-Y., Piriou, J.-M., Redelsperger, J.-L., & Soares, P. (2004). Sensitivity of moist convection to environmental humidity. *Q. J. R. Meteorolog. Soc.*, *130*, 3055–3079.

Derbyshire, S., Maidens, A., Milton, S., Stratton, R., & Willett, M. (2011). Adaptive detrainment in a convective parameterization. *Q. J. R. Meteorolog. Soc.*, *137*, 1856–1871. https://doi.org/10.1002/qj.875

de Roode, S., Duynkerke, P., & Siebesma, A. (2000). Analogies between mass-flux and reynolds-averaged equations. *J. Atmos. Sci.*, *57*, 1585–1598. https://doi.org/10.1175/1520-0469(2000)057<1585:ABMFAR>2.0.CO;2

de Roode, S., Sandu, I., van der Dussen, J., Ackerman, A., Blossey, P., Jarecka, D., Lock, A., Siebesma, A., & Stevens, B. (2016). Large-eddy simulations of euclipse–gass lagrangian stratocumulus-to-cumulus transitions: Mean state, turbulence, and decoupling. *J. Atmos. Sci.*, *73*, 2485–2508. https://doi.org/10.1175/JAS-D-15-0215.1

de Roode, S., Siebesma, A., Jonker, H., & de Voogd, Y. (2012). Parameterization of the vertical velocity equation for shallow cumulus clouds. *Mon. Weather Rev.*, *140*, 2424, 2436. https://doi.org/10.1175/MWR-D-11-00277.1

de Rooy, W. C. (2014). The fog above sea problem: Part 1 analysis [(last access: 11 January 2022)]. *ALADIN-HIRLAM Newsletter*, *2*, 9–16. http://hirlam.org/index.php/hirlam-documentation/doc_download/1490-aladin-hirlam-newsletter-no-2-april-2014

de Rooy, W. C., Bechtold, P., Fr ohlich, K., Hohenegger, C., Jonker, H., Mironov, D., Siebesma, A. P., Teixeira, J., & Yano, J. (2013). Entrainment and detrainment in cumulus convection: An overview. *Q. J. R. Meteorolog. Soc.*, *139*, 1–19. https://doi.org/10.1002/qj.1959

de Rooy, W. C., de Bruijn, E., Tijm, A., Neggers, R., Siebesma, A., & Barkmeijer, J. (2010). Experiences with harmonie at knmi [(last access: 11 January 2022)]. *Hirlam Newsletter*, *56*, 21–29. http://hirlam.org/index.php/hirlam-documentation/doc_download/1793-hirlam-nl56-nov2010

de Rooy, W. C., de Vries, H., & et al. (2017). Harmonie verification and evaluation [(last access: 11 January 2022)]. *Hirlam Technical report*, (70), 93. http://hirlam.org/index.php/publications-54/hirlam-technical-reports-a/doc_download/1805-hirlam-technicalreport-70

de Rooy, W. C., & Kok, K. (2004). A combined physical–statistical approach for the downscaling of model wind speed. *Weather Forecasting*, *19*, 485–495. https://doi.org/10.1175/1520-0434(2004)019<0485:ACPAFT>2.0.CO;2

de Rooy, W. C., & Siebesma, A. (2008). A simple parameterization for detrainment in shallow cumulus. *Mon. Weather Rev.*, *136*, 560–576. https://doi.org/10.1175/2007MWR2201.1

de Rooy, W. C., & Siebesma, A. (2010). Analytical expressions for entrainment and detrainment in cumulus convection. *Q. J. R. Meteorolog. Soc.*, *136*, 1216–1227. https://doi.org/10.1002/qj.640

de Rooy, W. C., Siebesma, A., Baas, P., Lenderink, G., de Roode, S., de Vries, H., van Meijgaard, E., Meirink, J. F., Tijm, S., & van 't Veen, B. (2022). Model development in practice: A comprehensive update to the boundary layer

schemes in harmonie-arome cycle 40. *Geosci. Model Dev.*, *15*, 1513–1543. https://doi.org/10.5194/gmd-15-1513-2022

Dorrestijn, J. (2016). *Stochastic convection parameterization*. https://doi.org/10.4233/uuid:d80246c5-41dc-451d-9beb-c293c445a8f3

Duynkerke, P. (1991). Radiation fog: A comparison of model simulation with detailed observations. *Mon. Weather Rev.*, *119*, 324–341.

Dyer, A. (1974). A review of flux-profile relationships. *Boundary-Layer Meteorol.*, *7*, 363–372. https://doi.org/10.1007/BF00240838

Frogner, I., Andrae, U., Bojarova, J., Callado, A., Escribà, P., Feddersen, H., Hally, A., Kauhanen, J., Randriamampianina, R., Singleton, A., Smet, G., van der Veen, S., & Vignes, O. (2019). Harmoneps—the harmonie ensemble prediction system. *Weather and Forecasting*, *34*, 1909–1937.

Golaz, J., Larson, V. E., & Cotton, W. R. (2002). A pdf-based model for boundary layer clouds. part i: Method and model description. *J. Atmos. Sci.*, *59*, 3540–3551.

Grant, A. (2001). Cloud-base fluxes in the cumulus-capped boundary layer. *Q. J. R. Meteorolog. Soc.*, *127*, 407–422. https://doi.org/10.1002/QJ.49712757209

Grant, A., & Brown, A. (1999). A simililarity hypothesis for shallow cumulus transports. *Q. J. R. Meteorolog. Soc.*, *125*, 1913–1936.

Gregory, D. (2001). Estimation of entrainment rate in simple models of convective clouds. *Q. J. R. Meteorolog. Soc.*, *127*, 53–72.

Gregory, D., Morcrette, J.-J., Jakob, C., Beljaars, A. C. M., & Stockdale, T. (2000). Revision of convection, radiation and cloud schemes in the ecmwf integrated forecasting system. *Q. J. R. Meteorolog. Soc.*, *126*, 1685–1710.

Gregory, D., & Rowntree, P. (1990). A mass flux convection scheme with representation of cloud ensemble characteristics and stability- dependent closure. *Mon. Weather Rev.*, *118*, 1483–1506.

Helfer, K. C., Nuijens, L., & Dixit, V. V. (2021). The role of shallow convection in the momentum budget of the trades from large-eddy-simulation hindcasts. *Q. J. R. Meteorolog. Soc.*, *147*, 2490–2505. https://doi.org/10.1002/qj.4035

Heus, T., & Jonker, H. J. J. (2008). Subsiding shells aroud shallow cumulus clouds. *J. Atmos. Sci.*, *65*, 1003–1018.

Heus, T., Jonker, H. J. J., van den Akker, H., Griffith, E., Koutek, M., & Post, F. (2009). A statistical approach to the life cycle analysis of cumulus clouds selected in a vitual reality environment. *J. Geophys. Res.*, *114*, 19. https://doi.org/10.1029/2008JD010917

Heus, T., Pols, C. F. J., Jonker, H. J. J., Van den Akker, H. E. A., & Lenschow, D. H. (2009). Observational validation of the compensating mass flux through the shell around cumulus clouds. *QRMS*, *135*, 101–112. https://doi.org/10.1256/qj.08.66

Heus, T., van Dijk, G., Jonker, H. J. J., & van den Akker, H. (2008). Mixing in shallow cumulus clouds studied by lagrangian particle tracking. *J. Atmos. Sci.*, *65*, 2581–2597.

Heus, T., van Heerwaarden, C., Jonker, H., Siebesma, A., Axelsen, S., van den Dries, C., Geoffroy, O., Moene, A., Pino, D., de Roode, S., & de Arellano, J. V.-G. (2010). Formulation of the dutch atmospheric large-eddy simulation (dales) and overview of its applications. *Geosci. Model Dev.*, *3*, 415–444. https://doi.org/10.5194/gmd-3-415-2010

Holland, J. (1972). Comparative evaluation of some bomex measurements of sea surface evaporation, energy flux and stress. *J. Phys. Oceanogr.*, *2*, 476–486.

Holland, J., & Rasmusson, E. (1973). Measurement of atmospheric aass, energy and momentum budgets over a 500-kilometer square of tropical ocean. *Mon. Weather Rev.*, *101*, 44–55. https://doi.org/10.1175/1520-0493(1973)101<0044:MOTAME>2.3.CO;2

Holloway, C., & Neelin, J. (2009). Moisture vertical structure, column water vapor, and tropical deep convection. *J. Atmos. Sci.*, *66*, 1665–1683.

Holton, J. (1973). A one-dimensional cumulus model including pressure perturbations. *Mon. Weather Rev.*, *101*, 201–205.

Honnert, R., Masson, V., & Couvreux, F. (2011). A diagnostic for evaluating the representation of turbulence in atmospheric models at the kilometric scale. *J. Atmos. Sci.*, *68*, 3112–3131. https://doi.org/10.1175/JAS-D-11-061.1

Houghton, H., & Cramer, H. (1951). A theory of entrainment in convective currents. *J. Meteor.*, *8*, 95–102.

Jakob, C. (2003). An improved strategy for the evaluation of cloud parametrizations in gcm's. *Bull. of the Amer. Met. Soc.*, *84*, 1387–1401.

Jakob, C. (2010). Accelerating progress in global atmospheric model development through improved parameterizations: Challenges, opportunities, and strategies. *Bull. of the Amer. Met. Soc.*, *91*, 869–875. https://doi.org/10.1175/2009BAMS2898.1

Jakob, C., & Siebesma, A. (2003). A new subcloud model for mass-flux convection schemes; influence on triggering, updraught properties and model climate. *Mon. Weather Rev.*, *131*, 2765–2778.

Janjic, Z. I. (1994). The step-mountain eta coordinate model: Further developments of the convection, viscous sublayer, and turbulence closure schemes. *Mon. Weather Rev.*, *122*, 927–945.

Jensen, J. B., Austin, P. H., Baker, M. B., & Blyth, A. M. (1985). Turbulent mixing, spectral evolution and dynamics in a warm cumulus cloud. *Journal of the Atmospheric Sciences*, *42*(2), 173–192. https://doi.org/10.1175/1520-0469(1985)042<0173:TMSEAD>2.0.CO;2

Jonker, H. J. J., Heus, T., & Sullivan, P. P. (2008). A refined view of vertical mass transport by cumulus convection. *J. Geophys. Res.*, *35*. https://doi.org/10.1029/2007GL032606

Jonker, H., Verzijlbergh, R., Heus, T., & Siebesma, A. (2006). The influence of the sub-cloud moisture field on cloud size distributions and the consequences for entrainment. *Extended abstract from the 17th Symposium on Boundary Layers and Turbulence, San Diego, USA*, 1–4. http://ams.confex.com/ams/pdfpapers/111021.pdf

Jonker, S. (2005). *Evaluation study of the kain fritsch convection scheme* (KNMI Technical report, TR275). KNMI.

Kähnert, M., Sodemann, H., de Rooy, W. C., & Valkonen, T. (2021). On the utility of individual tendency output: Revealing interactions between parameterized processes during a marine cold air outbreak. *Weather Forecasting*, *36*, 1985–2000. https://doi.org/10.1175/WAF-D-21-0014.1

Kain, J. S., & Fritsch, J. M. (1990). A one-dimensional entraining/detraining plume model and its application in convective parameterization. *J. Atmos. Sci.*, *47*, 2784–2802. https://doi.org/10.1175/1520-0469(1990)047<2784:AODEPM>2.0.CO;2

Kain, J. S., & Fritsch, J. (1993). Convective parameterization for mesoscale models. The Kain-Fritsch scheme. *Meteorological Monographs*, *24*, 165–170.

Kain, J. (2004). The kain-fritsch convective parameterization: An update. *J. Appl. Meteor.*, *43*, 170–181.

Khairoutdinov, M., Krueger, S. K., Moeng, C., Bogenschutz, P., & Randall, D. (2009). Large-eddy simulation of maritime deep tropical convection. *J. Adv. Model Earth Syst.*, *1*, 13pp.

Khairoutdinov, M., & Randall, D. (2006). High-resolution simulation of shallow to deep convection transition over land. *J. Atmos. Sci.*, *63*, 3421–3436.

Klocke, D., Pincus, R., & Quaas, J. (2011). On constraining estimates of climate sensitivity with present-day observations through model weighting. *J. Climatol.*, *24*, 6092–6099.

Köhler, M., Ahlgrimm, M., & Beljaars, A. (2011). Unified treatment of dry convective and stratocumulus-topped boundary layers in the ecmwf model. *Q. J. R. Meteorolog. Soc.*, *137*, 43–57. https://doi.org/10.1002/qj.713

Kuang, Z., & Bretherton, C. S. (2006). A mass-flux scheme view of a high-resolution simulation of a transition from shallow to deep cumulus convection. *J. Atmos. Sci.*, *63*, 1895–1909.

Kuo, H. L. (1962). On the controlling influences of eddy diffusion on thermal convection. *J. Atmos. Sci.*, *19*, 236–243.

Lamer, K., Kollias, P., & Nuijens, L. (2015). Observations of the variability of shallow trade wind cumulus cloudiness and mass flux. *J. Geophys. Res. D: Atmos.*, *120*, 6161–6178. https://doi.org/10.1002/2014JD022950

Lamontagne, R. G., & Telford, J. W. (1983). Cloud top mixing in small cumuli. *Journal of the Atmospheric Sciences*, *40*(9), 2148–2156. https://doi.org/10.1175/1520-0469(1983)040<2148:CTMISC>2.0.CO;2

Lancz, D., Szintai, B., & Honnert, R. (2018). Modification of a parametrization of shallow convection in the grey zone using a mesoscale model. *BLM*, *169*, 483–503. https://doi.org/10.1007/s10546-018-0375-1

Lappen, C.-L., & Randall, D. (2001). Toward a unified parameterization of the boundary layer and moist convection. part ii: Lateral mass exchanges and subplume-scale fluxes. *J. Atmos. Sci.*, *58*, 2037–2051.

Lenderink, G., & Holtslag, A. (2004). An updated length-scale formulation for turbulent mixing in clear and cloudy boundary layers. *QJRMS*, *130*, 3405–3427. https://doi.org/10.1256/qj.03.117

Lenderink, G., & Siebesma, A. (2000). Combining the mass flux approach with a statistical cloud scheme. *Proceedings of 14th Symposium on Boundary Layers and Turbulence, Aspen, USA*, 66–69.

Lenderink, G., Siebesma, A., Cheinet, S., Irons, S., Jones, C., Marquet, P., Muller, F., Olmeda, D., Calvo, J., Sanchez, E., & Soares, P. (2004). The diurnal cycle of shallow cumulus clouds over land: A single-column model intercomparison study. *QJRMS*, *130*, 3339–3364. https://doi.org/10.1256/qj.03.122

Li, D., & Bou-Zeid, E. (2011). Coherent structures and the dissimilarity of turbulent transport of momentum and scalars in the unstable atmospheric surface layer. *Boundary-Layer Meteorol.*, *140*, 243–262. https://doi.org/10.1007/s10546-011-9613-5

Lin, C., & Arakawa, A. (1997). The macroscopic entrainment processes of simulated cumulus ensemble. part 1: Entrainment sources. *J. Atmos. Sci.*, *54*, 1027–1043.

List, R., & Lozowski, E. (1970). Pressure pertubations and buoyancy in convective clouds. *J. Atmos. Sci.*, *27*, 168–170.

Ludlam, F. H., & Scorer, R. (1953). Convection in the atmosphere. *Q. J. R. Meteorolog. Soc.*, *79*, 94–103.

Mellor, G. (1977). Subgrid scale condensation in models of nonprecipitating clouds. *J. Atmos. Sci.*, *34*, 1483–1484.

Mironov, D. (2009). Turbulence in the lower troposphere: Second-order closure and mass-flux modelling frameworks. In *Interdisciplinary aspects of turbulence* (pp. 161–221). Springer-Verlag.

Morton, B., Taylor, G., & Turner, J. (1956). Turbulent gravitational convection from maintained and instantaneous sources. *Proc. Roy. Soc. London*, 1–23.

Murphy, J., Sexton, D. H., Barnett, D. N., Jones, G. S., Webb, M. J., Collins, M., & Stainforth, D. A. (2004). Quantification of modelling uncertainties in a large ensemble of climate change simulations. *Nature*, *430*, 768–772.

Neggers, R., Ackerman, A. S., Angevine, W. M., Bazile, E., Beau, I., Blossey, P. N., Boutle, I. A., de Bruijn, C., Cheng, A., van der Dussen, J., Fletcher, J., Gesso, S. D., Jam, A., Kawai, H., Kumar, S., Larson, V. E., Lefebvre, M.-P., Lock, A. P., Meyer, N. R., … Xu, K.-M. (2017). Single-column model simulations of subtropical marine boundary-layer cloud transitions under weakening inversions. *JAMES*, *9*, 2385–2412. https://doi.org/10.1002/2017MS001064

Neggers, R., Duynkerke, P., & Rodts, S. (2003). Shallow cumulus convection, a validation of large-eddy simulation against aircraft and landsat observations. *Q. J. R. Meteorolog. Soc.*, *129*, 2671–2696.

Neggers, R., Köhler, M., & Beljaars, A. (2009). A dual mass flux framework for boundary layer convection. part i: Transport. *J. Atmos. Sci.*, *66*, 1464–1487. https://doi.org/10.1175/2008JAS2636.1

Neggers, R., Siebesma, A., & Jonker, H. (2002). A multiparcel method for shallow cumulus convection. *J. Atmos. Sci.*, *59*, 1655–1668. https://doi.org/10.1175/1520-0469(2002)059<1655:AMMFSC>2.0.CO;2

Neggers, R., Siebesma, A., Lenderink, G., & Holtslag, A. (2004). An evaluation of mass flux closures for diurnal cycles of shallow cumulus. *Mon. Weather Rev.*, *132*, 2525–2536.

Nordeng, T. E. (1994). *Extended versions of the convective parameterization scheme at ecmwf and their impact ont he mean and transient activity of the model in the tropics* [Technical memorandum No. 206, ECMWF, 41pp.].

Paluch, I. R. (1979). The entrainment mechanism in colorado cumili. *J. Atmos. Sci.*, *36*, 2467–2478.

Quaas, J. (2012). Evaluating the "critical relative humidity" as a measure of subgrid-scale variability of humidity in general circulation model cloud cover parametrizations using satellite data. *J. Geophys. Res. D: Atmos.*, *117*, 1–10. https://doi.org/10.1029/2012JD017495

Raga, G., Jensen, J., & Baker, M. (1990). Characteristics of cumulus band clouds off the coast of hawaii. *J. Atmos. Sci.*, *47*, 338–355.

Randall, D. A., Krueger, S. K., Bretherton, C. S., Curry, J. A., Moncrieff, M., Ryan, B. F., Miller, M. J., Rossow, W. B., Tselioudis, G., & Wielicki, B. (2003). Confronting models with data: The gewex clouds systems study. *Bull. of the Amer. Met. Soc.*, *84*, 455–469.

Randall, D. (1980). Conditional instability of the first kind upside-down. *J. Atmos. Sci.*, *37*, 125–130.

Randall, D., & Huffman, G. (1982). Entrainment and detrainment in a simple cumulus cloud model. *J. Atmos. Sci.*, *39*, 2793–2806.

Rauber, R. M., Stevens, B., III, H. T. O., Knight, C., Albrecht, B. A., Blyth, A. M., Fairall, C. W., Jensen, J. B., Lasher-Trapp, S. G., Mayol-Bracero, O. L., Vali, G., Anderson, J. R., Baker, B. A., Bandy, A. R., Burnet, E., Brenguier, J.-L., Brewer, W. A., Brown, P. R. A., Chuang, P., ... ZuidemaRauber, P. (2007). Rain in shallow cumulus over the ocean: The rico campaign. *Bull. of the Amer. Met. Soc.*, *88*, 1912–1928.

Raymond, D., & Blyth, A. (1986). A stochastic mixing model for nonprecipitating cumulus clouds. *J. Atmos. Sci.*, *43*, 2708–2718.

Redelsperger, J. L., & Sommeria, G. (1981). Methode de representation de la turbulence d'echelle inferieure a la maille pour un modele tri-dimensionnel de convection nuageuse. *Boundary-Layer Meteorol.*, *21*, 509–530. https://doi.org/10.1007/BF02033598

Reuter, G. W. (1986). A historical review of cumulus entrainment studies. *Bull. of the Amer. Met. Soc.*, *67*(2), 151–154.

Rio, C., & Hourdin, F. (2008). A thermal plume model for the convective boundary layer: Representation of cumulus clouds. *J. Atmos. Sci.*, *65*, 407–424. https://doi.org/10.1175/2007JAS2256.1

Rio, C., Hourdin, F., Couvreux, F., & Jam, A. (2010). Resolved versus parameterized boundary-layer plumes. part ii: Continuous formulations of mixing rates for mass-flux schemes. *BLM*, 469–483. https://doi.org/10.1007/s10546-010-9478-z

Romps, D. M. (2010). A direct measurement of entrainment. *J. Atmos. Sci.*, *67*, 1908–1927.

Rougier, J., Sexton, D., Murphy, J., & Stainforth, D. (2009). Analyzing the climate sensitivity of the hadsm3 climate model using ensembles from different but related experiments. *J. Climate*, *22*, 3540–3557.

Saggiorato, B., Nuijens, L., Siebesma, A. P., de Roode, S., Sandu, I., & Papritz, L. (2020). The influence of convective momentum transport and vertical wind shear on the evolution of a cold air outbreak. *J. Adv. Model. Earth Syst.*, *12*, 1–22. https://doi.org/10.1029/2019MS001991

Schlemmer, L., Bechtold, P., Sandu, I., & Ahlgrimm, M. (2017). Uncertainties related to the representation of momentum transport in shallow convection. *J. Adv. Model. Earth Syst.*, *9*, 1269–1291. https://doi.org/10.1002/2017MS000915

Seity, Y., Brousseau, P., Malardel, S., Hello, G., Bénard, P., Bouttier, F., Lac, C., & Masson, V. (2011). The arome-france convective-scale operational model.

Mon. Weather Rev., *139*, 976–991. https://doi.org/10.1175/2010MWR3425.1

Siebesma, A. (1998). Shallow cumulus convection. In E. Plate, E. Fedorovich, X. Viegas, & J. Wyngaard (Eds.), *Buoyant convection in geophysical flows* (pp. 441–486). Kluwer Academic Publishers.

Siebesma, A., Bretherton, C., Brown, A., Chlond, A., Cuxart, J., Duynkerke, P., Jiang, H., Khairoutdinov, M., Lewellen, D., Moeng, C.-H., Sanchez, E., Stevens, B., & Stevens, D. E. (2003). A large eddy simulation intercomparison study of shallow cumulus convection. *J. Atmos. Sci.*, *60*, 1201–1219. https://doi.org/10.1175/1520-0469(2003)60<1201:ALESIS>2.0.CO;2

Siebesma, A., & Cuijpers, J. (1995). Evaluation of parametric assumptions for shallow cumulus convection. *J. Atmos. Sci.*, *52*, 650–666. https://doi.org/10.1175/1520-0469(1995)052<0650:EOPAFS>2.0.CO;2

Siebesma, A., & Holtslag, A. (1996). Model impacts of entrainment and detrainment rates in shallow cumulus convection. *J. Atmos. Sci.*, *53*, 2354–2364.

Siebesma, A., & Jonker, H. (2000). Anomalous scaling of cumulus cloud boundaries. *Physical Review Letters*, *85*, 214–217. https://doi.org/10.1103/PhysRevLett.85.214

Siebesma, A., Soares, P., & Teixeira, J. (2007). A combined eddy diffusivity mass-flux approach for the convective boundary layer. *JAS*, *64*, 1230–1248. https://doi.org/10.1175/JAS3888.1

Siebesma, A., & Teixeira, J. (2000). An advection-diffusion scheme for the convective boundary layer, description and 1d-results. *Proceedings of 14th Symposium on Boundary Layers and Turbulence, Aspen, USA*, 133–136.

Simpson, J., & Wiggert, V. (1969). Models of precipitating cumulus towers. *Mon. Weather Rev.*, *97*, 471–489.

Soares, P., Miranda, P., Siebesma, A., & J.Teixeira. (2004). An eddy-diffusivity/mass-flux parameterization for dry and shallow cumulus convection. *Q. J. R. Meteorolog. Soc.*, *130*, 3365–3384. https://doi.org/10.1256/QJ.03.223

Sommeria, G., & Deardorff, J. (1977). Subgrid-scale condensation in models of non-precipitating clouds. *J. Atmos. Sci.*, *34*, 344–355. https://doi.org/10.1175/1520-0469(1977)034<0344:SSCIMO>2.0.CO;2

Squires, P. (1958). The microstructure and colloidal stability of warm clouds. part i. the relation between structure and stability. *Tellus*, *10*, 256–261.

Squires, P., & Turner, J. (1962). An entraining jet model for cumulo-nimbus updraughts. *Tellus*, *16*, 422–434.

Stevens, B., Ackerman, A., Albrecht, B., Brown, A., Chlond, A., Cuxart, J., Duynkerke, P., Lewellen, D., Macvean, M., Neggers, R., Sanchez, E., Siebesma, A., & Stevens, D. (2001). Simulations of trade-wind cumuli under a strong inversion. *J. Atmos. Sci.*, *58*, 1870–1891.

Stevens, B., Satoh, M., Auger, L., Biercamp, J., Bretherton, C. S., Chen, X., Düben, P., Judt, F., Khairoutdinov, M., Klocke, D., Kodama, C., Kornblueh, L., Lin, S.-J., Neumann, P., Putman, W. M., Röber, N., Shibuya, R., Vanniere, B., Vidale, P. L., … Zhou, L. (2019). Dyamond: The dynamics of the atmospheric general circulation modeled on non-hydrostatic domains. *Prog. Earth Planet. Sci.*, *6*(1), 61. https://doi.org/10.1186/s40645-019-0304-z

Stommel, H. (1947). Entrainment of air into a cumulus cloud. *J. Meteor.*, *4*, 91–94.

Stull, R. (1988). *An introduction to boundary layer meteorology*. Kluwer Academic Publishers.

Sušelj, K., Teixeira, J., & Chung, D. (2013). A unified model for moist convective boundary layers based on a stochastic eddy-diffusivity/mass-flux parameterization. *J. Atmos. Sci.*, *70*(7), 1929–1953. https://doi.org/10.1175/JAS-D-12-0106.1

Taylor, G. R., & Baker, M. B. (1991). Entrainment and Detrainment In Cumulus Clouds. *Journal of the Atmospheric Sciences*, *48*(1), 112–121. https://doi.org/10.1175/1520-0469(1991)048<0112:EADICC>2.0.CO;2

Tiedtke, M. (1989). A comprehensive mass flux scheme for cumulus parameterization in large-scale models. *Mon. Weather Rev.*, *177*, 1779–1800.

Tompkins, A. (2005). *The parametrization of cloud cover* (ECMWF Technical memorandum Moist Processed Lecture Note Series) [(last access: 11 January 2022)]. European Center for Medium-Range Weather Forecasts. https://www.ecmwf.int/node/16958

Tudor, M., & Mallardel, S. (2004). *Mesonh - arome upper air physics* (tech. rep.) [(last access: 11 January 2022)]. Croatian HydroMeteorological Service. https://www.rclace.eu/File/Physics/2004/Martina_Tudor.pdf

Turner, J. S. (1963). The motion of buoyant elements in turbulent surroundings. *J. Fluid Mech.*, *16*, 1–16.

Unden, P., Rontu, L., Jarvinen, H., Lynch, P., Calvo, J., Cats, G., Cuxart, J., K.Eerola, Fortelius, C., Garcia-Moya, J. A., Jones, C., Lenderink, G., McDonald, A., McGrath, R., Navascues, B., Nielsen, N. W., Odegaard, V., Rodriguez, E., Rummukainen, M., … Tijm, S. (2002). *Hirlam-5 scientific documentation.* (tech. rep.). SMHI.

van Meijgaard, E., van Ulft, B., van de Berg, W., Bosveld, F. C., van den Hurk, B., Lenderink, G., & Siebesma, A. (2008). *The knmi regional atmospheric climate model racmo version 2.1.* (tech. rep.) [(last access: 11 January 2022)]. KNMI, Technical Report 302, De Bilt, The Netherlands, 43 pp. https://www.knmi.nl/kennis-en-datacentrum/publicatie/the-knmi-regional-atmospheric-climate-model-racmo-version-2-1

van Meijgaard, E., van Ulft, L., Lenderink, G., de Roode, S., Wipfler, L., Boers, R., & Timmermans, R. (2012). *Refinement and application of a regional atmo-*

spheric model for climates scenario calculations of western europe (tech. rep.) [(last access: 11 January 2022), KVR Research Rep. 054/12, 44 pp]. Wageningen University. https://library.wur.nl/WebQuery/wurpubs/fulltext/312258

Voogd, Y. (2009). *Parameterization of the vertical velocity in shallow cumulus clouds* [Department of Multi-scale Physics, Delft University of Technology. Bachelor Thesis].

Wagner, T., & Graf, H. (2010). An ensemble cumulus convection parameterisation with explicit cloud treatment. *J. Atmos. Sci.*, *67*, 3854–3869.

Warner, J. (1955). The water content of cumuliform clouds. *Tellus*, 449–457.

Wyngaard, J., Cote, O. R., & Izum, Y. (1971). Local free convection, similarity, and the budgets of shear stress and heat flux. *J. Atmos. Sci.*, *28*, 1171–1182. https://doi.org/10.1175/1520-0469(1971)028<1171:LFCSAT>2.0.CO;2

Yanai, M., Esbensen, S., & Chu, J. (1973). Determination of bulk properties of tropical cloud clusters from large-scale heat and moisture budgets. *JAS*, *30*, 611–627.

Yano, J.-I., Guichard, F., Lafore, J.-.-P., Redelsperger, J.-L., & Bechtold, P. (2004). Estimations of massfluxes for cumulus parameterizations from high-resolution spatial data. *JAS*, *61*, 829–842.

Zhao, M., & Austin, P. (2005a). Life cycle of numerically simulated shallow cumulus clouds. part i: Transport. *J. Atmos. Sci.*, *62*, 1269–1290.

Zhao, M., & Austin, P. (2005b). Life cycle of numerically simulated shallow cumulus clouds. part ii: Mixing dynamics. *J. Atmos. Sci.*, *62*, 1291–1310.

CURRICULUM VITÆ

Ik ben geboren op 13 november 1963 in Breda als verreweg de jongste van 4. Omdat mijn moeder al overleed toen ik 2 jaar oud was is het overgrote deel van mijn liefdevolle opvoeding door mijn vader gedaan. Anderhalf jaar voor het einde van mijn lagere school verhuisden we naar Veghel waar ik in 1982 mijn Atheneum B diploma haalde op het Zwijssen College. De overgang van het schoolse karakter op de middelbare school naar het vrije studentenleven was voor mij wat te groot. Na 1 jaar op de TU Eindhoven stapte ik over naar de HTS Technische Natuurkunde. In 1988 studeerde ik daar af. Ook toen al had ik interesse in promotieonderzoek (dat was net direct vanuit de HTS mogelijk geworden). Interessante promotieplekken lagen echter niet voor het oprapen. En hoewel het grotendeels werkeloze leven mij uitstekend beviel besloot ik te solliciteren. In oktober 1989 werd ik aangenomen op het KNMI. Na enige tijd begon ik tijdens mijn werk aan een studie op de universiteit Utrecht, een mogelijkheid die het KNMI mij bood en die ik nog altijd waardeer. Samen met mijn KNMI collega Cisco de Bruijn zaten we duidelijk als ouwe lullen tussen de studenten maar ik kijk niettemin met veel plezier terug op de colleges. In maart 1992 behaalde ik het propedeutisch examen Natuurkunde (cum laude) en in augustus 1997 het vrij doctoraal examen meteorologie en fysische oceanografie (cum laude). Op het KNMI houd ik mij als onderzoeker al geruime tijd bezig met het verbeteren van de fysica in atmosfeermodellen, in het bijzonder op het gebied van convectie, turbulentie en wolken. Mijn bijdrage zit in het leggen van de wetenschappelijke basis, het implementeren hiervan in de modelcode en tot slot het optimaliseren en verifiëren van de betreffende fysicaschema's. Dit alles in nauwe nationale en internationale samenwerking, met name binnen het Hirlam consortium.

LIST OF PUBLICATIONS

de Rooy, W. and A. Siebesma, 2008: A simple parameterization for detrainment in shallow cumulus., *Mon. Wea. Rev.*, **136**, 560–576.

de Rooy, W. and A. Siebesma, 2010: Analytical expressions for entrainment and detrainment in cumulus convection. *Quart. J. Roy. Met. Soc.*, **136**, 1216–1227.

de Rooy, W., P. Bechtold, K. Fröhlich, C. Hohenegger, H.J.J. Jonker, D. Mironov, A. P. Siebesma, J. Teixeira, J.I. Yano, 2013: Entrainment and detrainment in cumulus convection: An overview. *Quart. J. Roy. Met. Soc.*, **139**, 1–19.

de Rooy, W. C., A.P. Siebesma, P. Baas, G. Lenderink, S.R. de Roode, H. de Vries, E. van Meijgaard, J. F. Meirink, S. Tijm, B. van 't Veen, 2022: Model development in practice: A comprehensive update to the boundary layer schemes in harmonie-arome cycle 40. *Geosci. Model Dev.*, **16**, 1–51.

de Rooy, W. and K. Kok, 2004: A Combined Physical Statistical Approach for the Downscaling of Model Wind Speed. *Weather and Forecasting*, **19**, 485-495.

de Bruijn, E.I.F., and W. C. de Rooy, 2012: Evaluation of HARMONIE in the KNMI Parameterisation Testbed. *Adv. Sci. Res.*, **8**, 167–170.

Holtslag, A., E. van Meijgaard, and W. de Rooy, 1995: A comparison of boundary layer diffusion schemes in unstable conditions over land. *Boundary-Layer Meteorology*, **76**, 69–95.

de Rooy, W. C. and A. Holtslag, 1999: Estimation of surface radiation and energy flux densities from single-level weather data. *J. Appl. Meteor. Clim.*, **38**, 526–540.

de Rooy, W., J.-I. Yano, P. Bechtold, and S. Böing, 2015: Entrainment and detrainment formulations for mass-flux parameterization. *Parameterization of Atmospheric Convection*, R. S. Plant and J.-I. Yano, Eds., World Scientific, 273–323.

Gryning, S.-E., E. Batchvarova, A. Baklanov, G. Grell, W. C. de Rooy, R. San José, J. Struzewska, M. Tombrou, R. S. Sokhi, 2018: Representation of boundary-layer,

radiation, cloud and aersosol processes in mesoscale models. *Mesoscale Modelling for Meteorological and Air Pollution Applications*, R. S. Sokhi, A. Baklanov, and K. H. Schlüunzen, Eds., Anthem Press, 69–106

Bengtsson, L., et al., U. Andrae, T. Aspelien, Y. Batrak, J. Calvo, W. de Rooy, E. Gleeson, B. Hansen-Sass, M. Homleid, M. Hortal, K.-I. Ivarsson, G. Lenderink, S. Niemel a, K. P. Nielsen, J. Onvlee, L. Rontu, P. Samuelsson, D. Santos Munoz, A. Subias, S. Tijm, V. Toll, X. Yang, M. Koltzow, 2017: The harmonie–arome model configuration in the aladin–hirlam nwp system. *Mon. Wea. Rev.*, **145**, 1919–1935.

Neggers, R., A. S. Ackerman, W. M. Angevine, E. Bazile, I. Beau, P. N. Blossey, I. A. Boutle, C. de Bruijn, A. Cheng, J. van der Dussen, J. Fletcher, S. Dal Gesso, A. Jam, H. Kawai, S. Kumar, V. E. Larson, M.-P. Lefebvre, A. P. Lock, N. R. Meyer, S. R. de Roode, W. de Rooy, I. Sandu, H. Xiao, K.-M. Xu, 2017: Single-column model simulations of subtropical marine boundary-layer cloud transitions under weakening inversions. *J. Adv. Model Earth Sy.*, **9**, 2385–2412.

de Rooy, W.C., H. de Vries, C. van Dalum, S. de Haan, J. Meirink, G. Lenderink, G. van Marseille, R. Scheele, 2017: Harmonie verification and evaluation. *Hirlam Technical report*, **70**, 93pp.

de Rooy, W.C., K. Kok, A.B.C. Tijm, D.H.P. Vogelezang, 2006: Een ontspoord Hirlam model? *Meteorologica*, 7-10

Kähnert, M., H. Sodemann, W. de Rooy, T. Valkonen, 2021: On the utility of individual tendency output: Revealing interactions between parameterized processes during a marine cold air outbreak. *Weather and Forecasting*, **36**, 1985–2000

Contreras Osorio, S., D. Martín Pérez, K.I. Ivarsson, K. Pagh Nielsen, W. C. de Rooy, E. Gleeson, E. McAufield, 2022: Impact of the Microphysics in HARMONIE-AROME on Fog. *Atmosphere*, **13**, 2127

A. Tsiringakisa, I. Frogner, W. de Rooy , U. Andrae, A. Hally, S. Contreras Osorio, S. van der Veen, J. Barkmeijer, 2023: An Update to the Stochastically Perturbed Parametrizations Scheme of HarmonEPS. Submitted to *Month. Wea. Rev.*.

Contreras Osorio, S., D. Martín Pérez, K.I. Ivarsson, K. Pagh Nielsen, W.C. de Rooy, E. Gleeson, E. McAufield, 2022: Impact of the Microphysics in HARMONIE-AROME on Fog. *Atmosphere*, **13**, 2127

DANKWOORD

Vele jaren kreeg ik de vraag: "Hoe gaat het met je promotie?" Mijn antwoord kwam altijd op hetzelfde neer: "Door andere werkzaamheden op het KNMI kom ik er nauwelijks aan toe maar volgend jaar...misschien?" Na verloop van tijd kreeg ik de vraag steeds minder, waarschijnlijk wilde men mij sparen. Maar nu ligt het proefschrift er dus toch!

Met de promotie verandert er voor mij en mijn werkzaamheden waarschijnlijk niets. Dat ik toch heb doorgezet heeft een aantal redenen. De eerste reden heeft te maken met degene aan wie ik het proefschrift heb opgedragen, mijn vader. Hoewel hij er zelf als geen ander van overtuigd was dat er na de dood niets is, en er dus niks van mee zal krijgen, zou hij deze promotie zeer hebben gewaardeerd. Mij en mijn broers stimuleerde hij altijd om kennis te vergaren en te studeren (op de middelbare school wel de nadruk leggend op muziek en wiskunde) om zo de kansen te pakken die hij zelf nooit gehad heeft. Nog belangrijker voor mij was zijn liefdevolle opvoeding en het via voorleven bijbrengen van liefde voor de medemens (ongeacht afkomst), dieren (hij was veganist, toen nog heel bijzonder) en de natuur. Ongemerkt pluk ik, en daarmee mijn zoons, daar nog steeds de vruchten van. Bedankt pa. Een prozaïschere reden voor de promotie is dat het een mooie afronding vormt en "last but not least" een goede aanleiding is voor een feestje.

Degene zonder wie ik niet eens in de buurt van het schrijven van een proefschrift zou zijn gekomen is mijn promotor en vriend Pier. Dat we nooit om gespreksstof verlegen zitten is een understatement. Onze gesprekken springen meestal van de hak op de tak en we associëren in het wilde weg maar ik kan daar erg van genieten. Daarbuiten was Pier dus ook essentiëel voor de totstandkoming van dit proefschrift. Op het kleine gebiedje waar ik wat van weet, weet Pier nog beduidend meer. Daarbij weet hij je als geen ander voor een onderwerp te enthousiasmeren. Hopelijk kan ik nog veel jaren met je samenwerken Pier. Buiten Pier zijn er natuurlijk nog meer onderzoekers die in belangrijke mate hebben bijgedragen aan dit proefschrift, b.v. als co-auteur. Zonder compleet te zijn wil ik hier in ieder geval Geert, Stephan en Peter noemen met wie ik zeer plezierig heb samengewerkt.

Ook de expertise, brede kennis en niet te vergeten de goede werksfeer op het KNMI hebben bijgedragen. Wat betreft die sfeer moet ik zeker het KNMI hardloopclubje noemen. Al sinds mijn indienstreding in oktober 1989, draagt dit

groepje bij aan een sectoroverschrijdende verbroedering en een gezonde geest in een gezond lichaam. De tijden op ons vaste rondje in het bos ($8.12 km$) lopen met de jaren op maar het enthousiasme blijft. Cisco, Rudolf, Jan, Theo, Hylke, Thomas, Steven, Isabel en anderen, blijf lopen! Behalve bij het hardlopen heb ik ook goede herinneringen aan KNMI collega's bij het zeilen, fietsen, borrelen en werken. Zonder compleet te zijn (sorry) noem ik er een paar: Maurice, Jan, Kees (nu 101 citaties voor ons probleemproject paper), Geert, Hylke, Sander, Isabel, Emiel, Jan Fokke, Natalie, Sebastian, Marieke, Bert (van Ulft), Bert (Holtslag), Toon, Cisco, Rudolf, Stephan (nu TU Delft), Jeanette, Jules, Janet. Ik zou over jullie een hoop mooie herinneringen kunnen ophalen maar dan wordt dit dankwoord erg lang.

Tenslotte wil ik nog een aantal mensen noemen die belangrijk voor me zijn. Allereerst mijn goede vrienden Roel en Hans die nu eindelijk hun rol als paranimfen kunnen vervullen. Onze open, kwetsbare en geanimeerde gesprekken zijn mij zeer dierbaar. Mark en Gert-Jan, onze vriendschap stamt al vanaf het begin van de middelbare school en zal altijd blijven. Mijn broers Hans, Jan en Frans; ik voel een warme, diepe en onverbrekelijke verbondenheid met jullie. Ik zou wel wat meer van jullie talenten, intelligentie en brede kennis willen hebben. Ook met mijn hartelijke en lieve schoonfamilie heb ik het erg getroffen.

En dan het belangrijkste voor het laatst. Allereerst mijn zoons Dijk en Wisse. Wat zijn jullie een ongelooflijk fijne mannetjes. Ik weet het, kinderen krijgen is in het licht van het klimaatprobleem niet verstandig. Maar als jullie elkaar een knuffel geven 's ochtends op het schoolplein, zie ik dat de omstaande ouders een glimlach op hun gezicht krijgen. Jullie maken de wereld een stukje, en mijn leven veel, mooier. Tenslotte Elske: Ik weet niet waar ik zo'n ongelooflijk lief, intelligent en mooi meisje aan verdiend heb maar ik hou van je, en hoop nog vele jaren mijn leven met je te delen.